Isotopic Composition of Galactic Cosmic Ray Boron, Carbon, Nitrogen, and Oxygen

Thesis by

P. Stinson Gibner

In Partial Fulfillment of the Requirements
for the Degree of
Doctor of Philosophy

California Institute of Technology
Pasadena, California

1992

(Defended March 23, 1992)

SRL 92-02

Acknowledgements

I would like to thank my advisor, Dr. Edward Stone, for his help and understanding through these many years. His insight and quick grasp of the pertinent issues always cut to the root of problems which arose during this analysis. Dr. Richard Mewaldt has never been at a loss for new suggestions and ideas. His help throughout this research and his comments and suggestions on the early drafts of this thesis are greatly appreciated. Dr. Stephen Schindler has also provided many useful suggestions as well as his considerable expertise in preparing and flying HEIST in the field, and the NSBF team did an excellent job of supporting the HEIST flight from Prince Albert. Dr. Thomas Garrard also deserves profuse thanks for miraculously putting a sparcstation on my desk, increasing my productivity 100%, and Dr. W. R. Webber has provided much assistance with cross sections and the propagation calculations.

I am indebted to many who preceded me in the development of HEIST, some who departed from Caltech before my arrival. I am especially grateful to Dr. Eric Grove who spent many hours of precious time teaching me the workings of the HEIST instrument and software during the period when he was finishing his thesis. He and Dr. Eric Christian are responsible for the development of much of the basic algorithms and software used in the analysis of HEIST data. James Weger and Dan Burke provided the engineering support needed to to calibrate and prepare HEIST for flight, and Biff Heindl provided much more than truck-driving and insulation expertise. Brownlee Gauld, Debby Kubly-Dunbar and Louise Sartain have provided assistance and a sympathetic ear for those occasional moments of frustration.

I wish to thank Mary Alice, Lea Ann, and Mikie, who have supported and encouraged me over the years and Stanley Frericks for his encouragement during my early years of study.

Finally, I want to thank LeThuy Dao who has been my companion and best friend for the last 12 years. Her help and advice have been invaluable.

Abstract

Relative abundances of the isotopes of galactic cosmic ray B, C, N, and O nuclei have been measured using the balloon-borne High Energy Isotope Spectrometer Telescope (HEIST). Analysis of data collected during the 1988 HEIST flight from Prince Albert, Saskatchewan, has resulted in mass histograms containing ~890 boron, ~3100 carbon, ~910 nitrogen, and ~3300 oxygen nuclei. Masses were derived using both the Cerenkov-Energy and $\Delta E - E'$ techniques, achieving a resulting rms mass resolution of ~0.26 amu. These isotopic composition measurements correspond to energy intervals at the top of the atmosphere of ~400-650 MeV/nucleon for boron, 430-670 MeV/nucleon for carbon, 440-680 MeV/nucleon for nitrogen, and 450-780 MeV/nucleon for oxygen, higher than previous direct isotope measurements for these elements.

The abundance ratios of carbon, nitrogen, and oxygen at the top of the atmosphere have been interpreted using an interstellar propagation model that includes improved fragmentation cross sections. Because cosmic ray boron is used as a "secondary tracer," the calculated isotope ratios of interest are insensitive to the value chosen for the solar modulation parameter, ϕ. The resulting abundance ratios for cosmic ray source material include $^{14}N/O = 0.042 \pm 0.014$ and $^{15}N/O \leq 0.040$, favoring no ^{15}N at the source. The carbon and oxygen isotopes at the cosmic ray source are $^{13}C/^{12}C = 0.005 \pm .011$ and $^{18}O/^{16}O = 0.0115 \pm .0038$, compared to solar system values of $^{13}C/^{12}C = 0.011$ and $^{18}O/^{16}O = 0.0020$. The derived cosmic ray source abundances show a possible enhancement of $^{18}O/^{16}O$ over the solar system value and a $^{13}C/^{12}C$ ratio consistent with solar system material. Taking a weighted average of our result with previous high resolution measurements of oxygen results in $^{18}O/^{16}O = 0.0075 \pm 0.0024$, an enhancement in ^{18}O of 3.75 times the solar system value.

Current isotope results are compared with models of cosmic ray origin. Both the supermetallicity model and the "anomalous" solar system model predict an ^{18}O excess in cosmic rays, however, the "anomalous" solar system model also predicts an excess in ^{13}C. The Wolf-Rayet model fits many of the currently observed isotopic excesses in cosmic rays, but the predictions for ^{18}O/^{16}O and the elemental N/O ratio are still in question. We conclude that although further refinements in the Wolf-Rayet model may explain ^{18}O and N/O, none of the presently available models account quantitatively for all of the observed differences in composition between cosmic rays and solar system material.

Table Of Contents

Acknowledgements ii

Abstract iii

1. Introduction 1

2. Instrument and Calibrations 13
  - 2.1. Instrument Description 13
    - 2.1.1. Detectors 13
    - 2.1.2. Trigger Logic Subsystem 17
    - 2.1.3. Data Recording 18
    - 2.1.4. Thermal Control 20
  - 2.2. Methods of Mass Analysis 20
    - 2.2.1. Cerenkov-Energy Method 21
    - 2.2.2. ΔE–E′ Method 23
  - 2.3. Bevalac Calibrations 28
    - 2.3.1. Mapping the NaI(Tl) Stack 29
    - 2.3.2. Mapping the Cerenkov Counters 33
    - 2.3.3. Energy Calibration of the Cerenkov Counters 44
  - 2.4. Event Positions and Trajectories 47
    - 2.4.1. Flight Position Resolution in the Na(Tl) Stack 53
    - 2.4.2. Position Resolution in the Cerenkov and Top Scintillator 59
    - 2.4.3. Trajectory Errors 63

3. Analysis Algorithms and Mass Resolution 66
  - 3.1. Energy Loss Algorithm 66
  - 3.2. Energy Loss Resolution 67
    - 3.2.1. Ionization Energy Loss Fluctuations 67

3.2.2. NaI(Tl) Photoelectron Statistics and Uniformity Errors 69
3.2.3. Summary of Single Layer Resolution 70
3.3. Total Energy Algorithm 72
3.4. Cerenkov Response Algorithm 73
3.5. Velocity Measurement 77
3.6. Mass Resolution for the Cerenkov-Energy Method 81
3.6.1. Contributions to Velocity Resolution 81
3.6.2. Total Energy Resolution 87
3.6.3. Resulting Mass Resolution 88
3.7. Mass Resolution for the ΔE–E' Method 104

4. Selection and Analysis of Flight Data 112
4.1. Flight Summary 112
4.2. Photomultiplier Stability and Drift Corrections 112
4.2.1. NaI(Tl) Stack 112
4.2.2. Cerenkov Counters 113
4.3. Preliminary Analysis of Stopping Events 116
4.3.1. Translate Tapes 116
4.3.2. Select Events Not Flagged 117
4.3.3. Select Events Which Miss Bottom Scintillator 117
4.3.4. Calculate Trajectories and Detector Responses 118
4.3.5. Identify Events Which Interact or Escape 119
4.3.6. Eliminate Center Plug Events 120
4.4. Selection and Analysis of Individual Elements 121
4.4.1. Charge Selection 121
4.4.2. Calculate Total Energy 126
4.4.3. Calculate Lorentz Factor, γ 127
4.4.4. Calculate Mass Estimators 127
4.5. Final Event Selections 142
4.5.1. Energy Cuts 142
4.5.2. Mass Agreement Cut Using ΔE–E' 143

4.5.3. Cerenkov Internal Agreement 144
4.5.4. Mass Agreement Cut 144
4.6. Mass Histograms 145

5. Abundance Analysis 161
5.1. Abundance Fitting 161
5.2. Corrections to Measured Abundances 163
5.2.1. Instrumental Corrections 163
5.2.2. Model of Atmospheric Interactions 170
5.3. Nuclear Interaction Cross Sections 173
5.4. Galactic Propagation 175

6. Interpretation and Conclusions 190
6.1. Isotopic Abundances at the Cosmic Ray Source 190
6.2. Models of Cosmic Ray Sources 193
6.2.1. Chemical Evolution of the ISM 206
6.2.2. Wolf-Rayet Stars 210
6.2.3. Supermetallicity Model 216
6.2.4. The Anomalous Solar System 217
6.3. Conclusions 218

References 220

Chapter 1

Introduction

When Thomas Wulf took an electroscope about 900 feet up the Eiffel Tower in 1910, he found that its rate of discharge decreased more slowly than expected by assuming that the ionizing radiation responsible for the discharge came from the ground. In 1911, Victor Hess began a series of balloon flights which found that after an initial decrease, an electroscope's discharge rate began to increase with altitude, becoming several times more rapid at an altitude of 17,500 feet. Hess correctly concluded that the increase in discharge rate was caused by an extraterrestrial source of ionizing radiation. These results were confirmed by a number of additional investigators including Robert Millikan who conducted a series of experiments measuring electroscope discharge rates at balloon altitudes and at various depths below the surfaces of two snow-fed lakes, and who is credited with introducing the term "cosmic rays" (e.g., Millikan and Cameron 1926). We now know that >98% of this penetrating radiation is atomic nuclei and <2% is electrons and positrons. At energies near 1 GeV/nucleon cosmic ray nuclei consist of ~87% protons and ~12% He. The remaining ~1% of the cosmic ray nuclei, which have nuclear charge $Z>2$, are dominated by B, C, N, and O, but span the natural periodic table with nuclei as heavy as $Z\sim 90$ having been detected.

Through studies of cosmic ray composition, we hope to identify the origins of cosmic rays and to use them as a probe of nucleosythesis and composition in other parts of the galaxy. The fundamental processes which determine the composition of the cosmic rays near Earth begin with the nuclear synthesis of cosmic ray material in stellar burning processes. The material must then be ejected from the stellar interior. Possible mechanisms include novae and supernovae events and quiescent winds from high mass loss stars (e.g., red giant, or Wolf-Rayet stars) or normal low-mass and intermediate-mass stars.

The elemental and isotopic composition of cosmic rays has been studied using a number of balloon and satellite experiments. The elemental composition of cosmic ray nuclei with nuclear charge, Z, ≤ 28 has been measured by satellite experiments including HEAO-3-C2 and IMP-8 (Engelmann et al. 1990, Garcia-Munoz and Simpson 1979) and by a variety of balloon-borne instruments (see reviews by Lund 1986, and Simpson 1983). High collection-area experiments, Ariel-VI and the HEAO Heavy Nuclei Experiment, have measured the much less abundant elements in the range from Z=34 up to about 90 (Fowler et al. 1987, Binns et al. 1989a, review by Binns et al. 1989b). Because of similarities between cosmic ray abundances and elemental abundances in the solar system and because the solar system is the only astrophysical location at which a nearly complete set of elemental and isotopic abundance measurements have been made, the solar system abundances (Cameron 1982, Anders and Grevesse 1989) are often used as a standard against which cosmic ray measurements are compared.

Cosmic ray elemental abundances show many similarities to those of solar energetic particles, which are known to have undergone selection effects based on their atomic first ionization potentials (FIP's) (Cassé and Goret 1978, and e.g. Breneman and Stone 1985). Elements which are less easily ionized (high FIP) are less abundant in the solar corona and solar energetic particles relative to their photospheric abundances, suggesting that the ionization state plays a role in the transport process from the photosphere to the corona. A similar FIP dependent fractionation appears to effect cosmic rays (e.g. Meyer 1985a). Figure 1.1 compares the elemental abundances of cosmic rays with those of solar energetic particles and shows the similarity of cosmic ray material to FIP fractionated solar system material. Important exceptions to the overall similarity in abundances are excess of carbon and the underabundance of nitrogen in the cosmic rays.

The acceleration mechanism for cosmic rays has not been conclusively identified, but it is likely that cosmic rays are accelerated by shock acceleration, powered by supernovae or by the terminal shocks from strong stellar winds. Models of shock acceleration predict that the resulting energy spectra at relativistic energies will be power laws in momentum (e.g., Blandford and Eichler 1987). After acceleration, the cosmic rays travel through the interstellar medium (ISM) where they gradually lose energy and occasionally collide with ISM material. These collisional nuclear interactions result in the original primary nucleus fragmenting to produce lighter "secondary" nuclei. One result of these fragmentations during galactic propagation of cosmic rays is the relatively high abundances of the elements lithium, beryllium, boron, and fluorine in cosmic rays. These elements are very rare in the solar system, and their abundances in cosmic rays are believed to be almost entirely due to the fragmentation of heavier "primary" nuclei. Cosmic rays are believed to be in a steady-state in which the acceleration of new source material is balanced by losses through escape from the galaxy, nuclear interactions, and energy loss to the ISM. A simple model of steady-state cosmic ray propagation has been constructed by assuming that cosmic rays are confined to travel inside a homogeneous volume which has a constant source input. When the border of the confinement volume is encountered a cosmic ray has a small chance of escape, hence the name "leaky-box" model. The mean escape length for cosmic rays appears to depend on cosmic ray energy, as can be seen from the energy dependence in the "secondary" to "primary", B/C ratio shown in Figure 1.2. The higher energy cosmic rays have, on average, traversed less material than the lower energy nuclei, and the B/C ratio can be fit by using a power law in rigidity to represent the mean escape length. This energy dependent escape length also softens the observed energy spectra of cosmic rays since the higher energy nuclei are lost more rapidly. Because fragmentation during galactic propagation plays an important role in determining observed cosmic ray abundances, accurate nuclear fragmentation cross sections are a critical input to any propagation model.

Finally, in order to get to Earth, the cosmic rays must propagate through the heliosphere where they undergo diffusion by scattering on magnetic field irregularities, are convected by the outward flow of the solar wind, and suffer adiabatic deceleration in the outwardly expanding magnetic field. Typical energy losses of

Figure 1.1

Ratios of cosmic ray source abundances to solar energetic particle abundances vs. atomic number, taken from Mewaldt (1983). The ratios are normalized at Si. Most of the abundance ratios are near unity suggesting that the composition and atomic selection effects are similar for both samples of material, but notable exceptions to the overall similarity are carbon, which is overabundant in cosmic rays, nitrogen, which is underabundant, and He.

Figure 1.1

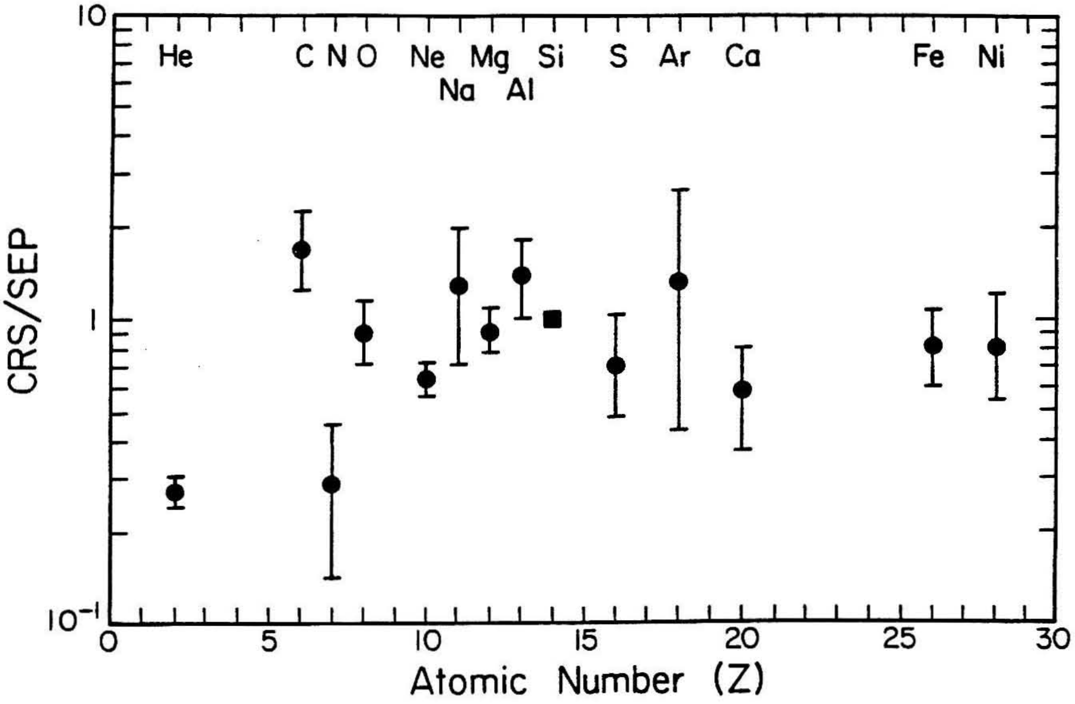

He
C
N
O
Ne
Na
Mg
Al
Si
S
Ar
Ca
Fe
Ni
10
1
10^{-1}
CRS/SEP
0
5
10
15
20
25
30
Atomic Number (Z)

Figure 1.2

Selected measurements of the "secondary" to "primary," B/C ratio in cosmic rays. Boron is thought to be absent at the cosmic ray source (or present in only minute quantities) and is created by the fragmentation of heavier cosmic ray nuclei during propagation through interstellar space. This secondary to primary ratio constrains the path-length through which the cosmic rays have traveled. Measurements: Open circle: this work. Solid circles: Krombel and Wiedenbeck 1988. Solid squares: Engelmann et al. 1990. Solid triangles: Swordy et al. 1990.

Figure 1.2

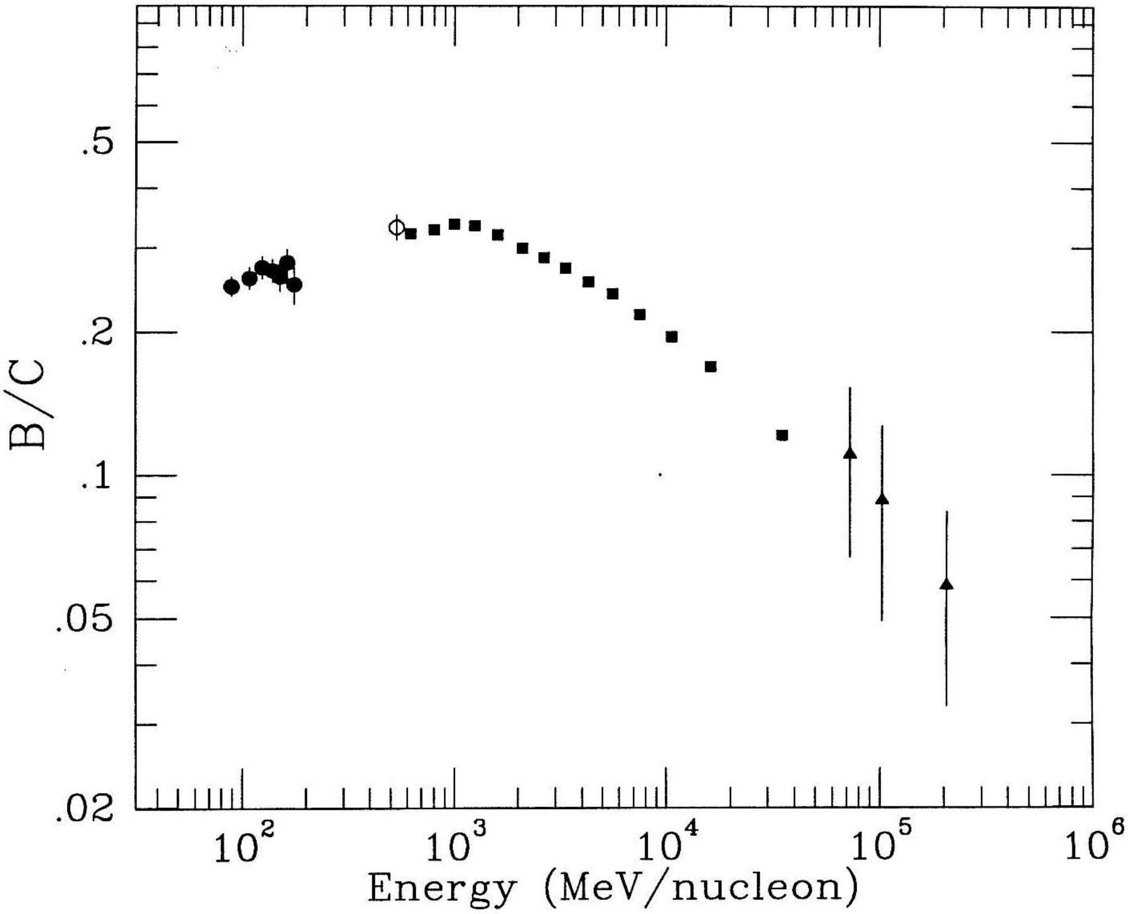

200-400 MeV/nucleon during propagation into the heliosphere strongly affect the intensities of cosmic rays below ~1 GeV/nucleon, and make it impossible to observe galactic cosmic rays with interstellar energies below ~300 MeV/nucleon. The effects of heliospheric propagation vary with the solar cycle and are termed "solar modulation."

Isotopic measurements are particularly interesting as probes of nuclear processing since they are less prone to the fractionation which may affect elemental abundance comparisons. However, isotope studies are more difficult than elemental measurements because they require much better resolution. From the isotope measurements which have been made, a number of differences from solar system abundances are indicated.

One of the first isotopic anomalies discovered is the large excess of ^{22}Ne in cosmic rays (see e.g., review by Mewaldt 1989 and refs. therein). The ^{22}Ne/^{20}Ne ratio at the cosmic ray source (CRS) has been found to be ~3.5 to 5.5 times the solar system value, depending on whether meteoritic neon-A or solar wind measurements are used for the solar system value. A number of measurements have also indicated an excess in the neutron-rich isotopes of Mg and a possible excess in silicon's neutron-rich isotopes. Also, the ^{12}C/^{16}O ratio in cosmic rays is found to be about twice the C/O ratio found in solar system material.

Analysis of nitrogen isotope measurements was controversial for some time. Before the recent improvements in fragmentation cross sections, propagation models which fit the observed B/C ratio had difficulty in producing the observed amount of ^{15}N without assuming a large ^{15}N enhancement at the cosmic ray source. An additional problem arose because low energy measurements corresponded to a N/O ratio ~3 times smaller than the solar system value, while high-energy measurements led to an N/O ratio at the CRS which was nearer to the solar system value (see review in Mewaldt 1989). Recent analysis of the nitrogen isotope measurements using recently measured fragmentation cross sections has led to the conclusion that the ^{14}N/^{16}O ratio at the CRS is ~1/3rd to 1/4th of the solar system value (Krombel and Wiedenbeck 1988; Gupta and Webber 1989).

Since the review by Mewaldt (1989) the cosmic ray source abundances of neon, magnesium, and silicon have been re-examined by Webber, Soutoul, Ferrando, and Gupta (1990) using a propagation calculation which included recently measured fragmentation cross sections (Webber et al. 1990a-c). These recent cross section measurements by the University of New Hampshire group include over 300 individual isotope cross sections measured at 600 MeV/nucleon and cover ~70% of the cosmic ray nuclei arriving at Earth (Gupta and Webber 1989). These measured cross section have uncertainties of ~10% or better and represent a great improvement over the previously used semi-empirical formula of Tsao and Silberberg (1979) which was estimated to have an rms error of ~35%. Cross sections not experimentally measured have been calculated using a new empirical formulation (Webber et al. 1990d) which is accurate to ~20%. Webber and co-workers have reinterpreted many previous cosmic ray isotope measurements using the new fragmentation cross sections. The results are shown in Table 1.1 for comparison with the abundances reported by Mewaldt (1989). Some of the differences in Table 1.1 result from different weightings of the experimental cosmic ray data as well as from revisions in the cross sections.

Table 1.1: Cosmic-Ray Source Composition

Normalized to Solar System Ratios

	CRS/(Solar System)	
Isotope Ratio	Mewaldt (1989)	Webber et al.(1990)
$^{12}C/^{16}O$	~ 2	
$^{14}N/^{16}O$	0.25 ± 0.1	$0.3 \pm 0.1^{*}$
$^{13}C/^{12}C$	1.6 ± 1.2	$0.3 \pm 0.5^{**}$
$^{22}Ne/^{20}Ne$	3.3 ± 0.5	3.8 ± 0.5
$^{25}Mg/^{24}Mg$	1.6 ± 0.3	1.2 ± 0.2
$^{26}Mg/^{24}Mg$	1.5 ± 0.2	1.4 ± 0.2
$^{29}Si/^{28}Si$	1.5 ± 0.3	0.9 ± 0.4
$^{30}Si/^{28}Si$	1.4 ± 0.4	0.9 ± 0.3
$^{34}S/^{32}S$	≤ 3	
$^{54}Fe/^{56}Fe$	≤ 1.7	
$^{57}Fe/^{56}Fe$	≤ 4	
$^{58}Fe/^{56}Fe$	≤ 10	
$^{60}Ni/^{58}Ni$	1.9 ± 1.3	

* Gupta and Webber (1989)

** Webber and Soutoul (1989)

Analyzing previous measurements using the new fragmentation cross sections, Webber and Soutoul (1989) find that ^{13}C relative to ^{12}C may be less abundant in cosmic rays than it is in the solar system. Webber et al. (1990) find that the excesses of ^{25}Mg and ^{26}Mg in the cosmic rays are slightly reduced by the new cross sections, and their average of silicon isotope measurements indicates that cosmic ray ^{29}Si and ^{30}Si abundances are very near solar system values. The silicon isotopic abundances remain controversial. Averaging the recent measurement of Si by the

ALICE experiment (Hesse et al. 1991) with the earlier high-resolution measurements by the Berkeley experiment on ISEE-3 (Wiedenbeck and Greiner 1981b) leads to an excess in ^{29}Si and ^{30}Si by a factor of $\sim 1.3 \pm 0.4$ over the solar system ^{29}Si/^{28}Si and ^{30}Si/^{28}Si ratios when interpreted with the propagation model used in chapter 5.

Differences between the isotopic composition of cosmic ray and solar system material indicate a different nucleosynthetic history for cosmic rays. If cosmic rays represent a sample of ISM material, then models of Galactic chemical evolution would predict that they would differ in composition from the solar system which formed some $\sim$4.5 billion years ago. Several models predict an increase in the ^{13}C/^{12}C ratio with galactic age (Tosi 1982; Greggio and Tosi 1986; Tosi 1988; Audouze 1985; Gusten and Mezger 1982). Models constructed by Audouze (1985) and Gusten and Ungerechts (1985) also predict a decrease with time in the ^{15}N/^{14}N ratio.

The discovery of the ^{22}Ne excess in cosmic rays led to a number of models of cosmic ray origin which might explain the excess. These models include suggestions that cosmic rays are produced by metal rich stars or by Wolf-Rayet stars which expel freshly synthesized He-burning products.

The "supermetallicity" model (Woosley and Weaver 1981) in which cosmic rays originate from metal-rich regions of the Galaxy predicts roughly equal enhancements for ^{18}O, ^{22}Ne, ^{25}Mg, ^{26}Mg, ^{29}Si, ^{30}Si, and other neutron-rich nuclei. When normalized to fit the ^{22}Ne excess, it predicts enhancements for the neutron rich Mg and Si isotopes that are larger than are observed. In the Wolf-Rayet model (Cassé and Paul 1982), a fraction of cosmic rays are from material which is expelled by Wolf-Rayet stars and then combines with "normal" cosmic ray source material to produce enhancements in cosmic ray ^{12}C, ^{16}O, ^{22}Ne, ^{25}Mg, and ^{26}Mg. The model, again normalized to fit the ^{22}Ne excess in cosmic rays, appears to fit the cosmic ray Mg and Si observations and predicts that the CRS ratio for ^{13}C/^{12}C should be lower than in the solar system. Whether the model can explain the N/O ratio in cosmic rays is still in question.

Finally, Olive and Schramm (1982) suggested that cosmic rays may be representative of the ISM composition and that the solar system may have formed as part of an OB association and been enriched by the ejecta of supernovae within the association. The resulting "anomalous" solar system would be enriched in α–particle nuclei such as ^{12}C, ^{16}O, and ^{20}Ne. Normalizing to this "anomalous" solar system composition, the model predicts that both the ISM and cosmic rays will show enhancements in C/O, ^{22}Ne, ^{17}O, ^{18}O, and ^{13}C, qualitatively consistent with the observations except for the predicted ^{13}C excess. A more detailed discussion of these models is given in chapter 6.

New measurements are presented here which further confirm the low ^{14}N/O abundance at the cosmic ray source, and which indicate an excess of ^{18}O in cosmic ray material. In this study, we have used a balloon-borne high energy isotope mass spectrometer to make new measurements of the isotopic composition of boron, carbon, nitrogen, and oxygen at energies higher than previous direct isotope measurements. Our results show consistency with earlier observations and indicate a possible underabundance of ^{13}C and an excess of ^{18}O relative to the solar system ^{13}C/^{12}C and ^{18}O/^{16}O ratios, respectively. In the following chapters we describe the instrument design and calibrations, the analysis method and achieved mass resolution, and the analysis of flight isotope data. Current results are then compared with measurements of the isotopic composition of molecular clouds in the ISM and with models of cosmic ray nucleosynthetic sources.

Chapter 2

Instrument and Calibrations

2.1. Instrument Description

HEIST (High Energy Isotope Spectrometer Telescope) is a balloon-borne mass spectrometer designed to measure cosmic ray isotopes from Be through Ni ($4 \leq Z \leq 28$) at energies in the range of ~400 MeV/nucleon to ~1200 MeV/nucleon. Figure 2.1 shows a schematic representation of the HEIST-2 detector elements. The instrument consists of a stack of 12 NaI(Tl) scintillators (L1 through L12), two plastic scintillators (S1 and S2), and two Cerenkov counters (C1 and C2). HEIST-2 has been modified from the HEIST-1 instrument which was flown in 1984, and which is described by Grove (1989) and Lau (1985). For simplicity, we refer to HEIST-2 as "HEIST" throughout this thesis. The discussion here concentrates on the major modifications and improvements to the instrument since the 1984 flight.

2.1.1. Detectors

The NaI(Tl) scintillator stack directly measures the ionization energy loss of cosmic ray nuclei. The stack also measures the trajectories of the cosmic rays. The scintillators, each nominally 52 cm in diameter and 2 cm thick, comprise a total thickness of 87.2 g/cm^2. As described in detail by Lau (1985), each "disk" of NaI(Tl) is mounted in an annular plexiglass light pipe and viewed by six 1.5" photomultiplier tubes (PMTs) mounted symmetrically around the edge of the disk. The layers are separated by light shields of black-painted aluminum foil.

The stack is hermetically sealed in a dry environment to protect the hygroscopic NaI(Tl). The thickness of the top and bottom walls of the hermetic can that

Figure 2.1

Schematic representation of the HEIST instrument, which consists of two plastic scintillators (S1 and S1), two Cerenkov counters (C1 and C2), and a stack of twelve layers of NaI(Tl) scintillator. The top plastic scintillator, S1, is used in the system trigger and for charge measurement. The C1 Cerenkov radiator is Teflon ($n = 1.36$), and the C2 Cerenkov radiator is Pilot-425 ($n = 1.51$). The geometry factor of the instrument is $\sim 0.25\ m^2sr$.

Figure 2.1

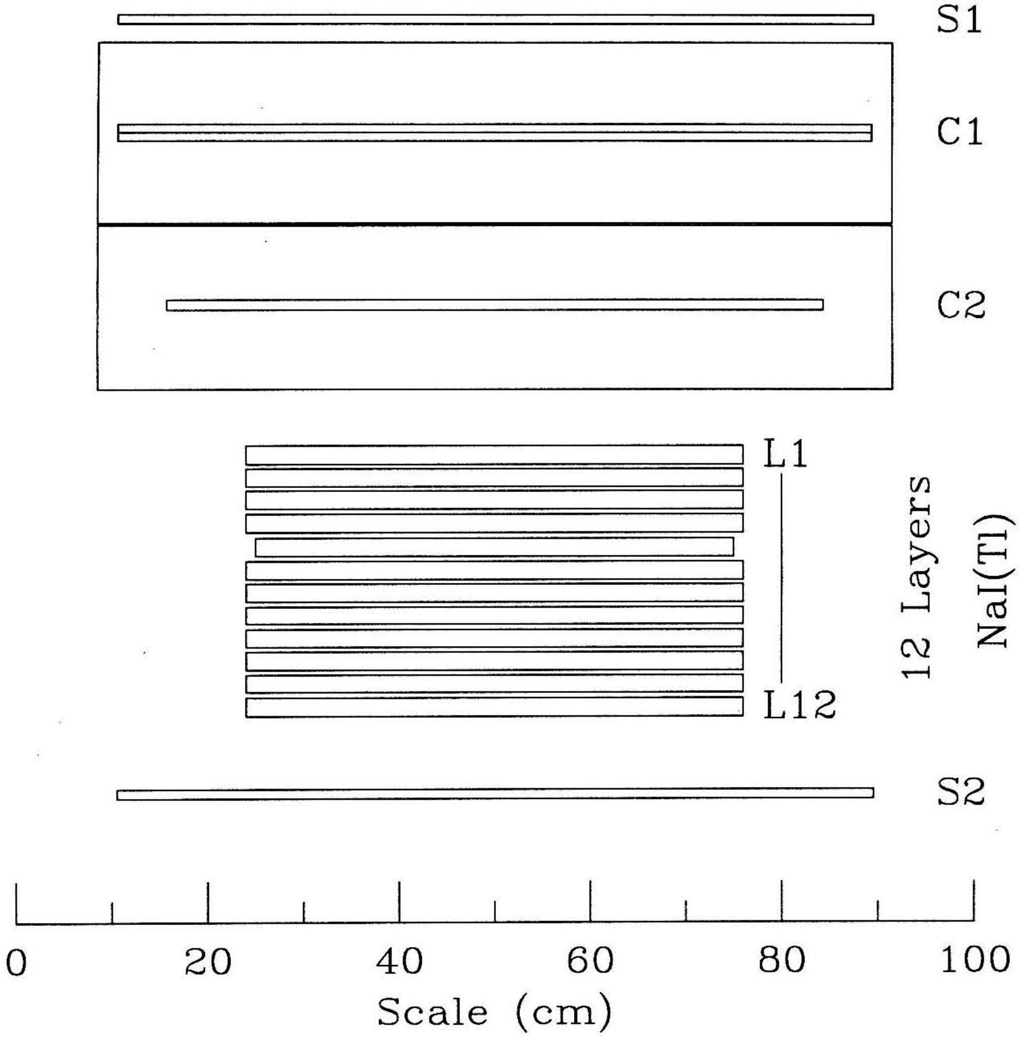

encloses the NaI(Tl) has been minimized to reduce the amount of passive material traversed by the measured cosmic rays. The hermetic can end walls consist of 0.41 cm (1.1 g/cm^2) of aluminum. An area 3.8 cm in radius at the center of each end has been reinforced with an Al plug 1.6 cm (4.3 g/cm^2) thick. These center plugs were provided as attachment points for stiffening plates used during transportation of the hermetic can. One of the PMTs viewing layer 3 failed after the stack was sealed in its hermetic can. The resulting degradation in energy resolution for layer 3 is small.

The top Cerenkov counter, C1, contains a radiator made by sandwiching together two 0.795 cm thick sheets of Teflon (TFE), after coating each sheet with PTP wave-shifter to improve light output. The resulting 1.59 cm (3.4 g/cm^2) thick radiator has a radius of 39.4 cm and is centered in a light collection box and viewed by 16 RCA S83006EM1 5″ PMTs. The effective index of refraction of ~1.36 corresponds to a threshold energy of 443 MeV/nucleon.

The second Cerenkov counter, C2, contains a Pilot 425 radiator which is 1.63 cm (1.94 g/cm^2) thick and 34.28 cm in radius. The index of refraction of ~1.52 corresponds to a threshold energy of 305 MeV/nucleon. This radiator is also centered in its light collection box and viewed by 16 RCA PMTs. The interiors of both light collection boxes were painted with high-reflectance white $BaSO_4$ paint to maximize light collection. The 16 PMTs in each counter are spaced symmetrically around the circumference of the light collection box and are sequentially numbered from 1 to 16. There are only 12 analog to digital converters (ADCs) available to digitize the signals from each counter, so each of the odd numbered tubes is paired with the diametrically opposite PMT. Thus, HEIST records 8 individual PMT responses and 4 responses from PMT pairs for each of the Cerenkov counters.

The top and bottom scintillators, S1 and S2 respectively, are made of NE110 plastic. The 1 cm thick, 79 cm diameter plastic scintillators are wrapped in an aluminum foil and black paper tape light shield. Six 1.5″ PMTs view each scintillator on its edge. The six PMT signals from the top scintillator are individually digitized and recorded. In addition, the top scintillator has two 1.5″ EMI D550 PMTs whose outputs go directly to the trigger subsystem. Two PMT signals from the bottom scintillator are individually digitized, and the outputs of the other four PMTs are paired into two additional ADCs.

2.1.2. Trigger Logic Subsystem

The trigger subsystem selects cosmic ray events which have a nuclear charge of 4 or greater, while discriminating against the much more numerous H and He events. The desired events are identified by a two step process. First, the subsystem requires a fast trigger from the two timing PMTs, T1 and T2, in the top scintillator. The outputs of these PMTs are tested by analog comparators against a threshold value corresponding to ~7 times the minimum-ionizing proton signal. The T1T2 fast trigger condition can be selected from four different states: "T1 or T2," "T1 and T2," T1 only, or T2 only. For all of the 1988 flight, the fast trigger condition was "T1 or T2."

Following a valid fast trigger condition, the trigger logic tests the slow coincidence condition which verifies that the event has a nuclear charge greater than Z=2. The slow coincidence tests the levels of the sums of PMTs in the top scintillator, S1, the fifth layer of the NaI(Tl) stack, L5, and the first two layers of the stack. Separate, commandable discriminator thresholds are provided for testing S1 and L5. The sum of PMTs in the top two stack layers is tested against two discriminator levels. The lower discriminator test yields trigger logic condition L12A, and the higher discriminator yields L12B. These two discriminators also have five levels which can be selected by command. The slow coincidence condition can be commanded into four states, but the condition "S1 and [(L12A and L5) or L12B]" was used throughout the 1988 flight. The discriminator thresholds used with this slow coincidence condition require that the top scintillator response must be greater than that from a minimum ionizing alpha particle. In addition, they require either that the first two stack layers' response be larger than that produced by a low energy Be nucleus (L12B condition) or that the first two layers have a response equivalent to a relativistic Be nucleus (L12A condition) and that layer 5 must have a response greater than a minimum ionizing alpha particle (L5 condition).

When this slow coincidence is satisfied, an event trigger is generated and the 108 PMT signals are digitized and recorded. In addition to the 108 measured signals, each recorded event includes eight words of trigger rate data. The first seven rates are the number of triggers since the last recorded event for: T1, T2, T1T2 coincidence, S1, L5, L12A, and L12B. The eighth word is the time in milliseconds since the last recorded event.

Triggers which we call External Triggers can be generated by an external pulser for electronic calibration of the ADCs, or they can be generated by two timeout mechanisms of the trigger logic itself. The trigger logic generates an External Trigger every 33 seconds in order to provide a means for monitoring the ADC pedestals throughout the flight. This provides a measure of the electronic noise at the ADCs. Also, an External Trigger is generated if no valid event trigger has occurred in the previous 1.5 seconds. This 1.5 second timeout was developed to protect against a failure mode of the data recording system.

The baseline restoration time of the pulse-shaping circuitry used in HEIST can be as long as $\sim 200\ \mu s$ for large signals. As a warning of possible pulse pile-up, the trigger logic sets the Hazard flag for any event which occurs within 256 μs after a prior T1T2 coincidence. The fast coincidence rate for the 1988 flight of 950 to 1000 per second resulted in 22.5% of the flight events flagged as Hazard events. As discussed in §4.3.2, the Hazard events were included in the data set used for isotope analysis.

2.1.3. Data Recording

There are a total of 116 PMTs on HEIST, whose outputs are used to calculate the event trajectory, velocity, energy, charge, and mass. Twenty of these PMTs are paired, and the remaining 96 are individually pulse height analyzed. In addition, the signal from the sum of the anode outputs from all 16 PMTs is digitized for each Cerenkov counter resulting in a total of 108 recorded pulse heights for each event.

The anode signals of the scintillator PMTs are connected to charge integration circuits. These circuits then connect to a sample and hold chip which can be read and digitized by a 12-bit (4096 channel) ADC. Since the Cerenkov counters produce much less light than the scintillators, the Cerenkov PMT final dynode signal goes through a charge sensitive pre-amplifier with a gain of ~70 before the signal is sent to the sample and hold circuit. The stack ADCs also have a high gain mode which uses the pre-amplifiers to increase the scintillator PMT signals to allow calibration and testing of HEIST with ground level muons. The ADC conversion takes about 35 μs , and the time required for the on-board microprocessor to read out all 108 ADCs is approximately 28 ms.

In addition to recording the ADC levels for each event, the microprocessor reads data from a number of housekeeping sensors including 15 temperature transducers, 2 internal pressure transducers, an altimeter, and 7 voltage monitors. The current state of HEIST's trigger logic subsystem, its thermal control subsystem, and the state of the relays which control the PMT high voltages and video cassette recorder (VCR) power are also monitored and encoded into 64 bits of digital housekeeping data. In addition, the microprocessor computes and records a checksum which can be used to test for bit errors in the data. The housekeeping information is combined with the ADC data for each event and is telemetered to the ground at a rate of about 9 events/sec (~20kbit/sec) where it is recorded. Since the telemetry rate is limited, all of the events are not sent to the ground station. The data are also stored on-board in a memory buffer which holds 200 events. When the 200 event buffer fills, the data are transferred to a 1000 event buffer, and when the 1000 event buffer fills, the video formatter reads the 1000 events and formats them into a video stream which can be recorded by one or both of two on-board VCRs used for data storage. Both VCRs recorded the event data in parallel throughout the 1988 flight. Each VCR tape has a capacity of about one million events.

2.1.4. Thermal Control

Since the responses of the NaI(Tl) scintillators in the stack and the PMTs are dependent on temperature, a number of measures were undertaken in order to control the on-board temperatures. The exterior of the HEIST aluminum pressure vessel was fitted with a 4 inch thick layer of Hitco insulation which was painted white in order to minimize absorptance. Inside the pressure vessel, another layer of insulation isolated the Cerenkov counters and the NaI(Tl) scintillators from the remainder of the instrument. In order to dissipate the heat from the 260 watts of electrical power required by the electronics and power conditioning subsystems, HEIST incorporates an active cooling system. The cooling system consists of a 50 liter capacity aluminum torus with a valving system for venting to the near-vacuum outside the gondola. Prior to flight, the torus is partially filled with water. Periodically venting water vapor during the flight allows us to control the temperature within the instrument. A three valve design prevents any single point failure mode of the venting system. The valves can be controlled automatically by using feedback from temperature sensors, or they can be controlled from the ground. During the Prince Albert flight, we retained ground control of the cooling system throughout the flight and were able to keep the temperature of the NaI(Tl) stack constant to within $\pm 0.6^\circ$C. The maximum variation in NaI(Tl) response due to thermal effects should be less than 0.25% given the temperature dependence of $0.2\%/^\circ$C measured by Yamashita (1988). Gain changes in the PMTs due to temperature variations ($\sim 1\%/^\circ$C) and other effects are corrected as described in §4.2.

2.2. Methods of Mass Analysis

HEIST uses its Cerenkov counters to measure the velocity of cosmic ray events and the NaI(Tl) stack to measure the total energy of stopping events. The masses of cosmic ray nuclei are found using the Cerenkov-Energy technique as the primary method of mass estimation (Webber et al. 1973). This method can be used over the range of energies for which the nuclei are above threshold in one or both Cerenkov counters and are below the energy at which they will completely penetrate the stack of NaI(Tl) scintillators. Since the scintillator stack makes multiple energy loss measurements for each cosmic ray nucleus, we can also utilize the $\Delta E - E'$ method of mass estimation. The mass resolution resulting from this method limits its use to the lighter nuclei studied by HEIST.

2.2.1. Cerenkov-Energy Method

The mass, M, of a cosmic ray nucleus is related to its kinetic energy, E, and its β, the particle velocity divided by the speed of light. Expressed in terms of the Lorentz factor $\gamma = 1/\sqrt{(1-\beta^2)}$ this relation is

$$E = (\gamma - 1) Mc^2 . \tag{2.1}$$

Equivalently,

$$M = \frac{E}{c^2(\gamma-1)} . \tag{2.2}$$

HEIST provides information to obtain the velocities of nuclei which are above threshold in the Cerenkov detectors and also their total energy as they slow to a stop in the stack of NaI(Tl) scintillators. Once the velocity and total energy of an event is known, its mass may be calculated using Equation 2.2. Nuclei with energies sufficient to penetrate and escape the scintillator stack cannot be used for mass analysis since HEIST cannot measure their total energy.

Cerenkov radiation is created when a charged particle travels through a medium at a velocity greater than the local phase velocity of light in that medium. Light in a medium with an index of refraction n has a phase velocity $v_{ph} = c/n$. Thus to produce Cerenkov light an incident particle must have a velocity, β, greater than the threshold velocity, $\beta_0 = 1/n$. The amount of light generated can be calculated from the relation (Jelley 1958 or Ahlen et al. 1976):

$$C(\beta) = \frac{Z^2 e^2}{\hbar c^2} \int \int_{n\beta>1} \left[1 - \frac{1}{n^2(\omega)\beta^2} \right] d\omega \, dx , \tag{2.3}$$

where ω is the angular frequency of the emitted light, and $n(\omega)$ is the frequency dependent index of refraction of the medium. In practice, the amount of light collected from a Cerenkov counter also depends on the efficiency with which the light can escape the radiator without being absorbed, the collection efficiency of the counter, and the quantum efficiency of the PMTs. One way to increase Cerenkov light collection is to dope or coat the radiator with a wave-shifting material which converts short wavelength Cerenkov light into lower frequency light which can more easily escape the radiator and convert to photoelectrons at the PMT photocathode. We can integrate over both path-length and frequency so that $n(\omega)$ is replaced by an effective index of refraction, n. The resulting Cerenkov light generated by an above threshold particle is

$$C(\beta) = Z^2 N_\mu \sec\theta \; f(\beta) \,. \tag{2.4}$$

Where

$$f(\beta) = \left[\frac{1 - 1/(n^2\beta^2)}{1 - 1/n^2} \right] , \tag{2.5}$$

and where N_μ is the number of photoelectrons collected from the passage of a particle of charge $Z = 1$ and velocity $\beta = 1$ at normal incidence. The angle from normal incidence is given by θ, and $\sec\theta$ corrects for the increase in the nuclei's path-length through the radiator. The function $f(\beta)$ is the amount of light produced expressed as a fraction of primary Cerenkov light which would be produced by a particle with a velocity of $\beta = 1$. This fractional representation of light output will be referred to as the "fraction of relativistic light" and can also be expressed as a function of Lorentz factor γ as

$$f(\gamma) = \frac{\gamma^2(n^2-1) - n^2}{(n^2-1)(\gamma^2-1)} \,. \tag{2.6}$$

The fraction of relativisic light, $f(\gamma)$, and $df(\gamma)/d\gamma$ are shown in Figure 2.2 for three values of effective index of refraction. For particles with energies just above the energy corresponding to the Cerenkov threshold, where $df(\gamma)/d\gamma$ is large, a small change in velocity produces a large change in Cerenkov response, and the Cerenkov counter can provide a very accurate measure of velocity. By selecting a radiator material with the proper index of refraction we can choose the energy range over which the velocity measurement is most accurate.

In addition to Cerenkov light from the primary incident nucleus, there will be Cerenkov emission from secondary high-energy "knock-on" electrons produced by the passage of the primary through the radiator and the overlying material. Also, there will be Cerenkov light produced in the white $BaSO_4$ paint which covers the interior of the light integration box. There will be scintillation light from the N_2 atmosphere inside the counter, from the $BaSO_4$, and from the radiator material. A model which includes all these sources of background light is described in §2.3.3. This model has been used to fit calibration data taken at the Lawrence Berkeley Laboratory Bevalac accelerator in order to calculate the total light, $C_{tot}(Z,\gamma)$, produced by the counters as a function of particle charge and velocity. This function can then be inverted to calculate velocity as a function of counter response for nuclei of known charge. The dominant contributions to the mass resolution and the resulting resolution for the Prince Albert flight are discussed in chapter three.

2.2.2. ΔE−E′ Method

Over a limited interval of energies of interest, the range-energy relation for a proton can be approximated as a power law.

$$R_p(E) = kE^{\lambda}, \tag{2.7}$$

where k and λ are constants, and E is the proton's kinetic energy. To a reasonable approximation, the range of a nucleus of mass M and charge Z is

$$R(E) = \frac{M}{Z^2} R_p(E) \tag{2.8}$$

$$= \frac{M}{Z^2}\, k \left(\frac{E}{M}\right)^{\lambda}, \tag{2.9}$$

where E/M is the kinetic energy per nucleon.

Figure 2.3 illustrates the measurements used for the $\Delta E - E'$ method of mass estimation. A nucleus enters the first detector with kinetic energy E. It deposits energy ΔE in the first detector, and then deposits its remaining kinetic energy, E',

Figure 2.2

The fraction of relativistic Cerenkov light, $f(\gamma)$, and $df/d\gamma$ as a function of kinetic energy per nucleon for three values of index of refraction: The curves for $n = 1.36$ and $n = 1.51$ represent the Teflon and Pilot counter primary Cerenkov response. The curve for $n = 1.10$ is shown for comparison only. The Cerenkov response is a sensitive function of particle velocity in the regions where $f(\gamma)$ increases rapidly and $df/d\gamma$ is large.

Figure 2.2

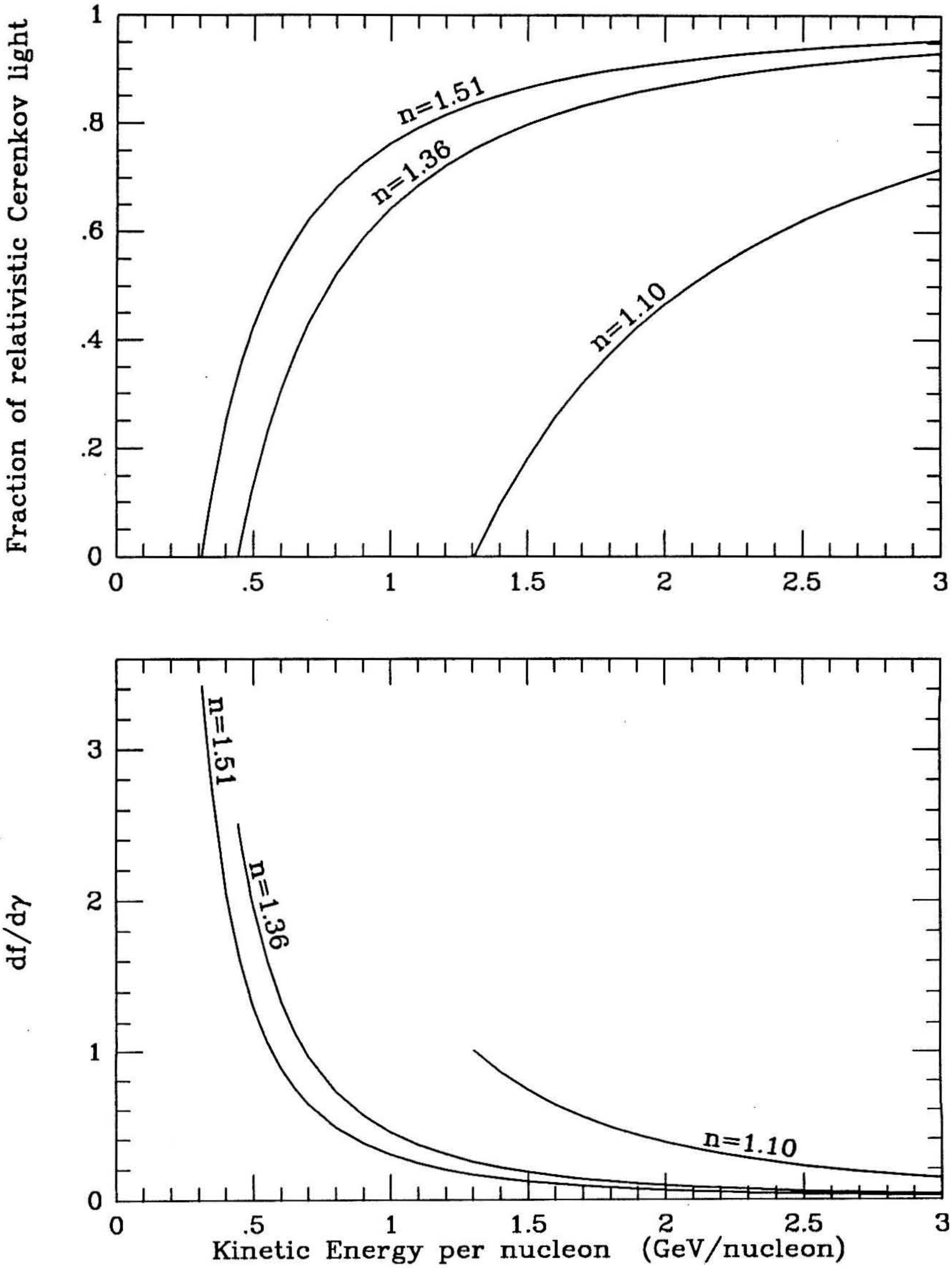
Fraction of relativistic Cerenkov light
1
.8
.6
.4
.2
0
0
.5
1
1.5
2
2.5
3
n=1.51
n=1.36
n=1.10
df/dγ
3
2
1
0
0
.5
1
1.5
2
2.5
3
n=1.51
n=1.36
n=1.10
Kinetic Energy per nucleon (GeV/nucleon)

Figure 2.3

The ΔE–E' method of isotope identification. A nucleus with mass M and charge Z enters the first detector with kinetic energy E. It deposits energy ΔE in the first detector, and then deposits its remaining kinetic energy, E' , in the second detector. Given the range-energy relation and the path-length traveled through the first detector, we can calculate the mass of the nucleus by solving the equation $R(E,Z,M) - R(E',Z,M) = T\sec\theta$ for mass, M.

Figure 2.3

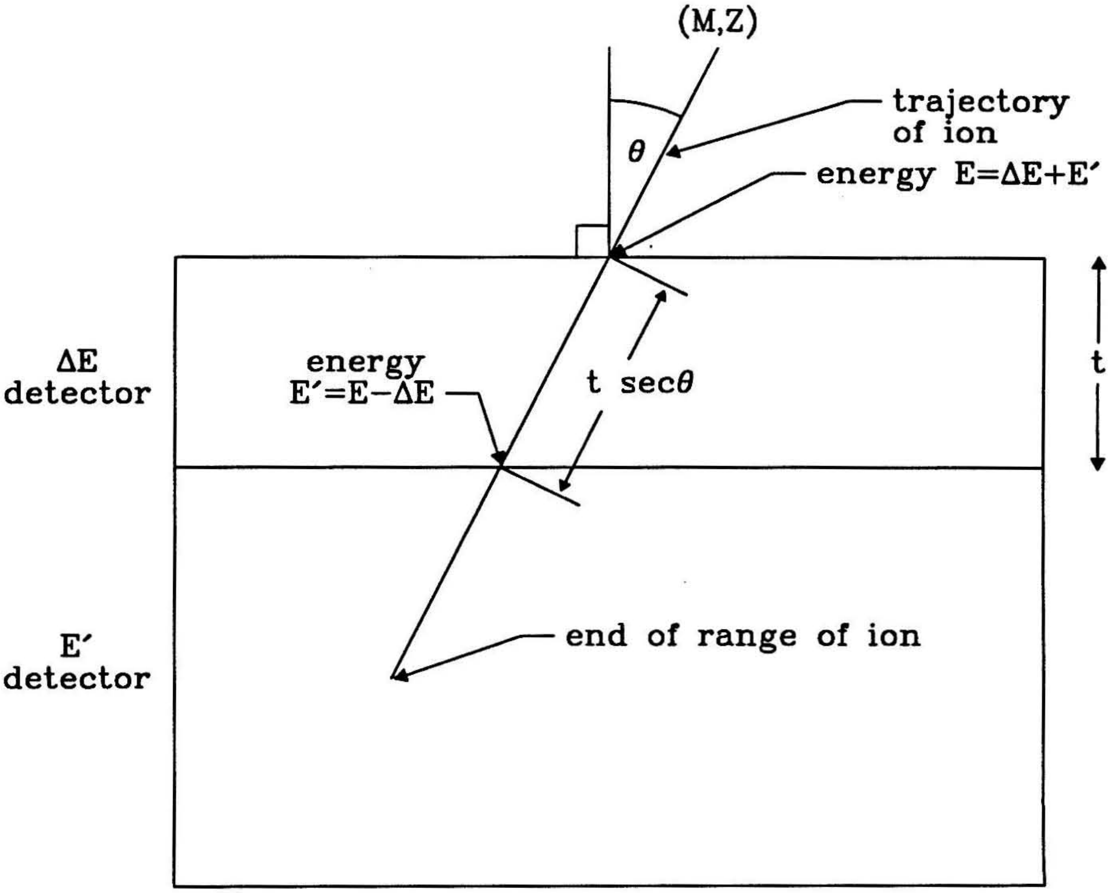
(M,Z)
trajectory of ion
θ
energy E=ΔE+E′
t
t secθ
ΔE detector
energy E′=E−ΔE
end of range of ion
E′ detector

in the second detector. If we know the nucleus' range-energy relation and the path-length traveled through the first detector, we can calculate the mass of the nucleus. That is, we can solve the equation

$$R(E,Z,M) - R(E',Z,M) = t\sec\theta \tag{2.10}$$

for mass, M, where $t\sec\theta$ is the path-length traveled through the ΔE detector. Substituting from Equations 2.8 and 2.9 we have

$$M = \frac{Z^2\, t\sec\theta}{R_p(E) - R_p(E')} \tag{2.11}$$

$$= \left[\frac{Z^2\, t\sec\theta}{k(E^{\lambda} - E'^{\lambda})}\right]^{\frac{1}{1-\lambda}} . \tag{2.12}$$

Since the NaI(Tl) stack consists of twelve layers, multiple mass estimates can be calculated using different combinations of the layers. For a nucleus stopping in layer 12, there are eleven different possible layer combinations for the E' measurement. Averaging over the multiple mass measurements improves the mass resolution of this method, and requiring consistency among the mass measurements provides a method of eliminating events which fragment in the instrument. Section 3.7 discusses the mass resolution resulting from this method of isotope measurement.

2.3. Bevalac Calibrations

Detectors used in the HEIST instrument have been tested and calibrated using ion beams at the Lawrence Berkeley Laboratory Bevalac accelerator. In November 1982, the full HEIST-1 detector system, configured as flown in 1984, was calibrated at the Bevalac. After the 1984 flight, the two HEIST-1 Cerenkov counters were replaced with the Pilot counter and the Teflon counter which were used during the 1988 flight. These two new counters were taken to the Bevalac and calibrated with heavy ion beams in November 1987, but the NaI(Tl) stack was not recalibrated.

2.3.1. Mapping the NaI(Tl) Stack

In 1982, a ^{55}Mn beam was used to map the positional dependence of the scintillator stack response. The 1752 MeV/nucleon ^{55}Mn beam penetrated most of the stack, stopping in layers 11 and 12. The approximately 900,000 events recorded covered ~95% of the detector area. As discussed in Grove (1989), the calibration data suffered from PMT gain variations on the order of a few percent. These variations were named "spill-gain" and "run-gain" variations because they are dependent on the number of the event in each beam spill and on the number of the spill in each run. A set of stack maps constructed in 1984 was used for analysis of the 1984 flight data. In 1989, the Bevalac data were re-analyzed in order to include correction factors for the "spill-gain" and "run-gain" variations. The areas of the stack maps not covered by the calibration were completed by interpolation and extrapolation from the surrounding map data. This new set of stack maps was used in the analysis of the 1988 flight data.

Figures 2.4(a) and 2.4(b) show isometric views of the response map of Layer 1 PMT A and for the sum of all six PMTs viewing layer 1. In Figure 2.4(a), the location of the PMT face is adjacent to the region of largest response. Similarly in Figure 2.4(b) there are six areas of increased response around the circumference of the map, corresponding to the six PMTs which view the layer. The PMTs are optically coupled to the NaI(Tl) by plexiglass light pipes. Notice the low response "blind regions" to the sides of the PMT and the reflection regions on the side opposite from the tube. These features of the stack PMT maps are not seen in the single tube maps of the Cerenkov counters, as shown in Figure 2.6, where the PMTs view the interior of a light diffusion box.

Because the ^{55}Mn beam stopped in layers 11 and 12 of the stack, maps were constructed from the Bevalac data only for layers 1 through 10. Layer 11, layer 12, and the plastic top scintillator were mapped using high energy flight events which penetrate the entire NaI(Tl) stack.

Figure 2.4(a)

An isometric view of the map representing the light collection efficiency of stack layer 1 PMT tube A out to a radius of 26.5 cm. The face of the PMT is near the region of greatest response. The scale is linear, and the ratio of the peak response to the response at the opposite plateau is ~3.6. An area of very low collection efficiency can be seen to the "side" of the PMT, and reflection zones across the disk from the PMT are noticeable.

Figure 2.4(b)

An oblique view of the response map representing the light collection of the sum of all six PMTs of layer 1. The six areas of increased response around the circumference of the map correspond to the locations of the six PMTs which view the NaI(Tl) disk.

Figure 2.4(a)

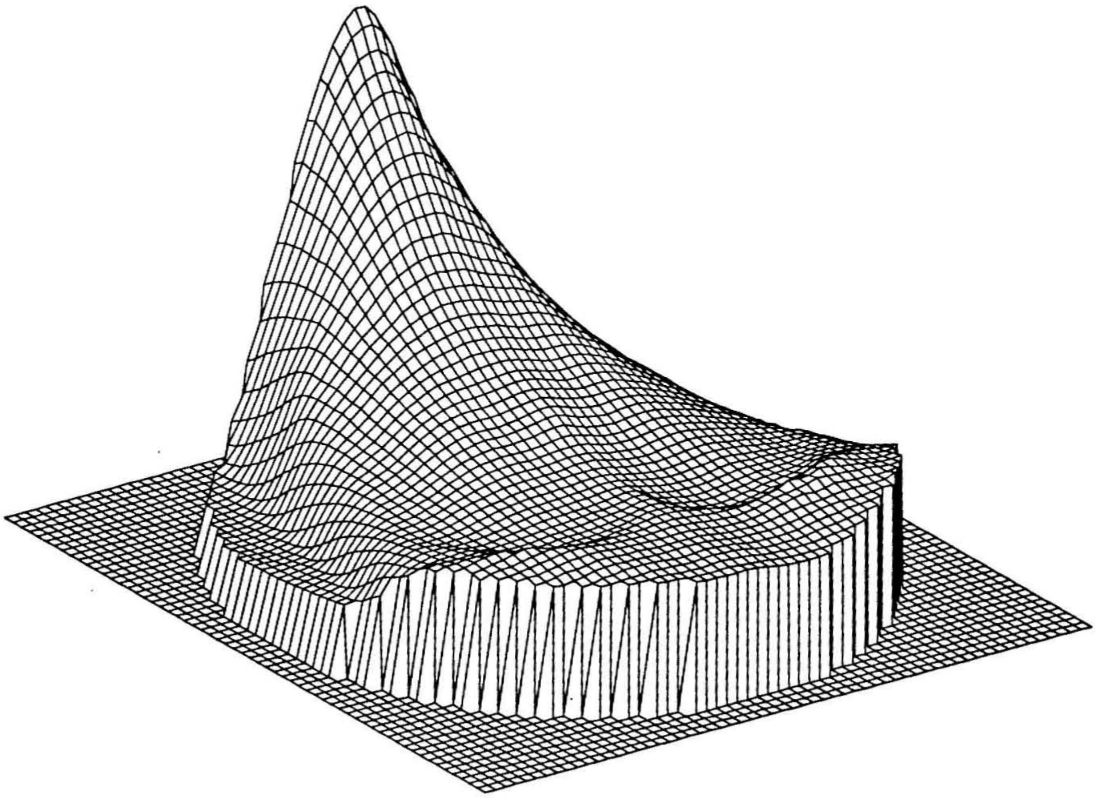

Layer 1 PMT A

Figure 2.4(b)

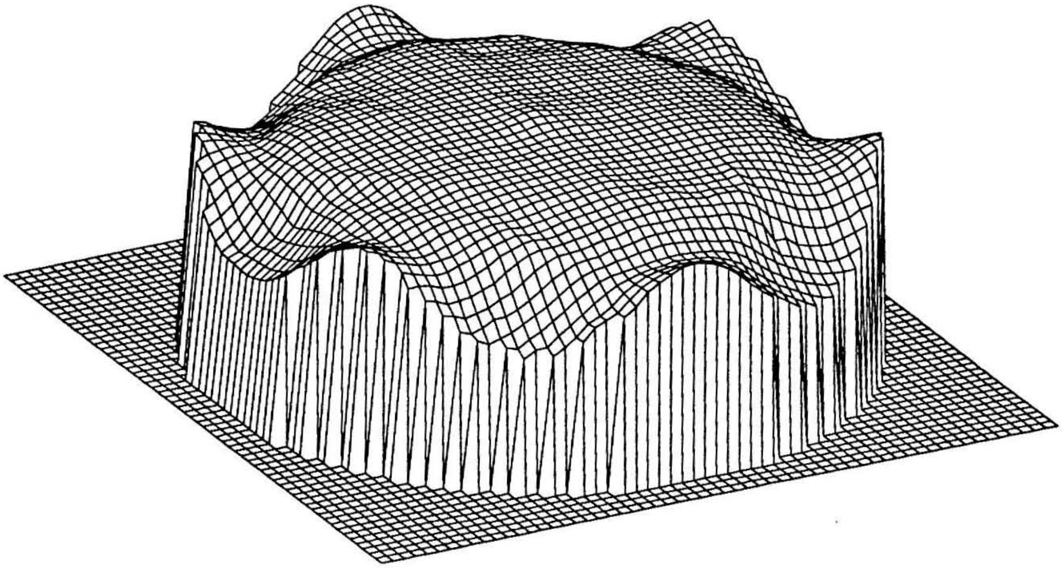

Layer 1 Sum of PMT's

2.3.2. Mapping the Cerenkov Counters

In November 1987, the Teflon and Pilot Cerenkov counters were taken to the Bevalac for mapping with a 1700 MeV/nucleon ^{56}Fe beam. The response of each PMT was individually recorded during a series of runs chosen to cover the entire area of the Cerenkov radiators. The position of each event was measured using two multiwire proportional counters (MWPCs), and events undergoing charge changing interactions were identified using plastic scintillators and a small Cerenkov test box which were mounted behind the main Cerenkov counters. Imaging the hole pattern of a 0.5 inch thick brass "mask" substituted in place of the Cerenkov counters established the relationship between the position measured by the MWPCs and the absolute position on the Cerenkov radiator.

Since data acquisition was limited to 16 channels, only half of the 16 PMTs of a counter could be monitored during a given run. The Pilot counter mapping runs recorded approximately 176,000 iron events, and the Teflon counter runs recorded about 240,000 iron events. These events are divided roughly equally in number between the two sets of PMTs which were alternately monitored. The calibration data were used to construct maps which show the response of each PMT as a function of the incident particle's position. The maps were constructed by dividing the area of the radiator into a matrix of 1.4 by 1.4 cm squares. The "map" for each square was found by fitting a quadratic surface to the data in that square and the eight surrounding squares. The Pilot radiator can be covered using a 50 x 50 matrix, while the larger Teflon radiator maps use 60 x 60 element matrices. The Cerenkov maps are constructed so that PMT 1 of each counter is aligned with the Y-axis of the map; therefore, the coordinate system of the Cerenkov counter maps is rotated by fifteen degrees from the scintillator stack's coordinate system, as shown in Figure 2.5.

Figures 2.6(a) and 2.6(b) show isometric views of the response maps of PMT 1 of the Teflon and Pilot counters respectively. Since the tubes look into a light diffusion box, the amount of light collected increases for particles incident near the PMT, and the gradient in the light collection is largest near the tube face. The

Figure 2.5

The relative orientation of the coordinate systems used for constructing the response maps for the NaI(Tl) stack layers and for the Cerenkov counters. The positive Y axis for the Cerenkov counters is aligned with PMT 1. The positive Y axis for the stack maps is aligned with PMT A of the odd numbered stack layers. The relative orientations of the stack PMTs (labeled A-F) and the Cerenkov PMTs (numbered 1-16) are shown. Note that the PMTs for even numbered stack layers are rotated by 30 degrees from the odd numbered stack layer PMTs.

Figure 2.5

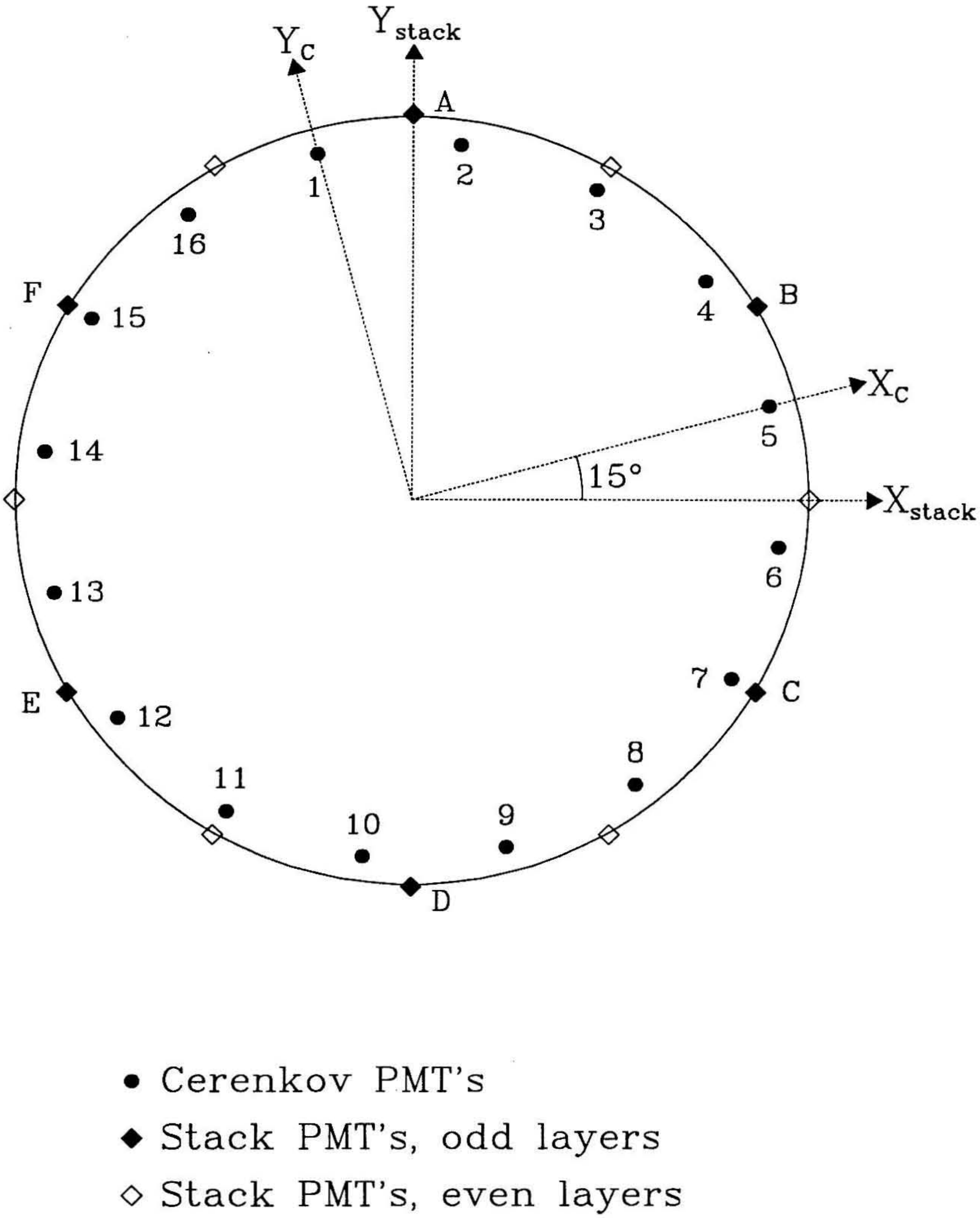
Y_{stack}
Y_C
X_C
X_{stack}
15°
A
B
C
D
E
F
1
2
3
4
5
6
7
8
9
10
11
12
13
14
15
16
● Cerenkov PMT's
◆ Stack PMT's, odd layers
◇ Stack PMT's, even layers

Figure 2.6(a)

An oblique view of the response map for Teflon Cerenkov counter PMT 1 shown to the 36.2 cm maximum radius used. The ratio of peak response to response at the opposite edge is ~17.

Figure 2.6(b)

An oblique view of the response map for Pilot Cerenkov counter PMT 1 normalized so that the response near the center of the map is the same as in Figure 2.6(a). The map is shown to the maximum radius used in this analysis. The ratio of peak response to response at the opposite edge is ~4.2.

Figure 2.6(a)

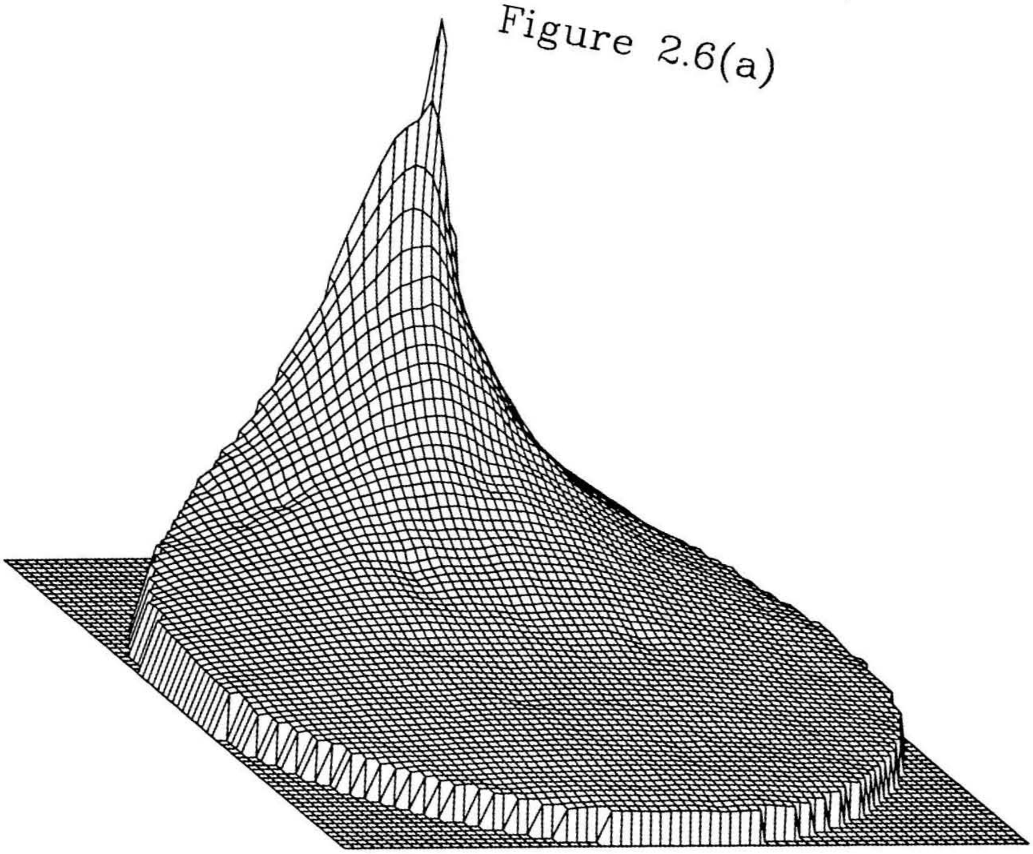

Teflon Counter Single PMT

Figure 2.6(b)

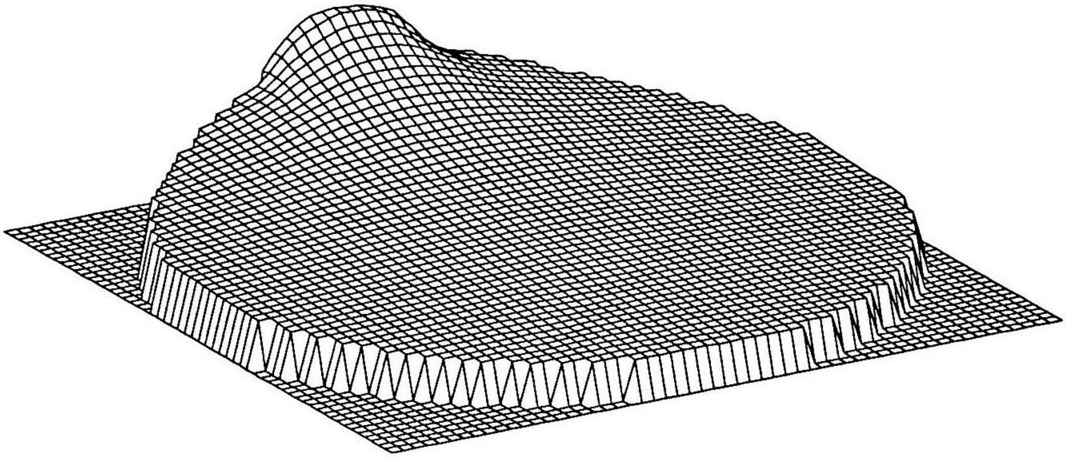

Pilot Counter Single PMT

Figure 2.7(a)

An oblique view of the response map for the sum of all sixteen Teflon Cerenkov counter PMTs. The map is shown to the maximum radius used in this analysis.

Figure 2.7(b)

A view of the response map for the sum of all sixteen Pilot Cerenkov counter PMTs. The map is shown to the maximum radius used in this analysis. The map is normalized so that the response near the center of the map is the same as in Figure 2.7(a).

Figure 2.7(a)

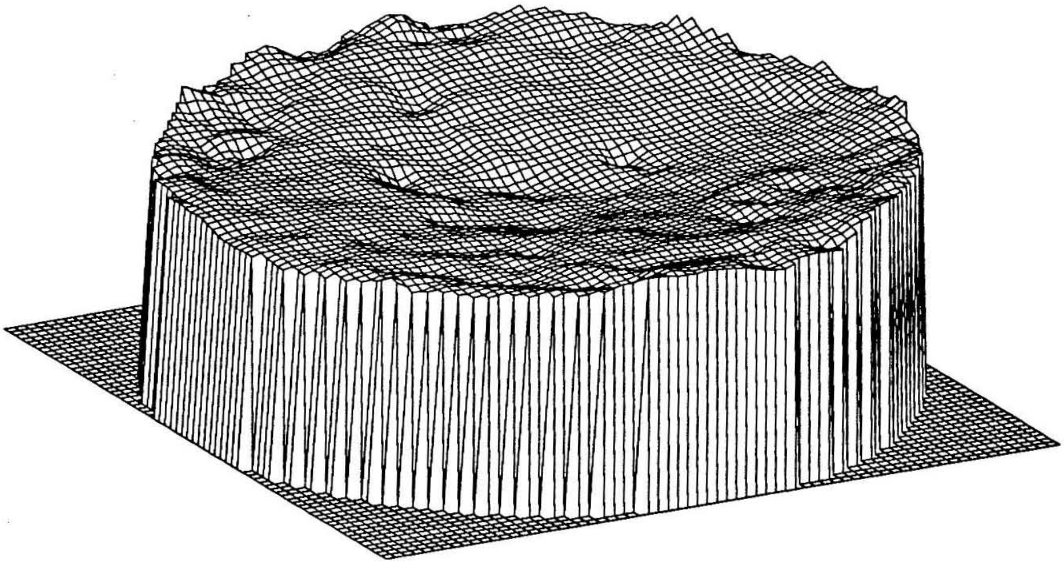

Teflon Counter Sum of All PMT's

Figure 2.7(b)

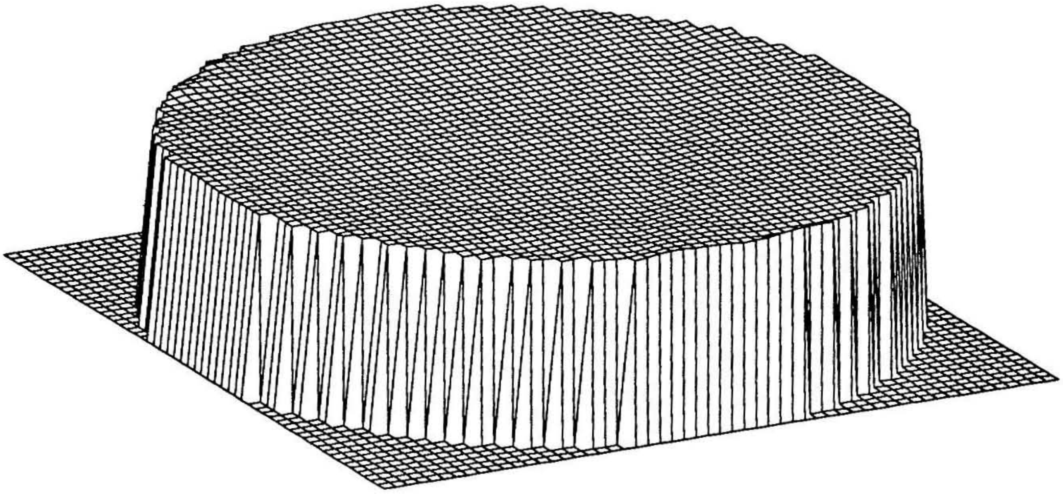

Pilot Counter Sum of All PMT's

Figure 2.8

The relative Cerenkov response shown along a randomly chosen diameter for each Cerenkov counter. The normalization of the two counter's responses is arbitrary. The Pilot counter exhibits much better uniformity of response than the Teflon counter.

Figure 2.8

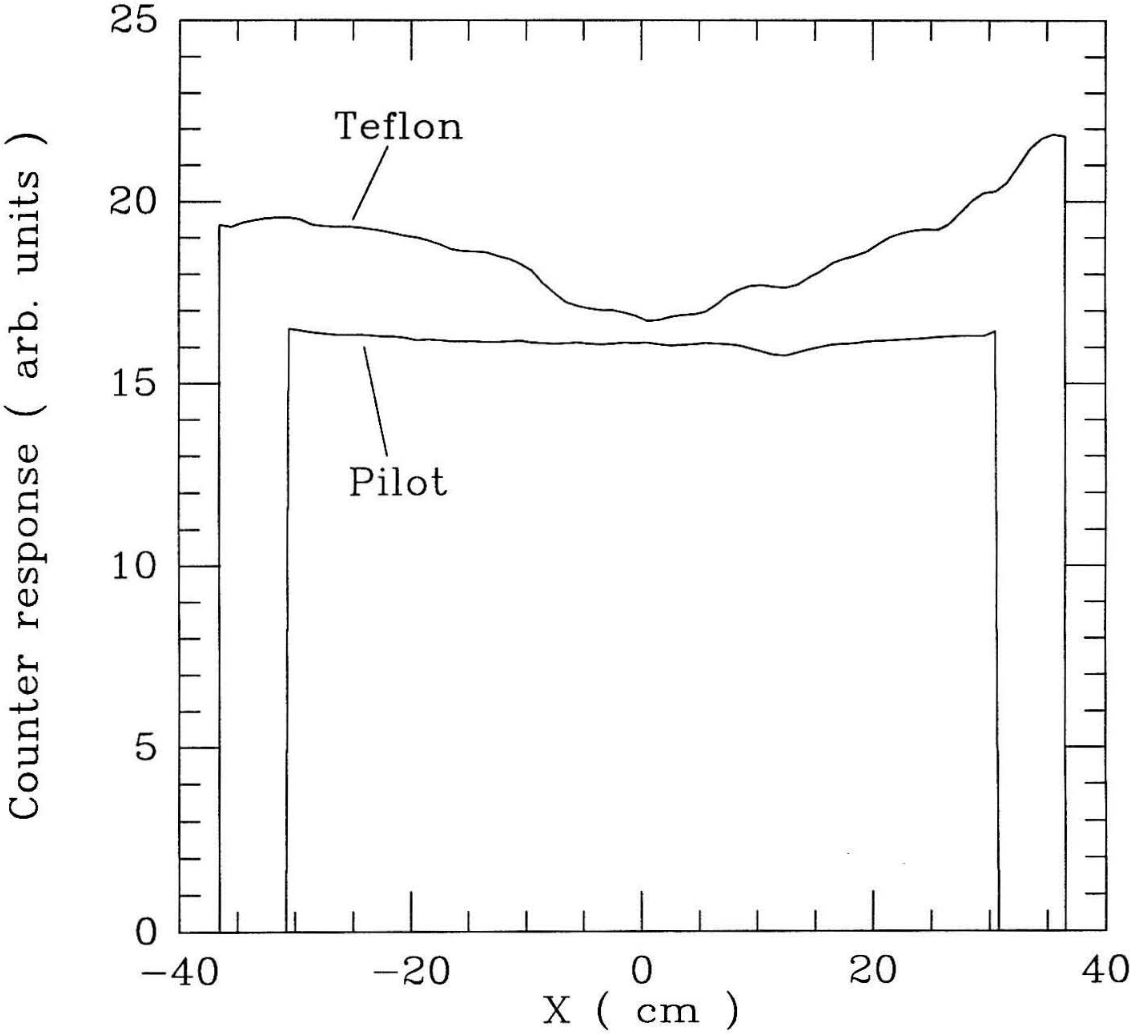
Teflon
Pilot
Counter response (arb. units)
X (cm)
0
5
10
15
20
25
−40
−20
0
20
40

PMTs viewing the Teflon counter are mounted only about 2 cm away from the physical edge of the Teflon radiator. The area of the Teflon radiator used for analyzing flight events begins at a radius of 36.2 cm from the center of the counter, 3.2 cm inside the physical edge. The smaller Pilot radiator's edge is about 7 cm from the PMT faces, and its useful area begins 10.7 cm away from the tubes. The Teflon counter exhibits higher gradients in light collection efficiency than the Pilot counter, both for individual PMTs and for the sum of all 16 PMTs. Figures 2.7(a) and 2.7(b) show isometric views of the response of the sum of all 16 tubes for each counter, and figure 2.8 gives a more quantitative comparison of the response variations across a diameter of each counter. As can easily be seen, the Pilot counter displays a much more uniform response than the Teflon. The non-uniform variations in response shown by the Teflon counter may be due, in part, to nonuniformity of the wave-shifter coating which covers each sheet of Teflon. The PTP wave-shifter was applied to the radiator in May 1986, and may have degraded over time since its application. Non-uniform degradation of the wave-shifter is a likely cause of at least some of the variations seen in the November 1987, Bevalac response maps. Thickness variations of the Teflon radiator have been measured to be less than 0.02% on length scales of 10's of cm.

2.3.3. Energy Calibration of the Cerenkov Counters

In addition to mapping the position dependence of the Cerenkov counters' responses, the counters' responses as a function of energy were also calibrated. Both counters were exposed to nitrogen, argon, and iron beams at various energies. The energy of the beams at the detector was varied by inserting different combinations of copper absorbers into the beam line upstream of the Cerenkov counters. The resulting response curves for the three beams were then simultaneously fitted to a four component model designed to account for the various contributions to the total observed light produced by the counters.

$$C_{tot} = C + C_k + C_p + S \tag{2.13}$$

The four components contributing to the total light are the primary Cerenkov light, C, the secondary Cerenkov light produced by knock-on electrons, C_k, the Cerenkov light, C_p , produced in the $BaSO_4$ paint which covers the interior of the light collection box, and S, the scintillation light which may be produced in the Pilot-425, the $BaSO_4$, and the air inside the light collection boxes. These four components were modeled as described below.

The primary Cerenkov light can be closely approximated as

$$C = C_0 Z^2 t \left[1 - \frac{1}{(n_0^2 - 1) p_i p_f} \right] . \tag{2.14}$$

Where p is a dimensionless momentum, $p = \beta\gamma$, and p_i (p_f) is the initial (final or threshold) momentum (Ahlen et al. 1976). The term n_0 represents the effective index of refraction of the radiator, and t is the radiator thickness or the depth at which the particle energy goes below threshold. C_0 is an overall normalization factor.

The production of Cerenkov light from knock-ons is given by

$$C_k = C_0 Z^2 f_k(\gamma) . \tag{2.15}$$

Where $f_k(\gamma)$ is found by using a knock-on model developed by Grove (1989) who built his algorithm upon the treatment by Lezniak (1976)(also see Grove and Mewaldt 1992). The following functional form provides a very good fit to the results of the Grove knock-on model.

$$f_k(\gamma) = k_0 + k_1 \log(\gamma - 1) + k_2 \beta + k_3 \beta^2 \tag{2.16}$$

The values of the coefficients used for both counters are given in Table 2.1.

Table 2.1 Coefficients of Knockon Model

Parameter	Teflon	Pilot
k_0	0.1146	0.0921
k_1	0.0599	0.0446
k_2	0.0558	0.0367
k_3	-0.177	-0.1236

The Cerenkov light produced by the $BaSO_4$ paint is estimated by

$$C_p = B_0 C_0 Z^2 \frac{1 - \frac{1}{n_p^2 \beta^2}}{1 - \frac{1}{n_p^2}} . \tag{2.17}$$

Where n_p, the index of refraction of the paint, is taken to be 1.6 (Ahlen and Salamon 1979), and the free fitting parameter, B_0, normalizes the light production of the paint to the primary Cerenkov light from the radiator.

The scintillation term has been represented in the form given by Tarle et al. (1979).

$$S = C_0\, A_s \left[\frac{(1-f_s)\frac{dE}{dx}}{1 + B_s(1-f_s)\frac{dE}{dx}} + f_s \frac{dE}{dx} \right] . \tag{2.18}$$

Where A_s, B_s, and f_s are free parameters which are varied to simultaneously fit the data from nitrogen, argon, and iron beams as shown in Figure 2.9. In this model of scintillation, the light production near the core of the scintillation track is allowed to saturate; that is, the scintillation efficiency drops as dE/dx increases. The saturating light from the core of the track is represented by the first term while the second term is simply proportional to dE/dx and represents a halo region created by δ-rays.

The parameter values resulting from simultaneously fitting this response model to data from Bevalac nitrogen, argon, and iron runs are given in Table 2.2, and the resulting fits to the data are shown in Figure 2.9. The model fits the observed Pilot counter response to ~1% for all three beams. The fit to the Teflon counter is also to better than ~1% for the most energies above Cerenkov threshold, but the near threshold and below threshold data from the nitrogen beam runs deviate from the model curve. Since the HEIST mass analysis uses the Cerenkov response only for above threshold events, the ~5% errors evident in the below threshold nitrogen data are not considered significant.

Table 2.2 Cerenkov Model Parameters

Parameter	Teflon	Pilot	
C_0	arb. units	arb. units	
n_0	1.363	1.516	
B_0	0.0751	0.0485	
A_s	0.0546	0.0467	(MeV^{-1})
B_s	0.0295	0.0172	(MeV^{-1})
f_s	0.203	0.297	

2.4. Event Positions and Trajectories

HEIST's stack of NaI(Tl) scintillators provides the measurements used to calculate trajectories of cosmic ray events as well as their energy deposition. Positions are found by making use of the position dependence of the response of the six PMTs in each layer. The energy and charge of a nucleus determines the total

Figure 2.9(a)

Teflon Cerenkov response to iron, argon, and nitrogen nuclei at various energies. The solid curve is the resulting model described in the text.

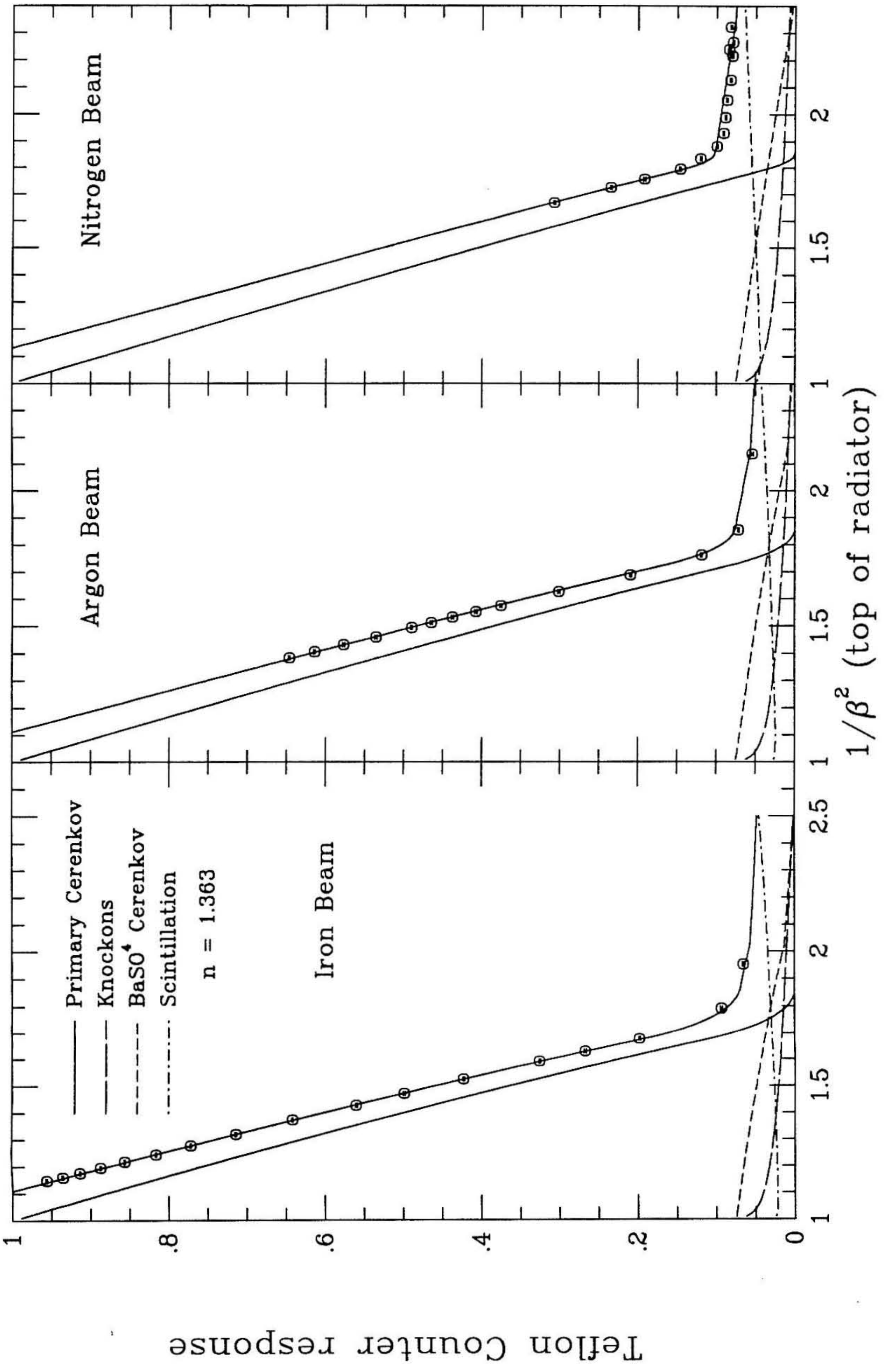
Nitrogen Beam
Argon Beam
Iron Beam
Primary Cerenkov
Knockons
BaSO^4 Cerenkov
Scintillation
n = 1.363
1
1.5
2
2.5
1/β^2 (top of radiator)
Teflon Counter response
0
.2
.4
.6
.8
1

Figure 2.9(a)

Figure 2.9(b)

Pilot Cerenkov response to iron, argon, and nitrogen nuclei at various energies. The solid curve is the resulting model described in the text.

Figure 2.9(b)

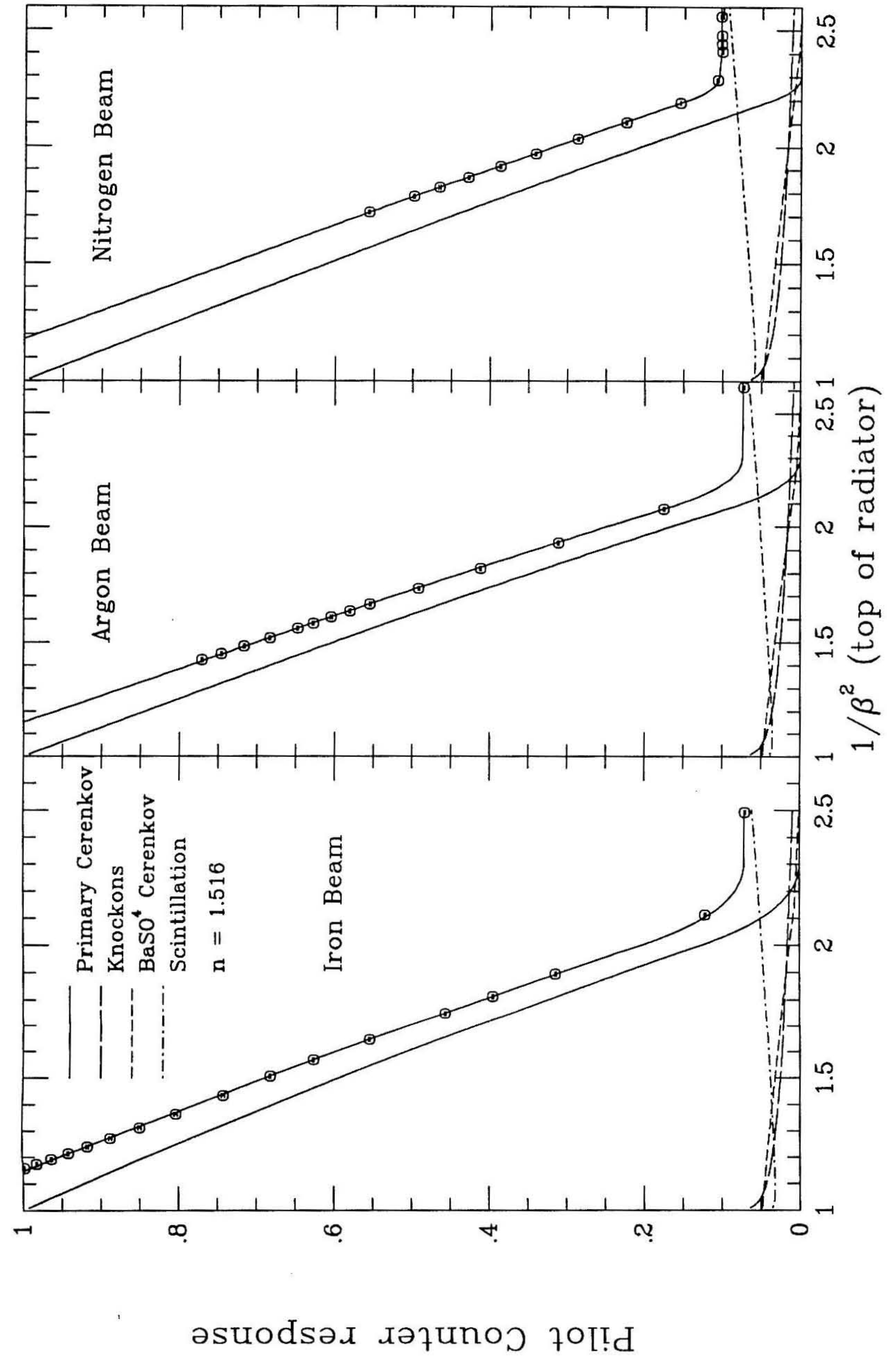
Primary Cerenkov
Knockons
BaSO^4 Cerenkov
Scintillation
n = 1.516
Iron Beam
Argon Beam
Nitrogen Beam
1
1.5
2
2.5
1/β² (top of radiator)
0
.2
.4
.6
.8
1
Pilot Counter response

amount of scintillation light created, but the position of the scintillation track determines how the total collected light is distributed among the PMTs. Taking ratios of the PMT responses provides information about the position of an event. In order to find the location of a scintillation track which passes through a layer of NaI(Tl), we use nine different ratios formed from combinations of the PMTs of that layer. The ratios used are listed in Table 2.3, where the PMTs of each layer are sequentially labeled A through F as shown in Figure 2.5. These ratios are compared with ratio "maps" which were constructed from the Bevalac calibration of the scintillator stack. The calculated best position is at the location which minimizes d^2, a measure of the difference between the observed ratios and the maps of the ratios.

$$d^2 = \sum_i (\log R_i - \log M_i)^2 , \qquad (2.19)$$

where $\log R_i$ and $\log M_i$ are the observed and mapped values of the logarithm of ratio i of PMTs. Because of the failure of one of the PMTs viewing layer 3, positions from layer 3 are less reliable than positions from the other stack layers, and layer 3 positions were not used in isotope analysis. A more detailed description of the development and implementation of the position algorithm is given by Grove (1989), who used a subset of six of the nine ratios listed in Table 2.3.

In addition to using the NaI(Tl) layers to calculate event positions, the top plastic scintillator provides positions through the same method. The Teflon Cerenkov counter also can provide positions using this method. The resulting position resolution is discussed below.

Once event positions have been found in the various detectors, a best fit straight line trajectory is found. The trajectory algorithm weights the individual positions by the expected resolution in each detector type (i.e., NaI(Tl), plastic scintillator, or Cerenkov counter). The trajectory algorithm identifies individual positions which are unlikely "outliers" to the resulting trial trajectories and eliminates them from the fit. Outliers are not rejected when there are three or fewer positions used in the trial trajectory. Example trajectories from the 1988 flight data are shown for two carbon events in Figure 2.10.

Table 2.3: Photomultiplier Ratios for Position Algorithm

Layer	Ratios
S_1, L_1–L_{10} excluding L_3	(A+B+C)/(D+E+F) (B+C+D)/(E+F+A) (C+D+E)/(F+A+B) A/B, C/D, E/F B/C, D/E, F/A

2.4.1. Flight Position Resolution in NaI(Tl) Stack

In order to estimate the resolution achieved during the 1988 flight for positions in the NaI(Tl) stack, a data set of high energy, mostly non-fragmenting events was chosen for analysis. Only events which completely penetrated all 12 layers of NaI(Tl) were chosen. Requiring a loose agreement between the responses in adjacent layers eliminated most events undergoing charge changing fragmentations within the stack. This data set, which we will call the "penetrating data set," was used for the analysis of position uncertainties and for other calibrations described in chapters 3 and 4.

Position errors are estimated from the differences between individual positions found by the position algorithm and the positions along the resulting trajectory fit through the stack. Position resolution varies little from layer to layer, so the sum of the residuals can be approximated by a χ^2 distribution with the number of degrees of freedom given by the number of coordinates calculated (two per layer) minus the number of parameters found by the trajectory fit (four). Thus, the distribution of

Figure 2.10

Example trajectories for two carbon cosmic ray nuclei which completely penetrated the NaI(Tl) stack. The top two panels show the trajectory for one carbon nuclei projected onto the x and y axes of HEIST's coordinate system. The bottom two panels show the same projections for a second carbon event. Positions are shown for measurements from S1, C1, and stack layers 1 through 10, excluding layer 3. The solid line is the resulting trajectory fit. Error bars on the S1 and C1 positions show the expected position resolution for these detectors.

Figure 2.10

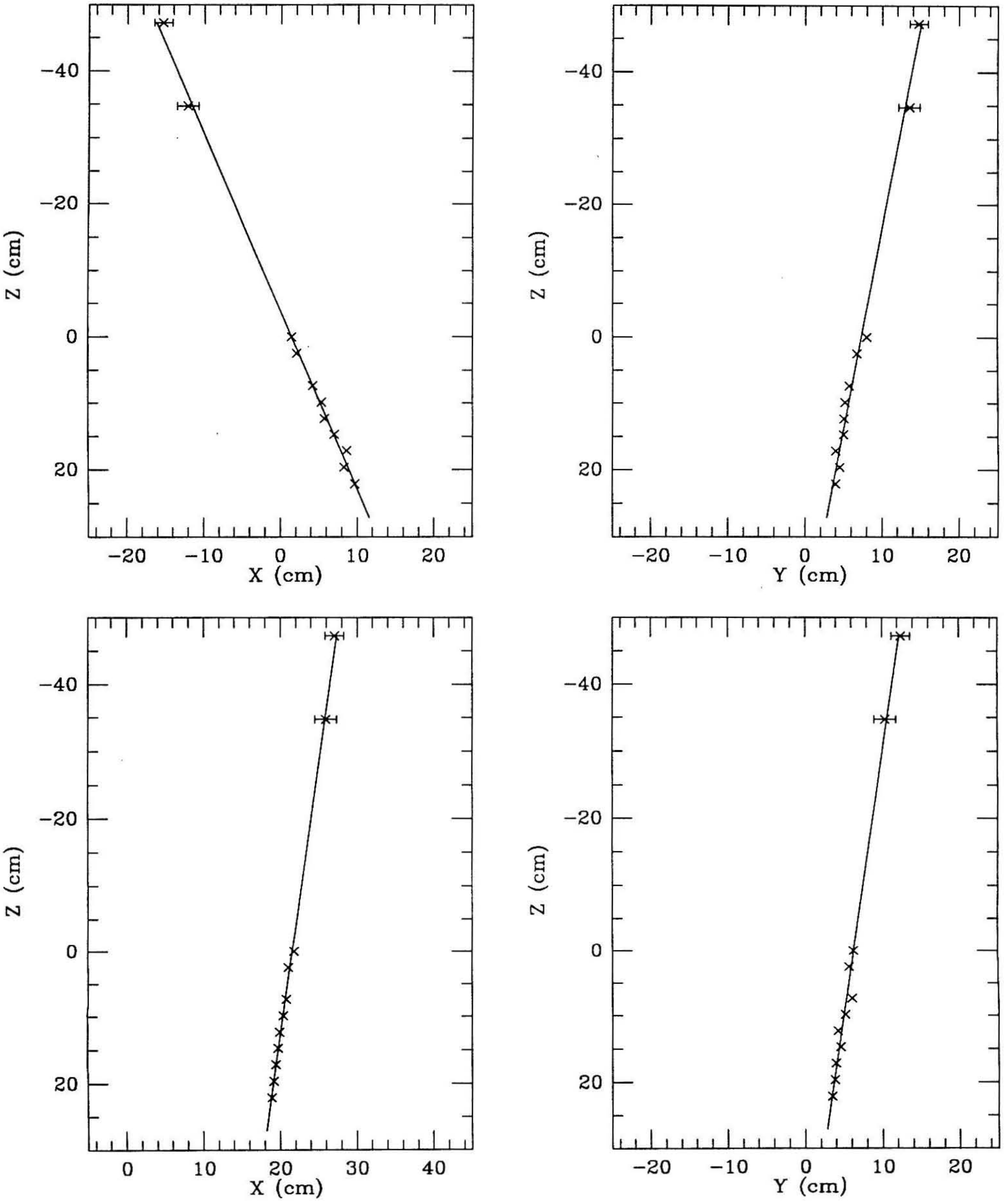

Figure 2.11

Position residuals for carbon, oxygen, magnesium, and iron events which penetrated the stack. Calculated χ^2 distributions have been fit to the data in order to estimate the achieved position resolution of the NaI(Tl) layers.

Figure 2.11

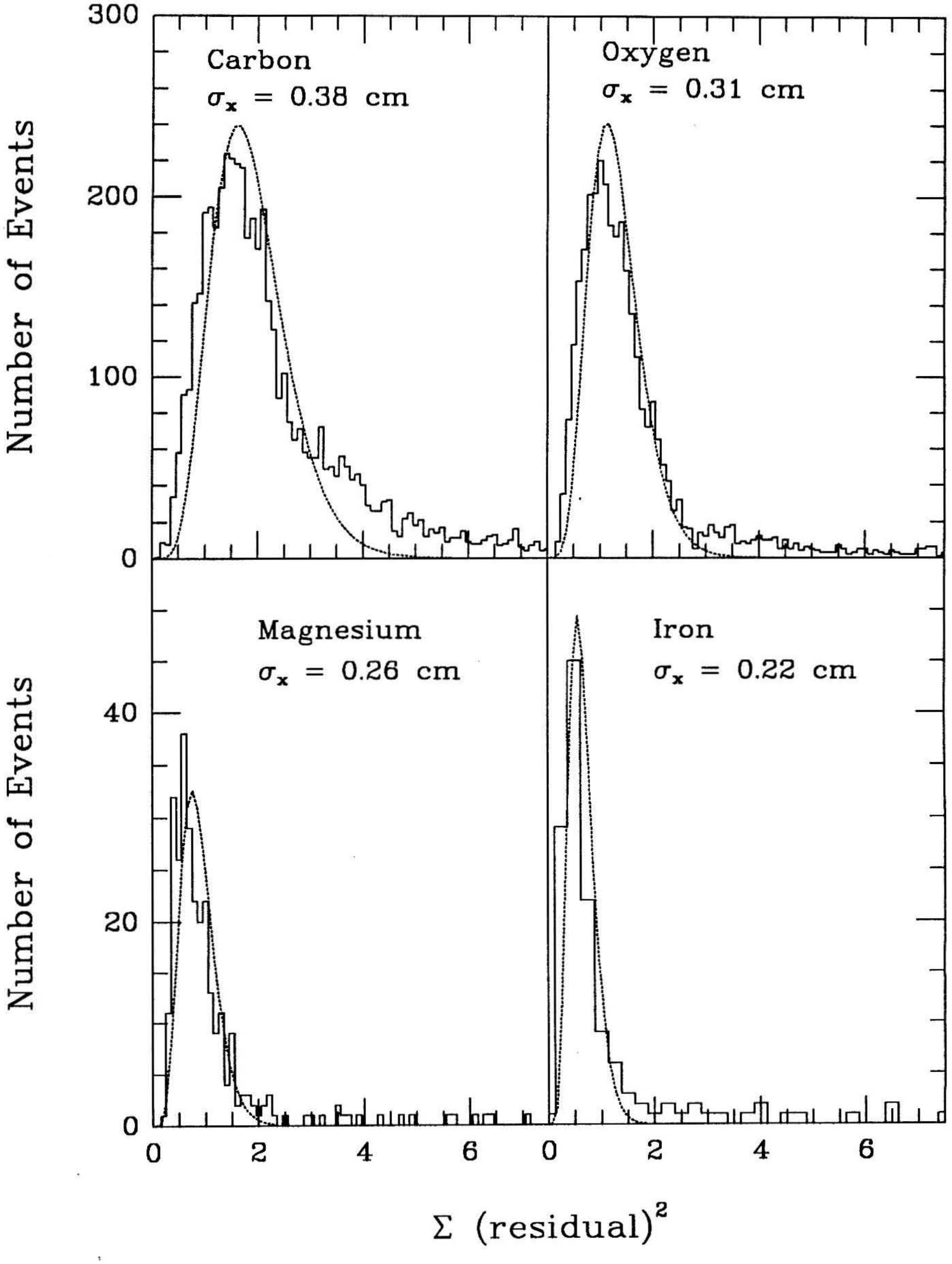
Carbon
σ_x = 0.38 cm
Oxygen
σ_x = 0.31 cm
Magnesium
σ_x = 0.26 cm
Iron
σ_x = 0.22 cm
Number of Events
Number of Events
300
200
100
0
40
20
0
0
2
4
6
0
2
4
6
Σ (residual)^2

the residuals is given by:

$$\sigma_x^2 \chi^2(\nu) = \sum_i (\vec{r}_i^{\,calc} - \vec{r}_i^{\,traj})^2 , \tag{2.20}$$

where σ_x is the resolution in a single dimension, $\vec{r}_i^{\,calc}$ is the position in layer i calculated by the position algorithm, and $\vec{r}_i^{\,traj}$ is the position in layer i given by the trajectory fit. The number of degrees of freedom, ν, is $9 \times 2 - 4 = 14$, because the trajectories used in the fit are found from the calculated positions in nine layers.

Figure 2.11 shows the distributions of residuals for carbon, oxygen, magnesium, and iron. The solid curves are $\sigma^2\chi^2(14)$ distributions which have been fit to estimate the σ_x of the residuals. As can be seen, the actual distributions do not look like pure χ^2 distributions because of the existence of non-Gaussian tails caused by a background of fragmenting events which were not rejected by the loose agreement criteria used to select the penetrating data set. Another contribution to the non-Gaussian nature of the resulting distributions is the non-uniformity of position resolution over the area of each stack layer. Position resolution degrades for events near the edge of the NaI(Tl) disk. Nevertheless, these fits to $\sigma^2\chi^2$ distributions do give us reasonable estimates of the resulting position resolution for the majority of flight events. Note that the main peaks of the distributions in Figure 2.11 correspond to better position resolution than is given by the overall χ^2 fits. The estimated uncertainty in one dimension for a position in a layer of the NaI stack is:

Table 2.4 Estimated Stack Position Resolution, σ_x

Carbon	0.38 cm
Oxygen	0.31 cm
Magnesium	0.26 cm
Iron	0.22 cm

These values are compared to the estimated position resolution achieved at the

Bevalac in Figure 2.12 . The resolution achieved in flight is slightly degraded from that measured in accelerator calibrations. The achieved flight resolution is excellent in view of the fact that the Bevalac positions were calculated from events which were taken over a much shorter time period, which are all near normal incidence, and which cover only a limited area of the stack. The flight events represented have no angle or area cuts other than those imposed by the instrument trigger geometry.

The flight position resolution found from this penetrating data is significantly better that the position resolution of 0.47 cm for iron found from the 1984 HEIST flight (Grove 1989). Improvements in the trajectory algorithm can account for ~10% improvement in σ_x. Using nine ratio maps instead of only the six used for finding positions for the 1984 flight also improves the resolution slightly. The remaining improvement may be due to the greater care taken in correcting for stack PMT drifts over this flight as discussed in §4.2. We know of no other significant differences between the 1984 and 1988 flight trajectory analyses.

2.4.2. Position Resolution in the Cerenkov and Top Scintillator

As described above, each of the two HEIST Cerenkov counters has a circular radiator mounted in the center of its light collection box and viewed, edge-on, by 16 PMTs. Eight of the PMTs have their response's individually digitized and recorded. The outputs of the other eight PMTs are paired into four ADCs by pairing each PMT with the PMT on the opposite side of the radiator.

Positions in the Cerenkov counters were found using the same method as was employed in finding NaI(Tl) stack layer positions. Only the unpaired PMT responses were used since the paired tubes response maps had relatively small spatial response gradients. Maps were made using the logarithm of the ratio of the sum of four adjacent tubes to the sum of four opposite tubes. Four maps of this type were made from the four possible combinations of neighboring unpaired tubes. In addition to the "sum of four" over "sum of four" ratio maps, eight maps of ratios of the individually digitized PMTs which are nearest neighbors were used,

Figure 2.12

Position resolution for the 1988 flight is compared to the position resolution found from analyzing 1982 Bevalac calibration data. The Bevalac data is comprised of events near normal incidence over a limited area near the center of the stack. The 1988 flight data has no geometry cut except that required by the trigger logic. For comparison, the position resolution for Fe in the 1984 flight data was 0.47 cm.

Figure 2.12

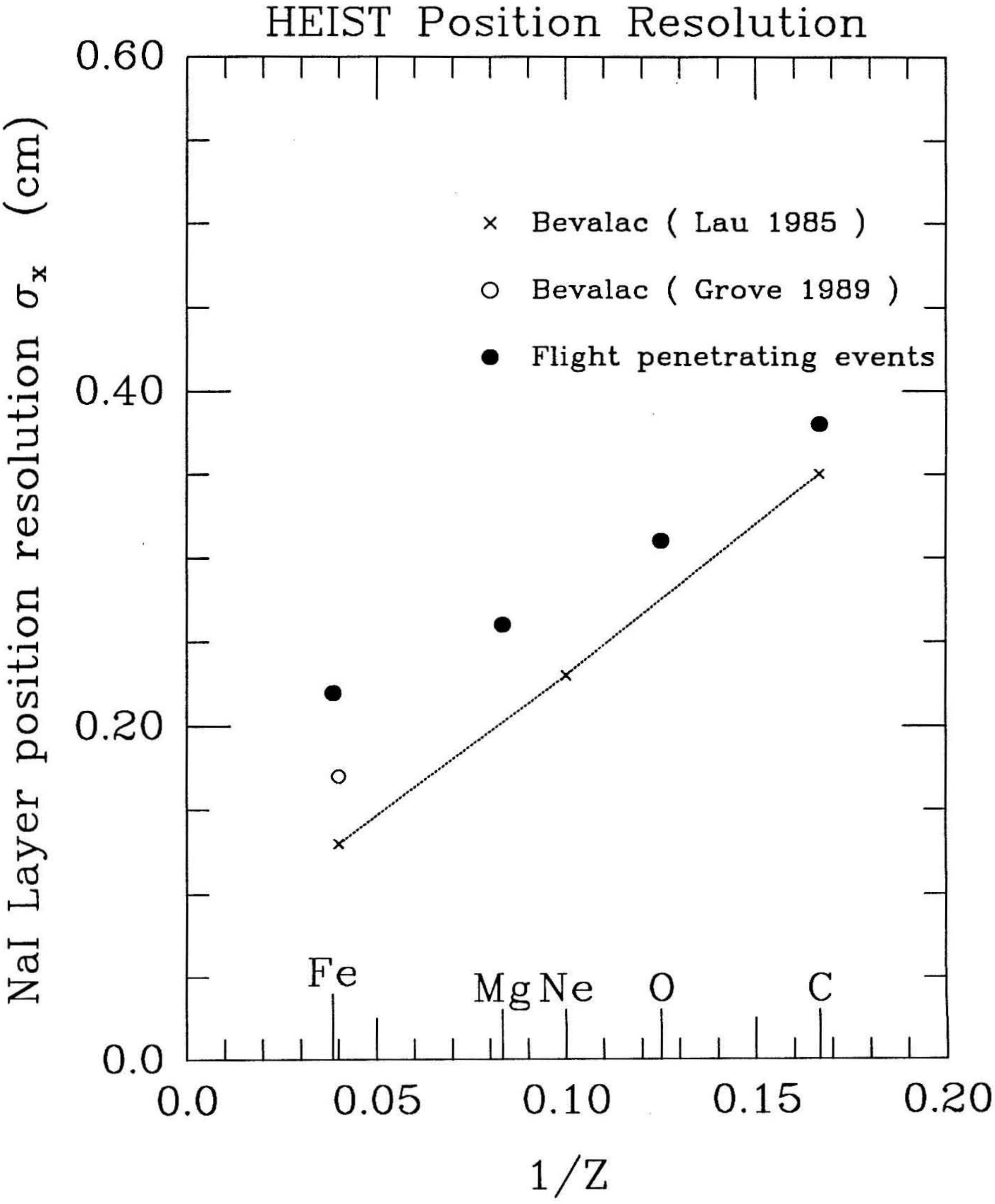
HEIST Position Resolution
NaI Layer position resolution σ_x (cm)
0.60
0.40
0.20
0.0
0.0
0.05
0.10
0.15
0.20
1/Z
× Bevalac (Lau 1985)
○ Bevalac (Grove 1989)
● Flight penetrating events
Fe
Mg
Ne
O
C

following the method used with the stack ratio maps. Using these eight additional ratio maps resulted in a small incremental improvement in the calculated positions.

We calculated positions for Bevalac iron beam events in both counters. The Teflon counter position resolution was σ_x=0.37 cm, neglecting the uncertainty in the wire chamber measured positions. The Pilot counter map gradients are much smaller than in the Teflon counter, which makes the Pilot counter better designed for velocity measurements, but poorer for calculating event positions. The Pilot counter Bevalac position resolution for iron was σ_x=0.58 cm, again neglecting wire chamber contributions.

The penetrating data set was used to estimate the flight position resolution of both Cerenkov counters although the Pilot counter positions were not used for finding flight trajectories due to their larger uncertainties. Since the true positions of the flight events are unknown, we must use trajectories found from fits to the stack positions as an estimate of the true position in the Cerenkov counters. We then subtract the estimated contributions to the position errors due to multiple scattering between the stack and the Cerenkov counters and due to the finite resolution of the stack positions.

$$\sigma_{tef}^2 = \sigma_{tot}^2 - \sigma_{traj}^2 - \sigma_{scat}^2 \qquad (2.21)$$

Table 2.5 shows estimates of flight resolution. The measured position resolution in the Cerenkov counters is consistent with that estimated by combining the counters' response uncertainties due to photoelectron statistics with their PMT response map gradients.

Top scintillator positions were calculated using the same algorithm as used for the stack. Most of the top scintillator PMTs were replaced between the time of the 1984 Bevalac calibration runs and the 1988 flight, and so the top scintillator maps were made using flight data instead of data from the Bevalac calibration. The resulting maps are of poorer quality than the NaI(Tl) stack maps and the Cerenkov counter maps made from Bevalac calibration runs, and the position resolution in the top scintillator appears to be limited by the map errors instead of photoelectron

Table 2.5 Flight Teflon Counter Position Resolution

Nuclei	σ_{tot} (cm)	σ_{traj} (cm)	σ_{scat} (cm)	σ_{tef} (cm)
Carbon	1.7	0.8	0.56	1.4
Oxygen	1.4	0.64	0.56	1.1
Magnesium	1.1	0.54	0.56	0.8

statistics as in the Cerenkov counters. Table 2.6 shows the estimated position resolution in the top scintillator. Notice that unlike the Cerenkov and stack position resolution, the top scintillator resolution does not improve significantly with increasing nuclear charge.

Table 2.6 Flight Plastic Scintillator Position Resolution

Nuclei	σ_{tot} (cm)	σ_{traj} (cm)	σ_{scat} (cm)	σ_{scint} (cm)
Carbon	1.75	1.0	0.76	1.2
Oxygen	1.55	0.82	0.76	1.2
Magnesium	1.5	0.68	0.76	1.1

2.4.3. Trajectory Errors

Once the position resolution in each detector has been characterized, we can calculate the resulting uncertainty of the event trajectory. Consider the resulting trajectory errors in one dimension. To find the trajectory, we do a least squares fit to a set of positions, y_i, measured by detectors at locations, z_i, along the trajectory. The fitted trajectory gives the calculated position, $\hat{y}(z)$ as a function of depth, z , through the instrument.

$$\hat{y} = \hat{a}+\hat{b}z \, . \tag{2.22}$$

Neglect multiple scattering and assume that the errors, σ_i , in the positions, y_i , used in the trajectory fitting are uncorrelated, then the expected error in $\hat{y}$, the position along the fitted trajectory, is given by (cf Bevington 1969, or Yost 1984)

$$\hat{\sigma}_y^2(z) = \sigma_a^2 + z^2\sigma_b^2 + 2z\mathrm{Cov}(a,b) \, , \tag{2.23}$$

$$= \frac{\sum \frac{z_i^2}{\sigma_i^2} + z^2 \sum \frac{1}{\sigma_i^2} - 2z \sum \frac{z_i}{\sigma_i^2}}{\sum \frac{1}{\sigma_i^2} \sum \frac{z_i^2}{\sigma_i^2} - \left(\sum \frac{z_i}{\sigma_i^2}\right)^2} \, . \tag{2.24}$$

Note that for the special case where all the σ_i are equal, $\sigma_i = \sigma_y$, and where the coordinate system is chosen such that the z_i are symmetric about the origin, the equation for the resulting uncertainty reduces to

$$\hat{\sigma}_y(z) = \sigma_y \left[\frac{1}{n} + \frac{z^2}{\sum z_i^2} \right]^{1/2} \, , \tag{2.25}$$

where n is the number of position measurements used in the trajectory fit. Recall that σ_y is the estimated error in one dimension; so, Equation 2.25 gives the uncertainty along one direction. The total uncertainty in two dimensions will be larger than the result of Equation 2.25 by $\sqrt{2}$.

The expression for the error in secθ calculated from the trajectory fit is also useful and is given by

$$\sigma_{\sec\theta} = \sqrt{2} \sin\theta \left[\frac{\sum \frac{1}{\sigma_i^2}}{\sum \frac{1}{\sigma_i^2} \sum \frac{z_i^2}{\sigma_i^2} - \left(\sum \frac{z_i}{\sigma_i}\right)^2} \right]^{1/2} \, . \tag{2.26}$$

In the special case mentioned above, this expression reduces to

$$\sigma_{\sec\theta} = \sqrt{2}\,\sin\theta\,\frac{\sigma_y}{\sqrt{\sum z_i^2}}\,. \tag{2.27}$$

Expressing the angular uncertainty as a fraction of $\sec\theta$ we have,

$$\frac{\sigma_{\sec\theta}}{\sec\theta} = \frac{\sin 2\theta}{\sqrt{2}}\,\frac{\sigma_y}{\sqrt{\sum z_i^2}}\,. \tag{2.28}$$

Table 2.7 shows an example calculation of the uncertainties for a stopping carbon trajectory. We have modeled a carbon event which has position measurements available from the top scintillator, S1, and from stack layers 1, 2, and 4.

Table 2.7 Example Calculation of Trajectory Uncertainty

Detector	position measurement uncertainty (cm)	depth, z (cm)	resulting 1-D trajectory uncertainty (cm)
S1 - Top Scint.	1.2	-47.3	1.14
C1 - Teflon Counter	--	-34.8	0.86
C2 - Pilot Counter	--	-15.9	0.45
L1 - Layer 1	0.37	0.0	0.21
L2	0.37	2.44	0.21
L3	--	4.88	0.22
L4	0.37	7.34	0.25

For this example trajectory, the fractional uncertainty in $\sec\theta$ is given by

$$\frac{\sigma_{\sec\theta}}{\sec\theta} = 0.016\,\sin 2\theta\,. \tag{2.29}$$

Chapter 3

Analysis Algorithms and Mass Resolution

In this chapter, we describe the algorithms used to calculate velocities and energies of cosmic ray nuclei using the measured PMT responses of the various HEIST detectors. The limitations on energy and velocity resolution are discussed, and a model of mass resolution is compared to the resulting resolution for the 1988 flight.

3.1. Energy Loss Algorithm

Each of the six PMTs viewing a layer of the NaI(Tl) stack sees a fraction of the total scintillation light yield from an event. The individual PMT response maps made with the 1984 Bevalac calibration of HEIST characterize the collection efficiency of the PMTs as a function of event position in the layer. By using these response maps, each individual PMT response provides an estimate of the total scintillation light from an event. These six measurements are then combined in a weighted sum to produce a final measurement of the light yield in the layer. To find the corrected response for stack layer m, we interpolate from each PMT map at the event position given by the trajectory algorithm, using the six-point method (Abramowitz and Stegun 1964, Relation 25.2.67). We apply the interpolated map values, M_i, in the weighted sum,

$$L_m = \sum_i \frac{P_i}{M_i} w_i \,, \tag{3.1}$$

where

$$w_i = \frac{(P_i/\nabla M_i)}{\sum\limits_k (P_k/\nabla M_k)} \,, \tag{3.2}$$

and P_i is the gain-balanced response of tube i, i.e., the raw ADC output minus its zero offset and divided by its time dependent gain (see §4.2.1 on PMT drifts). The values M_i and ∇M_i are the interpolated response map value and the response map gradient for PMT i. The response/gradient weighting favors map regions with large response and small gradient, where position errors have minimal effect. Initially, the summation runs over all six PMTs. Then the algorithm may reject up to two of the six signals if there are PMT responses which differ from the weighted average response by more than a maximum specified residual. The maximum residual was chosen such that a typical PMT was rejected in about 2% of the events in the penetrating data set. The rejection of individual PMTs was included in the energy algorithm after confirming that at least one of the PMT response maps has a small region of incorrect values. The rejection of outlier PMT values improved the energy loss resolution when tested on the penetrating data set.

3.2. Energy Loss Resolution

In order to measure the resolution of individual layer energy loss measurements, ratios of adjacent layer responses were found for flight events of known charge and energy. Individual layer resolution has been estimated from histograms of these ratio distributions. Known contributions to the energy resolution such as ionization energy loss fluctuations, photoelectron counting statistics, amplifier noise, and uniformity errors not corrected by the response maps can be estimated and compared with the observed resolution.

3.2.1. Ionization Energy Loss Fluctuations

As a charged particle passes through material, it loses energy by excitation and ionization along its track and through creation of energetic knock-on electrons or δ–rays. For highly relativistic particles and for non-relativistic particles traversing thin counters, the maximum possible energy which can be transferred to an electron in a single collision is much larger than the average energy transfer. Since the probability of transferring near the maximum possible energy to an electron is low in these cases, the distribution of energy loss, given by the treatment of Landau, is asymmetric with a tail in the direction of high energy loss (e.g., Ahlen 1980 and references therein). For our case of particle energies of several hundred MeV/nucleon passing through thick ($\sim 7 g/cm^2$) detectors, there are a large number of collisions resulting energy transfers over the entire spectrum of possible values and the resulting distribution of energy loss for an ensemble of nuclei is Gaussian. In this case, the small variations in energy loss from particle to particle are often termed ionization energy loss fluctuations or Bohr/Landau fluctuations.

For a beam of nuclei with charge Z and velocity β, the variance of the energy loss distribution due to stochastic fluctuations is (e.g., Rossi 1952)

$$\sigma_{BL}^2 \approx 0.301\, Z^2\, m_e c^2 \,\frac{Z_T}{A_T}\,\left(\frac{1}{\beta^2} - \frac{1}{2}\right) t\, E'_{max}\,, \tag{3.3}$$

where $E'_{max} = 2m_e c^2 \beta^2 \gamma^2$ is the maximum energy that can be imparted to a knock-on electron. The values Z_T and A_T are the charge and mass number of the target material, and t g/cm^2 is the thickness of the target. In order to make clear the energy dependence of σ_{BL}^2, Equation (3.3) can be written as

$$\sigma_{BL}^2 \approx 0.301\, \frac{Z_T}{A_T}\, m_e c^2\, t_L \sec\theta\, Z^2\, (\gamma^2+1)\,. \tag{3.4}$$

We have expressed the target thickness as the layer thickness, t_L times the $\sec\theta$ path-length correction factor. Substituting for the electron mass in units of MeV and using a typical layer thickness of 7.2 g/cm^2 of NaI(Tl), the equation reduces to

$$\sigma_{BL}^2 \approx 0.242 \sec\theta\, Z^2\, (\gamma^2+1) \quad (\mathrm{MeV})^2\,. \tag{3.5}$$

In order to find σ_{BL} as a fraction of the energy deposited by the particle, the energy loss in a layer of NaI(Tl) can be found from a simple approximation. For light nuclei with energies of 300 to 800 MeV/nucleon, energy loss in NaI(Tl) is well approximated by

$$\frac{dE}{dx} \approx Z^2 \left[0.43 + \frac{0.74}{\beta^2}\right] \quad (\mathrm{MeV/g\,cm^{-2}})\,. \tag{3.6}$$

Using this approximation and neglecting the change in velocity within a layer, the fractional energy loss fluctuations in a single stack layer of NaI(Tl) can be written as

$$\frac{\sigma_{BL}}{\Delta E} = \frac{0.0584}{Z \sec^{1/2}\theta} \frac{(\gamma^2+1)^{1/2}}{(0.36+0.64/\beta^2)} \ . \tag{3.7}$$

For carbon, these Bohr/Landau fluctuations increase with energy from about 0.9% at 330 MeV/nuc to 2.7% at energies near minimum ionizing. In the special case where the incident nucleus loses a large fraction of its total energy in the energy loss detector, the energy loss fluctuations are underestimated by this analysis and must be increased by a correction factor (Spalding 1983, or see Ahlen 1980). For HEIST, this special case would only apply for the NaI(Tl) layer which immediately precedes the layer in which a nucleus comes to a stop.

3.2.2. NaI(Tl) Photoelectron Statistics and Uniformity Errors

Statistical fluctuations in the number of photoelectrons collected by the PMTs viewing each layer are another contribution to the layer energy resolution. The estimated number of photoelectrons can be estimated from

$$N_{pe} = \frac{\Delta E}{<h\nu>} \frac{dl}{dE} \epsilon_{geom} \epsilon_K \ . \tag{3.8}$$

The number of photoelectrons, N_{pe}, is equal to the number of scintillation photons created times the geometrical collection efficiency, ϵ_{geom}, times the quantum efficiency of the photomultiplier tubes, ϵ_k. The energy loss for minimum ionizing ^{12}C in layer 1 is ~390 MeV. The absolute scintillation efficiency, dl/dE, of sodium iodide for light nuclei is ~14% (van Sciver and Bogart 1957). The photons produced have an average energy $<h\nu> \sim 3$ eV. The geometric light collection efficiency ϵ_{geom} is ~1%, and the photocathode efficiency ϵ_K is typically about 15%. Using these values, ^{12}C nuclei should produce about 2.7 10^4 photoelectrons, resulting in statistical variations of ~0.6% for a single NaI(Tl) layer. Minimum ionizing ^{56}Fe nuclei produce about ten times as many photoelectrons corresponding to a statistical uncertainty of 0.2% .

The stack response maps created from the 1982 Bevalac calibration data are used to "correct" for the positional dependence of the collected scintillation light. There are two types of residual errors which may not be corrected in the mapped response. First, there may be response variations in the NaI(Tl) on length scales shorter than the scale on which the response is mapped, or there may be errors from incorrect map values over some areas of the response maps. These variations remain a constant fraction of total scintillation light regardless of the light level. We shall call this type error "uniformity" errors. A second type of mapping error results from the uncertainty in the event's trajectory. Errors in the trajectory result in errors in the mapped responses calculated in each layer. We have termed these errors "map-position" errors. Since position resolution scales approximately as 1/Z, fractional map-position errors should also scale roughly as 1/Z.

In order to estimate the contribution of uniformity and map-position errors, the flight energy resolution was measured for Li, C, O, Si, and Fe. The observed resolution was fit with a model which included Bohr/Landau fluctuations, photoelectron statistics, and which allowed the level of uniformity and map-position errors to be free parameters of the fit. The fit results in fractional errors of ~0.7% due to small scale uniformity errors, and predicts that map-position errors due to position uncertainty are about 1.5 times the size of the photoelectron statistical fluctuations. This size map-position error corresponds to a fractional error of about 0.9% for stopping carbon.

3.2.3. Summary of Single Layer Resolution

Table 3.1 shows the energy resolution, expressed as a fraction of energy deposition, measured for a single stack layer for penetrating flight events. Also shown are the calculated statistical fluctuations in energy loss, the variation due to photoelectron statistics, and the resulting residual energy resolution, σ_R, which we attribute to map-position and residual uniformity errors.

$$\sigma_R^2 = \sigma_{tot}^2 - \sigma_{PE}^2 - \sigma_{BL}^2 \ . \tag{3.9}$$

Table 3.1 Single Layer Energy Resolution
(fraction of layer response)

Nuclei	σ_{tot}	σ_{BL}	σ_{PE}	σ_R
Carbon	0.027	0.025	0.006	0.008
Oxygen	0.022	0.020	0.005	0.008
Iron	0.012	0.006	0.002	0.010

We see that the Bohr/Landau fluctuations dominate the layer resolution for the ~1800 MeV/nuc carbon and oxygen nuclei. If mapping correction errors due to trajectory uncertainty were the only contributor to the residual resolution, then the residual errors should be worse for the lighter nuclei. Instead, the approximately constant residual resolution of about 1% suggests that the NaI(Tl) scintillators have response variations on scales smaller than that for which the maps can correct. Recall that the maps are effectively smoothed on the scale of about 1 cm., while the trajectory error for penetrating carbon is only ~0.2 cm.

It is interesting to note that the 1.2% resolution measured for iron is very close to the resolution of 1.1% measured by Grove (1989) for both the HEIST Bevalac calibration with ^{55}Mn and the HEIST 1984 flight ^{56}Fe events. After accounting for Bohr/Landau fluctuations, Grove estimated that position variations of $\sigma_x = 0.5$ cm. resulted in response map variations of $\sigma_{map} = \sim 0.8\%$, leaving residual unexplained errors of ~0.5% for the 1984 flight ^{56}Fe events. The position accuracy for the 1988 Prince Albert flight is a significant improvement over the 1984 flight positions, yet the energy resolution for iron shows little improvement. This fact supports the hypothesis that, at least for iron, trajectory errors are not the main contributor to single layer energy resolution.

3.3. Total Energy Algorithm

In order to find the total energy of a cosmic ray nucleus which stops in the NaI(Tl) stack, we first sum the responses in all layers of NaI(Tl) from the top of the stack down to the stopping layer. The resulting total response must then be corrected for saturation, for energy loss in the "dead" material between the Cerenkov radiator and the top of the stack, and for energy loss in the thin light shields between stack layers.

We have calculated these correction factors using an algorithm which models the energy loss of nuclei as they slow down in the instrument and which incorporates the scintillation efficiency of NaI(Tl) in order to predict detector response as a function of particle energy. The results of the model are then used to find the average scintillation efficiency, <dl/dE>, and the fraction of energy lost in the dead layer, $\Delta E_{above}/\Delta E_{stack}$, as a function of total detector response. Calculated $\Delta E_{above}/\Delta E_{stack}$ versus stack light output is shown for carbon in Figure 3.1. Note that the term <dl/dE> accounts for the energy loss in the light shields between NaI(Tl) layers and for the effects of saturation.

The total energy of an event can be found by applying these corrections to the observed stack responses.

$$E_{tot} = \frac{\sum_{i=1}^{stop} L_i}{<\frac{dl}{dE}>} \left(1 + \frac{\Delta E_{above}}{\Delta E_{stack}}\right), \qquad (3.10)$$

where L_i is the response in layer i.
The ionization energy loss used for modeling HEIST detector response is calculated using software developed by Newport, Klarmann, and Waddington (Newport, 1986). Their calculation of dE/dx in various media is based on the energy loss model of Salamon (1980).

Saturation of the NaI(Tl) scintillation light has been estimated using a fit done by Grove (1989) to experimental data from the HEIST Bevalac calibrations and which also agrees with experimental data from Salamon and Ahlen (1981). The HEIST Bevalac results and the experiments of Salamon and Ahlen show that the scintillation efficiency, dl/dE, can be approximated as a function only of dE/dx, independent of particle charge and mass. Grove finds the relative scintillation efficiency to be

$$\frac{dl}{dE} = 0.273 - 0.0251\ln(\frac{dE}{dx}) , \tag{3.11}$$

where dE/dx has units of MeV/(g/cm^2) .

3.4. Cerenkov Response Algorithm

In order to optimize the velocity resolution of the Cerenkov counters, data from the 1987 Bevalac calibration were used to test different weighting schemes for combining the individual PMT responses. The weighting factors tested included weighting by PMT response, by response divided by map gradient, and by inverse map gradient. The optimal weighting found for the Bevalac data is simply unit weighting, i.e., giving each PMT signal equal weight. Positions for the Bevalac events were measured by a multi-wire proportional counter and are accurate to better than 0.1 cm., but the positions of flight events have uncertainties of about 1 centimeter at the Cerenkov counters. In order to more realistically simulate the flight data, normally distributed random fluctuations with σ_x = 0.8 cm were added to the Bevalac positions. Unit weighting remained the best weighting scheme when tested with the less accurate positions.

For the Bevalac calibration, all of the PMTs had their responses individually digitized and recorded, but in flight eight of the PMTs are paired into four recorded responses. How should the four paired responses be weighted relative to the eight single tube responses for each counter? By the method of maximum likelihood, a response is weighted by its inverse variance, $1/\sigma^2$. The variances of the single and paired tube responses were estimated from distributions of ΔC_i for the penetrating data set.

$$\Delta C_i = \frac{C_i - C_{ave}}{C_{ave}} . \tag{3.12}$$

Figure 3.1

Correction factors used to correct the total energy for losses in the "dead" layer between the bottom of the Cerenkov radiator and the top of the NaI(Tl) stack are shown for carbon. Dead layers corresponding to the material below the Teflon counter and for material below the Pilot counter are both presented. The energy range shown is from near the threshold energy of each counter up to the maximum energy used for carbon isotope analysis.

Figure 3.1

Dead Layer Corrections

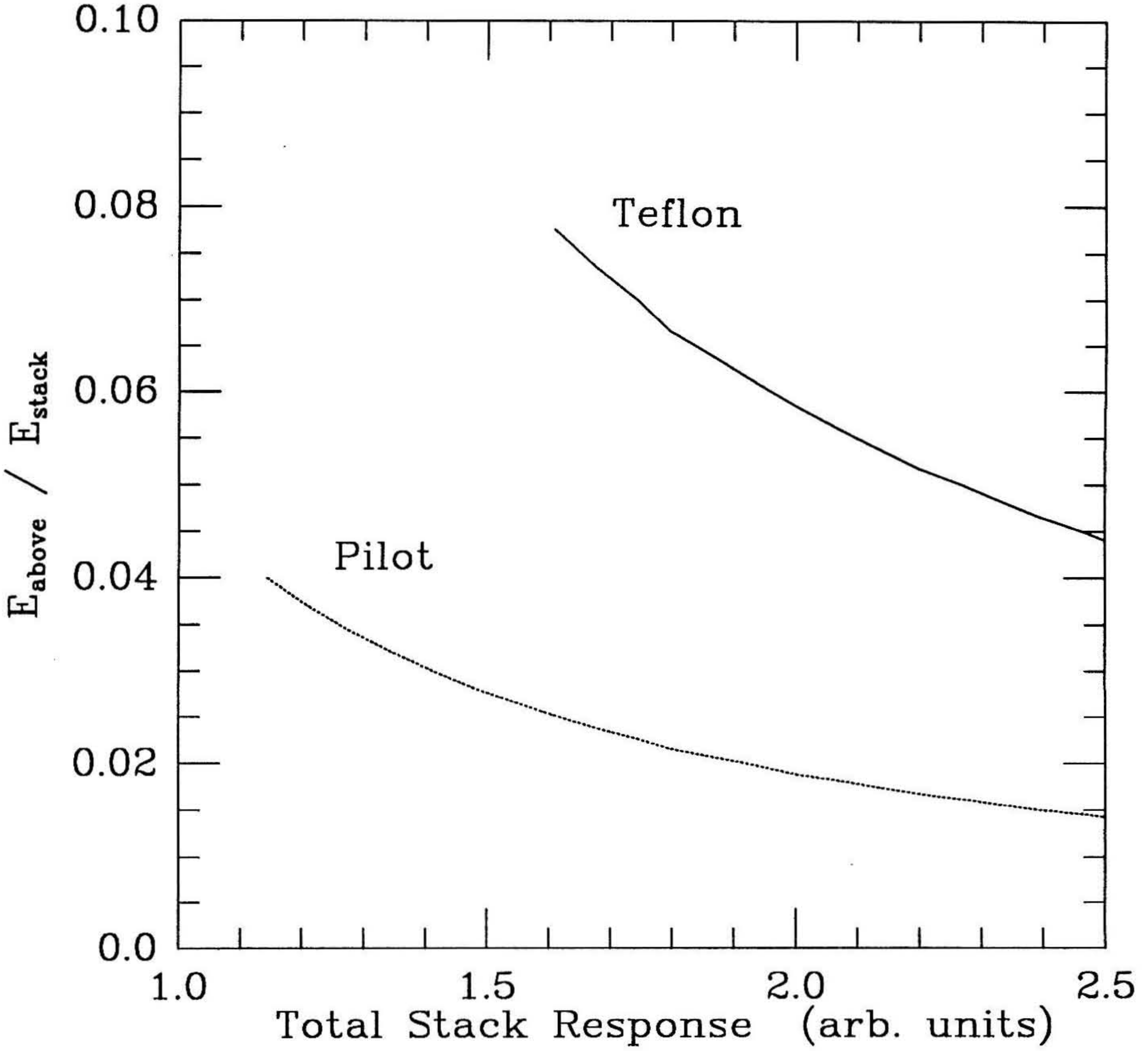

Where C_i are the map corrected responses for individual ADCs, and C_{ave} is the average of the C_i. If the variances were due to photoelectron statistics alone and each tube collected an equal fraction of the total light, then the single tube variances would be twice as large as the paired tube variances. From looking at carbon, magnesium, and iron penetrating events for the Pilot Cerenkov counter, we found the single tube variance to be ~2.3 times the paired tube variance. For the Teflon counter, the single tubes had variances of ~1.6 times the paired tube variances. A ratio of unpaired to paired tube variance of greater than 2.0 means that the errors in the paired tube responses have some anticorrelation. Since the paired tubes are on opposite sides of the Cerenkov counters, we would expect event position errors to produce anticorrelated errors in the two responses; thus, a ratio of 2.3 seems plausible. The same argument for anticorrelation should hold for the Teflon counter, but the Teflon variance ratio of 1.6 means that the response errors in the paired tubes are correlated. This correlation may be due to small scale variations in the Teflon radiator response that are not adequately accounted for by the PMT response maps.

The mapped Cerenkov response in each counter is calculated as,

$$C = \sum_i \frac{P_i}{g_i M_i} w_{ind} + \sum_j \frac{P_j}{g_{j1} M_{j1} + g_{j2} M_{j2}} w_{pair} \cdot \tag{3.13}$$

Where the sum over i includes the eight individually measured PMTs and the sum over j includes the four pairs of PMTs. P_i is the ADC response minus its zero offset. M_i is the value of the tube's response map at the event position calculated by the trajectory algorithm, and g_i is the gain factor which normalizes the response map to the flight PMT gain. Since all the response maps characterize individual PMT responses, the sum of two maps is used to correct the position dependence of the paired PMT responses. The ratio of the paired PMT to individual PMT weighting factors, w_{pair}/w_{ind} is 1.6 and 2.3 for the Teflon and Pilot counters respectively, as discussed above.

The Cerenkov response algorithm also calculates QC, Cerenkov quality, which is a root-mean-square measure of the internal agreement of the 12 measured signals within each counter.

$$QC = \left[\sum_i \frac{(C_i - C)^2 w_i}{C} \right]^{1/2}, \qquad (3.14)$$

where C_i is the map corrected response of each of the 12 Cerenkov signals from given counter. The weighting factor, w_i equals 1.0 for individual tube signals and equals w_{pair} for paired tube signals. This agreement criterion has been calculated for the Teflon counter, QC_1, and the Pilot counter, QC_2. A large value of QC indicates inconsistencies in 12 measured signals which could be caused, for example, by a knock-on electron hitting a PMT face or by an incorrect trajectory assignment for the event. Events with large values of QC were eliminated from the isotope analysis as described in §4.5.

3.5. Velocity Measurement

The Cerenkov response model described in §2.3.3 allows calculation of the Cerenkov counter response as a function of particle charge, energy, and angle of incidence. When the charge of an event is known, this response model can be inverted to yield γ as a function of Cerenkov response and angle of incidence. The errors in the angle of incidence for typical event trajectories can be estimated using equation 2.26. For carbon events, these errors in $\sec\theta$ are significant except for events near normal incidence. We can avoid using $\sec\theta$ from the trajectory fit by using the ratio of the Cerenkov signal to the layer 1 scintillation light, C_{tot}/L_1, as our measure of velocity (Christian et al. 1987). In this ratio, the $\sec\theta$ path-length corrections for the two detectors cancel one another.

Although this technique avoids introducing trajectory $\sec\theta$ uncertainties, errors in the measured layer 1 scintillation now contribute to uncertainties in the velocity. However, using C_{tot}/L_1 to determine γ has an added advantage. Let us

Figure 3.2

A comparison of the mass uncertainty resulting from uncertainties in calculated event trajectories and in stack layer 1 response measurement for carbon events.

Figure 3.2

Comparison of Trajectory
and Layer 1 Errors

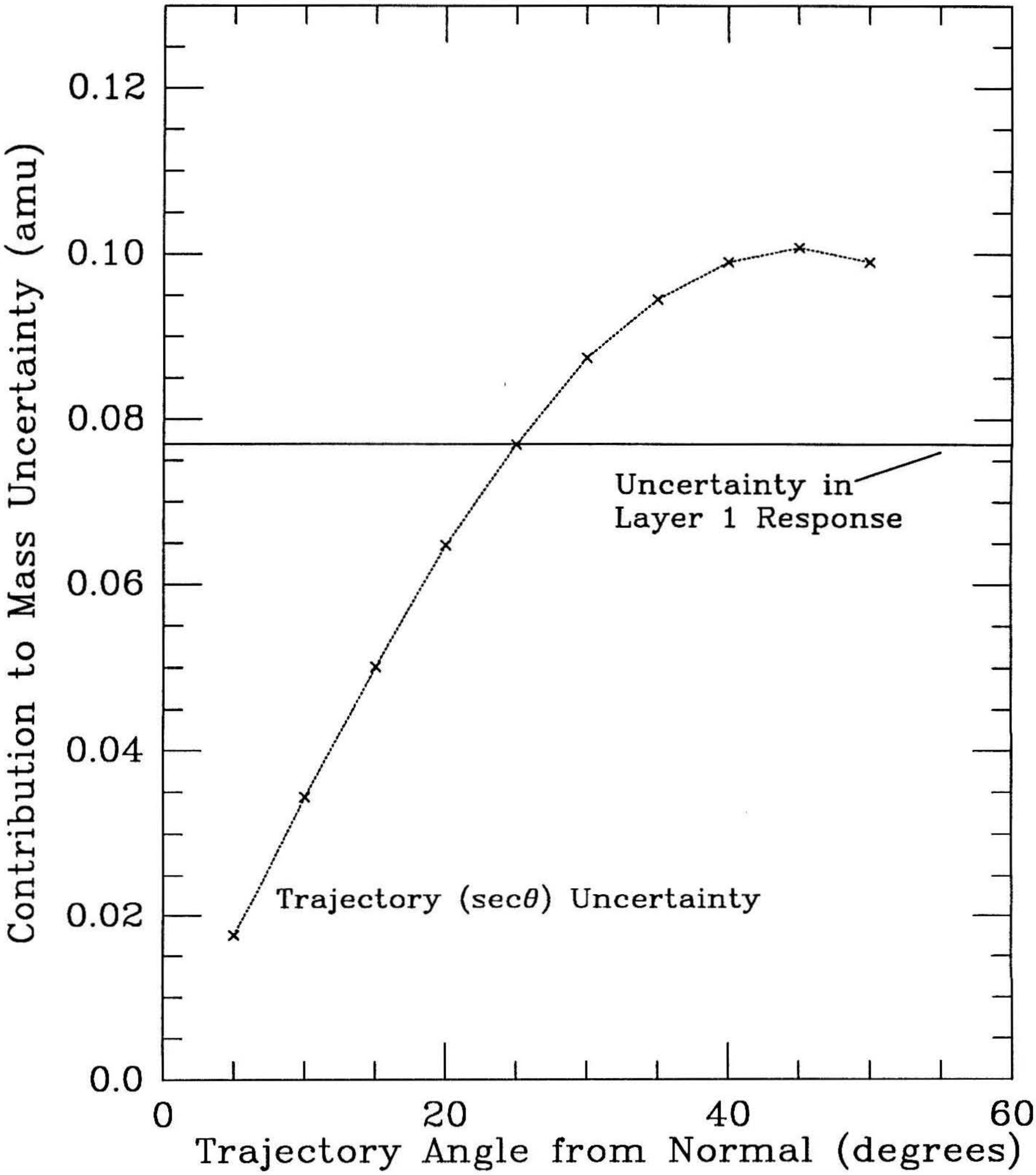

define $\Omega \equiv \frac{C_{tot}}{L_1}$. If we use $\Omega(\gamma)$ to measure γ, then the uncertainty in γ is

$$\delta\gamma = \frac{d\gamma}{d\Omega}\,\delta\Omega. \tag{3.15}$$

Since layer 1 scintillation decreases as a function of γ and the Cerenkov response increases as a function of γ, determining γ using C_{tot}/L_1 improves velocity resolution by increasing the signal variation as a function of particle velocity. In other words, $d\gamma/d\Omega < d\gamma/dC$, so that a given uncertainty in response results in a smaller uncertainty in γ when $\gamma(\Omega)$ is used in place of $\gamma(C)$. Thus, aside from the tradeoff of $\sec\theta$ versus L_1 uncertainties, using $\Omega(\gamma)$ reduces the errors due to other factors such as photoelectron statistics and uniformity variations in the Cerenkov counters.

Figure 3.2 compares the uncertainty in layer 1 response to the $\sec\theta$ errors for carbon events with energies of 400 MeV/nuc in the Pilot counter. The trajectory errors were estimated for an example event which has position measurements available from the plastic top scintillator and from stack layers 1, 2, and 4. Some flight trajectories will be better due to additional position measurements of deeper stack layers, and some will be worse due to the non-Gaussian errors evident in the position error distributions shown in §2.4. Errors in measuring single layer energy loss increase gradually as a function of energy as discussed in §3.2 and are of the same order as the average $\sec\theta$ errors from using event trajectories. The resulting mass uncertainty contribution from these two methods for path-length correction is much smaller than the contribution from Cerenkov photoelectron statistics; thus, the C_{tot}/L_1 method was used for our mass analysis. For heavier nuclei, the layer 1 fluctuations become relatively more important in contributing to the total mass resolution, and using $\sec\theta$ instead of, or in addition to C_{tot}/L_1 might improve the overall resolution.

3.6. Mass Resolution for the Cerenkov-Energy Method

As discussed in §2.2.1, the Cerenkov-Energy method allows the mass of a cosmic ray nucleus to be calculated given measurements of its velocity and total energy.

$$M = \frac{E}{c^2(\gamma-1)} \ . \tag{3.16}$$

By approximating the nuclear mass as the atomic number, A, times the atomic mass unit, m_a, we have

$$A = \frac{1}{m_a c^2} \frac{E}{(\gamma-1)} \ . \tag{3.17}$$

Differentiating this equation to find a expression for resolution gives

$$\delta A = A \left[\left(\frac{\delta E}{E}\right)^2 + \left(\frac{\delta\gamma}{\gamma-1}\right)^2 \right]^{1/2} . \tag{3.18}$$

The major contributors to the uncertainty in γ are Cerenkov photoelectron statistics, stochastic variations in knock-on electron production, detector non-uniformity, and mapping errors due to trajectory uncertainty. In addition we have $\sec\theta$ errors when we use trajectories to correct the Cerenkov response, or we have layer one energy uncertainties if we use C_{tot}/L_1 to find γ.

3.6.1. Contributions to Velocity Resolution

In this section, the main contributions to the uncertainties in the calculated Cerenkov responses from both Cerenkov counters are discussed. Some contributions to the uncertainty in γ, such as photoelectron statistics and variations in knock-on electron light, scale as 1/Z and result in a contribution to mass resolution which is roughly independent of nuclear species. Other contributions, such as response map errors result in a fractional uncertainty in γ which is independent of nuclear charge, Z. These uncertainties become relatively more important with increasing nuclear charge and mass. A model of mass resolution which includes these contributions has been constructed using flight data and pre-flight calibrations and is compared with the mass resolution achieved for the 1988 flight. For further discussion of mass resolution of the Cerenkov-Energy method, including some detailed derivations, see Grove (1989).

3.6.1.1. Photoelectron Statistics

Photoelectron statistics in the Cerenkov counters is the dominant contributor to Cerenkov-Energy mass resolution over the charge range analyzed in this work. Statistical fluctuations in the number of photoelectrons collected are governed by Poisson counting statistics. Since C has units of photoelectrons, $\delta C = \sqrt{C}$. The contribution to velocity resolution is

$$\delta\gamma_{pe} = \frac{\partial\gamma}{\partial\Omega}\,\frac{\partial\Omega}{\partial C}\,\delta C_{pe} \tag{3.19}$$

$$= \Omega\,\frac{\partial\gamma}{\partial\Omega}\,\frac{\delta C_{pe}}{C}\,. \tag{3.20}$$

Neglecting background and secondary light in the Cerenkov counters, we can use equation 2.4 to find that

$$\frac{\delta C_{pe}}{C} = \frac{1}{\sqrt{C}} \approx \frac{1}{Z}\,\frac{1}{\sqrt{\sec\theta\ N_{\mu}\ f(\gamma)}}\,. \tag{3.21}$$

The velocity uncertainty from photoelectron statistics scales as 1/Z. For the nuclei analyzed by HEIST, $A \approx 2Z$, and so the resulting contribution to mass resolution expressed in amu is roughly constant for all nuclei measured. We also see that mass resolution improves with increasing N_{μ}; so, it is advantageous to construct Cerenkov counters which produce and collect as much light as possible. In order to optimize the light production and collection of the HEIST counters, the Teflon radiator was coated with a wave-shifter which increases light output in the wavelength range to which the PMTs are sensitive. The Pilot-425 material also incorporates a wave-shifter during its manufacture. To increase light collection efficiency, the interiors of both light collection boxes were painted with very high reflectance $BaSO_4$ paint which minimizes absorptance of Cerenkov light by the walls of the boxes.

We have measured the number of photoelectrons collected by the two HEIST counters by a number of methods. The counters' response to relativistic ground-level muons was measured and the corresponding number of produced photoelectrons was estimated from calibrations with pulsed LEDs within each counter. LED calibrations were also compared with the counters' response to nitrogen, argon, and iron beams at the Bevalac accelerator to measure the produced number of photoelectrons. Finally, Prince Albert flight data was used to verify Cerenkov photoelectron production by measuring the variance of the ratios of PMT responses. These three methods give a consistent measure of N_μ, the number of photoelectrons produced by the passage of a $Z=1$, $\beta=1$ particle. The Pilot Cerenkov counter has $N_\mu \approx 84$ photoelectrons, and the Teflon counter produces less light, $N_\mu \approx 64$ photoelectrons.

3.6.1.2. Map-Position and Uniformity Errors

As discussed in §3.3.2 on map-position and uniformity errors in the NaI(Tl) stack, there are two types of errors that occur because of spatial nonuniformity of the measured response. One type is uniformity error due to inaccuracies in the response maps and to small scale variations in response for which the maps cannot correct. The resulting uncertainty in γ is given by:

$$\begin{aligned} \delta\gamma_U &= \frac{\partial\gamma}{\partial\Omega}\,\frac{\partial\Omega}{\partial C}\,\delta C_U \\ &= \Omega\,\frac{\partial\gamma}{\partial\Omega}\,\frac{\delta C_U}{C} \\ &= \Omega\,\frac{\partial\gamma}{\partial\Omega}\,\sigma_U\,. \end{aligned} \tag{3.22}$$

For these errors the fractional uncertainty in Cerenkov response, $\sigma_U \equiv \delta C_U/C$, is constant, independent of the energy or charge of the incident nucleus. Therefore, the mass uncertainty from these errors becomes relatively more important with increasing nuclear mass.

The second type of error, which we have called map-position error, is due to the errors in map corrections caused by uncertainty in the event trajectory. As for the uniformity errors,

$$\delta\gamma_U = \Omega \frac{\partial\gamma}{\partial\Omega} \frac{\delta C_{MP}}{C} = \Omega \frac{\partial\gamma}{\partial\Omega} \sigma_{MP} \, . \tag{3.23}$$

The trajectory position resolution improves with increasing nuclear charge, but $\delta C_{MP}/C$ will decrease slightly more slowly than 1/Z. So, δM_{MP} will be larger for heavier nuclei.

The uniformity errors due to small scale response variations, σ_U, were estimated by finding residual errors in Bevalac calibration data after subtracting out the uncertainties due to photoelectron statistics. The resulting uniformity errors for the Pilot Cerenkov counter are estimated to be $\sigma_U \approx 0.5\%$, and for the Teflon counter, $\sigma_U \approx 1.0\%$. However, the mass resolution for flight Ne and Fe events, where uniformity errors are a dominant contribution to mass resolution, suggests that σ_U may be as high as 2% for the Teflon counter, and this value is used in the mass resolution model. One of the causes of the poor uniformity of the Teflon counter may be a degradation of the wave-shifter over time. The two Teflon disks which comprise the Teflon radiator were coated with wave-shifter in May of 1986. The PTP wave-shifter is somewhat volatile and may have partially evaporated by the time of the November 1987 calibration at the Lawrence Berkeley Laboratory Bevalac. This degradation could account both for the observed non-uniformity and for a possible decrease in photoelectron yield over this time period. Any further change in the wave-shifter between the 1987 mapping and the August 1988 flight would cause inaccuracies in the constructed response maps.

We can estimate map-position errors for flight events from the known response gradients and trajectory uncertainties at the Cerenkov counters. The gradient in total light collection efficiency for the Pilot counter has a root mean square (rms) value of about 0.3%/cm. The position uncertainty of about one centimeter for stopping carbon leads to a map-position error of 0.3%. The Teflon counter has larger light collection gradients, leading to an rms error of about 0.9%/cm. Stopping carbon events have position uncertainties in the Teflon counter of slightly more than a centimeter; so for carbon, the expected map-position error of about 1% is half the size of the uniformity error.

3.6.1.3. Knock-on electrons

Energetic knock-on electrons produced as the incident nucleus passes through the instrument contribute to the observed Cerenkov response, and fluctuations in the number and energy of the knock-ons result in random fluctuations in the Cerenkov signal. As in the previous sections, the resulting uncertainty in γ can be expressed as

$$\delta\gamma_{kn} = \Omega \frac{\partial\gamma}{\partial\Omega} \frac{\delta C_{kn}}{C} . \tag{3.24}$$

Again approximating C by the primary Cerenkov light as given in Equation 2.4, $C \approx Z^2 N_\mu \sec\theta\, f(\gamma)$, the fluctuations in knock-on electron Cerenkov light can be expressed as $\delta C_{kn} = Z N_\mu \sec^{1/2}\theta\, \sigma_k(\gamma)$. The resulting fractional uncertainty in Cerenkov response is

$$\frac{\delta C_{kn}}{C} \approx \frac{1}{Z \sec^{1/2}\theta} \frac{\sigma_k(\gamma)}{f(\gamma)} . \tag{3.25}$$

The knock-on model developed by Grove (1989) predicts the knock-on contribution to total Cerenkov light and calculates the expected variation of knock-on signal as a function of energy (see also Grove and Mewaldt 1992). For nuclei incident with energies greater than a few GeV/nucleon, the knock-on production depends on the amount of overburden above the Cerenkov counters. For nuclei in the energy range used for this mass analysis, the contributing knock-ons are produced mainly within or just above the Cerenkov radiator, and the model predictions do not depend strongly on the amount of assumed overburden. A fit to the knock-on model predictions for the Teflon Cerenkov counter gives an rms variation, σ_k of

$$\sigma_{ktef} = 0.376 + 0.150(\gamma - 1) - 0.106\beta - 0.3\beta^2 . \tag{3.26}$$

For the Pilot counter, the knock-on model predicts rms fluctuations of

$$\sigma_{\mathrm{kpil}} = 0.369 + 0.116(\gamma-1) - 0.294\beta - 0.063\beta^2 \,. \tag{3.27}$$

Because the knock-on uncertainties are proportional to 1/Z, their contribution to mass resolution is approximately independent of nuclear species. For events with energy near 500 MeV/nuc, these fluctuations result in a Pilot-Energy mass uncertainty of ~0.1 amu and a Teflon-Energy mass uncertainty of 0.07 amu.

3.6.1.4. Cerenkov ADC Binning Error and Amplifier Noise

Errors due to the finite width of the ADC bins, or due to the small amount of noise from the ADC electronics are very small compared to the full range of the 4096 channel ADCs; however, since HEIST was designed to record events of nuclei ranging from Z=3 up to Z=28, these errors could be significant for the light nuclei. The binning error for an individual ADC is simply $1/\sqrt{12}$ of a bin, the rms error of a uniform distribution of unit width. Since there are 12 ADC channels for a Cerenkov counter, the total binning error is equal to one bin. The amplifier noise level was measured from the width of the ADC pedestal distributions generated by External Triggers during flight. (External Triggers were explained in §2.1.) The total error resulting from noise and binning errors for the Teflon counter is about 4 bins which corresponds to a signal level of ~16 photoelectrons. The total noise and binning error for the Pilot counter is about 3 bins, corresponding to a light level of ~10 photoelectrons. The uncertainty in γ is

$$\delta\gamma_{\mathrm{ADC}} = \Omega \frac{\partial\gamma}{\partial\Omega} \frac{\delta C_{\mathrm{ADC}}}{C} \approx \Omega \frac{\partial\gamma}{\partial\Omega} \frac{\delta C_{\mathrm{ADC}}}{Z^2 N_\mu \sec\theta\, (f(\gamma) + 0.1)} \,, \tag{3.28}$$

where we have included the "background" light from scintillation and secondary Cerenkov light estimated as 10% of the primary light from a "β=1" particle. This is a reasonable approximation for the background contribution for nuclei with $Z \leq 7$. Recall that the Pilot Cerenkov counter has $N_\mu \approx 84$ photoelectrons, and the Teflon counter has $N_\mu \approx 64$ photoelectrons. As can be seen by expressing these errors in terms of photoelectrons and as shown in Figures 3.3 and 3.4, the ADC noise is small compared to other contributions to mass resolution for all but the lightest elements measured with HEIST. The resulting mass uncertainty for Boron is ~0.06 amu for the Pilot-Energy method and ~0.12 amu for the Teflon-Energy method.

3.6.1.5. Uncertainty in Layer 1 Response

The contributions to uncertainties in the response of a NaI(Tl) layer has already been discussed in some detail in §3.2. Included in the discussion were uncertainties from fluctuations in ionization energy loss, photoelectron counting statistics in the NaI(Tl), and residual errors which are probably due to inadequacies of the PMT response maps. Both Bohr/Landau energy loss fluctuations and photoelectron counting statistics scale as

$$\frac{\delta L_1}{L_1} \propto \frac{1}{Z \sec^{1/2}\theta} , \tag{3.29}$$

and result in a contribution to $\delta\gamma$ given by

$$\delta\gamma_L = \Omega \frac{\partial\gamma}{\partial\Omega} \frac{\delta L_1}{L_1} . \tag{3.30}$$

The contribution to mass uncertainty for 500 MeV/nuc events is ~0.09 amu for Pilot-Energy mass and ~0.04 amu for Teflon-Energy mass, approximately independent of nuclear species.

The contribution to $\delta L_1/L_1$ from map errors is independent of Z. The resulting contribution to Pilot-Energy mass resolution grows with nuclear mass increasing from 0.07 amu for 500 MeV/nuc carbon to 0.11 amu for 500 MeV/nuc neon.

3.6.2. Total Energy Resolution

Uncertainties in the total energy measurement result mainly from inaccuracies in layer to layer normalizations, and errors in the individual layer responses. These uncertainties, in general, give a smaller contribution to the total mass resolution than uncertainties in γ; however, they may dominate mass resolution for those events which stop in the first few layers of the stack.

The absolute layer to layer gain normalization was found by choosing sets of penetrating carbon, oxygen, magnesium, and iron events with energies near minimum ionizing. Gains were chosen to best give an equal average response from each layer for all four data sets. The error in the resulting layer normalizations can be estimated from the residual differences of the layer responses. Using this method we find the gain uncertainty for a layer is $\sigma_{gain} \approx 1.0\%$, and so the resulting uncertainty in the total energy from gain balancing is

$$\frac{\delta E}{E} = \frac{0.01}{\sqrt{N_{lay}}}, \tag{3.31}$$

where N_{lay} is the number of layers included in the total energy sum.

The errors from individual layer uncertainties discussed in §3.2, with the exception of ionization energy loss fluctuations, will also contribute to the total energy resolution. These errors also scale with N_{lay} as in equation 3.25 and are of the same order of magnitude as the gain normalization errors. There are also small uncertainties arising from the correction for the "dead" material between the Cerenkov counters and the stack, but these give negligible contribution to the total mass uncertainty.

3.6.3. Resulting Mass Resolution

The resulting model for the mass resolution of the Cerenkov-Energy method of mass analysis incorporates the sources of uncertainty discussed above. Figures 3.3 and 3.4 show the predicted mass resolution for B, C, N, O, and Ne as a function of energy for the Pilot and the Teflon Cerenkov counters, respectively. For the Pilot counter, photoelectron statistics dominate the mass uncertainty for most energies with stack layer 1 uncertainties as the second most important contributor. The Teflon counter resolution is also dominated by photoelectron statistics for B, C, N, and O, but uniformity errors become more important at Ne. At the lowest energies, where the Cerenkov counters are the most accurate, the uncertainty in total energy is the largest contributor to mass resolution. Total energy becomes relatively more accurate as the event energy increases and more stack layers are traversed. Figure 3.5 shows the Pilot-Energy mass resolution for oxygen as a function of the angle of incidence of the cosmic ray nuclei. The gradual improvement in resolution as the angle from normal incidence increases is well fit by the model.

The modeled resolution is better than the measured resolution of the flight data with the discrepancy being larger for the Teflon resolution model than for the Pilot resolution model. There are possible explanations for this discrepancy. Possibly the largest contributor to mass resolution not accounted for in the resolution model is inaccuracy in the calculation of $\Omega(\gamma)$ from our detector response model. Because the response models for the Cerenkov counters and for stack layer 1 are not exact, the actual $C_{tot}(\gamma)/L_1(\gamma)$ will vary slightly from our calculated $C_{tot}(\gamma)/L_1(\gamma)$ and will cause the calculated mass of a given isotope to vary slightly as a function of γ. Mass errors of this type have not been included in the mass resolution model. There may also be inaccuracies in the measurements of the flight resolution. The resolution measurements have been made by attempting to select events of the dominant isotope for each element and then finding the rms deviation of these events. Another possible explanation is that the errors due to one or more of the major contributors to the mass resolution has been underestimated. For example, it is possible that the light yield of the Cerenkov counters has been overestimated. We would have to decrease our assumed light yield by $\sim$50% in order to fit the observed carbon and oxygen resolution for Teflon-Energy mass, but the observed internal agreement of the Cerenkov PMTs is inconsistent with this low light level.

The errors in the Pilot-Energy and Teflon-Energy masses are largely uncorrelated, suggesting that the underestimated contributions to mass resolution are in the Cerenkov response and not in the layer 1 or total energy measurements since errors in these measurements would produce correlated errors in both Cerenkov-Energy mass estimates. Recall that the final mass for each event is found by taking a weighted average of the available estimators; so, the overall mass resolution is better than the resolution from the individual measurements represented in these

Figure 3.3

Contributions to mass resolution for the Pilot Cerenkov-Energy method are shown for events at a 25° angle of incidence. Results of the model calculation are compared with the measured flight resolution. Figures a through e, show model curves and measured flight mass resolution for ^{11}B, ^{12}C, ^{14}N, ^{16}O, and ^{20}Ne, respectively.

Figure 3.3(a)

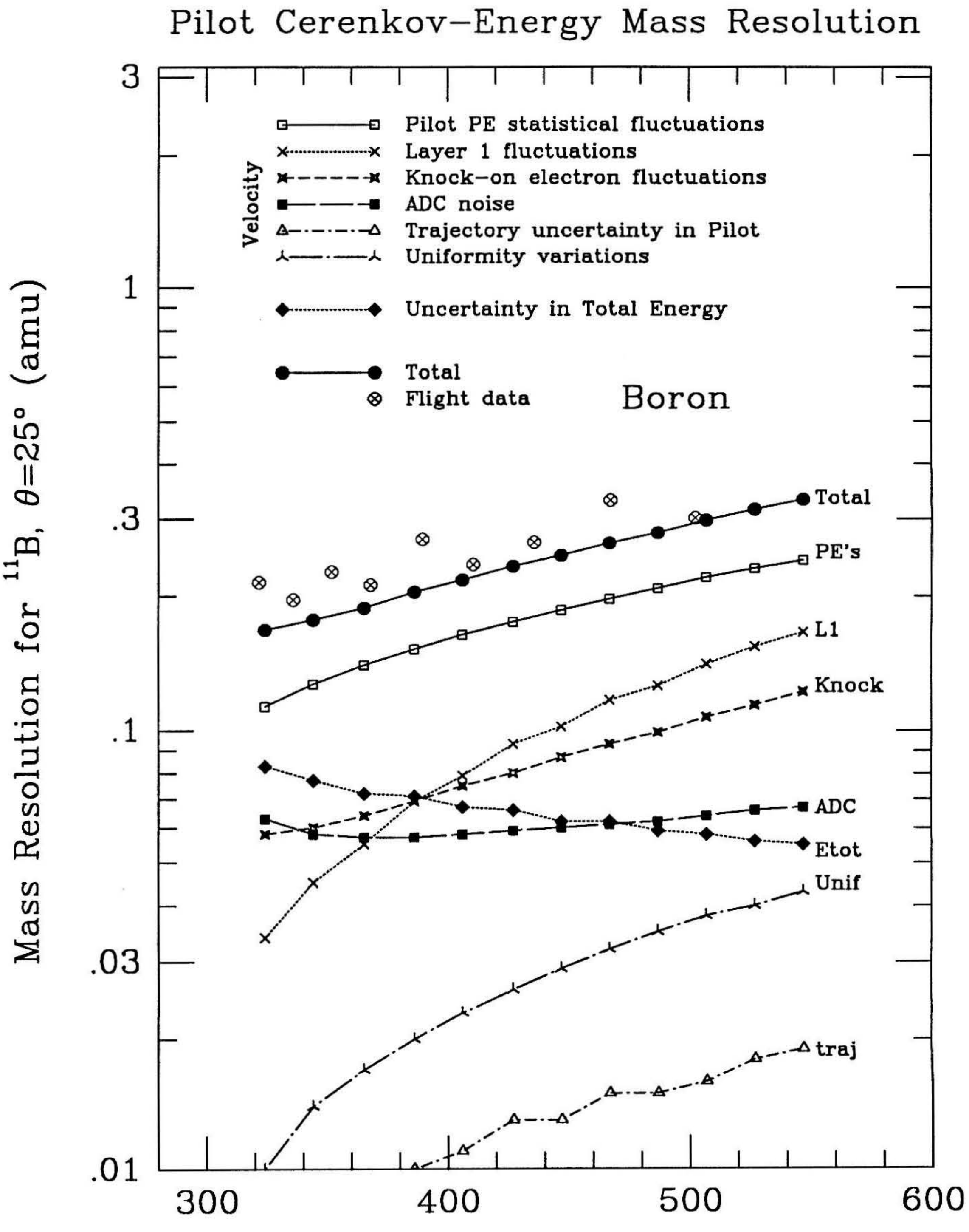
Pilot Cerenkov–Energy Mass Resolution
Mass Resolution for ^{11}B, θ=25° (amu)
Energy (MeV/nuc)
3
1
.3
.1
.03
.01
300
400
500
600
Velocity
Pilot PE statistical fluctuations
Layer 1 fluctuations
Knock-on electron fluctuations
ADC noise
Trajectory uncertainty in Pilot
Uniformity variations
Uncertainty in Total Energy
Total
Flight data
Boron
Total
PE's
L1
Knock
ADC
Etot
Unif
traj

Figure 3.3(b)

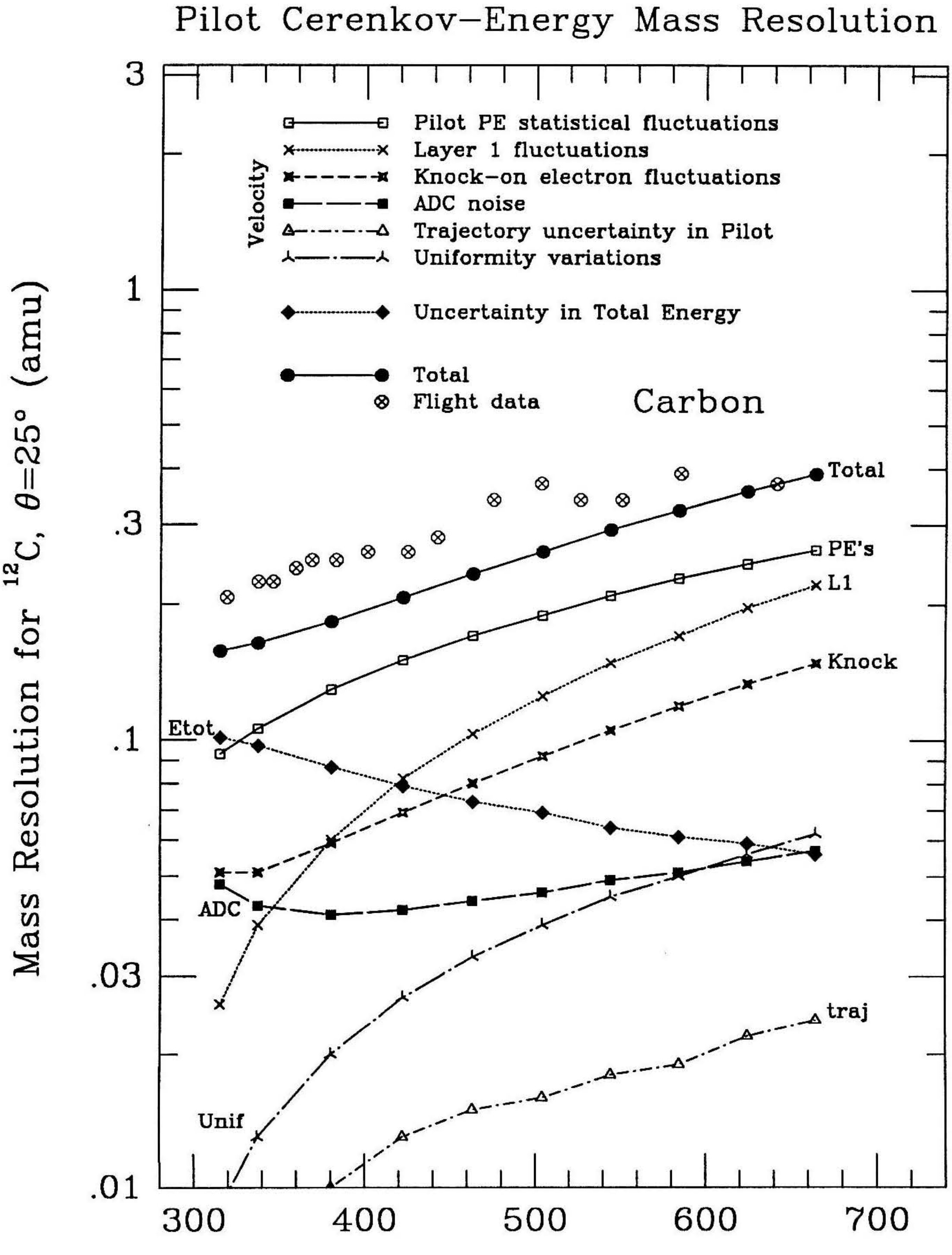
Pilot Cerenkov–Energy Mass Resolution
Velocity
Pilot PE statistical fluctuations
Layer 1 fluctuations
Knock-on electron fluctuations
ADC noise
Trajectory uncertainty in Pilot
Uniformity variations
Uncertainty in Total Energy
Total
Flight data
Carbon
Total
PE's
L1
Knock
Etot
ADC
Unif
traj
3
1
.3
.1
.03
.01
300
400
500
600
700
Energy (MeV/nuc)
Mass Resolution for ^{12}C, θ=25° (amu)

Figure 3.3(c)

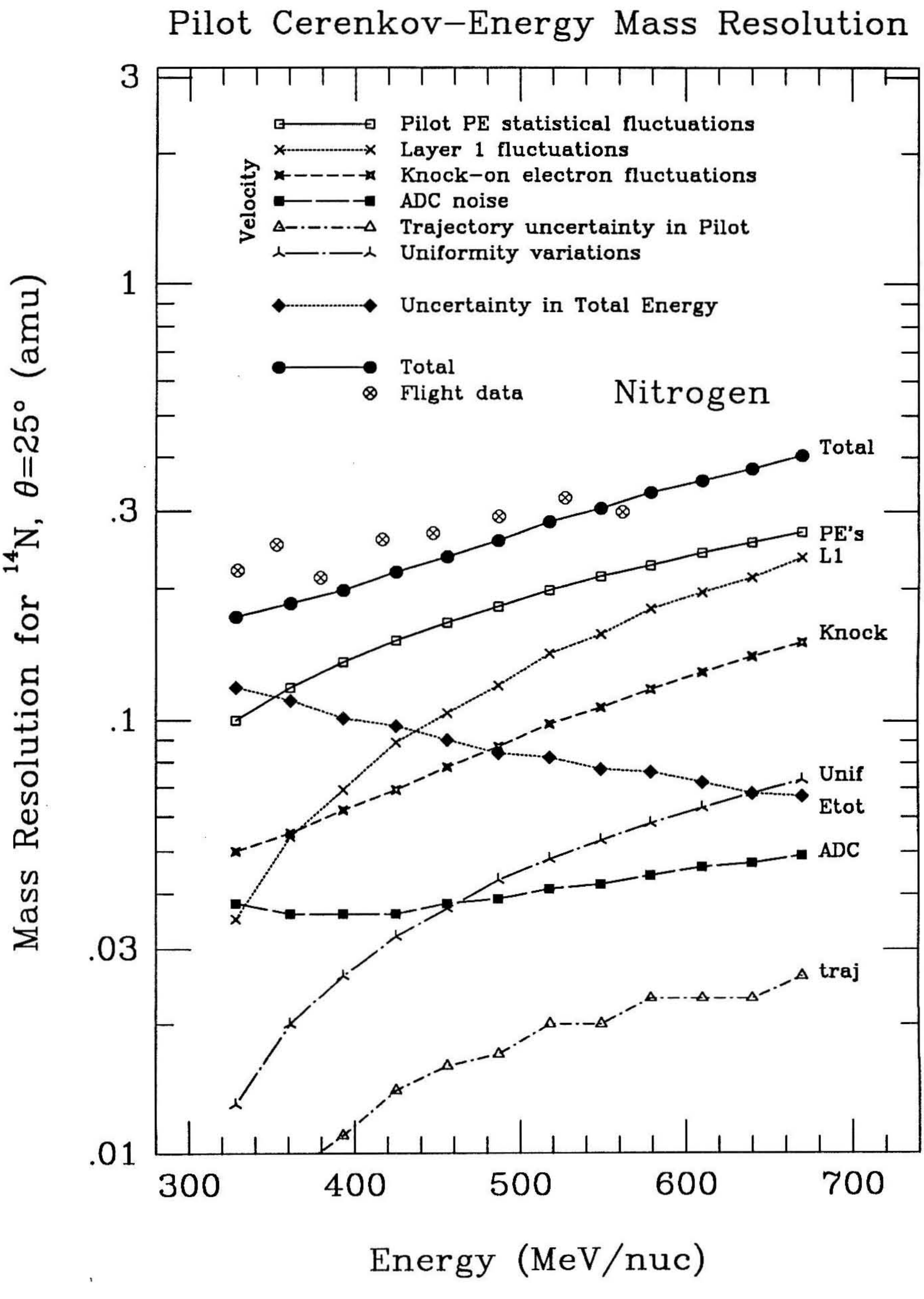
Pilot Cerenkov–Energy Mass Resolution
Velocity
Pilot PE statistical fluctuations
Layer 1 fluctuations
Knock–on electron fluctuations
ADC noise
Trajectory uncertainty in Pilot
Uniformity variations
Uncertainty in Total Energy
Total
Flight data
Nitrogen
Total
PE's
L1
Knock
Unif
Etot
ADC
traj
3
1
.3
.1
.03
.01
300
400
500
600
700
Mass Resolution for ^{14}N, θ=25° (amu)
Energy (MeV/nuc)

Figure 3.3(d)

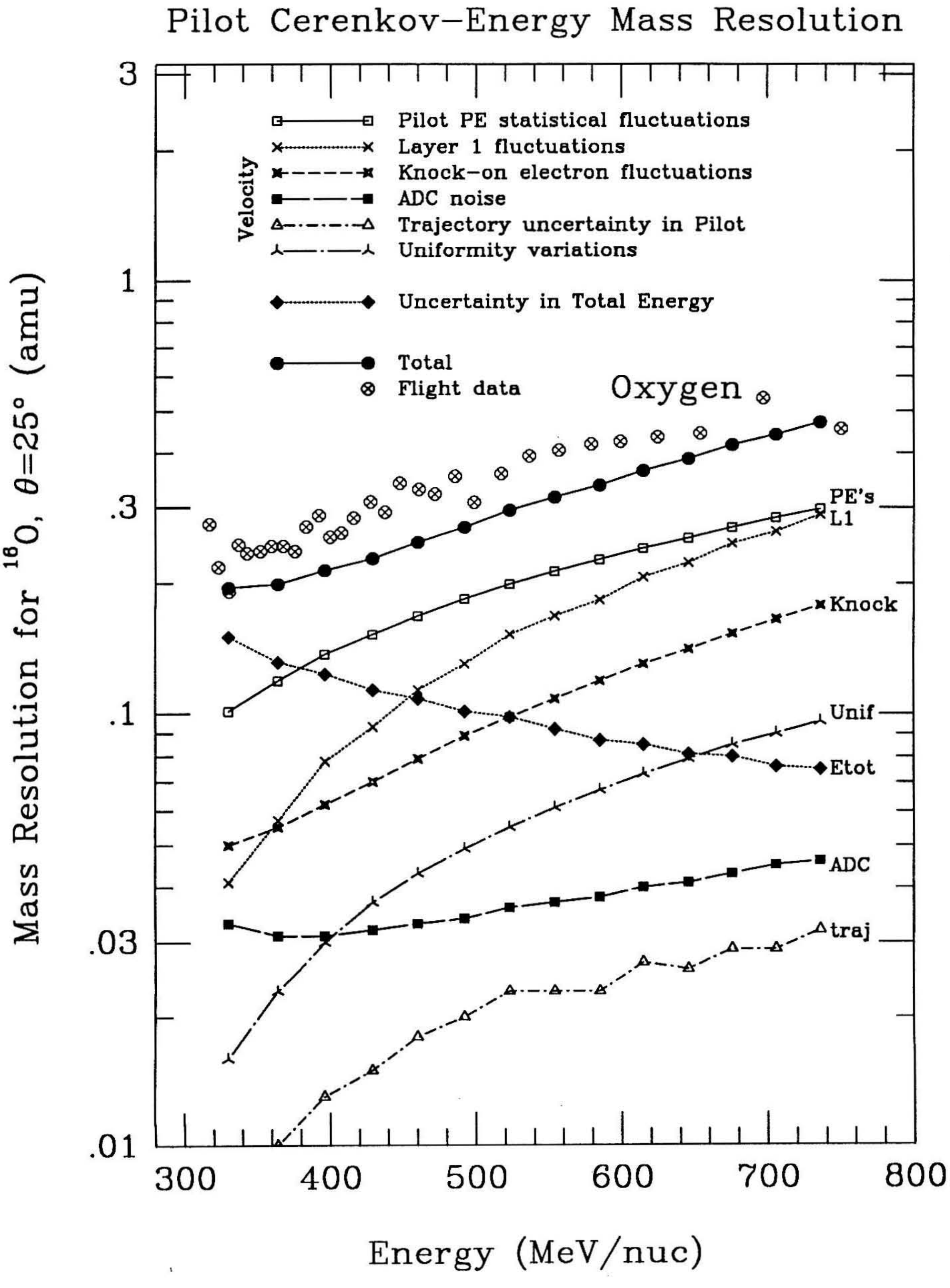
Pilot Cerenkov–Energy Mass Resolution
Velocity
Pilot PE statistical fluctuations
Layer 1 fluctuations
Knock–on electron fluctuations
ADC noise
Trajectory uncertainty in Pilot
Uniformity variations
Uncertainty in Total Energy
Total
Flight data
Oxygen
PE's
L1
Knock
Unif
Etot
ADC
traj
3
1
.3
.1
.03
.01
300
400
500
600
700
800
Energy (MeV/nuc)
Mass Resolution for ^{16}O, θ=25° (amu)

Figure 3.3(e)

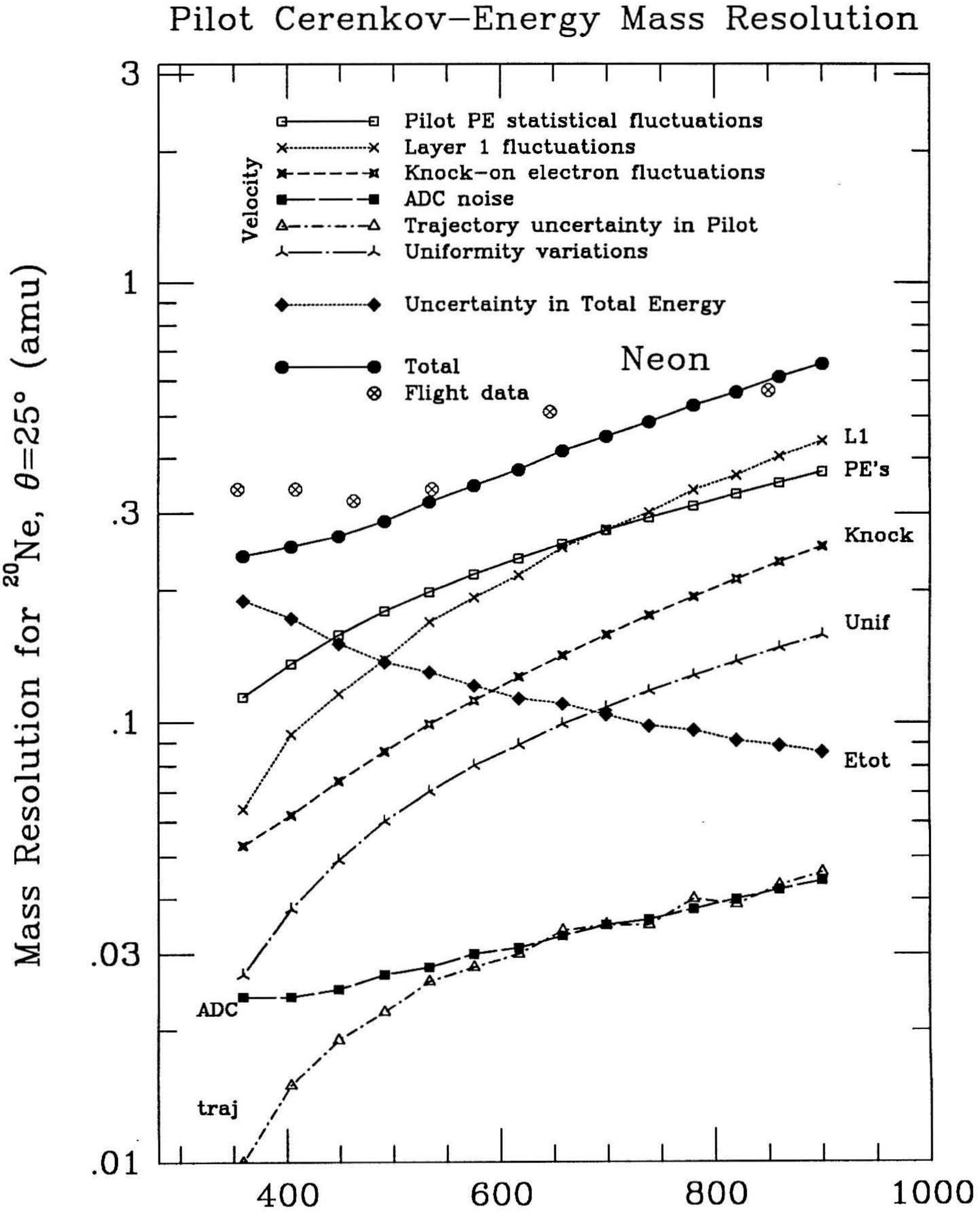
Pilot Cerenkov–Energy Mass Resolution
Velocity
Pilot PE statistical fluctuations
Layer 1 fluctuations
Knock-on electron fluctuations
ADC noise
Trajectory uncertainty in Pilot
Uniformity variations
Uncertainty in Total Energy
Total
Flight data
Neon
L1
PE's
Knock
Unif
Etot
ADC
traj
3
1
.3
.1
.03
.01
400
600
800
1000
Energy (MeV/nuc)
Mass Resolution for ^{20}Ne, θ=25° (amu)

Figure 3.4

Contributions to mass resolution for the Teflon Cerenkov-Energy method are shown for events at a 25° angle of incidence. Results of the model calculation are compared with the measured flight resolution. Figures a through e, show model curves and measured flight mass resolution for ^{11}B, ^{12}C, ^{14}N, ^{16}O, and ^{20}Ne, respectively.

Figure 3.4(a)

Teflon Cerenkov–Energy Mass Resolution

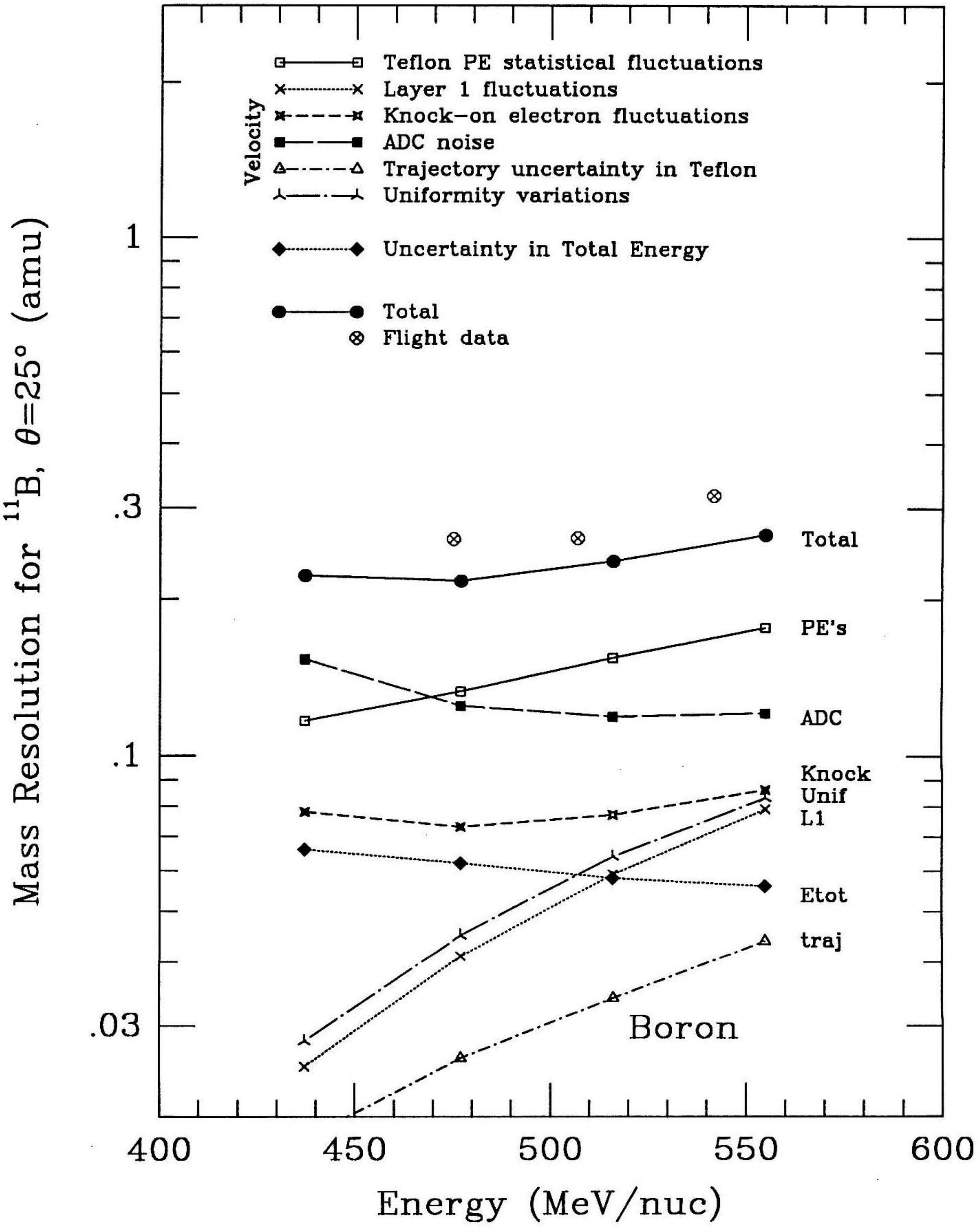

Figure 3.4(b)

Teflon Cerenkov–Energy Mass Resolution

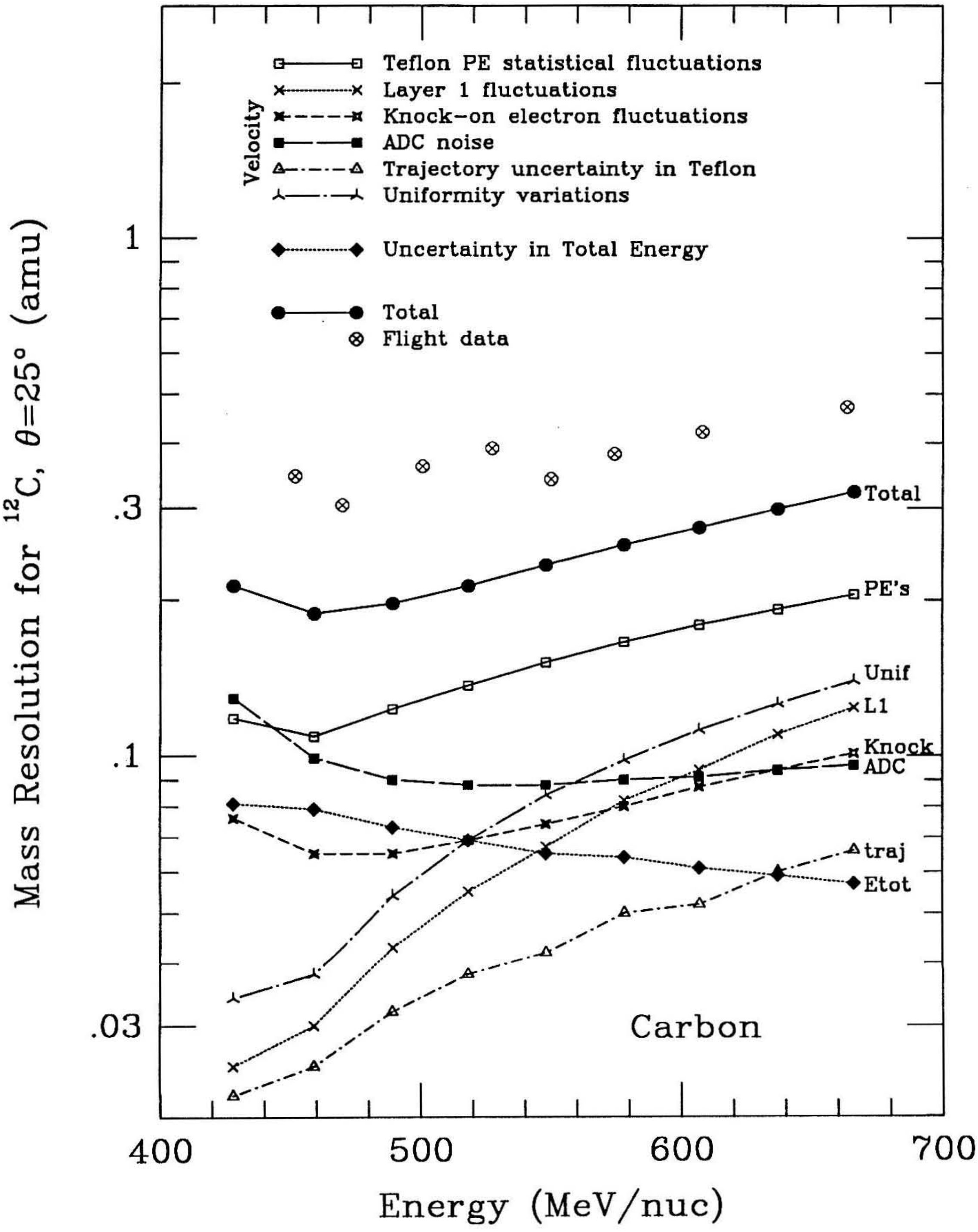

Figure 3.4(c)

Teflon Cerenkov–Energy Mass Resolution

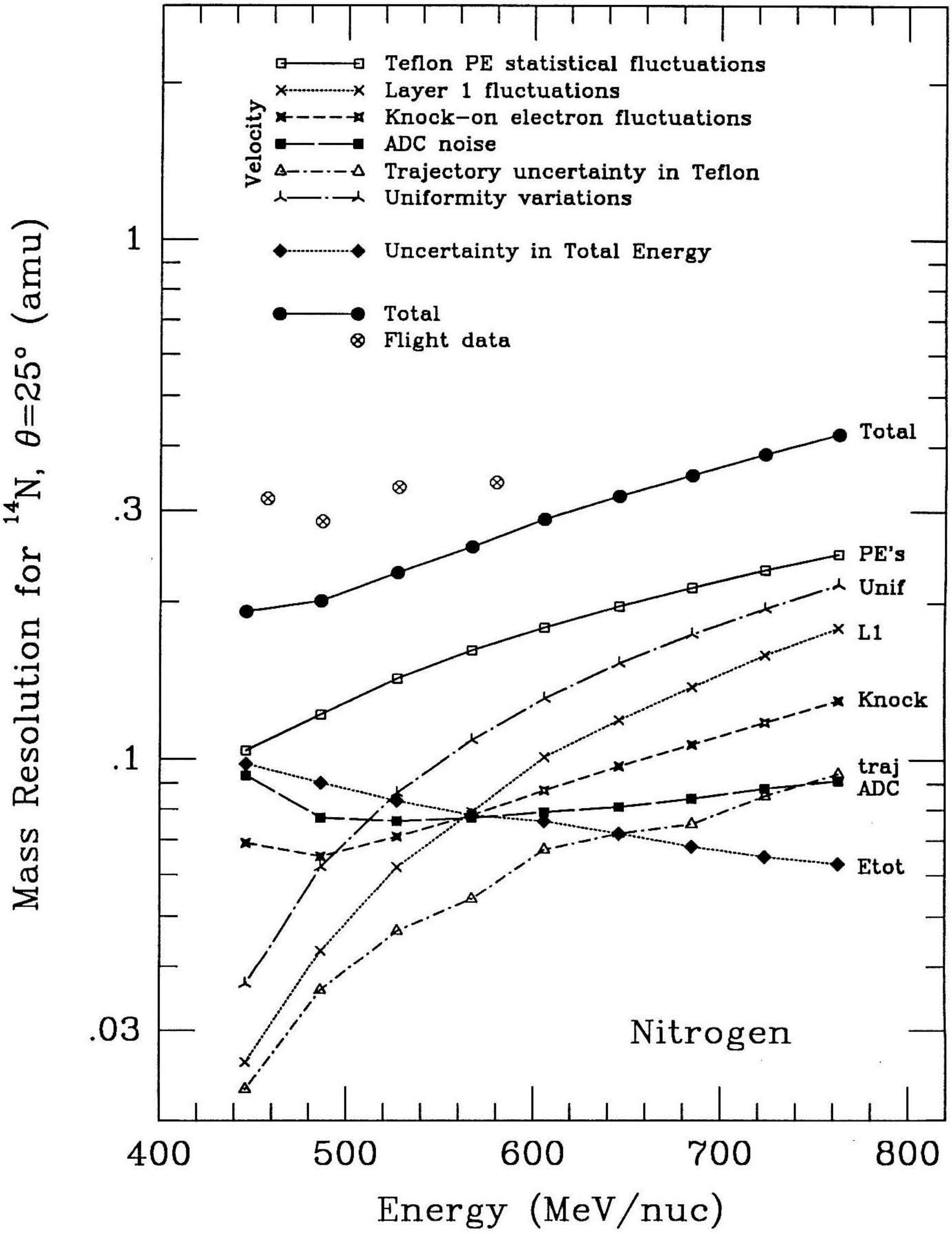

Figure 3.4(d)

Teflon Cerenkov–Energy Mass Resolution

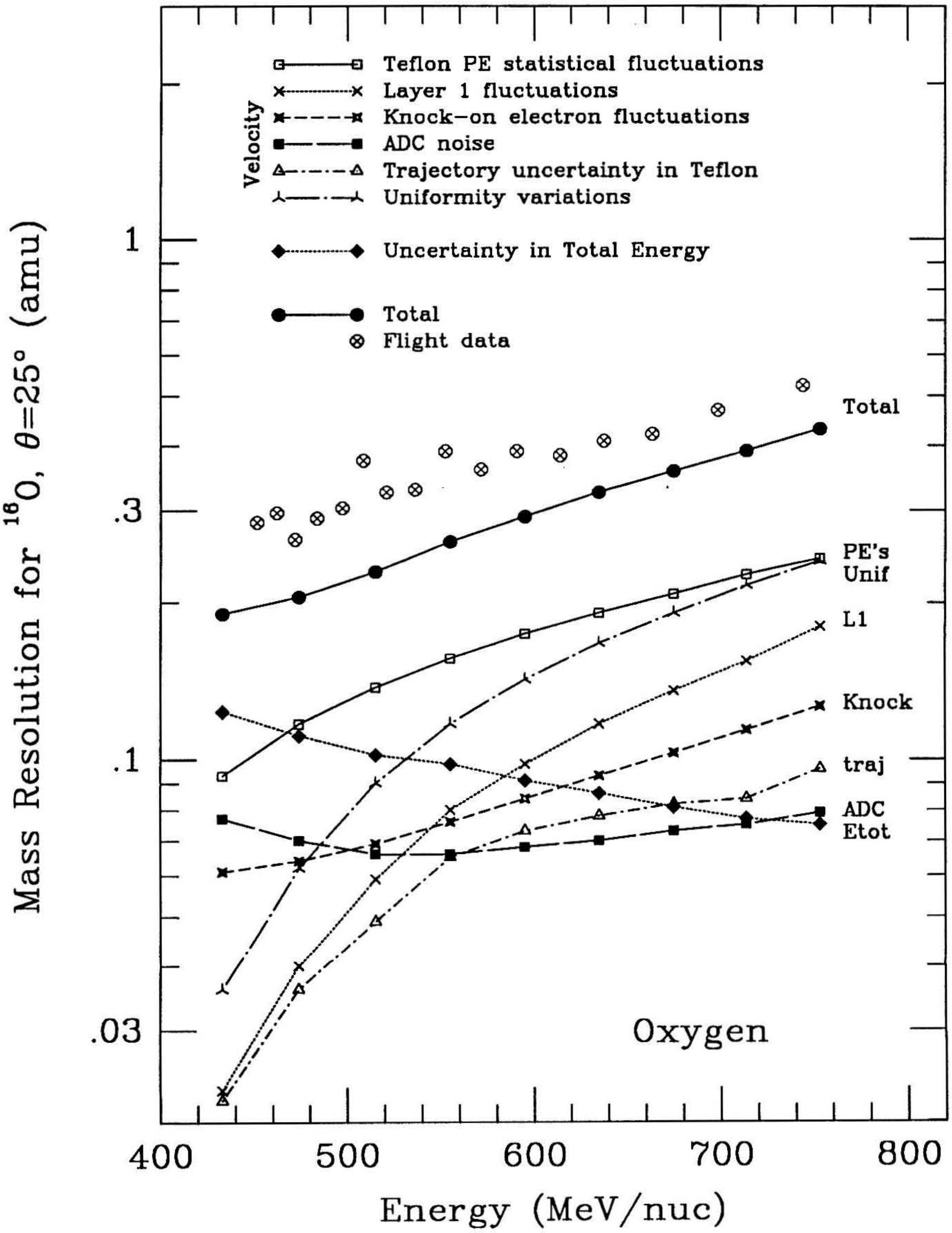

Figure 3.4(e)

Teflon Cerenkov–Energy Mass Resolution

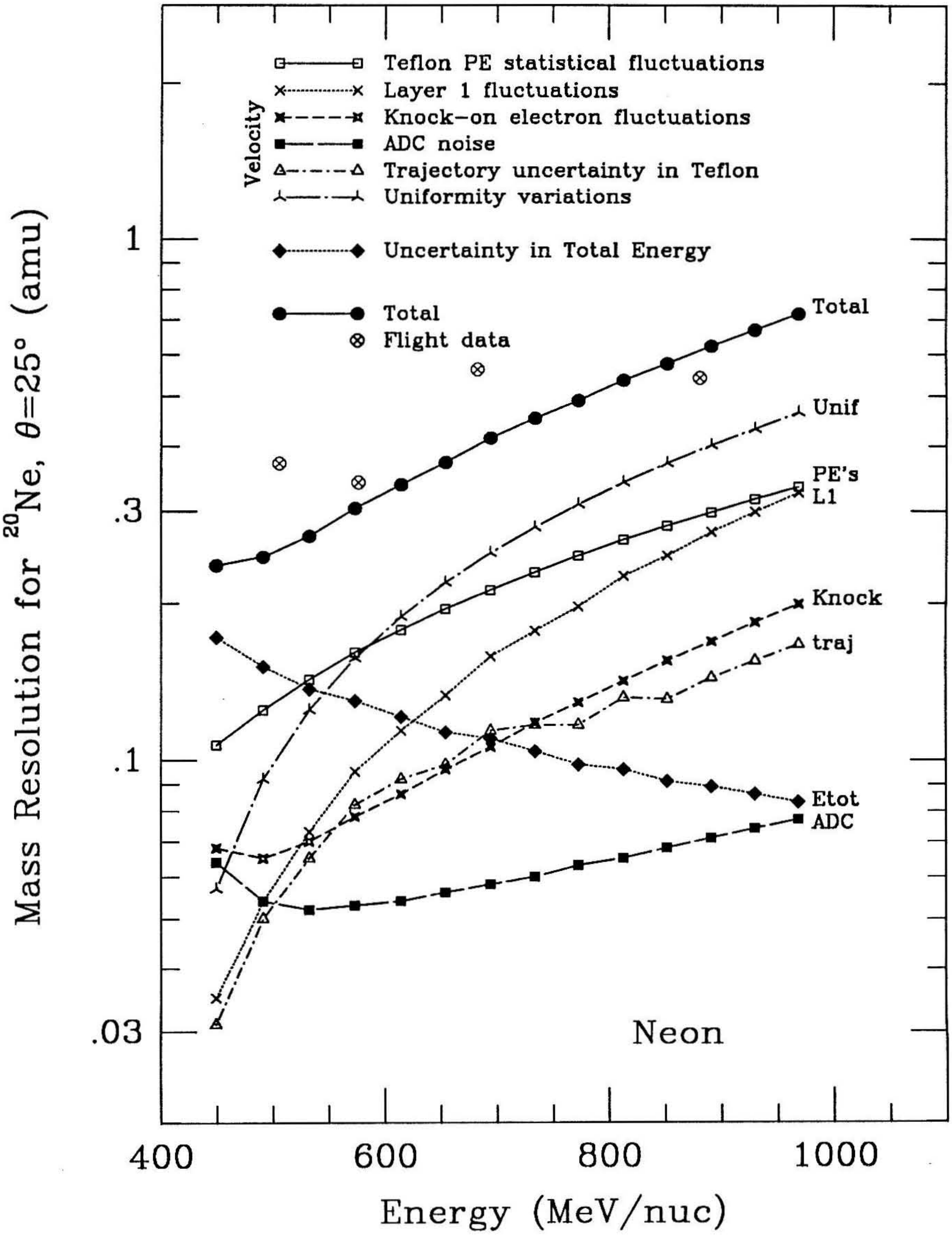

Figure 3.5

Contributions to mass resolution for the Pilot Cerenkov-Energy method are shown as a function of angle of incidence for 650 MeV/nucleon ^{16}O nuclei. Results of the model calculation are compared with the measured flight resolution. The flight data includes ^{16}O nuclei over the entire energy interval used in the mass analysis.

Figure 3.5

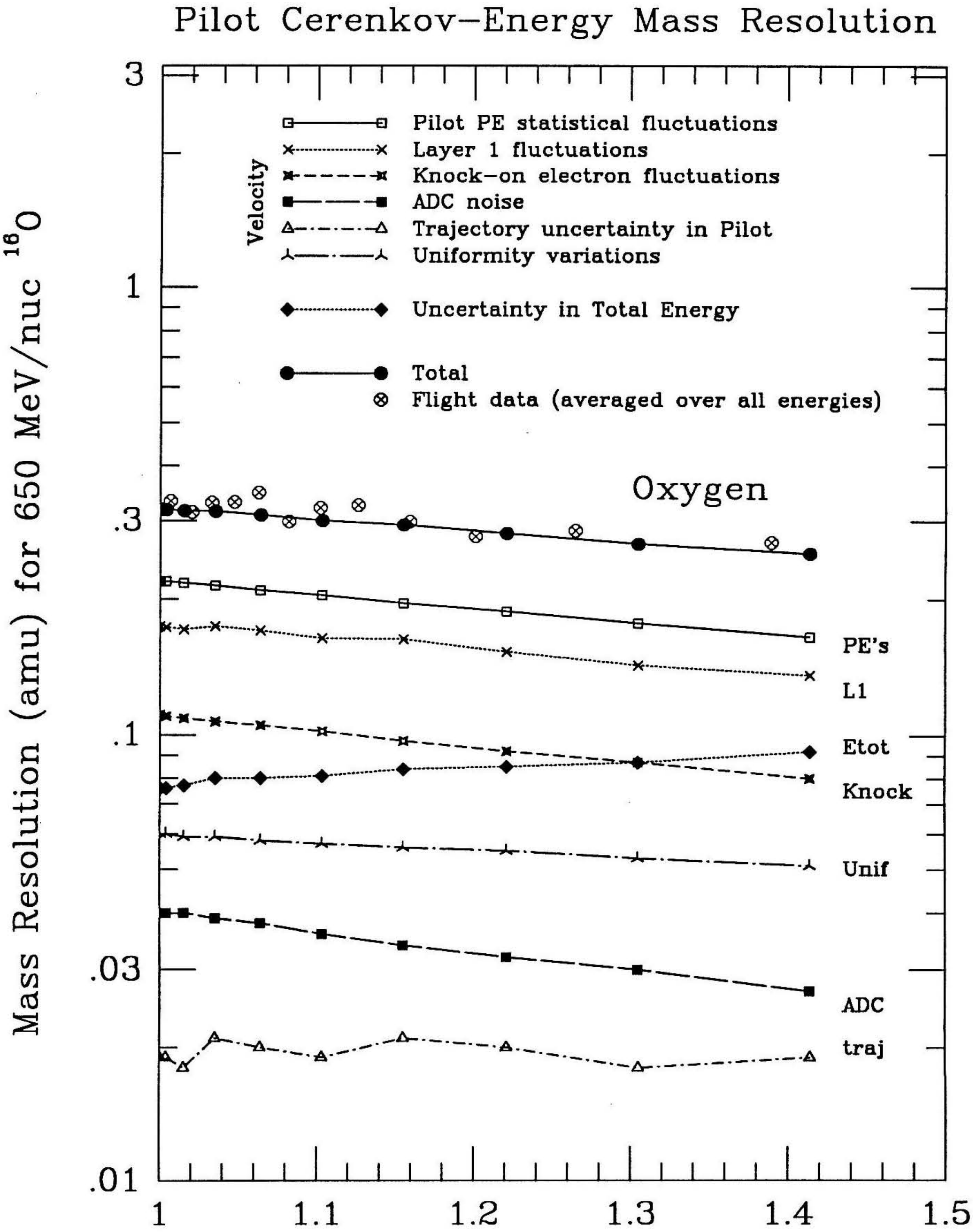
Pilot Cerenkov–Energy Mass Resolution
Mass Resolution (amu) for 650 MeV/nuc ^{16}O
Secant of angle from normal incidence
Velocity
Pilot PE statistical fluctuations
Layer 1 fluctuations
Knock–on electron fluctuations
ADC noise
Trajectory uncertainty in Pilot
Uniformity variations
Uncertainty in Total Energy
Total
Flight data (averaged over all energies)
Oxygen
PE's
L1
Etot
Knock
Unif
ADC
traj
3
1
.3
.1
.03
.01
1
1.1
1.2
1.3
1.4
1.5

figures. Table 3.2 gives the resulting mass resolution for boron, carbon, nitrogen, and oxygen, as found by the abundance fitting algorithm described in §5.1. Resolution for each mass estimation method and for a weighted average of the available methods are shown for two energy intervals, corresponding to velocities below and above the Teflon Cerenkov threshold.

Table 3.2 Average Mass Resolution

Nuclei	Pilot-Energy mass σ (amu)	Teflon-Energy mass σ (amu)	ΔE–E′ mass σ (amu)	Weighted average mass σ (amu)
Events with velocities below Teflon threshold				
Boron	0.25		0.40	0.25
Carbon	0.24		0.43	0.24
Nitrogen	0.25		0.62	0.25
Oxygen	0.25		0.66	0.25
Events with velocities above Teflon threshold				
Boron	0.35	0.33	0.33	0.24
Carbon	0.32	0.34	0.40	0.25
Nitrogen	0.31	0.36	0.51	0.26
Oxygen	0.36	0.34	0.53	0.27

3.7. Mass Resolution for the ΔE–E′ Method

Recall from §2.2.2 that mass is calculated as

$$M = \left[\frac{Z^2 \, t \sec\theta}{k(E^{\lambda} - E'^{\lambda})} \right]^{\frac{1}{1-\lambda}} . \qquad (3.32)$$

Uncertainty in the mass estimated using the ΔE–E' method results from uncertainties in the calculated quantities $t\sec\theta$, ΔE, and E' which result from finite position resolution, ionization energy loss fluctuations, photoelectron counting statistics, NaI(Tl) response map errors, and uncertainties in NaI(Tl) layer to layer normalization.

Uncertainty in the calculated trajectory of an event results in an uncertainty in the events angle of incidence at the ΔE detector. From Equation 3.32, we find that

$$\frac{\delta M_{\sec\theta}}{M} = \frac{1}{M}\frac{\partial M}{\partial \sec\theta}\bigg|_{\Delta E, E'} \sigma_{\sec\theta} \qquad (3.33)$$

$$= \frac{1}{\lambda - 1}\,\frac{\sigma_{\sec\theta}}{\sec\theta}\,.$$

The results of §2.4.3 can be used to estimate $\sigma_{\sec\theta}$. Recall that $\sigma_{\sec\theta}/\sec\theta \propto \sin 2\theta$, and so for events near normal incidence to NaI(Tl) layers, the error in $\sec\theta$ is negligible. For events at angles farther from normal incidence, $\sec\theta$ errors become the dominant contribution to mass uncertainty. Figure 3.6 shows the measured flight resolution for the ΔE–E' method as a function of angle of incidence. The mass resolution becomes worse at larger angles of incidence due to uncertainties in the angle of the measured trajectory. For carbon events incident at an angle of 33° ($\sec\theta = 1.19$), the expected fractional uncertainty in $\sec\theta$ is about 1.5% which results in a mass error of 0.35 amu, where λ has been taken to be 1.5 (see Table 4.2). Figure 3.7 compares the results of a model of mass resolution with the estimated resolution for flight oxygen events. The model agrees reasonably well with the data, predicting the observed dependence angle.

Of the remaining contributions to resolution included in the model, two are fundamental limitations of the detectors, and two contributions are due to the limitations of the trajectory measurement and the calibration of the detectors. Fluctuations in ionization energy loss, the Bohr/Landau fluctuations discussed in §3.2.1, are anticorrelated in the ΔE and E' measurements. Differentiating equation 3.32 with respect to ΔE while holding L and E' constant gives

$$\delta M_{BL} = \left.\frac{\partial M}{\partial \Delta E}\right|_{E} \sigma_{BL} = \left[\frac{\lambda}{\lambda - 1}\right] \left[\frac{R}{t \sec\theta} - 1\right] \frac{M}{E'} \sigma_{BL} , \tag{3.34}$$

where R is the total range over which the energy measurement is made. For example, a carbon event with a total energy of 400 MeV/nuc at the top of the stack will have σ_{BL}=5.6MeV. This event will lose about 44 MeV/nuc in the ΔE layer (~7.2secθ g/cm^2), and will have a total range in the stack of ~45 g/cm^2, resulting in δM_{BL} ~0.2 amu.

The additional contributions to mass resolution considered in the model result from uncertainties in the ΔE measurement which are not correlated to the E′ measurement. As noted in §3.6.2 the absolute normalization uncertainty for a given layer is $\sigma_{gain} \approx$ 1.0%, and as shown in §3.2.3 the residual uniformity error for a layer is ~0.8%, giving a combined uncertainty of 1.3%. Differentiating equation 3.32 with respect to ΔE while holding t secθ and E′ constant gives,

$$\delta M_{\Delta E} = \left.\frac{\partial M}{\partial \Delta E}\right|_{E', t\sec\theta} \sigma_{\Delta E} = \left[\frac{\lambda}{\lambda - 1}\right] \frac{M}{E} \left[\frac{R}{t\sec\theta}\right] \sigma_{\Delta E} . \tag{3.35}$$

The resulting mass uncertainty from the 1.3% normalization and uniformity uncertainties is ~0.3 amu. Errors in using the response maps due to trajectory uncertainty at the ΔE layer can be estimated using the rms map gradient for the sum of all six PMTs of ~2.7%/cm. Actually, the response map gradients vary with position from less than 1%/cm near the center of the NaI(Tl) disk up to >4% per cm near the edges of the disk. Combining this average gradient with a position uncertainty of 0.3 cm (Table 2.7) gives a resulting mass uncertainty of ~0.2 amu. Finally, photoelectron statistics give a minor additional contribution to the uncertainty in the ΔE measurement. The NaI(Tl) yields about 70 photoelectrons per MeV of ionization energy loss for the light elements considered here, and the uncertainty in the energy measurement due to counting statistics is $\sigma_{PE}=\sqrt{\Delta E/70}$. For our example carbon event, ΔE=528 MeV, and σ_{PE} = 2.7 MeV, a fractional uncertainty of 0.5%. The roundoff error in the ADC digitization of the signal is even smaller, about 0.26% for a single NaI(Tl) layer for carbon events and is not accounted for in our resolution model shown in Figure 3.7.

Taking an average of the multiple mass measurements, which come from using different layers for the ΔE measurement, improves the resolution of the ΔE–E' technique, but the improvement is less than the $\sqrt{n}$ improvement which would be expected if the errors in the individual measurements were completely uncorrelated. The model curves shown in Figure 3.7 assume that the normalization uncertainties, Bohr/Landau fluctuations, and photoelectron counting uncertainties are uncorrelated, but that the map-position errors and $\sec\theta$ uncertainties are correlated. The resulting model reasonably accounts for the achieved resolution in the 1988 flight data. For some further discussion of propagation of errors for the ΔE–E' method of mass analysis, see Spalding (1983) and Zumberge (1981).

Figure 3.6

The measured mass resolution for the ΔE–E′ method of isotope identification is shown for flight boron, carbon, and oxygen events. The resolution degrades with increasing cosmic ray angle of incidence suggesting that path-length errors due to trajectory uncertainty are a major contributor to the resolution.

Figure 3.6

ΔE−E′ Flight Mass Resolution

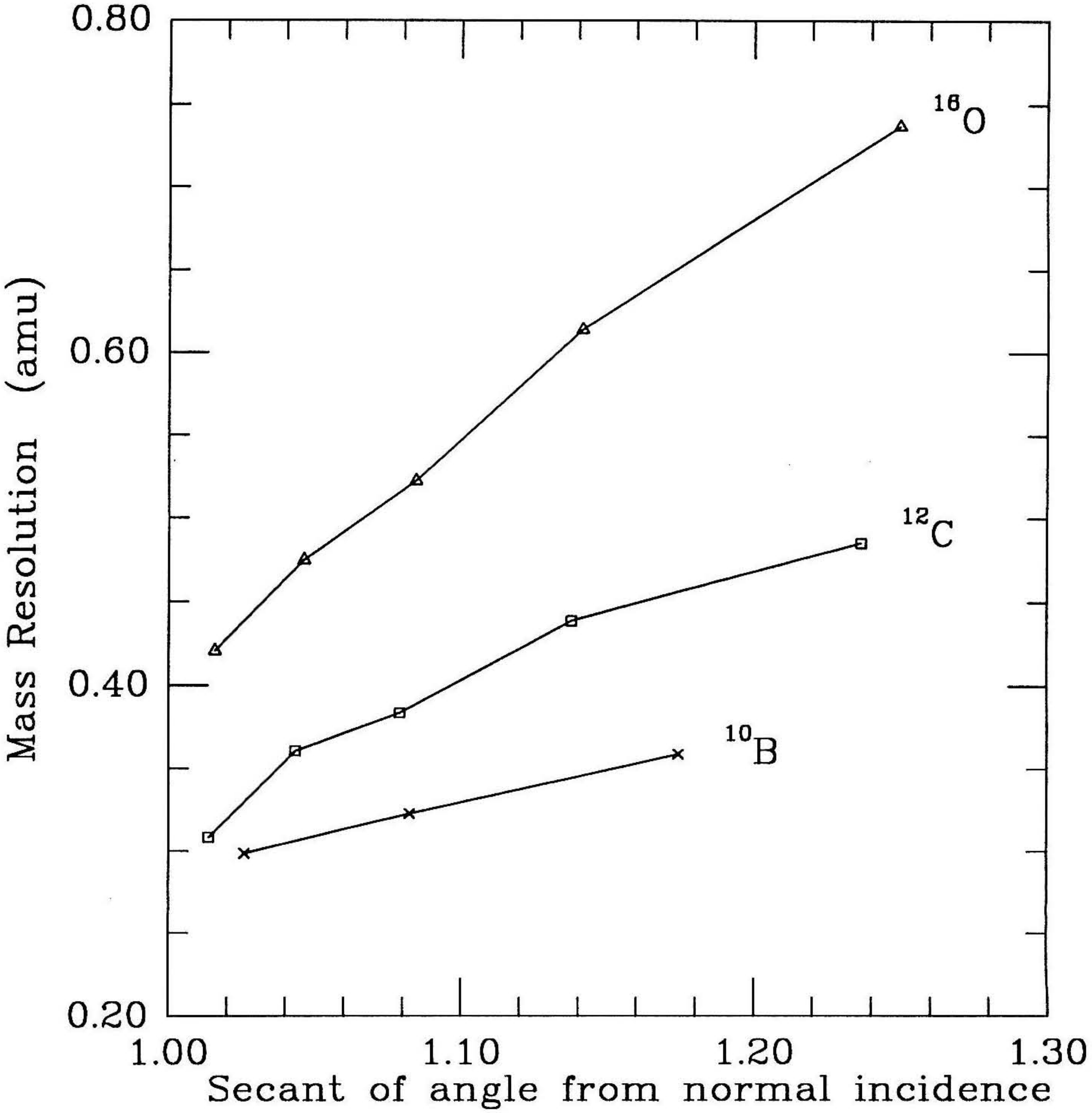

Figure 3.7

The modeled and measured mass resolution for the ΔE–E' method of isotope identification is shown for ^{16}O. Path-length errors due to trajectory uncertainty are the major contributor to the resolution for events with large angles of incidence. Mass uncertainties from errors in layer to layer normalizations are labeled "Norm." Uncertainties from map-position errors have been labeled "traj." Uncertainties from Bohr/Landau fluctuations and photoelectron statistical variations in the ΔE measurements have been labeled "Bohr/Landau" and "pe's," respectively. The discontinuity in the curve representing map-position errors is caused by a change in the number of stack layers from which position measurements are available for the modeled event.

Figure 3.7

ΔE−E′ Mass Resolution Model

Oxygen, 420 Mev/nuc

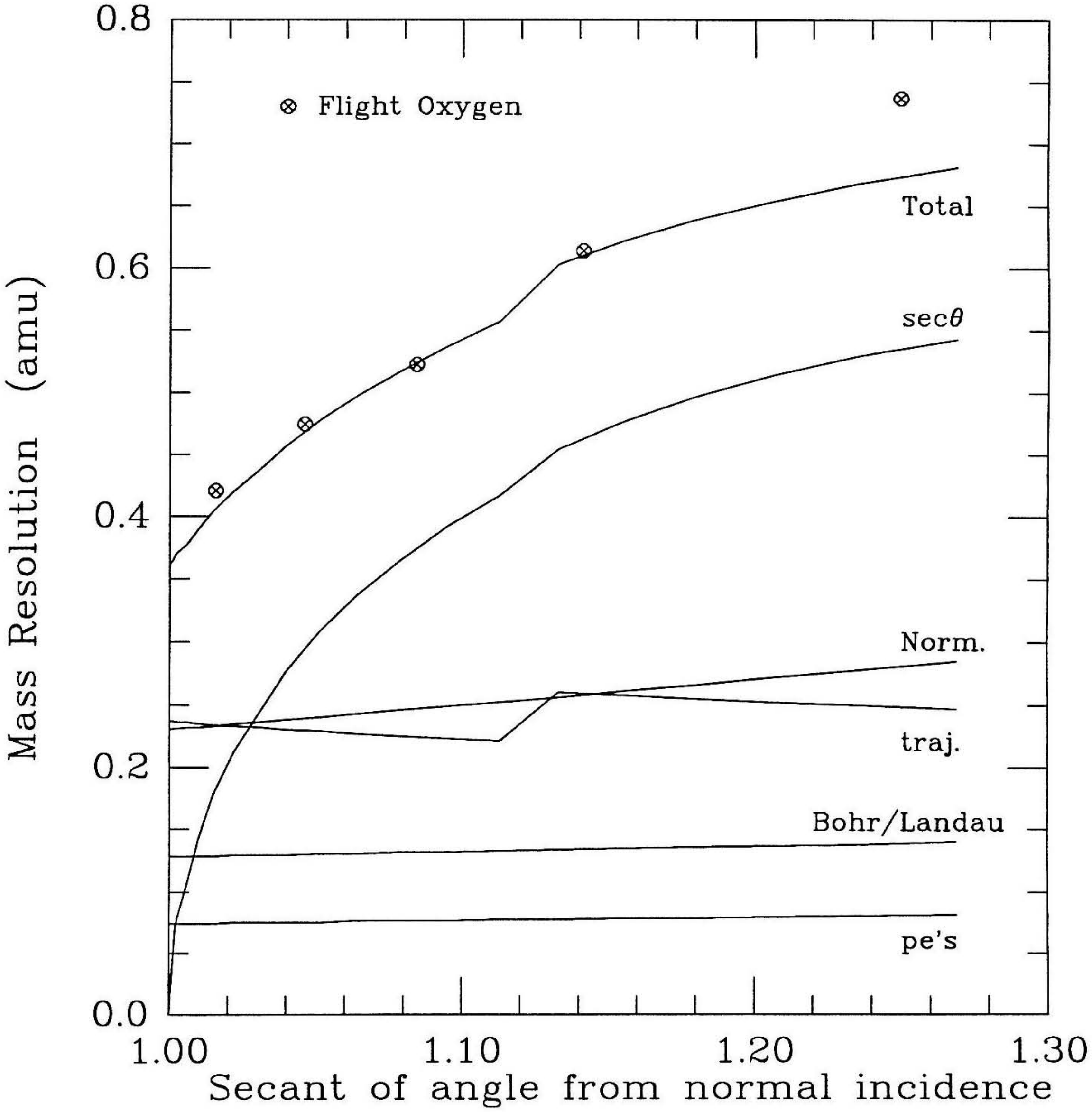

Chapter 4

Selection and Analysis of Flight Data

4.1. Flight Summary

HEIST was launched from Prince Albert, Saskatchewan on August 25th, 1988 at 2017 Mountain Daylight Time (MDT). Events used in the analyzed data set were recorded beginning at about 2340 MDT, when the instrument reached an altitude of 114,000 feet during its ascent. Two discriminator levels were changed at 0330 MDT on August 26th. The L5 level was lowered from 3 to 2, and the S1 level was lowered from 2 to 1. The instrument accumulated data at float altitudes of 5 to 6 g/cm^2 of residual atmosphere for 34 hours and was cut down at 1000 MDT on August 27th. Altitude during the flight, expressed in terms of residual atmosphere above the instrument, is shown in Figure 4.1. The vertical geomagnetic cutoff rigidity was less than 1.14 GV throughout the flight. This rigidity corresponds to an energy of 160 MeV/nuc for nuclei with A/Z=2 and is approximately a factor of two below the lowest energies of the nuclei accepted for mass analysis. The payload was recovered in good condition near Calgary, Alberta. During the 34 hours at float altitude, 619,176 events were recorded by the on-board VCRs.

4.2. Photomultiplier Stability and Drift Corrections

4.2.1. NaI(Tl) Stack

The gain of many of the PMTs viewing the layers of the NaI(Tl) stack drifted significantly during the 1988 flight. Of the 71 measured PMTs, 39 drifted less than 1% during the flight. Thirty-two PMTs had gain drifts between 1% and 5%, and PMT 6 of layer 9, which also had a large drift during the 1984 HEIST flight, drifted

26%.

The PMT drifts were measured by dividing the flight into 12 time periods. In each time period, the relative gain for each photomultiplier was found by requiring the ratio of the mapped response of a single PMT to the sum of all 71 PMT responses be constant when summed over events in the penetrating data set. Recall that the penetrating data are a set of mostly non-interacting events of high enough energy to penetrate the entire stack, and is dominated by carbon, nitrogen, and oxygen nuclei. Typical resolution for an individual PMT is ~2.5%, and given 800 events per time period, the calculated PMT gains have a statistical error of about 0.1% . We correct for the drifts during data analysis by interpolating linearly on event number between the 12 gain measurements for each PMT.

4.2.2. Cerenkov Counters

The gain balancing of the Cerenkov counters followed a method similar to that used for the scintillator stack, but since the outputs of some of the Cerenkov photomultipliers are paired instead of being individually digitized and recorded, balancing these PMTs is more complicated. For a scintillator stack PMT or an unpaired Cerenkov PMT, the mapped response of an individual PMT C_i is given by

$$C_i = \frac{P_i}{g_i\, M_i(\vec{r})}, \tag{4.1}$$

where P_i is the raw ADC output minus its pedestal value, g_i is the gain, and $M_i(\vec{r})$ is the position dependent map value. All of the maps are of individual PMT responses, so the paired PMTs must be corrected with a sum of two maps. If PMTs j and k are PMTs which are paired to produce a response P_i in ADC i, then

$$C_i = \frac{P_i}{(\, g_j M_j(\vec{r}) + g_k M_k(\vec{r})\,)} \;. \tag{4.2}$$

For each penetrating event, we can calculate P_i , $M_j(\vec{r})$, and $M_k(\vec{r})$, and we can estimate C_i from the responses of the unpaired Cerenkov PMTs. To find gains for

Figure 4.1

Altitude during the 1988 flight of HEIST expressed in terms of residual atmosphere above the instrument. Residual atmosphere of 6 g/cm^2 corresponds to an altitude of about 115,000 feet, and residual atmosphere of 5 g/cm^2 corresponds to about 119,000 feet.

Figure 4.1

Atmospheric Depth at Float

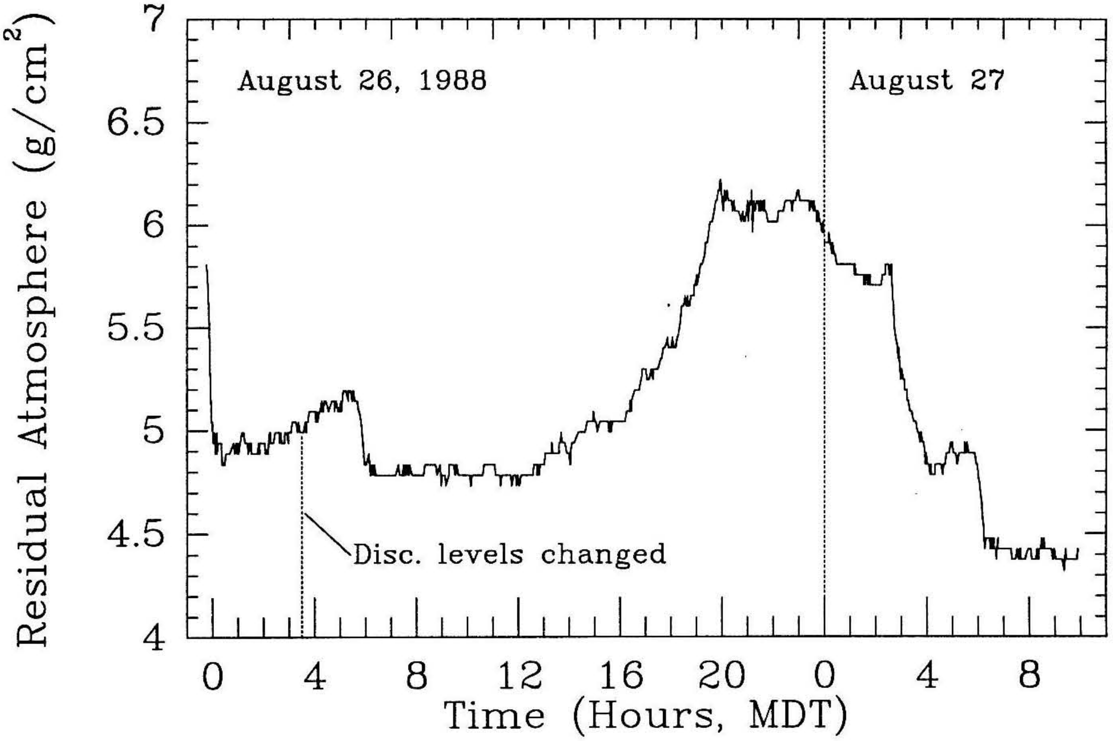

the paired PMTs, we do a least squares fit to

$$(g_jM_j(\vec{r}) + g_kM_k(\vec{r})) = \frac{P_i}{C_i}, \tag{4.3}$$

where g_j and g_k are the fitting parameters. The flight was divided into eight time periods, and gains for the photomultiplier PMTs of each counter were found relative to the average response of the eight unpaired PMTs in each time period. The calculated gain for a typical PMT has a statistical uncertainty of ~0.5% in each time period, and no statistically significant drifts in gain were observed in either Cerenkov counter.

4.3. Preliminary Analysis of Stopping Events

The mass can be determined for those nuclei which pass through the Cerenkov counters and then slow down and stop in the NaI(Tl) stack. This section describes the first stages of the event selection process used to choose a data set of stopping, mostly non-interacting events.

4.3.1. Translate Tapes

The HEIST instrument has two on-board VCRs which can be powered on individually. During the Prince Albert flight, both VCRs were powered on throughout the entire duration of data collection; thus, there are two complete, redundant VCR tapes of the flight data. The VCR tapes must be translated to 9-track magnetic tape. Two cuts on data quality are applied to the translated events. The video playback circuit requires that an event must begin with the proper 16-bit sync word in order for it to be translated to magnetic tape. Also, each event has a checksum which is tested to eliminate those events with noise or recording problems. During pre-flight testing of the VCRs and the tape translation process, subsequent translations of the same VCR tape rejected slightly different sets of events; thus, some noise is introduced in the translation process itself.

The initial translation of flight tape H88F02, recorded on flight VCR 2, resulted in a loss of about 7% of the flight events due to sync word and checksum errors. The same VCR tape was translated a second time, and the two translations were integrated into a final data set which contains approximately 99% of the 619,176 events recorded by the VCRs. The redundant VCR 1 tape was not translated.

4.3.2. Select Events Not Flagged

As a warning that the HEIST ADCs may not have settled to their baselines, the Hazard flag is set whenever an event is preceded within 256 μs by a T1T2 coincidence. These "Hazard events" were segregated and processed separately from the non-Hazard events. The resulting energy and mass resolution for both data sets was compared during the later stages of data analysis, and the Hazard events appear to be equal in quality to the non-Hazard data. Most T1T2 coincidences are due to He nuclei, which produce small pulse heights having short recovery times, so it is not surprising that the Hazard events have no detectable degradation in quality. In the final stages of mass analysis, both data sets were combined in order to improve statistics.

The T1T2 coincidence rate was typically in the range of 950 to 1000 s^{-1} during the flight which implies that $\sim$22% of the events should have the Hazard flag set. In addition, the 33 second External Trigger events should comprise 0.5% of the flight events. The External Trigger flag labels events which are internally generated by the HEIST trigger logic and are not cosmic ray events. In actual data selection, there were 472,397 unflagged (normal) events, 137,995 (22.5%) Hazard events, and 3207 (0.5%) External Trigger events.

4.3.3. Select Events Which Miss Bottom Scintillator

In order to select events which have stopped in the NaI(Tl) stack, only events which show no response in the bottom plastic scintillator are chosen. This set will include events which have escaped through the sides of the stack, have stopped within the stack, or have interacted within the stack in such a way that the fragments produced no appreciable signal in the bottom scintillator. In order to characterize a "zero" response in the bottom scintillator, a histogram of the bottom scintillator pedestal distribution was made using the flight External Trigger events. The peak of the distribution is in ADC channel 26. The full width at half maximum (FWHM) is less than one channel, but there are non-Gaussian tails on both sides of the peak. Scaling from carbon and oxygen in the penetrating data set, we estimate that minimum ionizing H gives a response in the sum of six bottom scintillator photomultipliers of 4 to 6 bins. In choosing a data set with a small response in the bottom scintillator, we have conservatively kept all events with a response of 40 channels or less. This cut is 14 bins above the pedestal, between relativistic H and He. Making this loose cut on the bottom scintillator response eliminates 73% of the remaining events, leaving 127,833 normal and 37,606 Hazard events. This selection will not eliminate all fragmentations that result in a particle with Z=1 penetrating the bottom scintillator, nor does it eliminate fragmentation interactions for which the fragments escape out the sides of the NaI(Tl) stack.

4.3.4. Calculate Trajectories and Detector Responses

Once the initial event selections have been made, positions and trajectories are calculated for each event. To find a trajectory for a stopping event, we must take care to only use valid positions which are found in the stack layers up to, and possibly including, the stopping layer. In order to use only layers through which the event has passed, positions are found only for those layers which have an unmapped response greater than 10% of the response in the first layer of the stack. Event positions are needed in order to find the map-corrected response in each layer, but the approximate "unmapped" response in each layer can be found by simply summing the PMT outputs for each layer. The position algorithm flags the positions in the stack below the assumed stopping layer. The trajectory algorithm subsequently ignores flagged layer positions in calculating the best fit trajectory.

After positions and trajectories for each event have been found, map-corrected responses in the stack layers, the Cerenkov counters, and the top scintillator are found using the algorithms described in §3.1 and §3.2.

4.3.5. Identify Events Which Interact or Escape

The stopping data set selected so far contains a large number of events which either escape out the sides of the NaI(Tl) stack before stopping, or which undergo nuclear interactions resulting in fragmentation of the incident cosmic ray nucleus. The event signature provided by the individual layer responses allows detection of most of the events which escape or undergo a charge changing interaction within the NaI(Tl) stack. An algorithm designed to recognize these signatures has been developed in order to generate an event flag which describes each event as an "Escape," an "Interacting event," or a "Clean" stopping event.

The method used to identify escaping and interacting events can be thought of as a two step process. The first step either identifies the event as an Escape or locates the "stopping layer," the stack layer in which the nucleus stops. An event trajectory is followed down from the first layer of the stack to the layer in which the response decreases or until the trajectory exits the side of the stack. If the nucleus appears to exit the side of the stack before its response decreases, then the event is labeled as an Escape. If its response decreases as the trajectory nears the edge of the stack, it is labeled as a "Possible Escape." The Possible Escape events were also eliminated from mass analysis. For those events which do not appear to exit the sides of the stack, the stopping layer is identified as the first layer in which the scintillation response has a definite decrease. If the layer in which the scintillation signal decreases has a zero response, then the previous layer is taken to be the stopping layer.

Now, the algorithm checks for any indication that the event underwent fragmentation. If any layer below the stopping layer has a raw response of more than MAXBINS above its pedestal value, then this response indicates that there was a particle passing though the layer, and the event is labeled as an interaction. MAXBINS is approximately the response generated by a minimum ionizing alpha particle. If any layer below the stopping layer has a response more than SMALLPED above its pedestal value, then the event is labeled as a possible fragmentation. SMALLPED is roughly the scintillation response from a minimum ionizing proton. If all layers below stopping have near zero response, the event is labeled as a Clean stopping event. Figure 4.2 shows examples of Interacting and Clean stopping events. Only those events which were labeled as Clean stopping events were used in this mass analysis.

As shown in Table 4.1, of the 165,439 events selected as having a low response in the bottom scintillator, 9.7% were identified as stopping before stack layer 3 (L3), 25% were identified as escapes, and 40.6% were identified as Interacting in the stack. This leaves 25,416 Clean stopping events as candidates for mass analysis. Of these events identified at this stage of analysis as stopping without interacting, there still remain some events which are actually escapes or interactions. Most of these escapes and interactions are removed by the additional data selections described in the following sections. Also, a small fraction, estimated to be ~1%, of Clean stopping events may have been misidentified as Possible Escapes or Interactions by the event flag algorithm.

4.3.6. Eliminate Center Plug Events

As noted in §2.1.1, the top wall of the aluminum hermetic can which encloses the NaI(Tl) stack has been reinforced over an area which is 3.8 cm in radius and is at the center of the wall. Events going through this "center plug" pass through more material than events which pass through the unreinforced areas of the hermetic can lid, and we wish to eliminate them from isotope analysis. Due to the limited position resolution of the event trajectories, we cannot be sure if events with trajectories near the edge of the center plug have passed through it or not. In order to eliminate all events which may have lost energy in the center plug material, we have discarded events with trajectory positions within 4.8 cm of the center of the hermetic can lid. This cut eliminates ~5% of the stopping events.

4.4. Selection and Analysis of Individual Elements

4.4.1. Charge Selection

Prior to identifying the masses of the stopping event, charge identification must be accomplished. Nuclei may undergo charge changing interactions as they travel through the instrument; so, we would like to identify the nucleus' charge at the "top" of the instrument and measure it again near the end of the nucleus' range in order to eliminate those which do interact.

There are two basic methods which HEIST uses to identity the charge of a cosmic ray nucleus. One method is to use Cerenkov response and dE/dx to measure charge. This method, which can only be used for nuclei which have velocities above the Cerenkov threshold velocity of the Pilot counter, yields excellent charge resolution when stack layer 1 (L1) is used for the dE/dx measurement. In order to measure the charge near the "top" of the instrument, we also use the Cerenkov-dE/dx method with the plastic top scintillator as the dE/dx detector.

Figure 4.3 is a crossplot of the stack layer 1 response as a function of Pilot Cerenkov response. The scale used for Figure 4.3 represents the arbitrarily chosen units of light output which have been used throughout the analysis of the 1988 flight data. For convenience, the units of the Pilot response will be called Pilot light units (plu), and the units of the scintillation response will be called scintillation light units (slu). The stripes corresponding to individual element tracks are clearly seen. Background events between the element tracks are mostly events in which the nucleus has undergone a charge changing fragmentation before penetrating stack layer 1. Nuclei with velocities below the Cerenkov threshold velocity produce the nearly vertical tracks at the left end of the figure.

Figure 4.4 is a similar crossplot showing the top scintillator response versus Pilot Cerenkov response. Model curves of the charge tracks of Figure 4.4 are shown in Figure 4.5. The energy resolution of the plastic top *scintillator* is not as

Figure 4.2

Example of interacting and non-interacting events. The scintillation responses in stack layers 1 through 12 are shown for six stopping carbon events. Events (a), (b), and (c) were identified as Clean stopping nuclei, while events (d), (e), and (f) were identified as having undergone fragmentation in the stack. The maximum allowed signal from the layers below the end of range of a Clean stopping nucleus corresponds to ~10% of a small tick interval on this figure's vertical scale.

Figure 4.2

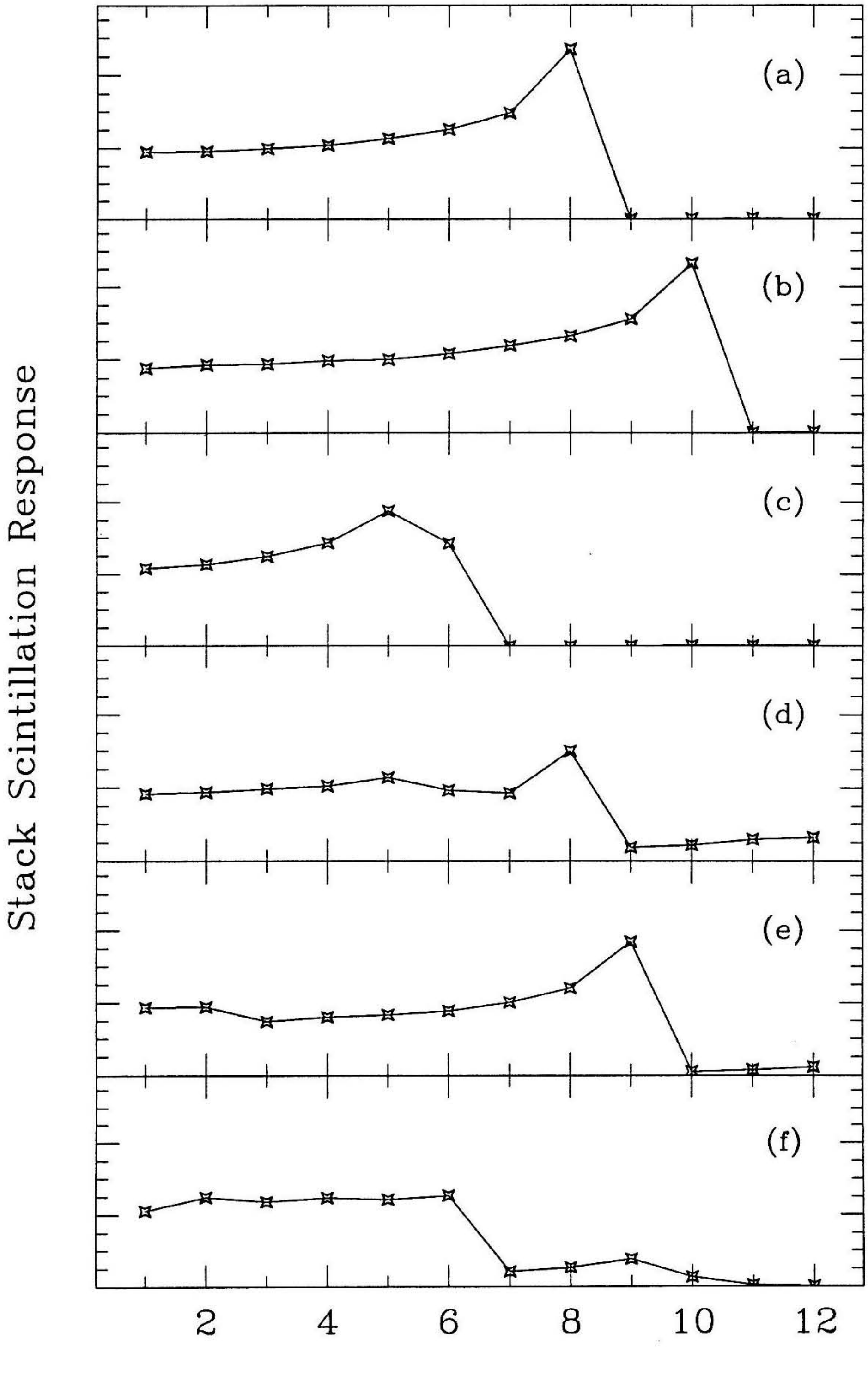
(a)
(b)
(c)
(d)
(e)
(f)
Stack Scintillation Response
2
4
6
8
10
12
Stack Layer

good as that of stack layer 1, so the charge resolution shown in Figure 4.4 is worse than that seen in Figure 4.3. The events in Figure 4.4 have velocities above the Pilot Cerenkov threshold. The background events to the left of the main element tracks are nuclei which have undergone a charge changing interaction in the material between the top scintillator and the Pilot radiator, and so the response in the top scintillator is high compared to the response in the Pilot Cerenkov counter.

Event charge can also be measured by using the energy loss information in the NaI(Tl) stack alone. This ΔE–E' technique follows the same method as was discussed in §2.2.2; except, now the approximation $A/Z=2$ is substituted into equation 2.11, and it is solved for Z. A charge histogram of the resulting ΔE–E' measurements for the Clean stopping events is shown in Figure 4.6. The charge resolution, estimated from the full width at half maximum of the carbon and oxygen peaks, is ~0.1 charge unit. Notice that the ^{6}Li and ^{7}Li isotopes are partially resolved, and that ^{7}Be and ^{9}Be are clearly separated, with the mass scale being 1 amu ≈ 1/8th of a charge unit.

Initial element selections are made using the Cerenkov-L1 charge, Z_{L1}. In order to select boron, carbon, nitrogen, and oxygen events, we have fit empirical model curves to each of the charge tracks shown in Figure 4.3. The resulting model curves are used to straighten the charge tracks for each element so that charge histograms with good resolution can be constructed. The charge resolution is 0.07 charge units at boron and 0.09 charge units at oxygen. Charge cuts have been made at the $\pm 3\sigma$ points on the charge histograms and are shown as solid lines on Figure 4.3.

In order to eliminate fragmentations occurring below layer 1, as well as most of the remaining mis-identified escaping events, we require that the ΔE–E' method gives a charge measurement consistent with the Cerenkov-layer 1 measurement. The ΔE–E' method has charge resolution almost as good as Cerenkov-L1 charge; however, $Z_{\Delta E-E}$ is correlated with mass, as discussed above. Because of this mass dependence, the cuts on $Z_{\Delta E-E}$ have been made sufficiently loose that no mass bias is introduced into the data selections. Figure 4.8 shows the cuts used on $Z_{\Delta E-E}$.

Table 4.1 Accounting of Event Classifications

Number of Events	Classification	Events Remaining
613599	Total events recorded	
3207	External Trigger events	610392
444953	High response in bottom scint.	165439
98348	Flagged as Interaction	67091
25641	Flagged as Escape	41450
16034	Stopping before Layer 3	25416
1237	$Z_{\Delta E-E'} \approx 3$ (Li)	
1275	$Z_{\Delta E-E'} \approx 4$ (Be)	
3064	$Z_{\Delta E-E'} \approx 5$ (B)	
7657	$Z_{\Delta E-E'} \approx 6$ (C)	
2406	$Z_{\Delta E-E'} \approx 7$ (N)	
5815	$Z_{\Delta E-E'} \approx 8$ (O)	
3762	$Z_{\Delta E-E'} > 8$	

The Cerenkov-top scintillator charge, Z_{S1}, is used primarily to eliminate events which have undergone charge changing interactions in the material above L1. Z_{S1} was calculated using the method of straightening the charge tracks as was done for the Pilot-layer 1 charge. The model curves used to straighten the charge tracks are shown in Figure 4.5, and the resulting charge histograms of events passing the previous Cerenkov-L1 charge cuts are shown in Figure 4.7. The selection cuts are tight on the high side of the charge peaks in order to eliminate events which interact between the top scintillator and layer 1. The cuts on the low side of the charge peaks are intentionally loose since the low values of Z_{S1} are thought to result mainly from errors in the top scintillator response maps.

Table 4.1 summarizes the classifications of events recorded during the 1988 flight. Out of the 613,599 events recorded, only 25,416 events are classified as Clean events which penetrate further than the first two layers of the NaI(Tl) stack. Many of these 25,416 events have velocities below the Pilot Cerenkov threshold velocity and can not be analyzed using the Cerenkov-Energy method. Table 4.2 continues this accounting for the events identified as B, C, N, and O in the stack.

Table 4.2 Classification of B, C, N, O Events

Element	Selected by $Z_{\Delta E-E'}$	Eliminated				Number of Events Remaining
		Below Cerenkov Threshold	Above Max. Velocity Cut	Center Plug	$Z_{\Delta E-E'}$, Z_{L1}, Z_{S1} Disagree	
B	3064	1288	0	120	587	1069
C	7657	2454	843	268	511	3581
N	2406	535	412	75	321	1066
O	5815	660	723	213	450	3769

4.4.2. Calculate Total Energy

Once the charge of an event has been identified, its map-corrected response has been found for each layer, and its stopping layer has been identified, we can calculate the total energy of the event. The total energy is calculated as described in §3.4. Saturation of the scintillation light and energy loss in the "dead" material between the bottom of the Cerenkov radiator and the top of the first stack layer are modeled separately for each element. Two values of "total" energy are computed. One gives the calculated total energy of the event as it exits the Pilot Cerenkov radiator, and the other value gives the total energy of the event as it exits the Teflon radiator.

4.4.3. Calculate Lorentz Factor, γ

As described in §3.5, the Lorentz factor, γ, for each event is found by modeling the ratio of the Cerenkov response to the layer 1 response, $\Omega(Z,\gamma) \equiv C_{tot}(Z,\gamma)/L_1(Z,\gamma)$. The result of this response model is inverted in order to find γ as a function of charge and detector response, $\gamma(Z,\Omega)$. Since the nuclear charge of each event has been determined, a value of γ_{pil} and γ_{tef} can be found from the models of the Pilot and Teflon responses, respectively. The normalizations of the modeled $\Omega(Z,\gamma)$ to the flight signal level were determined separately for each element by minimizing the systematic variation of calculated mass as a function of γ.

4.4.4. Calculate Mass Estimators

There are three possible ways in which HEIST can be used to measure the mass of a stopping cosmic ray event. A mass measurement using the ΔE–E' method is possible for all events which penetrate at least two layers of the stack of NaI(Tl) scintillators, and mass by Cerenkov-Energy may be found for events which are above Cerenkov threshold in the Pilot counter. A second Cerenkov-Energy measurement can be made for higher energy events which are above Cerenkov threshold in the Teflon as well as the Pilot counter. For the charge range including boron through oxygen, all events which are above Pilot Cerenkov threshold penetrate to at least layer 3 of the scintillator stack; thus, at least two mass estimators are available for all the events analyzed in this work. The higher energy events, those with velocities above the Teflon Cerenkov threshold, have three available mass estimators.

Once the Lorentz factors and the total event energies have been found, the Cerenkov-Energy mass is given by

$$M = \alpha \frac{E_{tot}}{(\gamma - 1)} , \tag{4.4}$$

Figure 4.3

Layer 1 versus Pilot Cerenkov response for those events labeled as Clean stopping by the "event flag" algorithm of §4.3.5. The units shown are the arbitrarily chosen Pilot light units (plu) and scintillation light units (slu) which were used throughout the analysis of the 1988 flight data. Individual charges are clearly resolved for the events above Cerenkov threshold. The solid lines represent charge cuts applied to select individual elements at the $\pm 3\sigma$ limits of the resulting charge peaks. Charge resolution is estimated to be 0.07 charge units for boron and 0.09 charge units for oxygen.

Figure 4.3

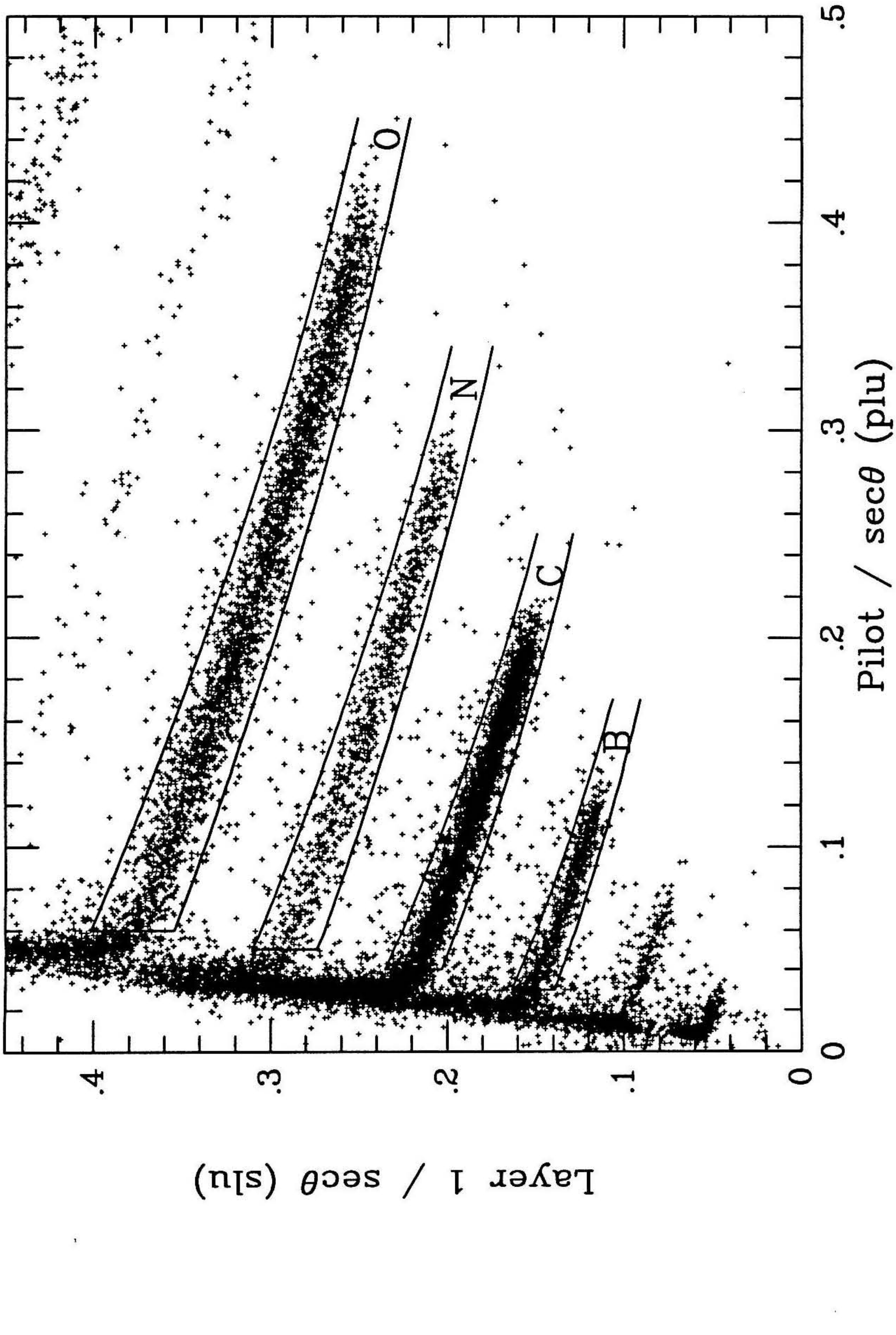

Figure 4.4

Top scintillator (S1) versus Pilot Cerenkov response for events above Pilot Cerenkov threshold. The energy resolution of S1 is not as good as in L1, resulting in poorer charge resolution (~0.23 charge units) than that shown in Figure 4.3. Cuts on the resulting charge histograms are shown in Figure 4.7. The background events to the left of the main element tracks are nuclei which have undergone a charge changing interaction in the material between the top scintillator and the Pilot Cerenkov radiator.

Figure 4.4

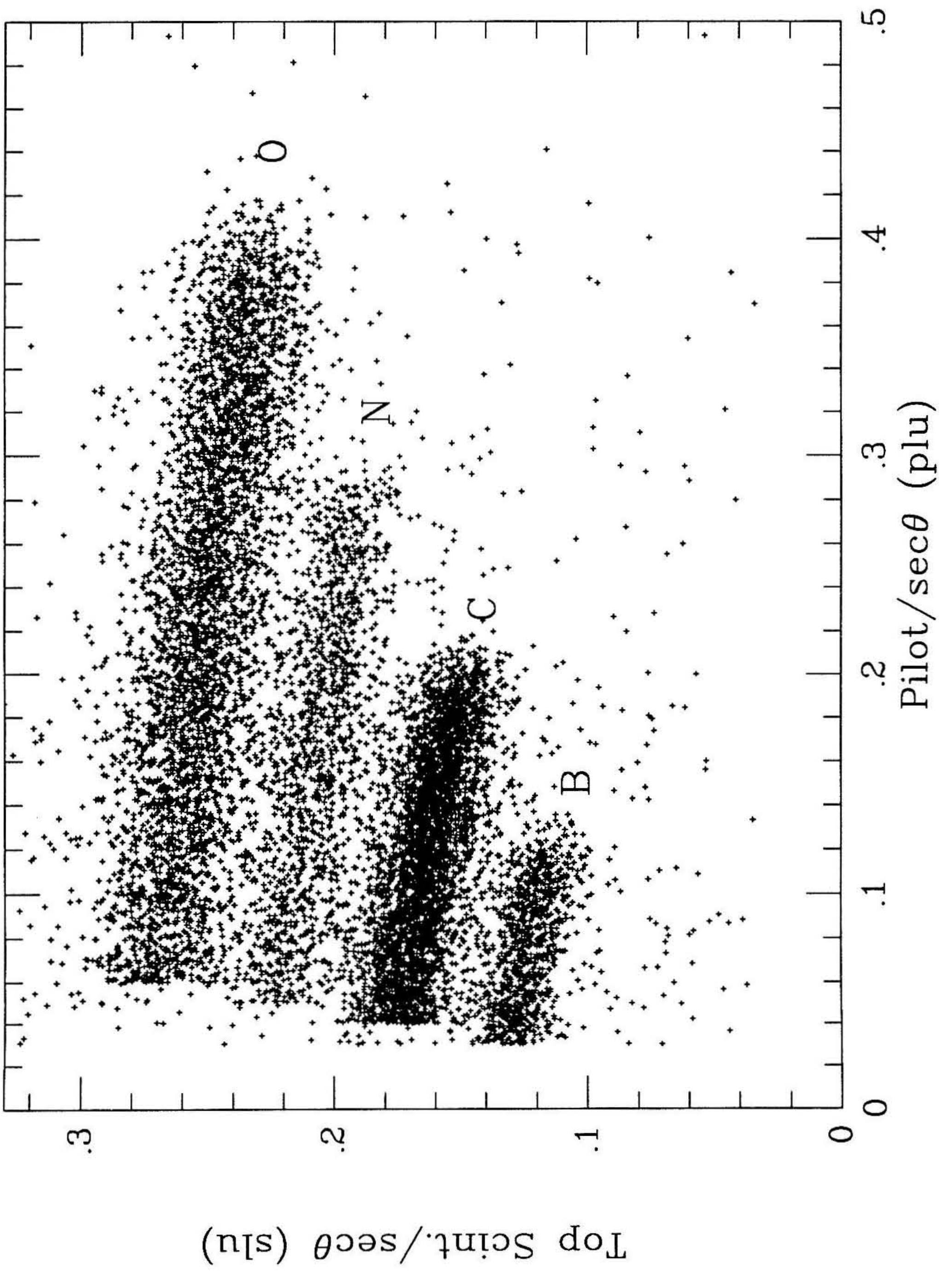

Figure 4.5

Model response curves which were used to assign charge Z_{S1} to the events in Figure 4.4. The resulting charge histograms and charge cuts are shown in Figure 4.7.

Figure 4.5

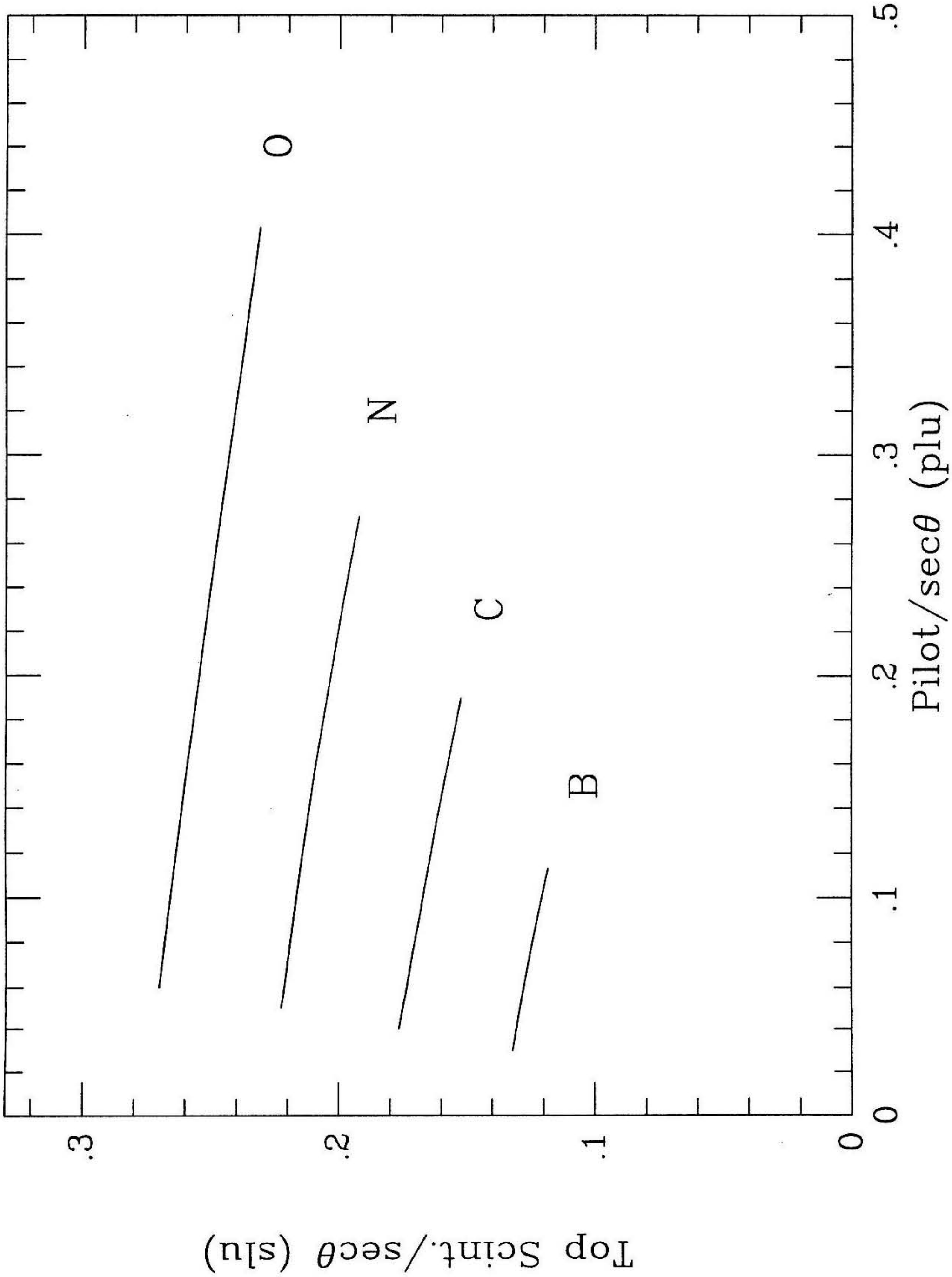

Figure 4.6

Charge histogram of $Z_{\Delta E-E}$ calculated using energy deposition in the NaI(Tl) stack. The charge scale is nonlinear due to approximations made in the range-energy relation and the saturation correction and has been only roughly normalized. Charge resolution is ~0.1 charge unit. Notice the ^{6}Li and ^{7}Li, and the more clearly separated ^{7}Be and ^{9}Be isotopes. The mass scale is 1 amu ≈ 1/8th charge unit.

Figure 4.6

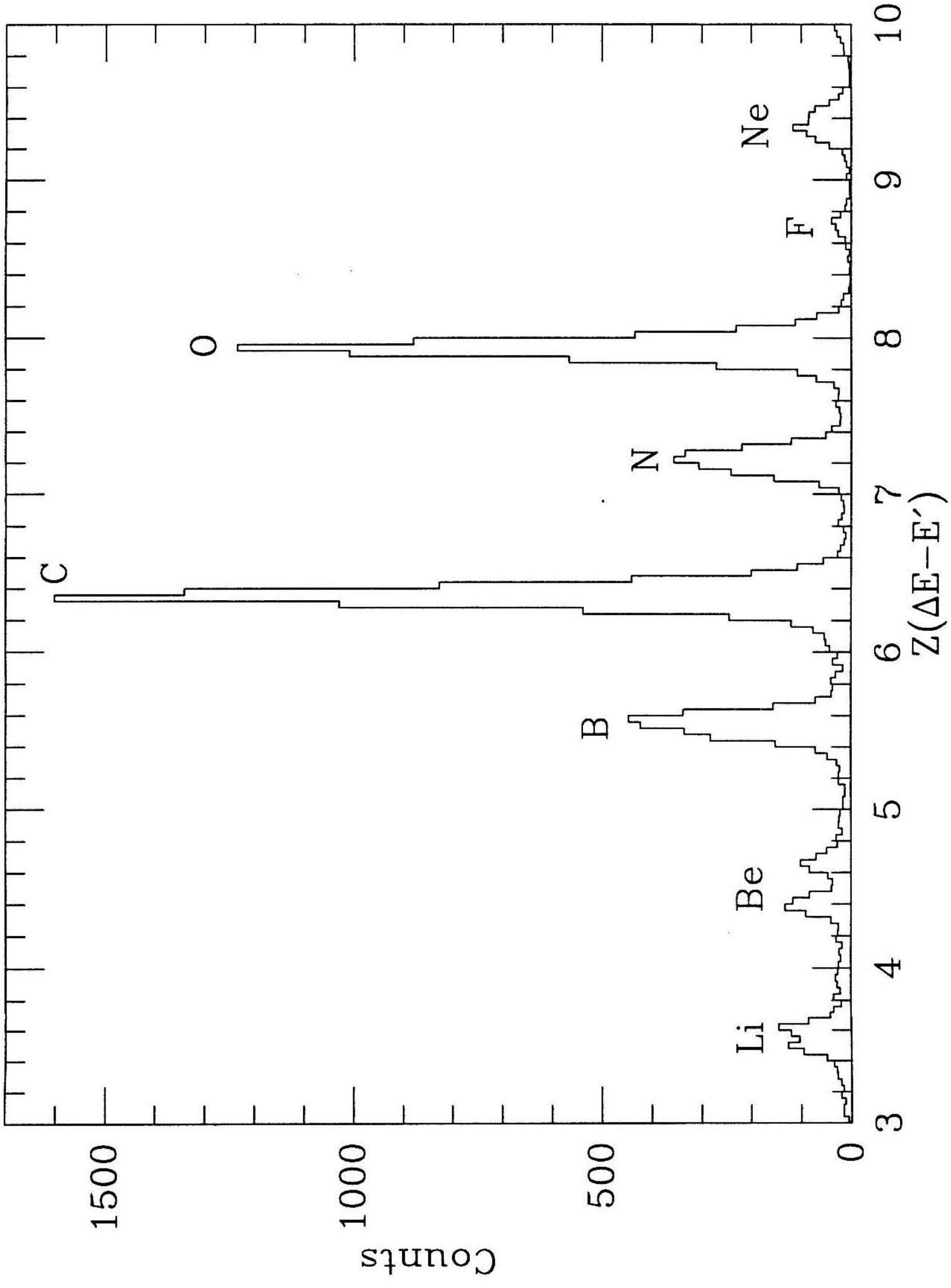

Figure 4.7

Charge cuts based on Z_{S1}, charge by Pilot Cerenkov-S1 response. The histograms are of events passing the Pilot Cerenkov-L1 charge selection cuts.

Figure 4.7

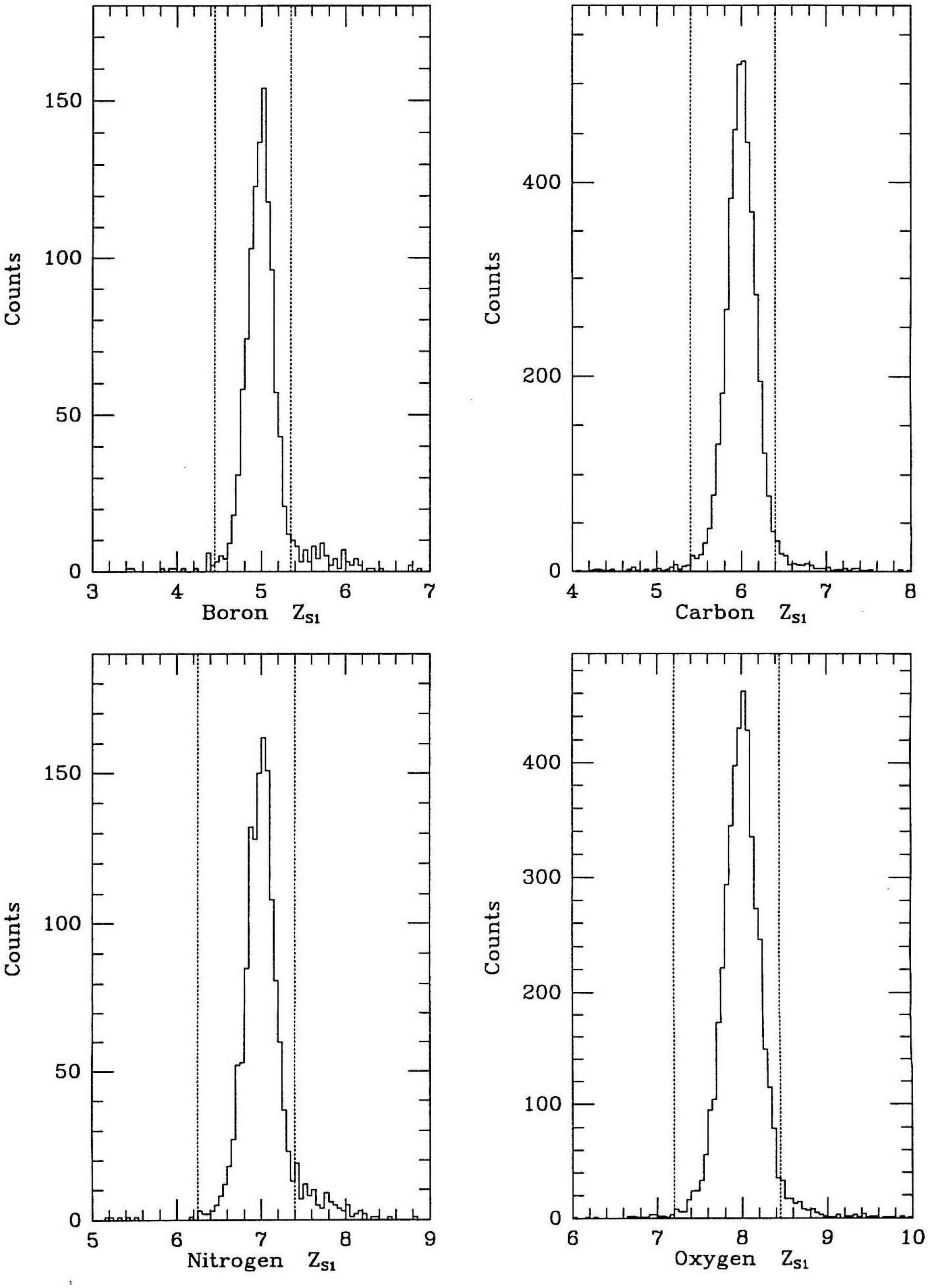
Counts
150
100
50
0
3
4
5
6
7
Boron Z_{S1}
Counts
400
200
0
4
5
6
7
8
Carbon Z_{S1}
Counts
150
100
50
0
5
6
7
8
9
Nitrogen Z_{S1}
Counts
400
300
200
100
0
6
7
8
9
10
Oxygen Z_{S1}

Figure 4.8

Charge cuts based on $Z_{\Delta E-E}$ calculated using energy deposition measurements in the NaI(Tl) stack. The nonlinear charge scale is the same as shown in Figure 4.6. The histograms are of events passing the Z_{L1} (Pilot Cerenkov-L1) and Z_{S1} (Pilot Cerenkov-S1) charge selections.

Figure 4.8

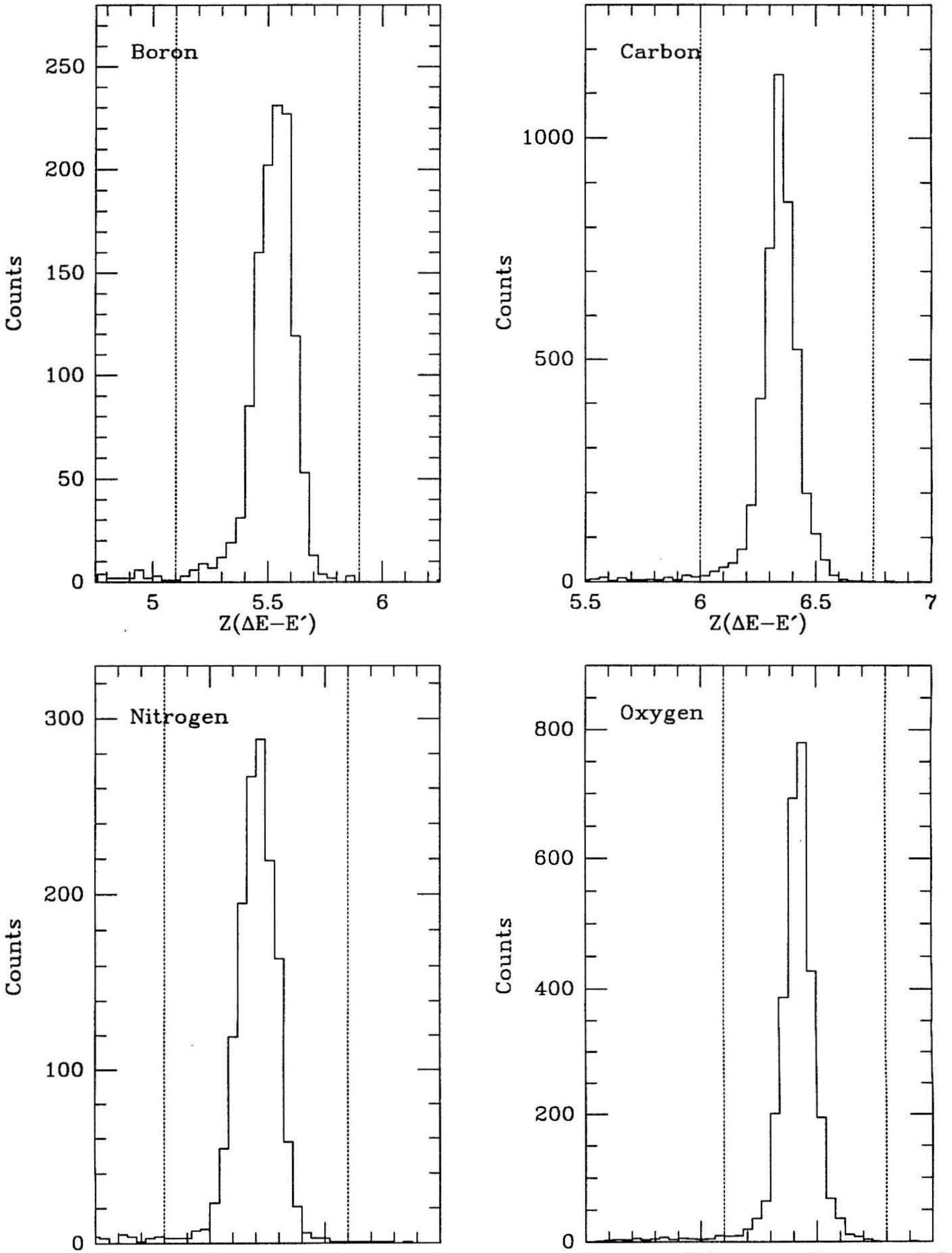
Boron
Counts
0
50
100
150
200
250
5
5.5
6
Z(ΔE−E′)
Carbon
Counts
0
500
1000
5.5
6
6.5
7
Z(ΔE−E′)
Nitrogen
Counts
0
100
200
300
6.5
7
7.5
8
Z(ΔE−E′)
Oxygen
Counts
0
200
400
600
800
7
7.5
8
8.5
Z(ΔE−E′)

where α is a normalization factor. The Cerenkov and stack response normalizations adopted do not preserve the correct mass scale and a further correction is needed. In order to correct the mass scale, it was normalized using an "offset and gain", α_f and α_g.

$$M = \alpha_f + \alpha_g \frac{E_{tot}}{(\gamma-1)} \quad . \tag{4.5}$$

The values for α_f and α_g were determined separately for each element using events with velocities near the Cerenkov threshold velocities. By using this high resolution data set, individual isotope peaks were identified and the absolute mass scale was unambiguously determined.

Table 4.3 lists the resulting normalization factors for each element.

Table 4.3 Mass scale normalization factors

Nuclei	Pilot-Energy		Teflon-Energy		ΔE–E′	
	α_g	α_f	α_g	α_f	α_g	α_f
Boron	1.149	1.37	1.087	0.326	1.20	2.17
Carbon	1.163	1.80	1.242	2.46	1.136	1.77
Nitrogen	1.100	1.19	1.150	1.60	1.25	3.15
Oxygen	1.150	2.19	1.150	2.11	1.205	3.28

Mass estimated by the ΔE–E′ method is found from

$$M_{Li} = \left[\frac{Z^2 \, t \sec\theta}{k(E^{\lambda} - E'^{\lambda})} \right]^{\frac{1}{1-\lambda}} \quad . \tag{4.6}$$

In order to find E and E′ from the scintillator stack light, L, we have followed the method used by Zumberge (1981) for mass measurements with Cesium Iodide scintillators. Zumberge corrects for the changing scintillation efficiency by assuming that

$$E = \alpha_0 L + \alpha_1 L^2 \ . \tag{4.7}$$

Best values for α_0, α_1, and λ were found for each element analyzed by selecting events of the dominant isotope using mass by Pilot Cerenkov-Energy, M_{Pil}, and then minimizing $\sum(M_{Pil}-M_{\Delta E-E})^2$. The resulting best fit values are given in Table 4.4.

Table 4.4 Values used in ΔE–E′ Mass Calculation

Element	α_0	α_1	λ
Boron	0.99	-0.0316	1.561
Carbon	0.99	-0.0321	1.528
Nitrogen	1.00	-0.0280	1.511
Oxygen	1.00	-0.0271	1.499

In cases where the cosmic ray nucleus has penetrated three or more layers, multiple mass measurements, M_{Li}, are calculated. In all cases, we have used a single NaI(Tl) layer for the ΔE measurement, and all layers below the ΔE layer are summed to find the value of E′. The final mass estimator, $M_{\Delta E-E}$, is found by taking the average of all of the possible measurements, M_{Li}. Again, we found that the mass scale of this estimator was compressed, and we corrected it by finding an effective offset as was done for the Cerenkov-Energy mass scales. The values of the mass scale normalization corrections are given in Table 4.3. In addition, the mass estimated using this method was found to have a small dependence on the angle of incidence of the event, so this dependence was measured and the resulting correction factor was applied to the data. This correction is linear in secθ of the event trajectory and increases the mass of the widest angle events by ~4%.

4.5. Final Event Selections

The final event selections are designed to choose events which have velocities above the Pilot Cerenkov threshold and to eliminate events which show inconsistencies in Pilot or Teflon internal PMT agreement or which have inconsistencies in their multiple masses measurements. Figure 4.11 shows the mass distributions for the events selected by the previously discussed charge cuts and the energy cuts described in §4.5.1. Figure 4.11(a) shows events with velocities above the Pilot Cerenkov threshold but below threshold in the Teflon Cerenkov counter, and Figure 4.11(b) shows events with velocities above Cerenkov threshold in both counters. There remain a number of events of questionable quality which are eliminated by the agreement cuts described in §4.5.2, §4.5.3, §4.5.4, and §4.5.5, and Figure 4.12 shows the resulting mass distribution after application of these final selection criteria.

4.5.1. Energy Cuts

In order to choose only events which are above Pilot Cerenkov threshold, a minimum response above the threshold level is required for the Pilot Cerenkov response. The minimum response used is shown in Figure 4.3 and listed in Table 4.5. The Pilot counter is also used to choose the velocity range used for the Teflon-Energy mass analysis. Again a cut on minimum Pilot signal is used to select events with velocities above Teflon Cerenkov threshold. Also, because the uncertainty in the calculated Cerenkov-Energy mass gets worse as the velocity of the cosmic ray nuclei increases, a maximum velocity cut has been used on the carbon, nitrogen, and oxygen events in order to improve the overall resolution of the final data sets. The Pilot response values at which these cuts have been chosen and their corresponding energies are given in Table 4.5.

Table 4.5 Velocity Cuts at Pilot Counter

Nuclei	Allowed Pilot Response (plu) Below Teflon Threshold	 Above Teflon Threshold
Boron	0.03 - 0.09	0.09 - no upper limit
Carbon	0.04 - 0.115	0.115 - 0.175
Nitrogen	0.05 - 0.14	0.14 - 0.24
Oxygen	0.06 - 0.19	0.19 - 0.35
	Corresponding Energy at Bottom of Pilot (MeV/nuc)	
Boron	310 - 442	442 -
Carbon	308 - 413	413 - 575
Nitrogen	302 - 390	390 - 565
Oxygen	300 - 398	398 - 650

4.5.2. Mass Agreement Cut Using ΔE–E′

In order to eliminate events which undergo fragmentation very near the end of the range in the stack and to identify any remaining events which may have escaped the stack without stopping, we have required consistency between the ΔE–E′ mass measured using the last two or three layers penetrated by the nucleus and the average ΔE–E′ mass measured using all layers of the stack down to the stopping layer. The difference, dM(ΔE–E′), was calculated as

$$dM = \frac{M_{ave} - M_{last}}{(1/2)(M_{ave} + M_{last})}. \tag{4.8}$$

For the B, C, N, and O nuclei, approximately 10% of the mass changing fragmentations will be neutron stripping interactions. A neutron stripping interaction in the stack would lead to a positive value of dM. The resulting dM distributions for B, C, N, and O, along with the adopted cuts are shown in Figure 4.9. In order to minimize the rejection of non-fragmenting events, these cuts on dM were chosen to be rather loose, and they will not reject all neutron stripping events. The cuts eliminated about 4% of the remaining events.

4.5.3. Cerenkov Internal Agreement

Loose cuts were made on QC_{pil} and QC_{tef}, the rms measures of agreement among the 12 measured signals within each Cerenkov counter defined by equation 3.14. These cuts, shown in Figure 4.10, serve to eliminate those events which have large internal inconsistencies among the PMT signals from each Cerenkov counter. These inconsistencies can be caused, for example, by incorrect trajectories, knock-on electrons hitting a PMT face, or fragmentation above the counter. The cut on Pilot internal agreement, QC_{pil} eliminated 1 - 2% of the remaining events, and the cut on Teflon internal agreement eliminated about 2 - 5% of the remaining events which have velocities above the Teflon Cerenkov threshold, as documented in Table 4.6.

4.5.4. Mass Agreement Cut

Agreement between the two or three available mass estimators can be used to eliminate many of the remaining events which interact in the instrument or suffer from other problems. In order to implement the mass agreement cut, a χ^2 measure of mass agreement was constructed for each event from the available mass estimators. Events below Teflon threshold have masses calculated from Pilot-Energy and by ΔE–E', and those above Teflon Cerenkov threshold also have a Teflon-Energy mass. A χ^2 probability distribution was fit separately to the "low" and "high" energy events for each element. The data were well represented by the χ^2 distributions and a loose agreement cut was placed on the events, eliminating those whose mass agreement was such that the probability of exceeding their χ^2 is less than 5%. These agreement cuts eliminated about 7% of the remaining events. Tighter agreement cuts were tested but did not significantly improve the final mass resolution.

Table 4.6 Summary of Final Event Selections

	Boron	Carbon	Nitrogen	Oxygen
Number passing charge cuts	1069	3581	1066	3769
	Fraction eliminated(% of remaining events)			
dM cut	6.8 %	3.5 %	5.0 %	3.6 %
Q_{pil} cut	1.9	1.4	1.7	0.9
Q_{tef} cut	5.2	3.8	3.0	2.3
χ^2 cut	7.1	6.9	6.1	6.8
Final number selected	892	3116	919	3314

4.6. Mass Histograms

The mass distributions resulting after application of all the described event selections are shown in Figures 4.12 through 4.16. Figure 4.12(a) shows masses found by the Pilot-Energy method versus mass found using ΔE–E′ for events below Teflon Cerenkov threshold. For events with velocities above the Teflon threshold, Figure 4.12(b) shows mass found by the Pilot-Energy and Teflon-Energy methods for B, C, N, and O. Mass histograms resulting from each of the isotope measurement methods are displayed in Figures 4.13, 4.14, 4.15, and 4.16. Also shown in these figures is a histogram of the weighted average mass calculated as described in §5.1. Mass by Pilot-Energy has, in general, the best resolution of all three mass estimators. For events with energies above Teflon threshold, the Pilot-Energy and Teflon-Energy methods are about equal in resolution. The ΔE–E′ method has the poorest resolution, although the resolution would be improved if wide angle events were eliminated from the data. The ΔE–E′ isotope resolution rapidly degrades with increasing nuclear mass; so, it contributes little useful information for oxygen. The resulting resolution for the weighted average masses is ~0.24 amu for boron, ~0.25 for carbon and nitrogen, and ~0.27 amu for oxygen.

Figure 4.9

Histograms showing the agreement between the average measured ΔE–E′ mass and the ΔE–E′ mass measured using the last layers of the particle's range. The agreement criteria, dM, is calculated as defined in equation 4.8. The adopted data selection cuts for each element are shown as vertical lines.

Figure 4.10(a)

Histograms showing the requirements for internal agreement of the 12 Cerenkov signals generated for each event by the Pilot counter. All events passing the charge cuts described in §4.4 are shown.

Figure 4.10(b)

Histograms showing the requirements for internal agreement of the 12 Cerenkov signals generated for each event by the Teflon counter. All above threshold events passing the charge cuts described in §4.4 are shown.

Figure 4.9

ΔE−E′ mass agreement

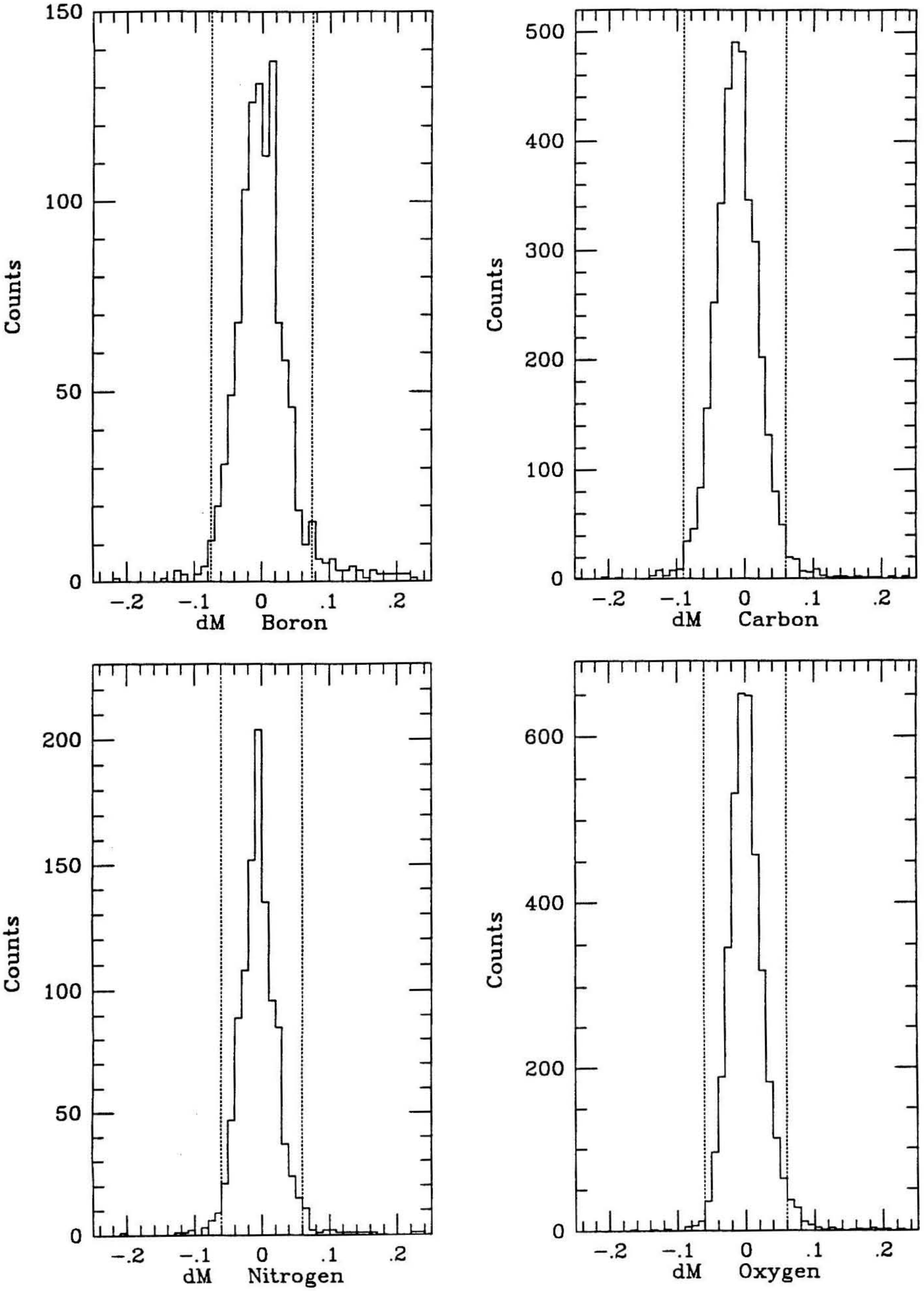

Figure 4.10(a)

Pilot PMT agreement

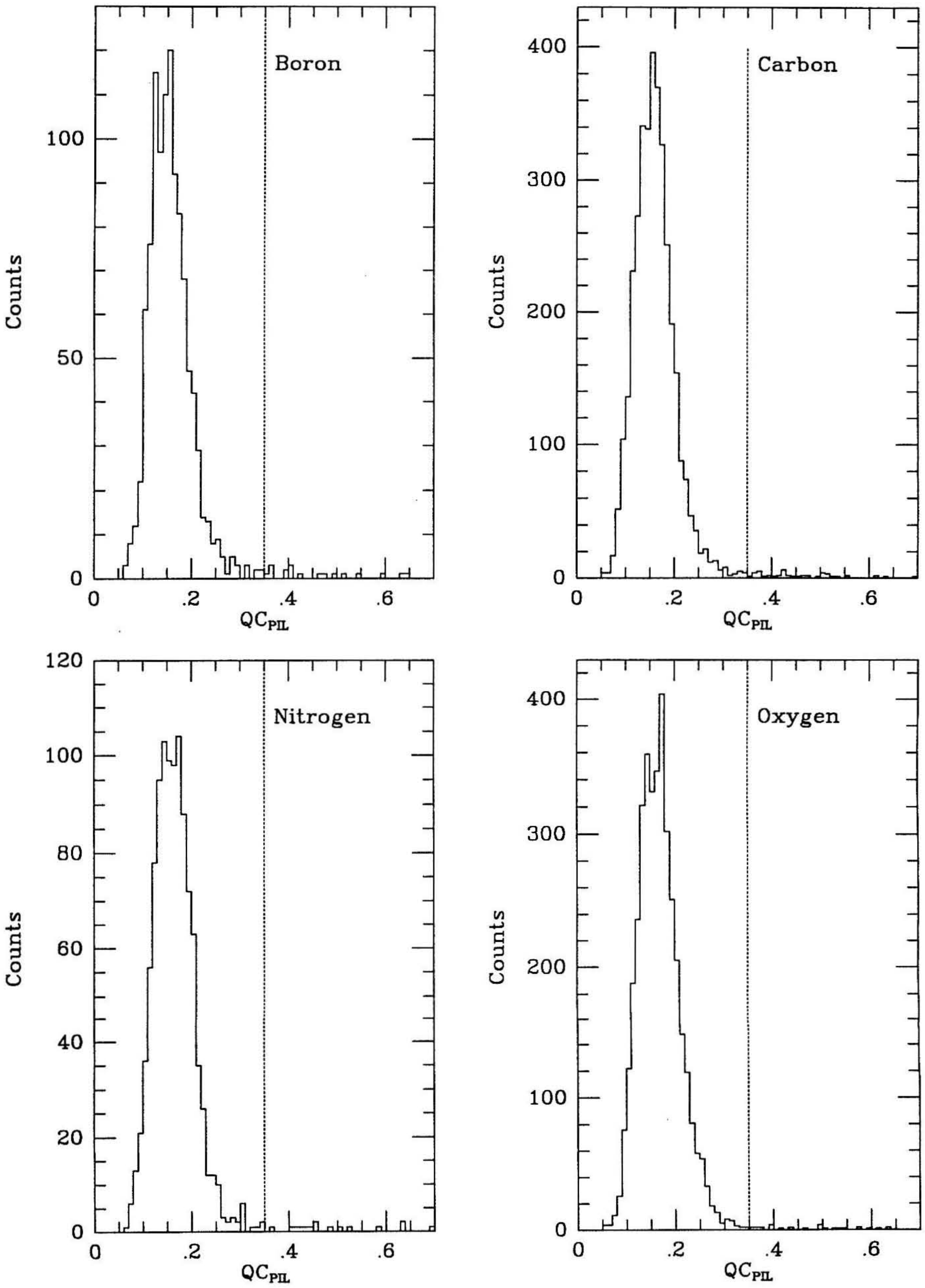

Figure 4.10(b)

Teflon PMT agreement

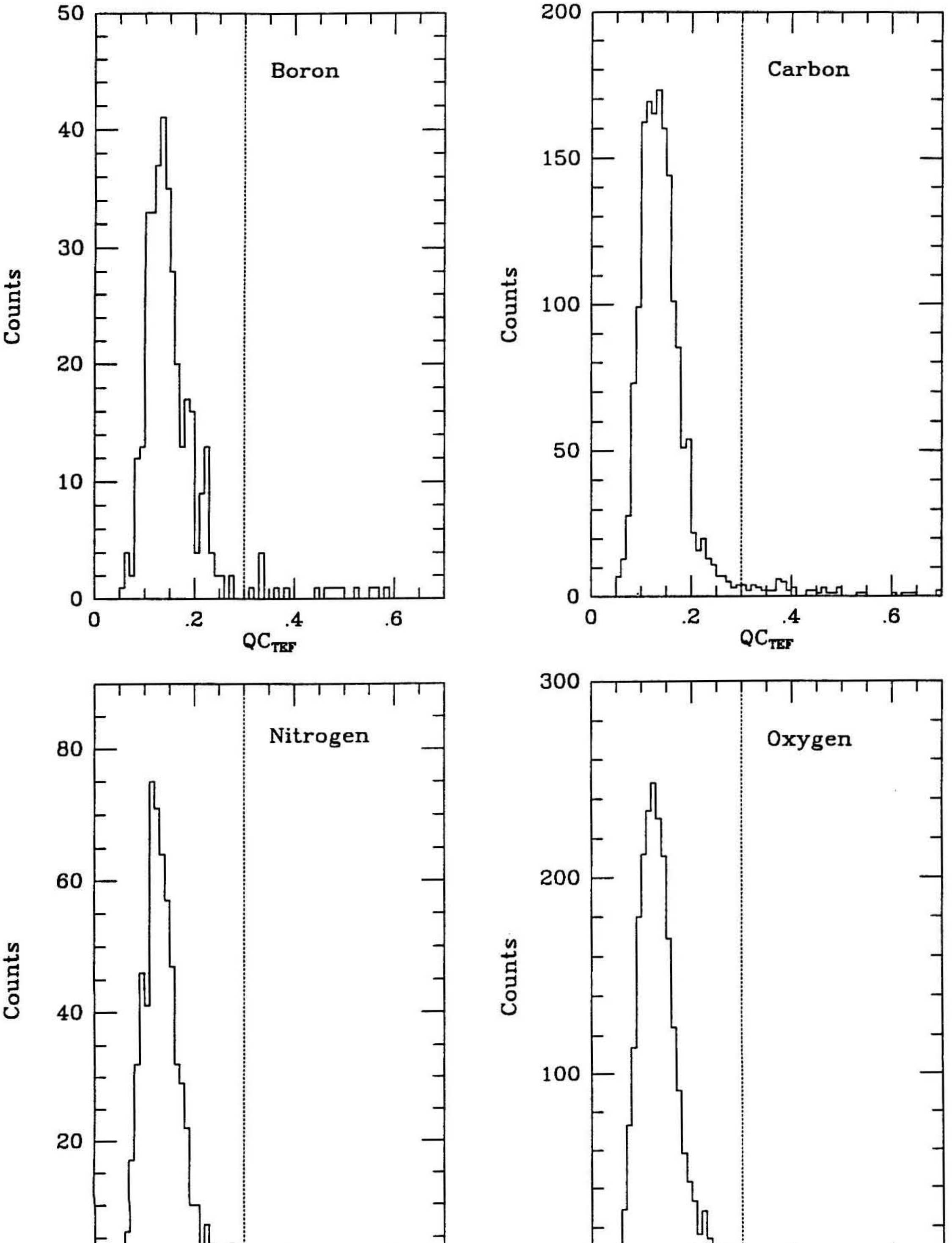

Figure 4.11(a)

Pilot-Energy and ΔE–E masses for events below the Teflon threshold velocity. These events have passed the charge cuts of §4.4 and the energy cuts of §4.5.1 but have not been subjected the remaining selection criteria, listed in Table 4.6.

Figure 4.11(b)

Pilot-Energy and Teflon-Energy masses for events above the Teflon threshold energy. These events have passed the charge cuts of §4.4 and the energy cuts of §4.5.1 but have not been subjected the remaining selection criteria, listed in Table 4.6.

Figure 4.12(a)

Pilot-Energy and ΔE–E masses for events below the Teflon threshold energy. Events shown have passed all selection criteria.

Figure 4.12(b)

Pilot-Energy and Teflon-Energy masses for events above the Teflon threshold energy. Events shown have passed all selection criteria.

Figure 4.11(a)

Mass distributions before final cuts

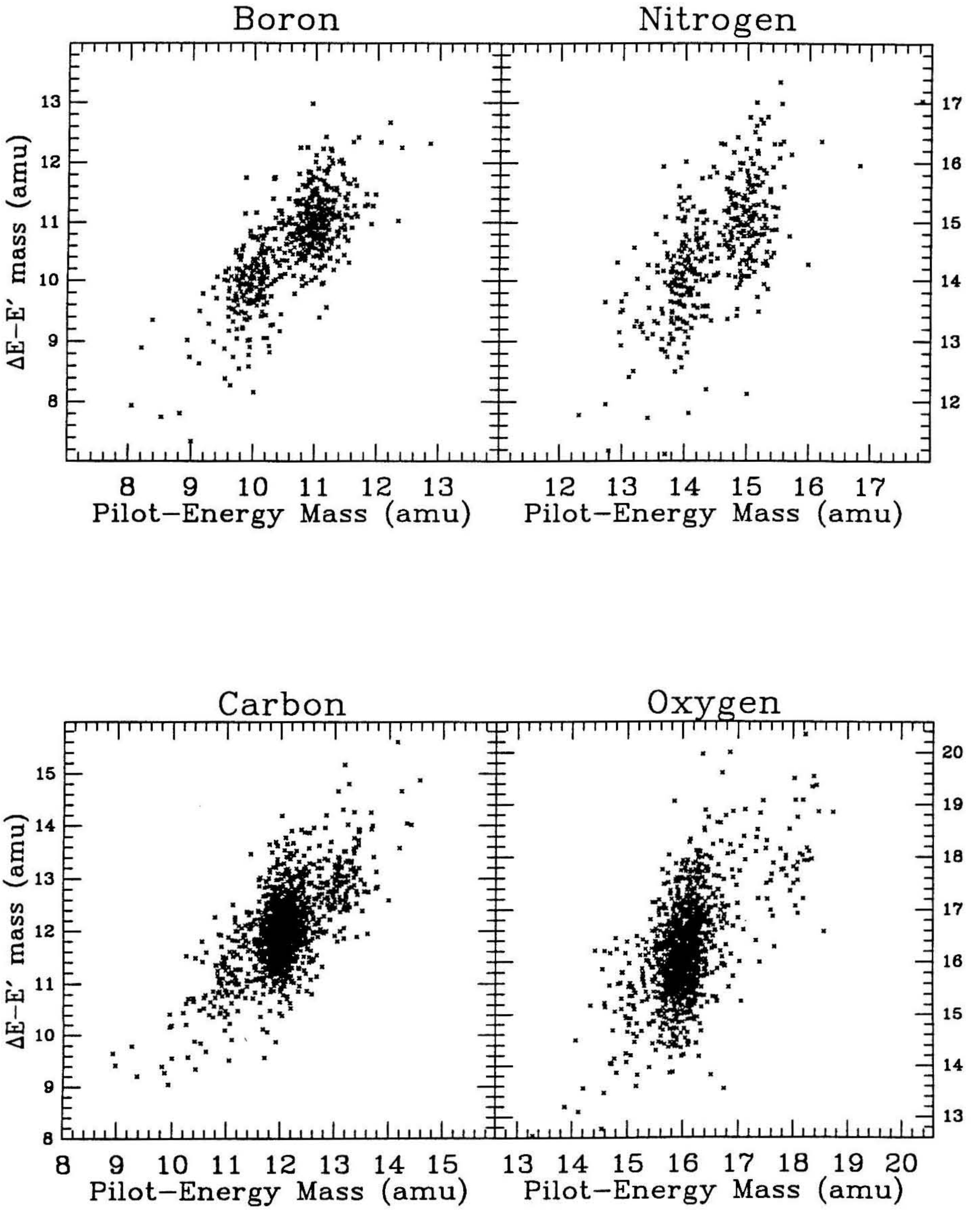

Figure 4.11(b)

Mass distributions before final cuts

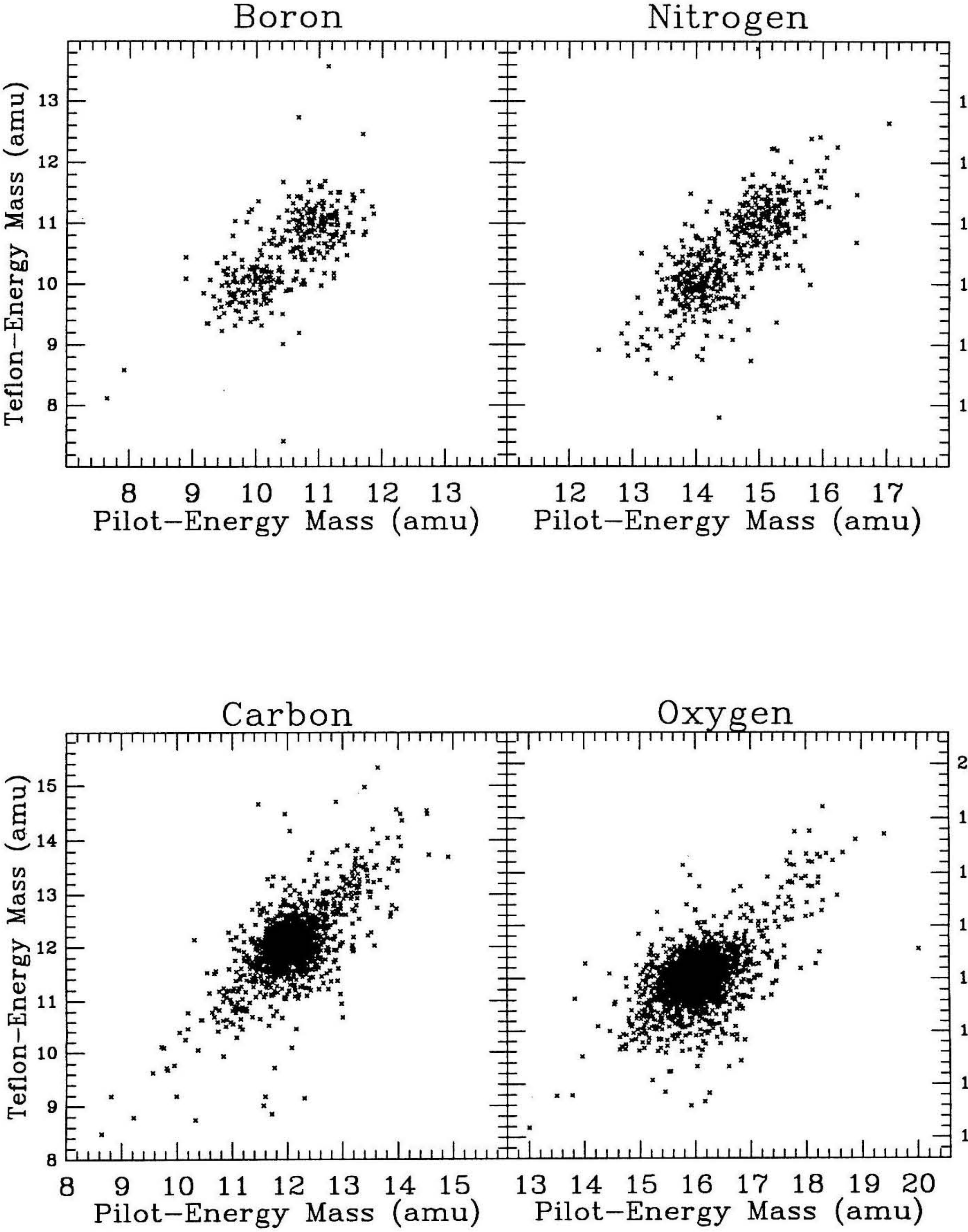

Figure 4.12(a)

Final Mass Distributions

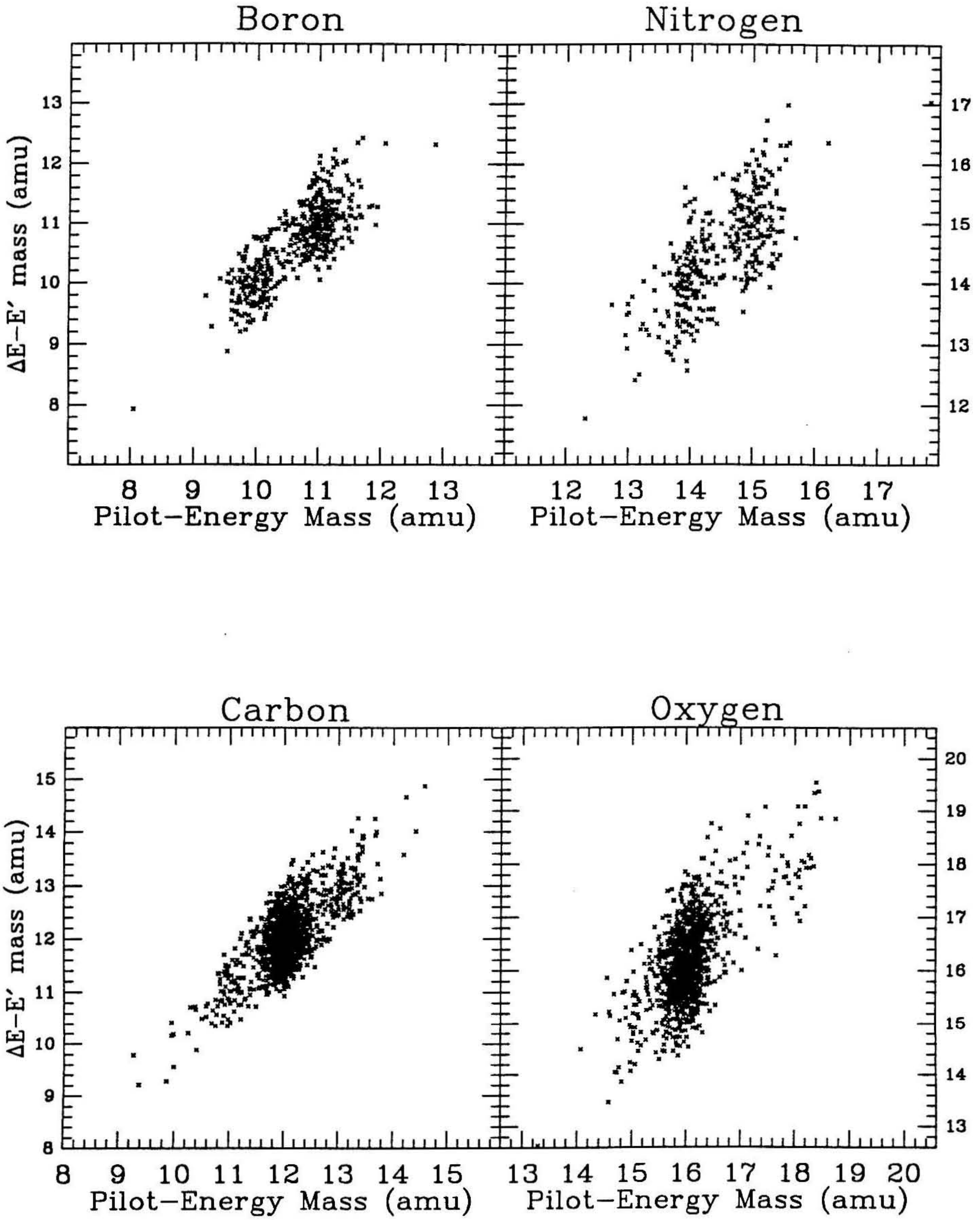

Figure 4.12(b)

Final Mass Distributions

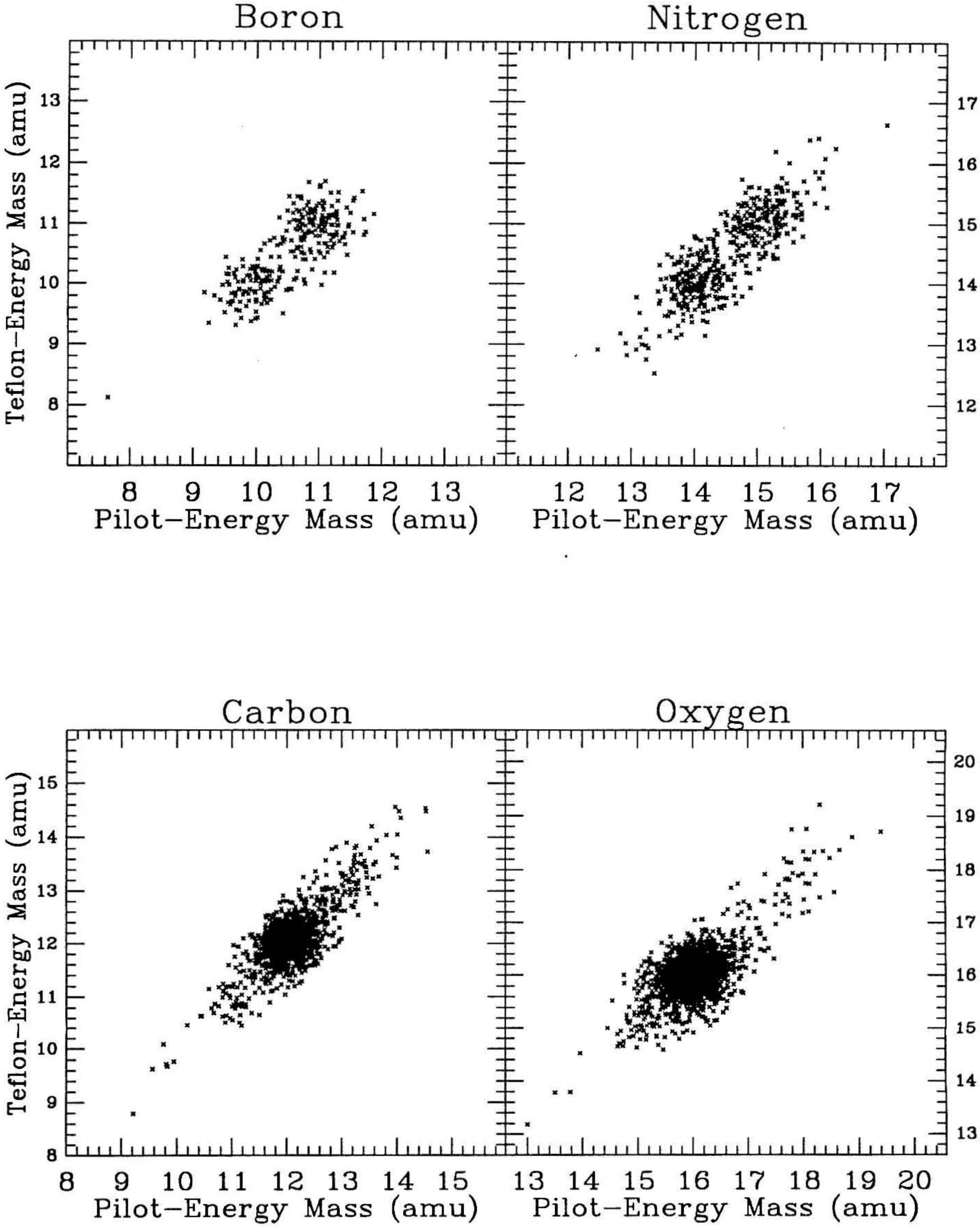

Figure 4.13

Boron mass histograms for each of the three calculated mass estimators and for a weighted average mass. The resulting mass resolution for the weighted average masses is ~0.24 amu.

Figure 4.14

Carbon mass histograms for each of the three calculated mass estimators and for a weighted average mass. The resulting mass resolution for the weighted average masses is ~0.25 amu.

Figure 4.15

Nitrogen mass histograms for each of the three calculated mass estimators and for a weighted average mass. The resulting mass resolution for the weighted average masses is ~0.25 amu.

Figure 4.16

Oxygen mass histograms for each of the three calculated mass estimators and for a weighted average mass. The ^{18}O peak is shown on an expanded scale for the weighted average mass. The resulting mass resolution for the weighted average masses is ~0.27 amu.

Figure 4.13

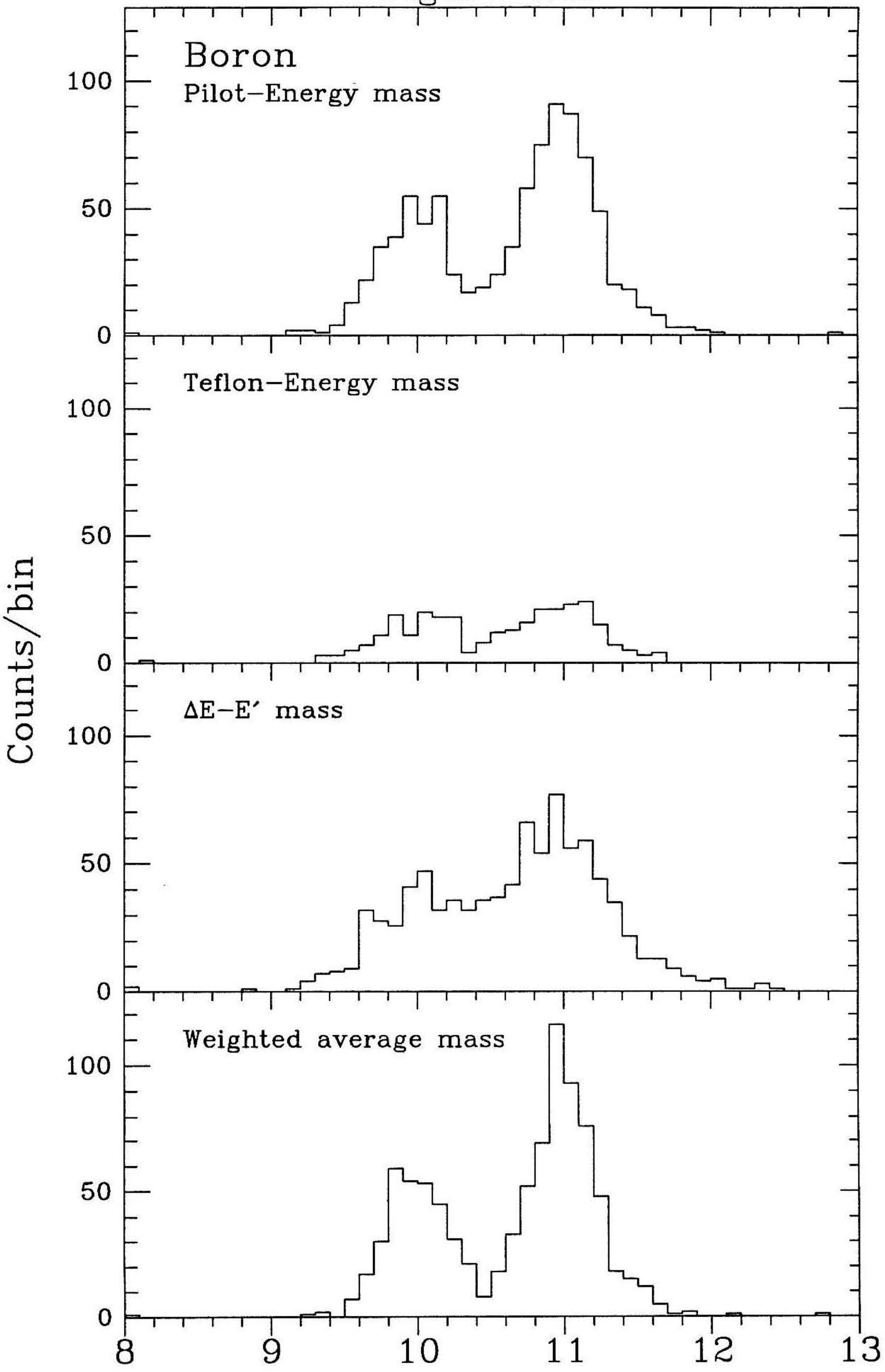
Boron
Pilot-Energy mass
Teflon-Energy mass
ΔE-E′ mass
Weighted average mass
Counts/bin
0
50
100
8
9
10
11
12
13
Mass (amu)

Figure 4.14

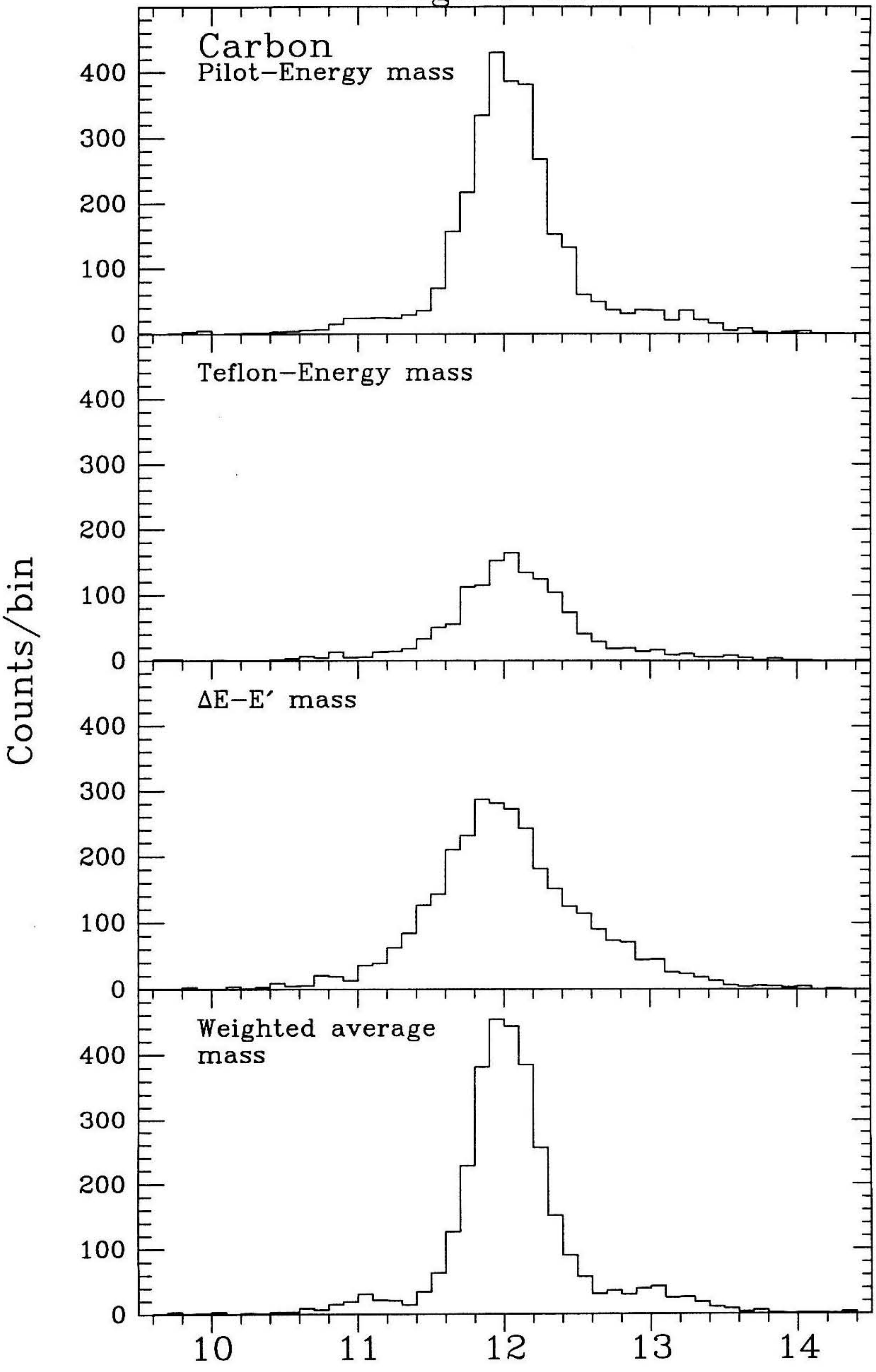
Carbon
Pilot-Energy mass
Teflon-Energy mass
ΔE-E′ mass
Weighted average
mass
Counts/bin
0
100
200
300
400
10
11
12
13
14
Mass (amu)

Figure 4.15

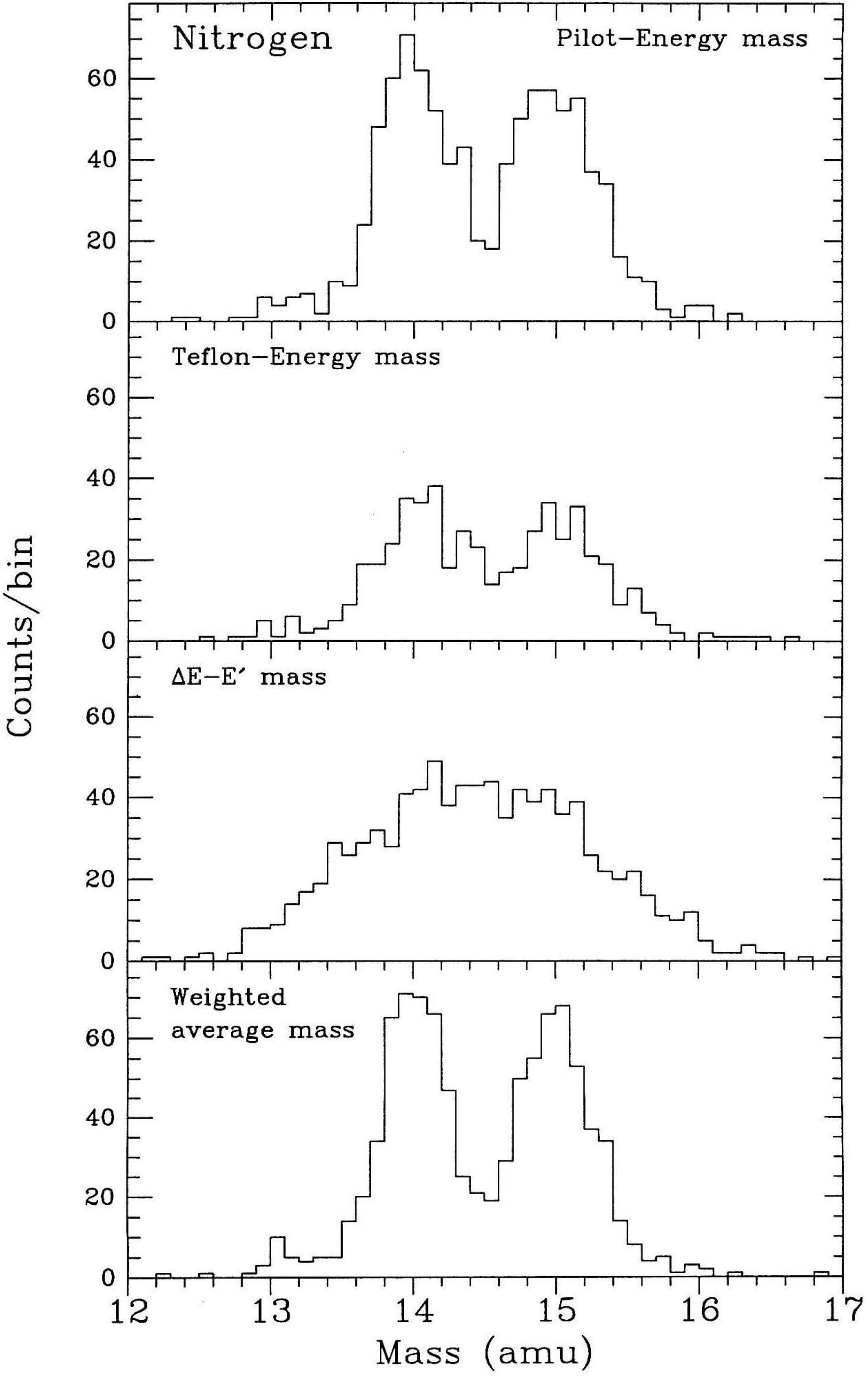
Nitrogen
Pilot-Energy mass
Teflon-Energy mass
ΔE-E′ mass
Weighted
average mass
Counts/bin
0
20
40
60
12
13
14
15
16
17
Mass (amu)

Figure 4.16

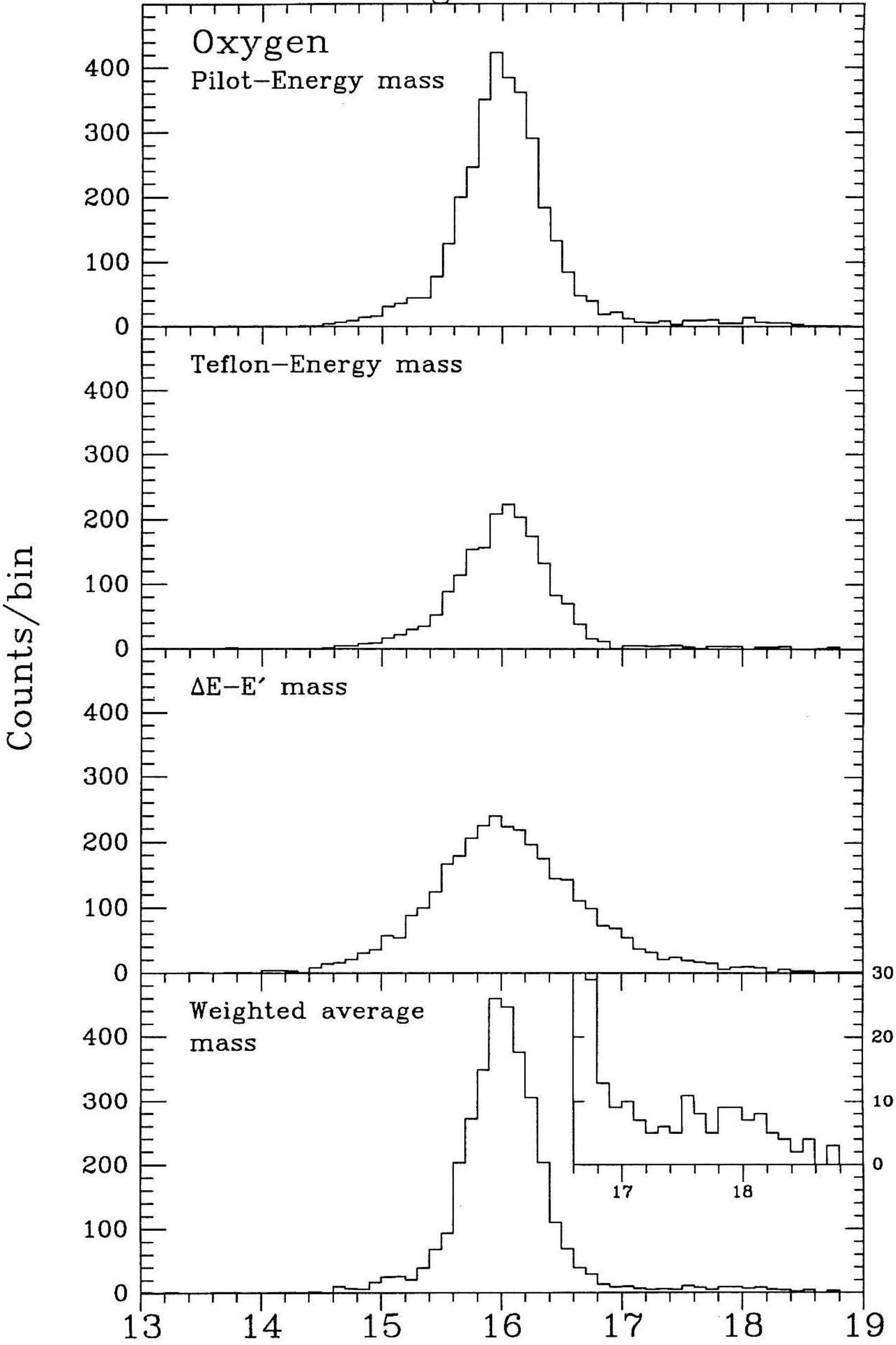
Oxygen
Pilot–Energy mass
Teflon–Energy mass
ΔE–E′ mass
Weighted average mass
Counts/bin
0
100
200
300
400
30
20
10
0
17
18
13
14
15
16
17
18
19
Mass (amu)

Chapter 5

Abundance Analysis

5.1. Abundance Fitting

The events chosen for mass analysis divide naturally into two energy ranges, those with velocities below and above the Teflon Cerenkov threshold. In order to use as much information as possible for each event, we have used an n-dimensional implementation of the maximum likelihood method to fit the events, where n is 2 for the events below Teflon threshold, and n is 3 for the above threshold events. An isotope "reference" probability distribution in n-dimensional "mass space" is used to fit the observed mass estimators. This reference distribution contains free parameters, $\vec{\alpha}$, which are optimized in order to maximize the likelihood function, $L(\vec{\alpha})$. For each event we calculate the probability $p(\vec{x}_j\ ,\ \vec{\alpha})$ that the event, which is described by the mass estimators, $\vec{x}_j$, would arise from the assumed parent reference distribution. The likelihood function is calculated by finding the product of the probabilities for all the events in the data set. In practice, the log of the likelihood function is calculated and maximized instead of the likelihood function itself.

$$\log(L(\vec{\alpha})) \ = \ \sum_j \log(\ p(\vec{x}_j,\vec{\alpha})\ )\ . \tag{5.1}$$

For each element, the model distribution consists of the sum of the reference distributions representing the individual isotopes. The parameters varied in order to maximize the likelihood function include the fractions of the total model distribution contributed by each isotope. All but one of these parameters are free since their sum is constrained to be unity. The additional free parameters are one offset and one width scaling factor per dimension of mass phase space so that the width and position of the model distribution can be adjusted in each dimension. For each element, the mass resolution of the isotopes is assumed to scale proportionally with nuclear mass.

For boron, carbon, and nitrogen, fits were done with two types of reference distributions. The elements were fit assuming Gaussian errors in the mass estimators and were also fit using reference distributions derived from the ^{16}O events. Oxygen was used to construct reference distributions because of its relatively good statistics and because the abundances of the ^{15}O and ^{17}O "satellite" peaks are small relative to ^{16}O. In order to construct the oxygen reference distributions, two and three dimensional histograms of the oxygen events were created. The histograms were smoothed by spline interpolation. Then, the ^{15}O and ^{17}O contributions to these histograms, as determined by the Gaussian maximum likelihood fits to oxygen, were subtracted in order to obtain a "pure" ^{16}O distribution which was used in the oxygen reference fits. A second set of oxygen reference distributions was constructed in the same fashion except with only half of the assumed ^{15}O and ^{17}O contributions subtracted from the smoothed distribution. This second set of distributions was used to test the sensitivity of the fit abundances to our method of constructing the reference distributions.

The oxygen reference distributions provide much better fits to the flight data than Gaussian distributions, which clearly underestimate the tails of the isotope peaks. The adopted abundances for B, C, and N come from the oxygen reference fits. Possible fitting errors arising from uncertainties in the form of the actual parent distribution for the isotope peaks were estimated from the differences between the oxygen reference and Gaussian fits. These uncertainties have been included in the total error bars for the measurements given in Table 5.7. The differences in fitted abundances were negligible for boron and nitrogen. Only ^{13}C was sensitive to the form of the fitting distribution as could be expected since it can be affected by the "tail" of the large ^{12}C peak. Even so, the abundances found by using oxygen reference and Gaussian distributions differed by less than the statistical error in the ^{13}C abundance.

For determining abundances of the observed oxygen isotopes, a ^{15}N reference distribution was constructed and used in addition to the fits assuming Gaussian errors. ^{15}N was chosen because there is a negligible amount of ^{16}N to affect the tail on the "high mass" side of the ^{15}N peak. Although we tried to eliminate the ^{14}N from the low side of the peak, the overall shape of the resulting distribution did not fit the oxygen data as well as the simple assumption of Gaussian errors. So, the adopted oxygen isotope abundances are from fits which assumed Gaussian errors, and, again, systematic uncertainties in the abundances have been estimated from the maximum differences found by using both types of isotope reference distributions. These uncertainties are quite large for ^{17}O since the ^{17}O abundance is very sensitive to the assumed form of the ^{16}O distribution. The fitted amount of ^{18}O is relatively insensitive to the assumed mass reference distribution since it is roughly equal in abundance to ^{17}O and is not strongly affected by the shape of the ^{17}O distribution. The results of the abundance fits are given in Table 5.1, and the fits are shown in Figure 5.1.

5.2. Corrections to Measured Abundances

In order to find isotopic abundances of cosmic rays outside the Earth's atmosphere, we have modeled the changes in composition which occur as the nuclei pass through the atmosphere above HEIST. We have also modeled the nuclear fragmentations which take place in the HEIST detectors. These models yield correction factors which can be applied to the observed abundances in order to calculate abundances at the top of the HEIST instrument and at the top of the atmosphere.

5.2.1. Instrumental Corrections

A large fraction of the nuclei which enter HEIST undergo nuclear interaction before stopping; therefore, the fraction of interacting events for each isotope must be calculated in order to correct the observed isotope abundances to find

Figure 5.1(a)

Maximum likelihood fits to boron and nitrogen events. The smooth curves are mass distributions found from scaling the multi-dimensional oxygen reference distribution and projecting on the axis of optimal resolution. The rms mass resolution is 0.24 amu for boron and 0.25 amu for nitrogen.

Figure 5.1(a)

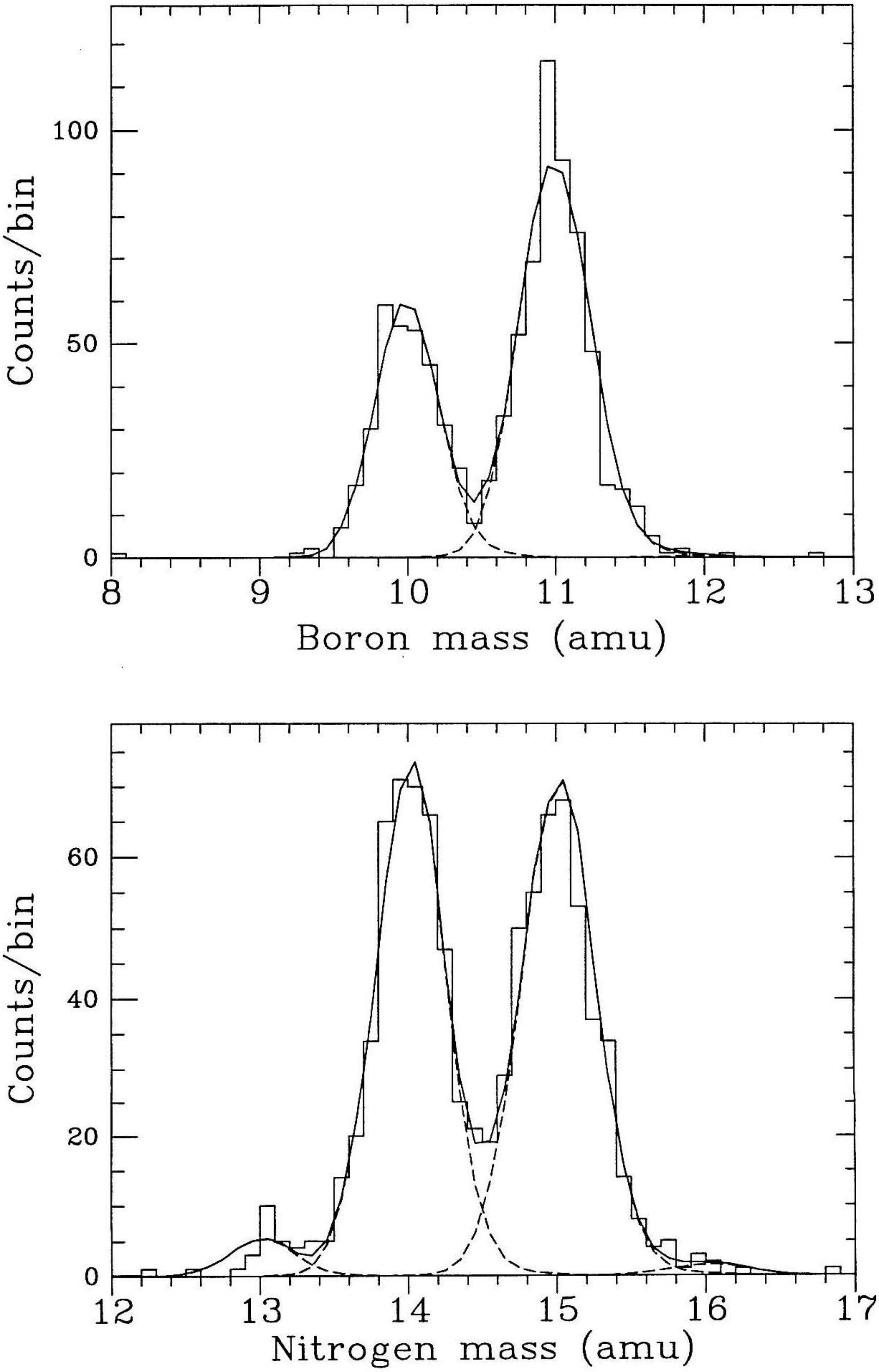
Counts/bin
0
50
100
8
9
10
11
12
13
Boron mass (amu)
Counts/bin
0
20
40
60
12
13
14
15
16
17
Nitrogen mass (amu)

Figure 5.1(b)

Maximum likelihood fits to carbon and oxygen events. The smooth curves fitting the carbon events are mass distributions found from scaling the multi-dimensional oxygen reference distribution and projecting on the axis of optimal resolution. The curves fitting the oxygen events result from assuming that the errors for each mass estimator are normally distributed. The rms mass resolution is 0.25 amu for carbon and 0.27 amu for oxygen.

Figure 5.1(b)

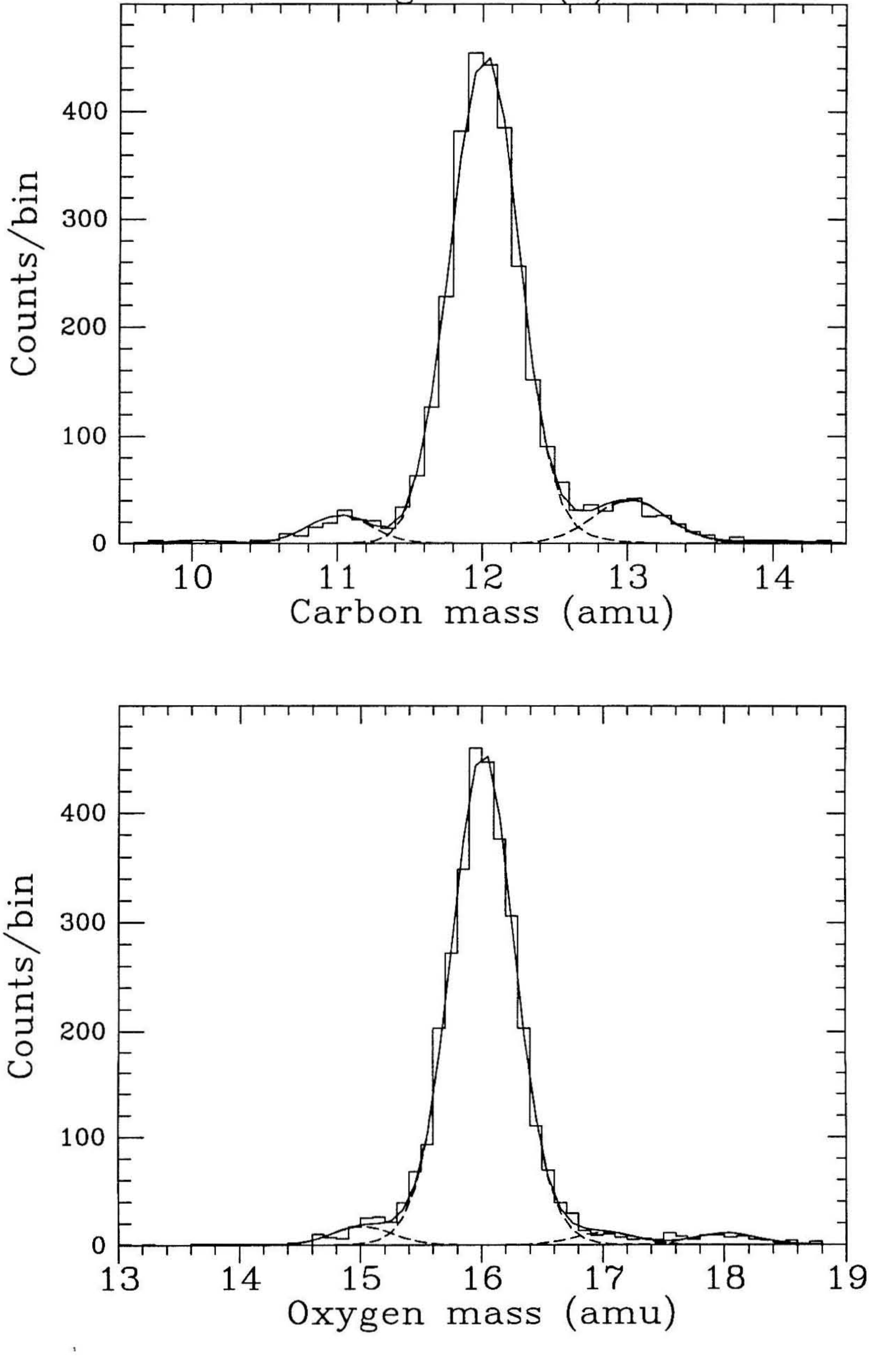
Counts/bin
400
300
200
100
0
10
11
12
13
14
Carbon mass (amu)
Counts/bin
400
300
200
100
0
13
14
15
16
17
18
19
Oxygen mass (amu)

Table 5.1 Abundances Observed in Instrument

Species	Energy Interval Top of Atmos. (MeV/nucleon)		Low Energy Events	High Energy Events	Total Events Observed
	Low	High			
$^{10}\mathrm{B}$	414-517	517-700	205 ±14	122 ±11	327 ±18
$^{11}\mathrm{B}$	405-510	510-690	392 ±20	170 ±13	562 ±24
$^{12}\mathrm{B}$			2	0	2
$^{10}\mathrm{C}$			9	5	14
$^{11}\mathrm{C}$			82	59	141
$^{12}\mathrm{C}$	431-520	520-674	1464 ±38	1222 ±36	2686 ±52
$^{13}\mathrm{C}$	422-513	513-666	147 ±13	110 ±12	257 ±18
$^{14}\mathrm{C}$			6	13	19
$^{13}\mathrm{N}$			15	14	29
$^{14}\mathrm{N}$	446-520	520-681	177 ±13	255 ±16	432 ±21
$^{15}\mathrm{N}$	437-513	513-673	204 ±14	244 ±16	447 ±21
$^{16}\mathrm{N}$			1	9	10
$^{14}\mathrm{O}$			3	3	6
$^{15}\mathrm{O}$			58	76	134
$^{16}\mathrm{O}$	463-547	547-777	1254 ±35	1772 ±49	3026 ±60
$^{17}\mathrm{O}$	454-539	539-769	48±8	30±16	77±18
$^{18}\mathrm{O}$	446-532	532-763	37 ±7	34 ±6	71 ±9

abundances of the incident cosmic rays. The instrument interaction model propagates nuclei from the top scintillator to the end of range in the NaI(Tl) stack in a series of steps chosen to be sufficiently small so that multiple interactions can be neglected within each step. Energy dependent interaction cross sections described in §5.3 are used to find the probability of an interaction occurring in each step. For each isotope, we use the observed angles of incidence and ranges in the stack for the selected flight events in order to analytically calculate an average fragmentation correction factor for each isotope. These correction factors are found separately for the events above and below Teflon threshold.

We assume that all charge changing interactions occurring between the top half of S1 and the stopping layer are detected and rejected by the various consistency criteria. Neutron stripping above the top of the stack goes undetected unless the neutron interacts in the stack. Neutron stripping events in the stack may be rejected due to inconsistency between the average mass in the stack and the mass calculated using the ΔE–E′ information from the last 2 or 3 stack layers. Neutron strips in the stack may also be rejected if the interaction deposits extra energy in the interacting layer. Neutron stripping interactions in the stack where neither daughter subsequently interacts are assumed to be rejected with 60% efficiency, and we assume 100% rejection if either daughter interacts. For those neutron stripping events which are not identified and rejected as interactions, those occurring above one-half the range in the NaI(Tl) are counted as the heavier daughter isotope. Those occurring later than one-half of the range in the stack are counted as the parent isotope. These identification efficiencies for neutron stripping events have been empirically chosen in order to achieve consistency with the number of events rejected by the stack mass consistency cuts described in §4.5.2, and with the number of observed ^{15}O and ^{11}C events, which, because of their short half lives, must have all been produced by nuclear interactions in the atmosphere and the instrument.

This calculation shows that 29% of the carbon events and 32% of the oxygen events incident at the top of the instrument survive and stop in the NaI(Tl) stack without undergoing a mass changing interaction. Carbon has a lower surviving fraction because its average range in the stack is longer than the average range for oxygen. Although the absolute value of these correction factors is quite large, the correction factors for adjacent isotopes differ by only 4-12%. Another correction must be applied for the difference in HEIST's geometrical collection efficiency for each isotope. For each element, the heavier isotopes have longer ranges and so have higher chances of escaping out the side of the NaI(Tl) stack. HEIST's geometrical collection efficiency can be parametrized as a function of range in the NaI(Tl), and the relative collection efficiency for each isotope has been calculated using the observed distribution of ranges found from the events selected for abundance fitting. The resulting correction changes the abundance ratio of adjacent isotopes by only 1-3% for C, N, and O. The corrections for boron are larger since we have selected an energy interval for boron which includes energies large enough to allow events near normal incidence to penetrate the entire NaI(Tl) stack. Resulting top of instrument isotope ratios are given in Table 5.7.

5.2.2. Model of Atmospheric Interactions

In order to find isotopic abundances at the top of the atmosphere which correspond to the abundances at the top of the instrument, we must account for changes in composition due to nuclear interactions occurring during propagation through the atmosphere. Following a similar approach to that used for the instrumental corrections, a model has been used to propagate the isotopes of elements in the range of $Z=5$ to 26 through the residual atmosphere above HEIST and the HEIST aluminum shell. An average value of 5.15 g/cm^2 of residual atmosphere was used in conjunction with an average secant of 1.113. For the isotopes of B, C, N, and O, about 20% of the nuclei undergo nuclear fragmentation during their propagation through the 5.72g/cm^2 of air.

In this "slab model," we calculate the change in abundance of all isotopic species in finite steps chosen to be small enough so that multiple interactions can be neglected within each step. The abundance of species s can be expressed in

Table 5.2

Contributions to Top of Instrument Abundance (Percent)

Observed Nuclide	Top of Atmosphere Source Nuclide										
	^{10}B	^{11}B	^{12}C	^{13}C	^{14}N	^{15}N	^{16}O	^{20}Ne	^{24}Mg	^{28}Si	other
^{10}B	80.0	3.8	8.3	0.2	0.7	0.3	5.0	0.4	0.4	0.2	0.7
^{11}B		87.3	6.4	0.5	0.5	0.8	3.1	0.2	0.2	0.2	0.8
^{12}C			96.3	0.2	0.4	0.3	1.9	0.2	0.2	0.1	0.4
^{13}C				82.7	0.7	2.4	9.3	0.7	0.6	0.5	3.1
^{14}N					84.2	2.0	10.4	0.9	0.6	0.5	1.4
^{15}N						86.4	9.6	0.8	0.6	0.4	2.2
^{16}O							98.9	0.2	0.2	0.1	0.6
	^{17}O	^{18}O	^{19}F	^{20}Ne	^{22}Ne	^{23}Na	^{24}Mg	^{25}Mg	^{26}Mg	^{28}Si	other
^{17}O	80.1	2.1	1.1	2.1	2.5	1.2	2.6	1.1	1.2	2.0	4.0
^{18}O		95.7	1.5	0.6	0.4	0.1	0.7	0.1	0.2	0.2	0.5

finite difference form as

$$N_s(x_0+\delta x) = N_s(x_0)\left[1-\frac{\delta x}{\lambda_s}\right] + \sum_{p>s} N_p(x_0)\,\frac{\delta x}{\lambda_{ps}}\,, \qquad (5.2)$$

where $N_s(x)$ is the abundance of isotopic species s at depth x, λ_s is the total mean-free-path for mass-changing interactions, and λ_{ps} is the partial mean-free-path for the spallation of parent species p into species s (see §5.3). We make the assumption that mass changing interactions do not change the velocity of the propagating nuclei; thus, the secondary nuclei leave the interaction with the same kinetic energy per nucleon as had the parent. As noted in §5.3, the *interaction cross* sections are approximated as energy independent in this model. Energy loss of the nuclei was modeled since it does have a small effect when correcting the abundances to equal energy intervals.

Table 5.2 shows the top of atmosphere source contributions to the nuclides at the top of HEIST expressed as a percentage of the top of instrument abundance. For example, 82.7% of the ^{13}C at the top of the instrument comes from ^{13}C at the top of the atmosphere, and 9.3 % of the top of instrument ^{13}C comes from top of atmosphere ^{16}O which fragments during its travel through the 5.72g/cm^2 of air.

The initially assumed elemental and isotopic abundances for elements with Z>4 were taken from the results of our galactic propagation model discussed in §5.4. The relative elemental abundances of B, C, N, and O from the galactic propagation model are in good agreement with our observed elemental abundances, listed in Table 5.4, and with the measurements of the HEAO-3-C2 experiment (Engelmann et al. 1990) and were not adjusted. The isotopic composition of oxygen, carbon, nitrogen, and boron at the top of the atmosphere was adjusted to fit the measured isotopic abundances. Abundances were corrected to equal energy intervals by assuming an energy spectrum given by our modeled oxygen spectrum, shown in Figure 5.2. Resulting top of atmosphere abundances are shown in Table 5.7.

Uncertainties in top of the atmosphere abundances due to possible inaccuracies in the atmospheric corrections have been estimated assuming uncorrelated errors of 20% in the production of secondaries. Webber, Kish, and Schrier find experimental uncertainties in their measured cross sections to be less than 6% in most cases (Webber et al., 1990c), however since these cross sections are being extrapolated to a nitrogen and oxygen target, the average uncertainty is estimated to be near 20%. Uncertainties of ≤10% in the exact top of atmosphere elemental abundances increase the total uncertainty by a small amount. The resulting abundance uncertainties are included in the errors quoted in Table 5.7.

Table 5.3 shows the agreement between the atmospheric model predictions for the short-lived isotopes produced in the atmosphere and the actual observed

Table 5.3 Predicted and Observed Radioactive Secondaries

Species	Model Prediction	Observed
^{12}B	7.4±1.2	2.2±3.5
^{10}C	9.9±1.5	14.2±4.1
^{11}C	141.1±14.5	140.6±12.4
^{14}C	11.0±1.8	18.7±5.3
^{13}N	24.5±2.2	29.5±5.9
^{16}N	4.9±1.2	10.3±5.4
^{14}O	8.4±0.5	5.7±2.8
^{15}O	158±12	134±22.5

numbers of these events. The errors on the model predictions include uncertainties in the fragmentation cross sections in the atmosphere and the instrument, and the quoted errors on the numbers of observed events include statistical and fitting uncertainties.

5.3. Nuclear Interaction Cross Sections

One of the critical inputs to any cosmic ray propagation model is a set of nuclear interaction cross sections. For the atmospheric propagation model, we require both total mass changing cross sections and partial cross sections for the production of daughter nuclei. We have used the cross sections for various nuclei incident on carbon targets provided by Webber, Kish, and Schrier (1990a-d). Webber and co-workers have made extensive measurements of total and partial cross sections for various beams on hydrogen, helium, and carbon targets at the LBL Bevalac accelerator and have developed an empirical formalism to calculate

Table 5.4 HEIST Observed Elemental Abundances

Element	Events Observed	Normalized to Carbon	Top of Instrument (equal ΔE)	Top of Atmos. (equal ΔE)	HEAO-3-C2 (620 MeV/n)
Boron	890 ± 30	286	368	331 ± 16	321 ± 7
Carbon	3116 ± 56	1000	1000	1000 ± 35	1000 ± 12
Nitrogen	919 ± 30	295	283	259 ± 12	284 ± 6
Oxygen	3314 ± 58	1064	829	886 ± 31	906 ± 11

partial cross sections for nuclei incident on hydrogen targets. Where possible, we have used Webber, Kish, and Schrier's published experimental cross sections and have used a modified form of the empirical model (Webber 1990) to find the additional needed partial cross sections for nuclei incident on carbon targets. The cross sections for carbon targets were then scaled to provide cross sections on nitrogen and oxygen in the atmosphere.

The energy dependence of the interaction cross sections is ignored in the atmospheric propagation model, but becomes significant as the nuclei slow and stop in the instrument. The instrument model requires only the total mass changing cross sections and the partial cross sections for neutron stripping since all charge changing interactions are assumed to be eliminated by consistency criteria. Energy dependent total cross sections are found using a parametrization taken from Kox et al. (1987) renormalized to the measurements of Webber et al.(1990a), and partial cross sections for neutron stripping, $\sigma_{ij}(E)$, are found from

$$\sigma_{ij}(E) = \sigma_{ijC}(600) \frac{\sigma(E)}{\sigma_C(600)} . \tag{5.3}$$

Here, $\sigma_{ijC}(600)$ is Webber's neutron stripping cross section on carbon at 600

MeV/nucleon, and $\sigma(E)$ is the total mass changing cross section predicted by the Kox model. The total mass changing cross section at 600 MeV/nucleon, $\sigma_C(600)$, is found from a modified Bradt-Peters formula which Webber, Kish, and Schrier have fit to measurements at 1500 MeV/nucleon (Webber et al. 1990a). This formula gives the total mass-changing cross section, σ_{BT}, for a beam of nuclei with mass number A_B incident on target material with mass number A_T.

$$\sigma_{BT} = 57.3 \left[A_T^{1/3} + A_B^{1/3} - b\right]^2 \quad \text{(mb)} . \tag{5.4}$$

where

$$b = \left[1.36 - 0.018\,A_T\right] - 0.065\,A_B^{1/3}\,A_T^{1/3} . \tag{5.5}$$

Webber et al. have found that from 600 to 1500 MeV/nucleon, the change in total cross section for various beams on carbon targets is less than 3%, and we have simply approximated the 600 MeV/nucleon cross section with this fit to 1500 MeV/nucleon data. The predictions of the Kox total cross section model have been compared to the Webber, Kish, and Schrier measurements over the energy interval of 350 to 1000 MeV/nucleon for carbon on carbon. The Kox model predicts the observed energy dependence, but gives cross sections about 10% larger than those reported by Webber. This difference is not due to inaccuracies in the Kox model, but is consistent with the experimental cross sections measured by Kox et. al. which are larger than those reported by Webber, Kish, and Schrier in the limited energy range for which the experiments overlap. Changing the total interaction cross sections by 10% does not significantly affect the resulting isotope ratios at the top of the instrument.

5.4. Galactic Propagation

To relate our observations at 1 AU to abundances at the cosmic ray source (CRS) a leaky-box propagation model has been used to correct for the effects of nuclear fragmentation, radioactive decay, and ionization energy losses during cosmic ray propagation through interstellar H and He. Leaky-box calculations assume that cosmic rays travel within a galactic containment volume and have a small probability of escape at each encounter with the boundary. This homogeneous, steady state model of cosmic ray propagation has been widely used in the interpretation of cosmic ray observations (e.g., Ormes and Protheroe 1983; Garcia-Munoz et al. 1987). The isotopes of cosmic ray helium through nickel have been included in our propagation calculations. Ionization energy losses have been accounted for assuming 16% ionized H and He/H=0.07 in the interstellar medium.

The mean-free-path for escape is dependent upon the cosmic ray's magnetic rigidity (R) and is given by $\lambda_e = 42.4\beta^{3/2}R^{-0.65}$ g cm^{-2} for rigidities above 3.7 GV and $\lambda_e = 18.1\,\beta^{3/2}$ g cm^{-2} for lower rigidities (model 2 in Table 5.5). Here, β is the particle velocity divided by the speed of light and rigidity is related to kinetic energy by

$$R = \frac{A}{Z}\sqrt{E_n(E_n + 2m_0)}\ , \tag{5.6}$$

where Z and A are the nuclear charge and mass number, E_n is kinetic energy per nucleon, and m_0 is one atomic mass unit (931.5 MeV). As discussed below, this path-length distribution was found by fitting to B/C elemental ratio measurements. Boron nuclei in cosmic rays are "secondaries," produced by the fragmentation of heavier nuclei whereas cosmic ray carbon is mostly primary material. The secondary to primary B/C ratio is sensitive to the path-length for escape, λ_e, and is well suited as a "tracer" of cosmic ray propagation. Like boron, fluorine is thought to be absent in cosmic ray source material. The results of the propagation model agree well with the observed F/Ne ratio (Figure 5.3) indicating that the model accurately accounts for the production of lighter fragments from Ne, Mg, and Si.

We assume a cosmic ray energy spectra at the source that has an energy dependence of $dJ/dE \propto R^{-2.3}$. Cosmic ray source elemental abundances have been taken from the analysis of HEAO-3-C2 measurements as reported by Engelmann et al.(1990) except that nitrogen has been adjusted so that N/O = 0.04 to agree with our observed N/O ratio as shown in Figure 5.3. CRS isotopic abundances were assumed to be the same as solar system abundances (Cameron 1982) except for the abundances of the neutron rich isotopes of Ne, Mg, and Si which were increased over their solar system values to agree with the abundances given in the review by Mewaldt (1989).

Solar modulation is accounted for using a spherically symmetric model which includes the effects of diffusion, convection, and adiabatic energy loss represented by a Fokker-Planck equation (Fisk 1971) in which the parameters are the solar wind velocity, the radius of the modulation region, and a diffusion coefficient. The modulation level (or modulation strength) at heliospheric radius r can be represented by the modulation parameter of Gleeson and Axford (1968),

$$\phi = \frac{1}{3} \int_{r}^{R_H} \frac{V(r')}{\kappa(r')} \, dr' , \qquad 5.7$$

where V(r') is the solar wind velocity taken to be 400 km/sec, $\kappa(r')$ is the radial part of the diffusion coefficient, and R_H is the radius of the heliosphere. In the "force-field" approximation, this modulation parameter corresponds to the mean energy loss of particles which penetrate the heliosphere to a radius r, given by

$$\Phi = | Ze | \, \phi(r) . \qquad 5.8$$

We have taken the interstellar oxygen spectrum from our galactic propagation model and found that a modulation level of ϕ = 650 MV fits the oxygen measurements of Engelmann (1990). Path-length values were then chosen to fit the B/C elemental ratio measurements made at low energies by Krombel and Wiedenbeck (1988) and at higher energies by Engelmann et al. (1990), since the solar modulation level at the time of their measurements was comparable to that during our flight. The actual solar modulation level is not known with certainty, and since the modulation levels adopted by Engelmann et al. (600 MV) and Krombel and Wiedenbeck (740 MV) differ from our level, we have tested the effects of adopting modulation levels from ϕ = 450 MV up to ϕ = 800 MV. Using other path-length distributions in conjunction with appropriate modulation levels shows that the isotopic ratios predicted for B, C, N, and O are insensitive to the choice of path-length and modulation level, given the constraint of fitting the B/C measurements and the observed oxygen energy spectrum. Therefore, uncertainties in the isotope ratios introduced by solar modulation can be greatly reduced by using a self-consistent approach in fitting the B/C ratio.

Table 5.5 Comparison of Path-Length/Modulation Combinations

Parameters		Model 1	Model 2	Model 3
ϕ (MV)		450	650	800
$\lambda_{e,}$ $R>R_0$		$42.4\beta R^{-0.65}$	$42.4\beta^{3/2}R^{-0.65}$	$44\beta^2R^{-0.65}$
$\lambda_{e,}$ $R<R_0$		$18.8\,\beta$	$18.1\,\beta^{3/2}$	$18.5\,\beta^2$
R_0 (GV)		3.5	3.7	3.8
Ratio	Energy (MeV/nuc)			
B/C	535	0.323	0.319	0.317
^{10}B/B	500	0.302	0.297	0.294
^{15}N/N	555	0.550	0.552	0.554
^{13}C/^{12}C	545	0.0951	0.0950	0.0950
^{17}O/^{16}O	600	0.0214	0.0212	0.0210
^{18}O/^{16}O	600	0.0176	0.0176	0.0177

The B/C ratios predicted by three models are shown in Figures 5.3 and 5.4. Table 5.5 presents the isotope ratios predicted using the three different combinations of modulation and escape path-length. All of the ratios except ^{10}B/B change by less than 2% although λ_e changes by ~20% at the energies of interest. Fitting the B/C ratio tends to hold the other ratios constant because all are ratios of secondary nuclei to primary nuclei where the secondary is neutron-rich. The one exception is the ^{10}B/B ratio where both ^{10}B and ^{11}B are secondary nuclei. Since boron is neutron rich relative to carbon, increasing the level of solar modulation will increase the B/C ratio, other factors being equal. Thus, the models with higher modulation levels require shorter path-lengths to produce the observed secondary boron. In the other ratios, the secondary component of the ratio is also neutron-rich, and so these ratios have the same qualitative dependence on modulation and path-length as does the B/C ratio.

A comparison of model 2 predictions to B/C, F/Ne, N/O, and C/O measurements is shown in Figure 5.3. The model is able to fit the B/C and N/O measurements, but can not simultaneously fit the C/O measurements from both Engelmann et al. (1990) and from Krombel and Wiedenbeck (1988) suggesting that there may be some systematic differences between these two sets of measurements or possibly a sudden change of composition with energy. The measurement of the C/O ratio from HEIST agrees better with the Engelmann et al. HEAO-3-C2 observations.

Table 5.6

Contributions to Galactic Secondary Production (Percent)

Observed Secondary Nuclide	Primary Nuclide (percentage contributed to total secondaries produced)								
	^{14}N	^{16}O	^{20}Ne	^{22}Ne	^{24}Mg	^{25}Mg	^{26}Mg	^{28}Si	other
^{13}C	2	71	5	2	7	1	1	7	6
^{14}N		74	5	1	6	1	1	6	5
^{15}N		75	5	1	6	1	1	6	5
^{17}O			14	9	26	6	6	26	13
^{18}O			27	6	26	6	5	23	7

In order to arrive at ^{13}C, ^{17}O, and ^{18}O, abundances at the cosmic ray source, the propagation model has been run with various source amounts of these isotopes in order to find the relation of the CRS abundance to the abundance at 1 AU.

Figure 5.2

The solid curve is the oxygen spectrum predicted by our galactic propagation model after correcting for solar modulation at a level of $\phi = 650$ MV (Model 2 of Table 5.4). Solid squares are the spectrum measured by HEAO-3-C2 during a time period when the solar modulation level was comparable to that during our flight (Engelmann et al. 1990).

Figure 5.2

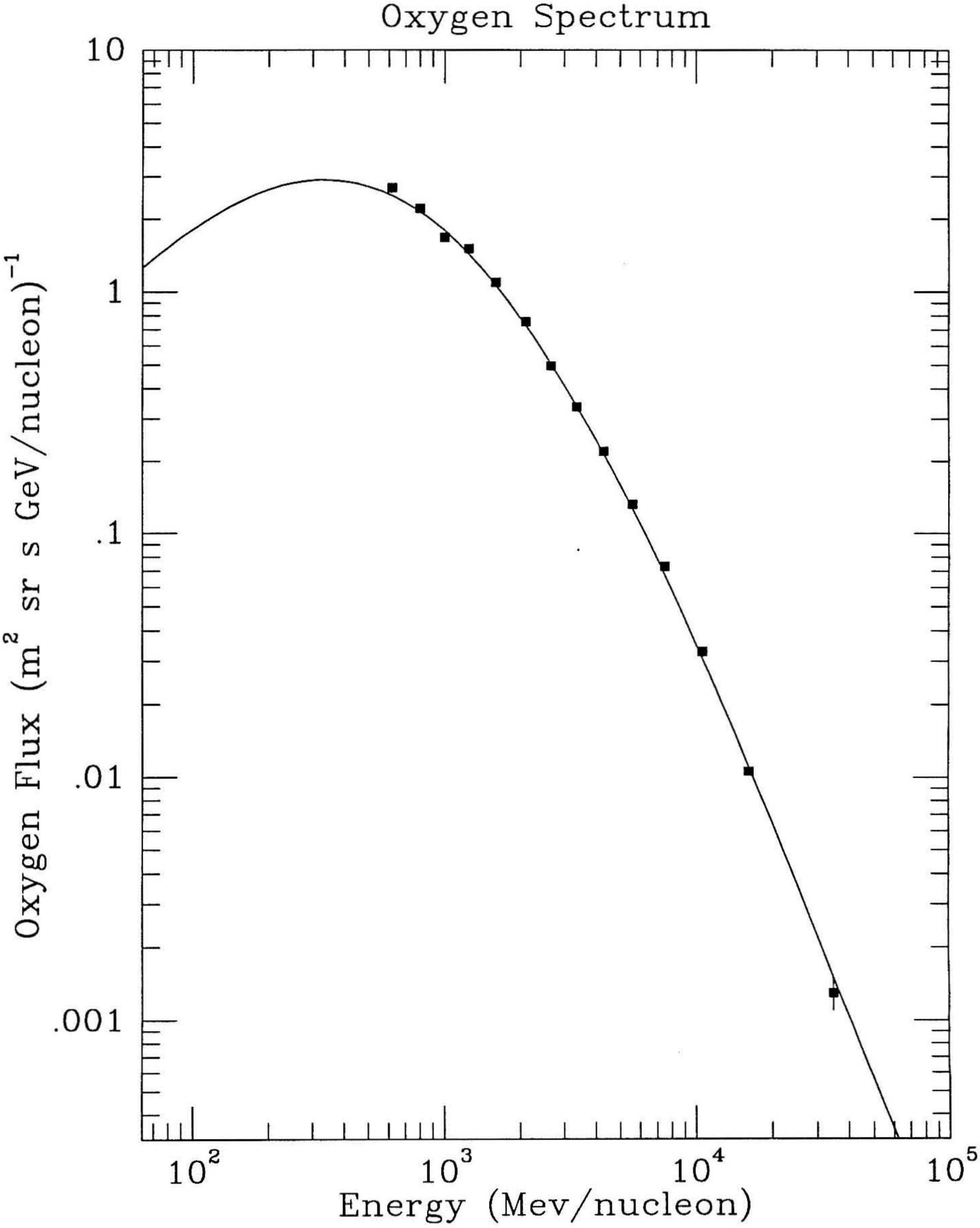

Oxygen Spectrum
10
1
.1
.01
.001
10^2
10^3
10^4
10^5
Energy (Mev/nucleon)
Oxygen Flux $(m^2$ sr s GeV/nucleon$)^{-1}$

Figure 5.3(a)

Measurements of the cosmic ray element ratios B/C and F/Ne. Boron and fluorine are thought to be absent at the cosmic ray source (or present in only minute quantities) and are created by the fragmentation of heavier cosmic ray nuclei during propagation through interstellar space. These "secondary" to "primary" ratios constrain the path-length through which the cosmic rays have traveled. The solid curves are results of the adopted galactic propagation model (Model 2 of Table 5.4). Measurements: Open circles: this work. Solid circles: Krombel and Wiedenbeck 1988. Solid squares: Engelmann et al. 1990. Open triangles: Dwyer and Meyer 1987. Solid triangle: Ferrando et al. 1991.

Figure 5.3(a)

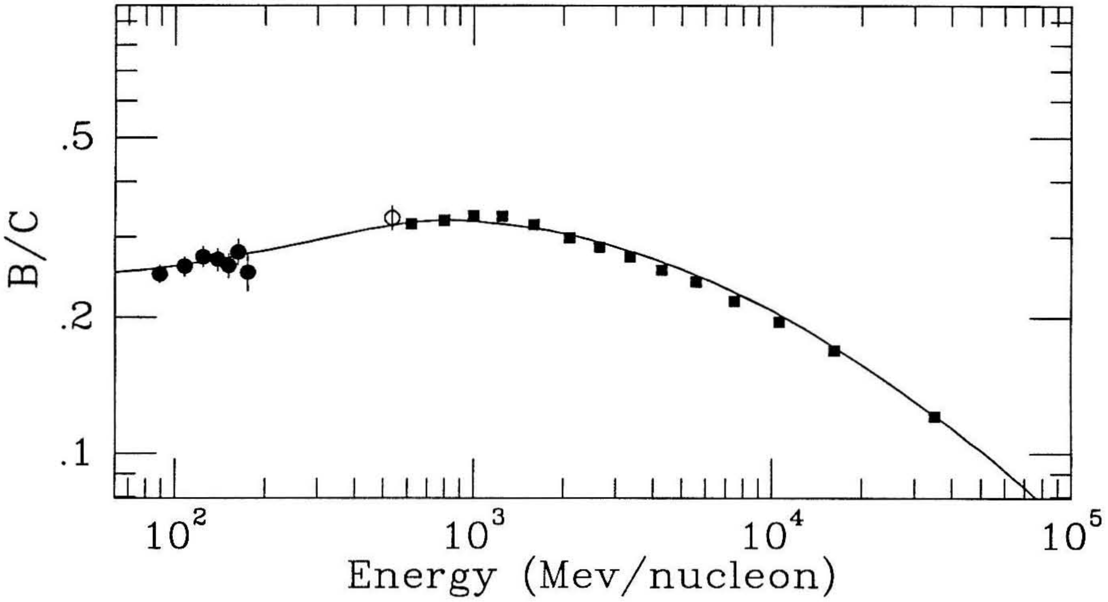
B/C
.5
.2
.1
10^2
10^3
10^4
10^5
Energy (Mev/nucleon)

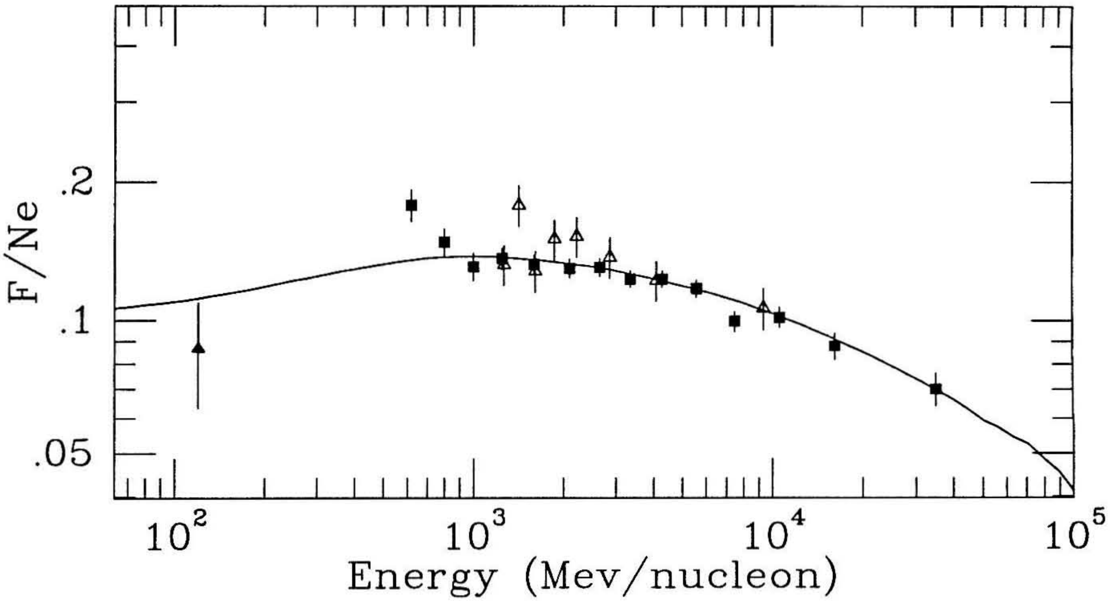
F/Ne
.2
.1
.05
10^2
10^3
10^4
10^5
Energy (Mev/nucleon)

Figure 5.3(b)

Measurements of the cosmic ray element ratios N/O and C/O. The solid curves are results of the galactic propagation model. Measurements: Open circles: this work. Solid circles: Krombel and Wiedenbeck 1988. Solid squares: Engelmann et al. 1990.

Figure 5.3(b)

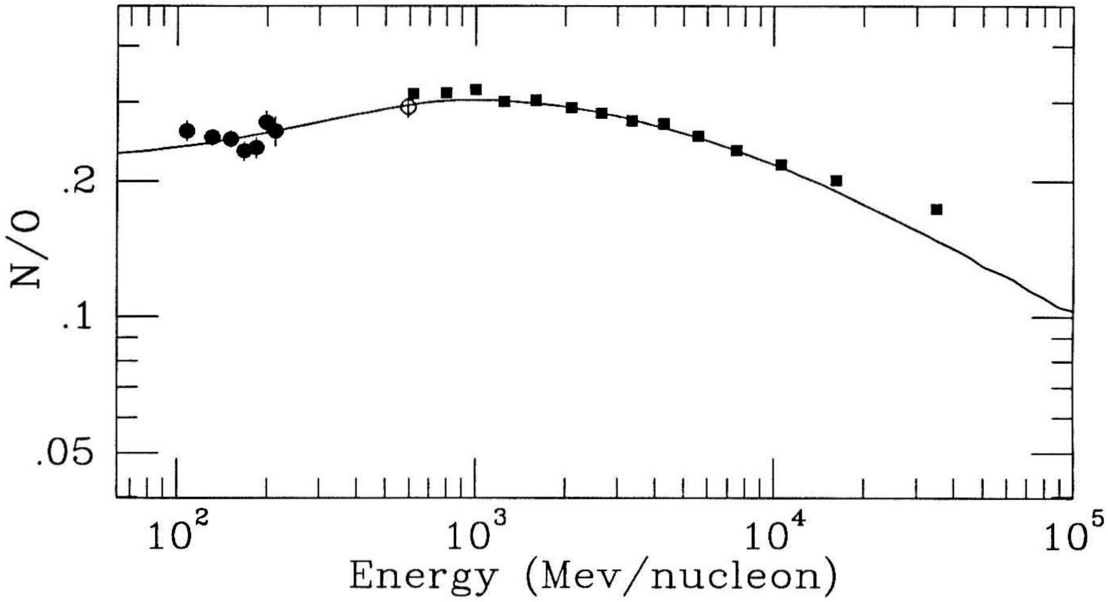
N/O
.2
.1
.05
10^2
10^3
10^4
10^5
Energy (Mev/nucleon)

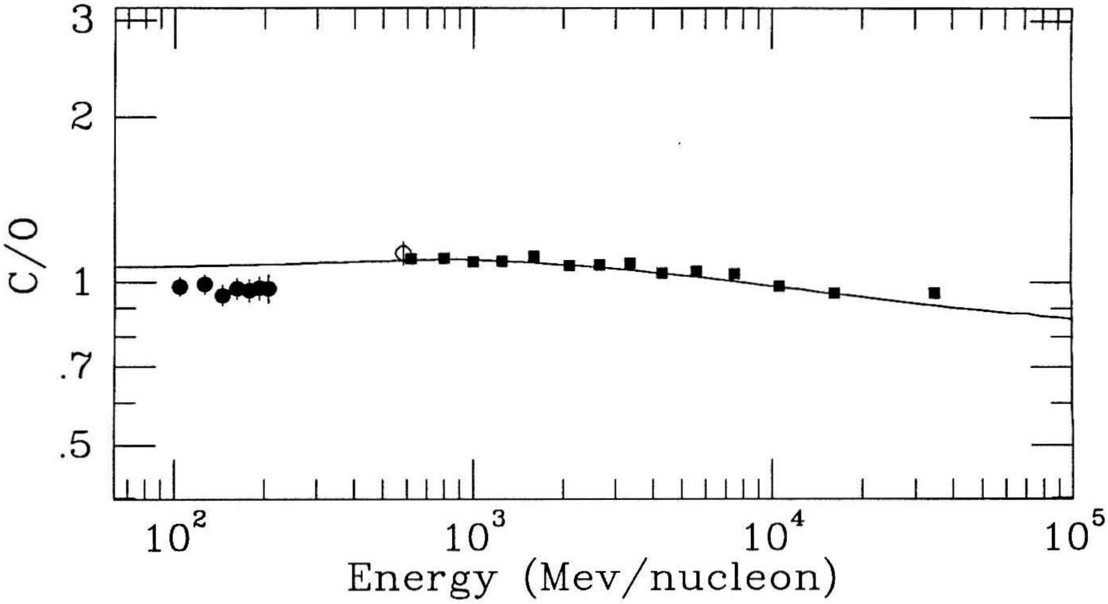
C/O
3
2
1
.7
.5
10^2
10^3
10^4
10^5
Energy (Mev/nucleon)

Figure 5.4

Solid curves show the B/C ratio predicted by the galactic propagation models after correcting for solar modulation (see Table 5.4 for model parameters). Measurements: Open circles: this work. Solid circles: Krombel and Wiedenbeck 1988. Solid squares: Engelmann et al. 1990.

Figure 5.4

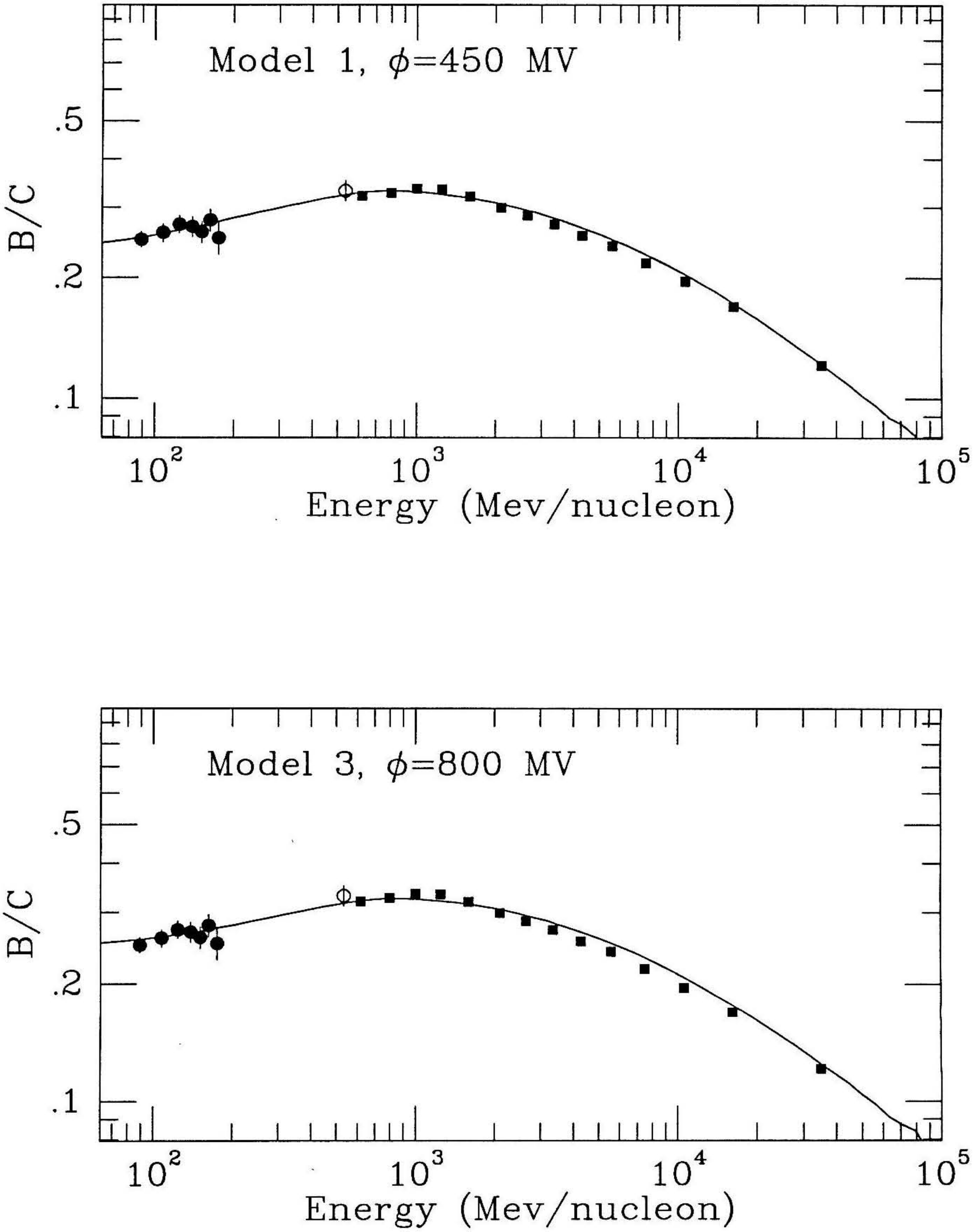
Model 1, ϕ=450 MV
B/C
.5
.2
.1
10^2
10^3
10^4
10^5
Energy (Mev/nucleon)
Model 3, ϕ=800 MV
B/C
.5
.2
.1
10^2
10^3
10^4
10^5
Energy (Mev/nucleon)

Then, the relation is inverted to find the CRS abundance as a function of observed abundance. The calculated source abundances are given in Table 5.7.

Table 5.7 HEIST Abundance Ratios

Ratio	Actual Observed	Top of Instrument (Equal ΔE)	Top of Atmosphere	CRS
$^{10}B/B$	$0.368 \pm .016$	$0.305 \pm .016$	$0.285 \pm .016$	...
$^{15}N/N$	$0.509 \pm .017$	$0.533 \pm .019$	$0.541 \pm .025$	< 0.490
$^{15}N/O$	$0.135 \pm .006$	$0.177 \pm .012$	$0.158 \pm .012$	< 0.040
$^{14}N/O$	$0.130 \pm .006$	$0.157 \pm .010$	$0.134 \pm .010$	$0.042 \pm .014$
$^{13}C/^{12}C$	$0.096 \pm .007$	$0.103 \pm .008$	$0.089 \pm .008$	$0.005^{+.011}_{-.005}$
$^{17}O/^{16}O$	$0.025 \pm .006$	$0.024 \pm .006$	$0.019 \pm .006$	< 0.007
$^{18}O/^{16}O$	$0.023 \pm .003$	$0.0278 \pm .0033$	$0.0273 \pm .0033$	$0.0115 \pm .0038$

CRS abundance uncertainties caused by possible inaccuracies in the propagation model calculations have been estimated and included in quoted errors in Table 5.7. The partial cross sections which determine the production of secondary cosmic-ray nuclei are assumed to have 10% uncertainties for those experimentally measured by Webber et al. and 20% uncertainties for those estimated from their empirical model. Webber et al. (1990c) report experimental uncertainties of 5% or better for the majority of the cross sections measured, so the 10% uncertainty used here is chosen to be a conservative value. They also report that comparisons of the empirical model predictions with cross sections measured by other experimenters typically yield's agreement of ~20%. The uncertainties in fragmentation production from the various primary nuclei were compounded assuming that the cross section errors are uncorrelated. Uncertainty in the escape mean-free-path for cosmic rays has also been included by compounding an estimated 3% uncertainty in fitting to the observed B/C ratio with uncertainties in the fragmentation production of boron, assuming no boron in the cosmic ray source. The resulting uncertainty in λ_e is $\sim$28%, resulting in 5% to 8% uncertainties in the isotopic ratios of interest.

Uncertainties in the source abundances of many cosmic ray species are dominated by uncertainties in fragmentation production during galactic propagation, so improving the accuracy of propagation calculations is of critical importance for finding accurate CRS abundances. By using improved fragmentation cross sections, including many which have recently been experimentally measured, and by modeling solar modulation and escape path-length in a self-consistent manner, secondary production has been evaluated more accurately than has been possible in most previous studies.

Chapter 6

Interpretation and Conclusions

6.1. Isotopic Abundances at the Cosmic Ray Source

The resulting HEIST measurements of the cosmic ray source abundances of carbon, nitrogen, and oxygen isotopes are summarized in Table 6.1. Figure 6.1 compares these measurements to previous satellite and balloon observations along with results from the propagation model, and Figure 6.2 shows a subset of these observations which have been selected by requiring that the mass resolution of the experiment be $\leq$0.30 amu. Also listed in Table 6.1 are the results of taking a weighted average of the high resolution results shown in Figure 6.2 after correcting back to the cosmic ray source using our propagation model. Propagation uncertainties, estimated as described in §5.4, have been included in the error bars of both the HEIST and the weighted average measurements.

Essentially all of the boron observed in cosmic rays is believed to be of "secondary" origin; that is, it is produced by the fragmentation of heavier "primary" cosmic ray nuclei such as carbon and oxygen as they pass through interstellar material. The agreement of the ^{10}B/B observations with the propagation model results shown in Figure 6.1 serves as a check on the model and its nuclear fragmentation cross sections.

More than 80% of the observed nitrogen in cosmic rays is also of secondary origin making a determination of the ^{15}N/N ratio at the source difficult. A variety of cosmic ray elemental and isotopic studies over the past decade and a half have shown that the ^{14}N/O ratio at the CRS is ~3 to 4 times smaller than in the solar system (Preszler et al. 1975; Mewaldt et al. 1981; Wiedenbeck et al. 1979; Webber

Table 6.1 Cosmic Ray Source and Solar System Abundance Ratios

Ratio	CRS HEIST	CRS Average	Solar System (Cameron,1982)
$^{15}N/N$	< 0.490	...	0.0037
$^{15}N/O$	< 0.040	...	0.0005
$^{14}N/O$	$0.042 \pm .014$	...	0.1255
$^{13}C/^{12}C$	$0.005^{+.011}_{-.005}$	$0.004 \pm .010$	0.0112
$^{17}O/^{16}O$	< 0.007	$0.0026 \pm .0030$	0.0004
$^{18}O/^{16}O$	$0.0115 \pm .0036$	$0.0075 \pm .0024$	0.0020

1983). As shown in Table 6.2, our observations of $^{15}N/N$ and N/O are consistent with this nitrogen underabundance as are the recent results of Krombel and Wiedenbeck (1988). Using our propagation model to correct back to CRS abundances favors no ^{15}N in cosmic ray source material. Gupta and Webber (1989) also derive similar source abundances for the nitrogen isotopes by fitting the results of their propagation model to a compilation of isotope measurements.

Silberberg, Shapiro, and Tsao (1975) suggested that the nitrogen abundance in cosmic rays could be used as to test whether cosmic rays represent recent supernova ejecta, which should have a low nitrogen abundance, or ISM material, which is observed to have an N/O ratio similar to the solar system (Hawley 1978; Peimbert and Torres-Peimbert 1977; York 1983) or possibly higher than the solar system (Cummings and Stone 1987). It is interesting to note that Rosa and Mathis (1985) have found an average N/O ratio of 0.038 ±0.011 in the H II region 30 Doradus, which contains a cluster of massive stars including blue supergiants and Wolf-Rayet stars. The most massive stars of such giant OB associations have already reached the last stages of their evolution and may have already produced

Table 6.2 Abundance of Nitrogen Isotopes at the CRS

Reference	$^{15}N/O$	$^{14}N/O$
Krombel and Wiedenbeck, 1988	<0.052	0.037 ± 0.017
Gupta and Webber, 1989	≤ 0.01	0.038 ± 0.010
This work	≤ 0.040	0.042 ± 0.014

supernova events, possibly altering abundances within the region. From the current derivations of a cosmic ray source ratio for N/O which is one-third of the solar system value, it appears that cosmic rays are not representative of the local ISM unless there exist a fractionation mechanism which would affect the N/O ratio.

Our $^{13}C/^{12}C$ measurement favors a CRS ^{13}C abundance that is lower than that in the solar system, as do all of the measurements in Figure 6.2(b) and a recent Voyager measurement at 22 AU (Lukasiak et al. 1991). However, taking into account the uncertainty in the production of secondary ^{13}C, our $^{13}C/^{12}C$ measurement is consistent with a range of values including a solar system ^{13}C abundance and with no ^{13}C in the CRS. Taking a weighted average of the measurements in Figure 6.2(b) we find $^{13}C/^{12}C = 0.004 \pm 0.010$ at the CRS, including propagation uncertainties. This result is slightly below the solar system value and 1 σ below the Stahl et al. level of ^{13}C in the ISM; however, it is 1.9 σ below the Hawkins and Jura $^{13}C/^{12}C$ ISM value (see §6.2.1). Webber and Soutoul (1989) have also concluded that the CRS $^{13}C/^{12}C$ ratio is below the Hawkins and Jura measurement. This difference between ISM and CRS abundances, if verified, would provide additional evidence that cosmic rays are not representative of ISM material. Additional measurements of partial cross sections, particularly for the fragmentation of ^{16}O, could verify whether the current measurements are free of systematic errors and further reduce the still substantial uncertainties in fragmentation production of ^{13}C,

^{14}N, ^{15}N, ^{10}B, and ^{11}B.

Our measured source abundance of ^{17}O is consistent with the near zero solar system ^{17}O abundance, and the weighted average of the ^{17}O measurements gives an ^{17}O excess of marginal significance. However, the derived ^{18}O abundance at the CRS indicates an enrichment of ^{18}O relative to the solar system ratio of ^{18}O/^{16}O = 0.0020 by a factor of 4 to 8. A CRS excess of ^{18}O is also indicated by all of the other measurements in Figure 6.2(c), when interpreted using our propagation model. It should be emphasized that recent improvements in the accuracy of the relevant fragmentation cross sections have allowed the determination of this ^{18}O excess. An ^{18}O excess above the solar system value is also indicated in the results of Lukasiak et al.(1991). Taking a weighted average of the ^{18}O measurements in Figure 6.2(c) after correcting back to the cosmic ray source using our propagation model results in a CRS value of ^{18}O/^{16}O = 0.0075±.0024, 2.3 σ above the solar system value, including propagation uncertainties discussed above. The interpretation of these earlier measurements as indicating an ^{18}O excess is due to recent measurements of many of the fragmentation cross sections. These measurements have improved the accuracy of the cross sections and have reduced the calculated secondary contribution to the observed ^{18}O. Approximately 53% of the secondary ^{18}O comes from primaries for which the fragmentation cross sections have been experimentally measured. Uncertainties in the weighted average cosmic ray source abundances of the oxygen isotope ratios come approximately equally from measurement uncertainties and propagation model uncertainties. Thus, determination of oxygen source abundances would benefit from both additional cosmic ray measurements and improvements in knowledge of the relevant fragmentation cross sections.

6.2. Models of Cosmic Ray Sources

A number of observations have found differences between the isotopic composition of the cosmic ray source and solar system material. Figure 6.3 has been adapted from Mewaldt (1989) in order to summarize the current status of isotope

Figure 6.1(a)

A comparison of collected cosmic ray isotope measurements for boron and nitrogen. The solid curves show the results of propagation calculations which assume solar system abundances of CNO isotopes at the cosmic ray source and assume a ^{14}N/O ratio of 0.04. Measurements: Open circle; this work. Filled circles: Krombel and Wiedenbeck 1988; Wiedenbeck and Greiner 1981a,b. Filled squares: Mewaldt et al. 1981. Filled triangles: Guzik 1981. Open triangles: Webber et al. 1985; Webber 1982; Webber and Kish 1979. Open squares: Brynak et al. 1983; Ferrando et al. 1988; Goret et al. 1983; Soutoul et al. 1983 (The open squares are mean mass measurements using the geomagnetic cutoff method.).

Figure 6.1(a)

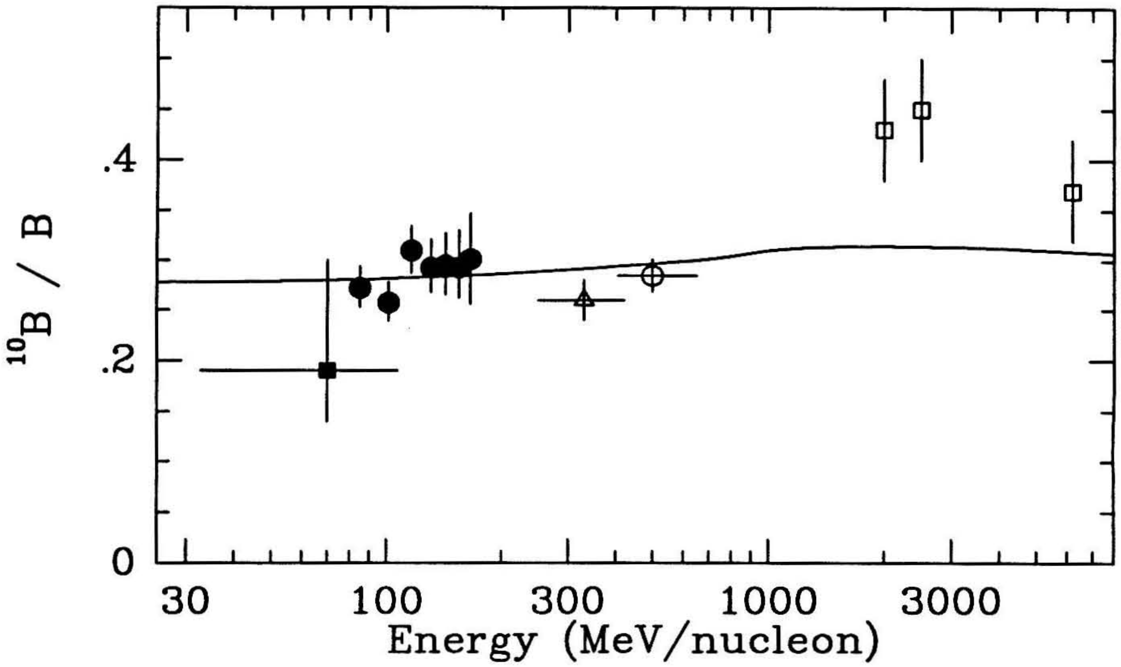

^{10}B / B
0
.2
.4
30
100
300
1000
3000
Energy (MeV/nucleon)

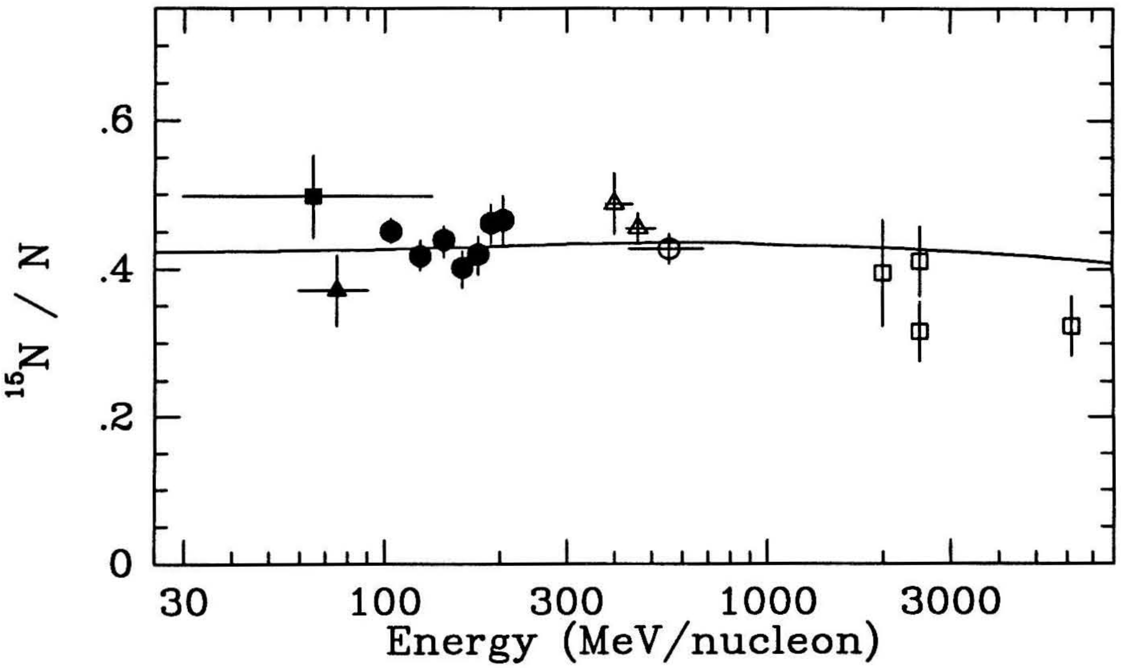

^{15}N / N
0
.2
.4
.6
30
100
300
1000
3000
Energy (MeV/nucleon)

Figure 6.1(b)

A comparison of collected cosmic ray isotope measurements for carbon. The solid curve shows the results of propagation calculations which assume solar system abundances of CNO isotopes at the cosmic ray source and assume a ^{14}N/O ratio of 0.04. Measurements: Open circle; this work. Filled circles: Krombel and Wiedenbeck 1988; Wiedenbeck and Greiner 1981a,b. Filled squares: Mewaldt et al. 1981. Filled triangles: Guzik 1981. Open triangles: Webber et al. 1985; Webber 1982; Webber and Kish 1979. Open squares: Brynak et al. 1983; Ferrando et al. 1988; Goret et al. 1983; Soutoul et al. 1983 (The open squares are mean mass measurements using the geomagnetic cutoff method.).

Figure 6.1(c)

A comparison of collected cosmic ray isotope measurements for oxygen. The solid curve shows the results of propagation calculations which assume solar system abundances of CNO isotopes at the cosmic ray source. Measurements: same as Figure 6.1(b).

Figure 6.1(d)

A comparison of collected cosmic ray isotope measurements of the ^{14}N/O and ^{15}N/O ratios. The solid curve shows the results of propagation calculations which assume that N/O=0.04 and solar system abundances of CNO isotopes at the cosmic ray source. Measurements: same as Figure 6.1(b).

Figure 6.1(b)

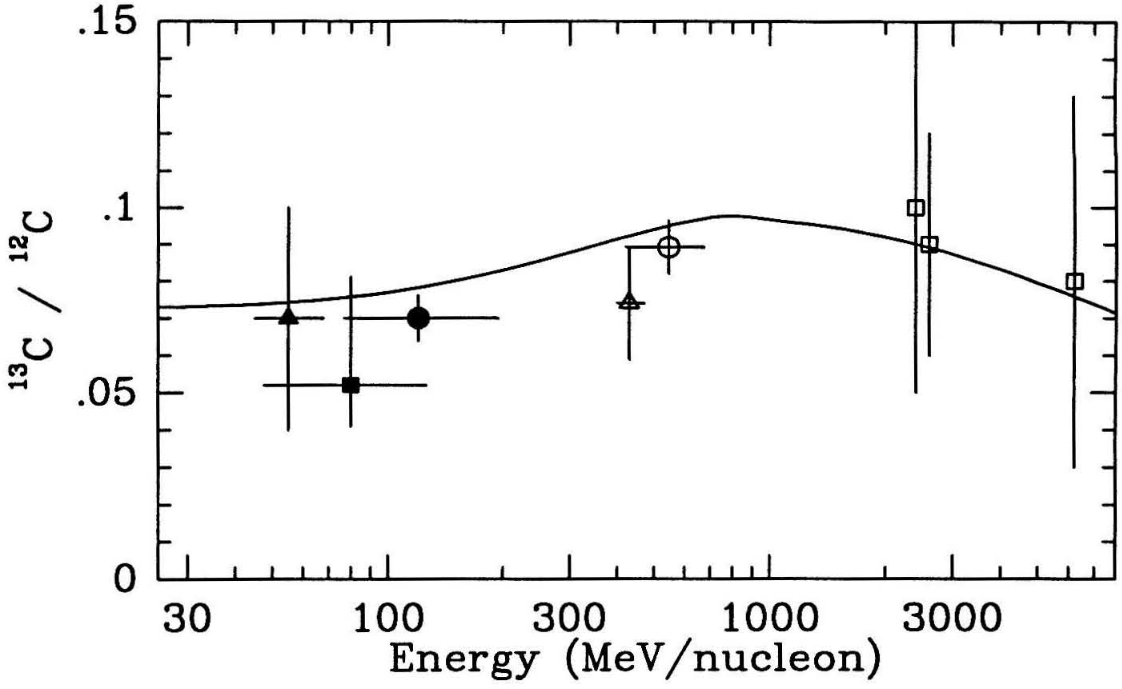

Figure 6.1(c)

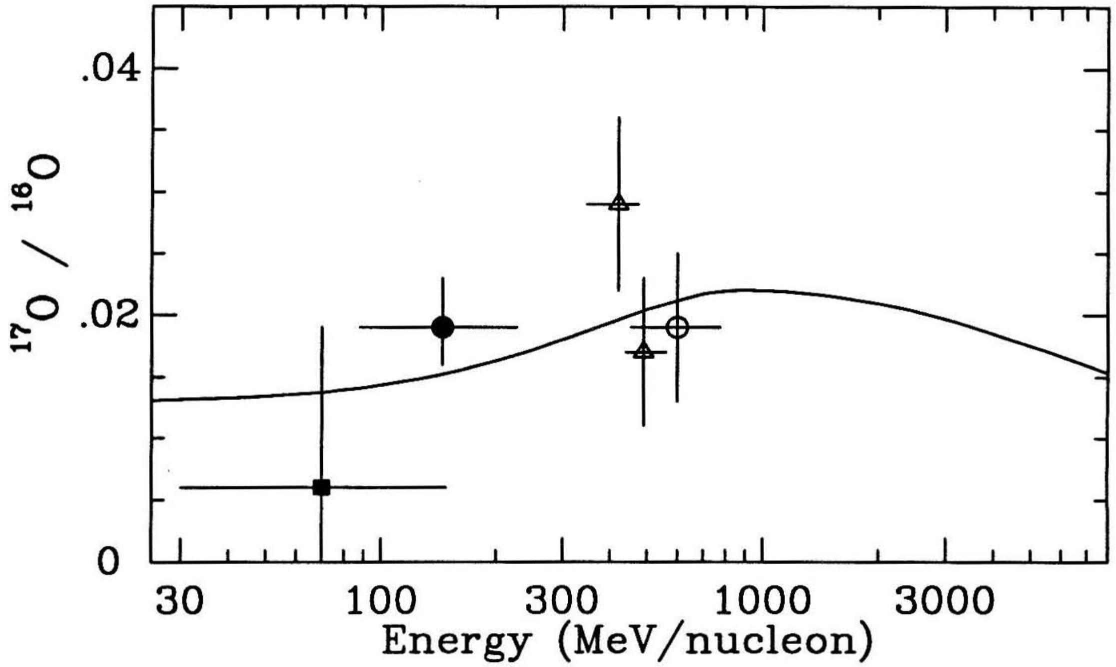
.04
.02
0
^{17}O / ^{16}O
30
100
300
1000
3000
Energy (MeV/nucleon)

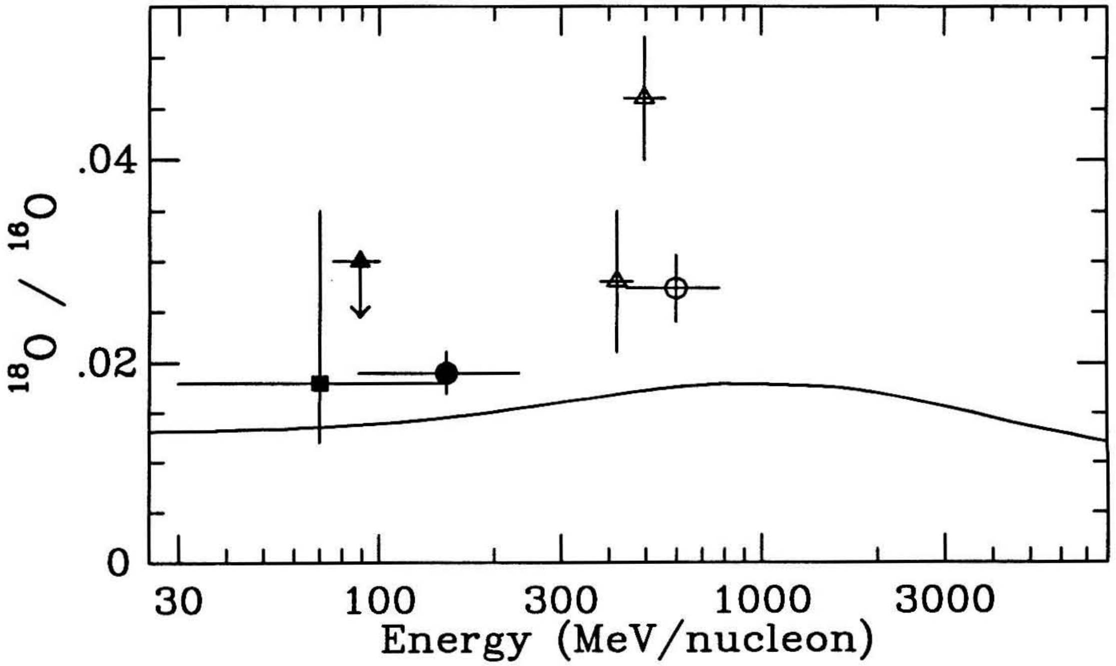
.04
.02
0
^{18}O / ^{16}O
30
100
300
1000
3000
Energy (MeV/nucleon)

Figure 6.1(d)

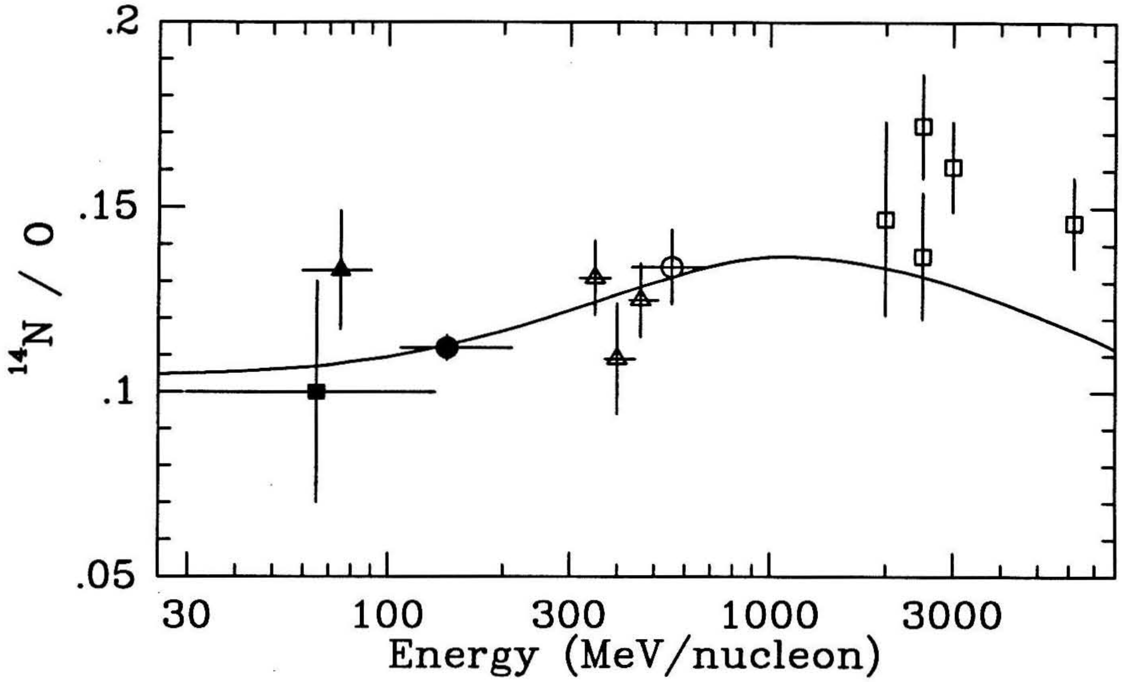
.2
.15
.1
.05
^{14}N / O
30
100
300
1000
3000
Energy (MeV/nucleon)

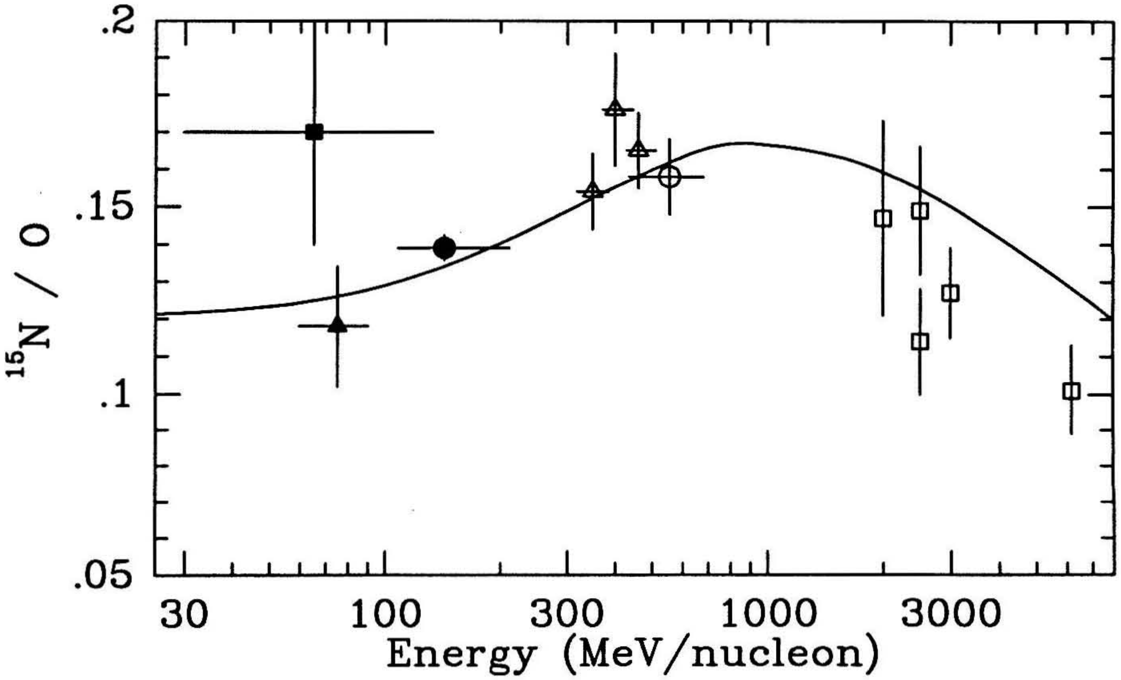
.2
.15
.1
.05
^{15}N / O
30
100
300
1000
3000
Energy (MeV/nucleon)

Figure 6.2(a)

A comparison of collected cosmic ray isotope measurements for boron and nitrogen having resolution better than 0.3 amu. The solid curves show the results of propagation calculations which assume solar system abundances of CNO isotopes at the cosmic ray source and assume a ^{14}N/O ratio of 0.04. Measurements: Open circle; this work. Filled circles: Krombel and Wiedenbeck 1988; Wiedenbeck and Greiner 1981a,b. Filled squares: Mewaldt et al. 1981. Open triangles: Webber et al. 1985; Webber 1982.

Figure 6.2(b)

A comparison of collected cosmic ray isotope measurements for carbon having resolution better than 0.3 amu. The solid curve shows the results of propagation calculations which assume solar system abundances of CNO isotopes at the cosmic ray source. The dashed curve assumes zero abundance of ^{13}C at the source. Measurements: same as Figure 6.2(a).

Figure 6.2(c)

A comparison of collected cosmic ray isotope measurements for oxygen having resolution of 0.3 amu or better. The solid curve shows the results of propagation calculations which assume solar system abundances of CNO isotopes at the cosmic ray source. The dashed curve results from an ^{18}O/^{16}O ratio of 0.0075 at the source. Measurements: same as Figure 6.2(a).

Figure 6.2(a)

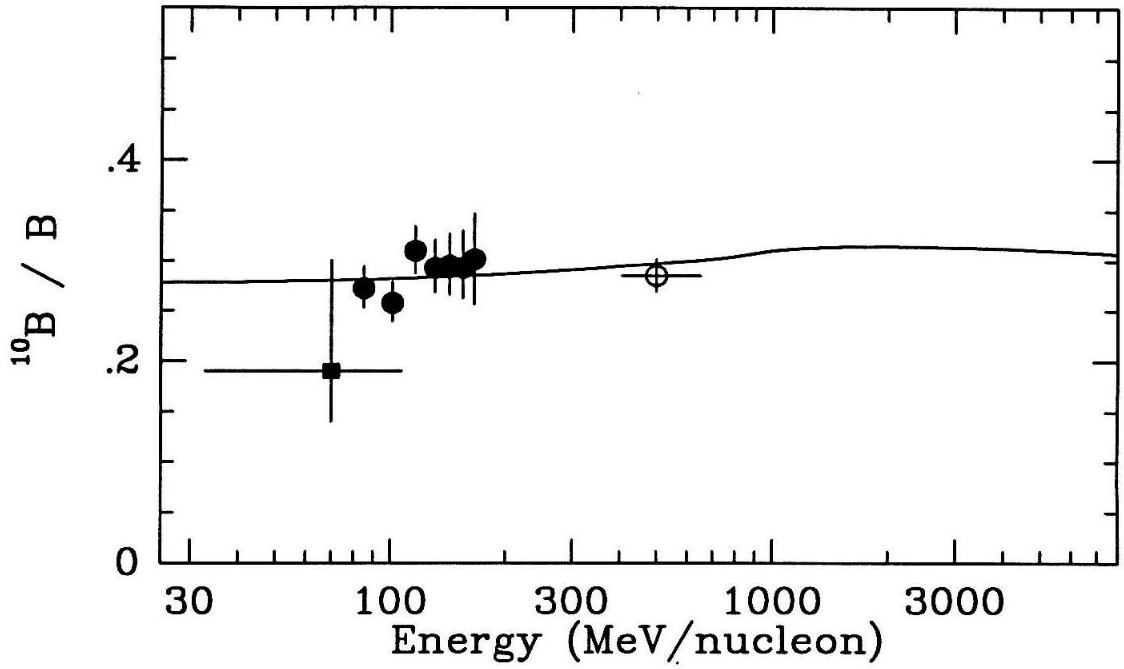

^{10}B / B
0
.2
.4
30
100
300
1000
3000
Energy (MeV/nucleon)

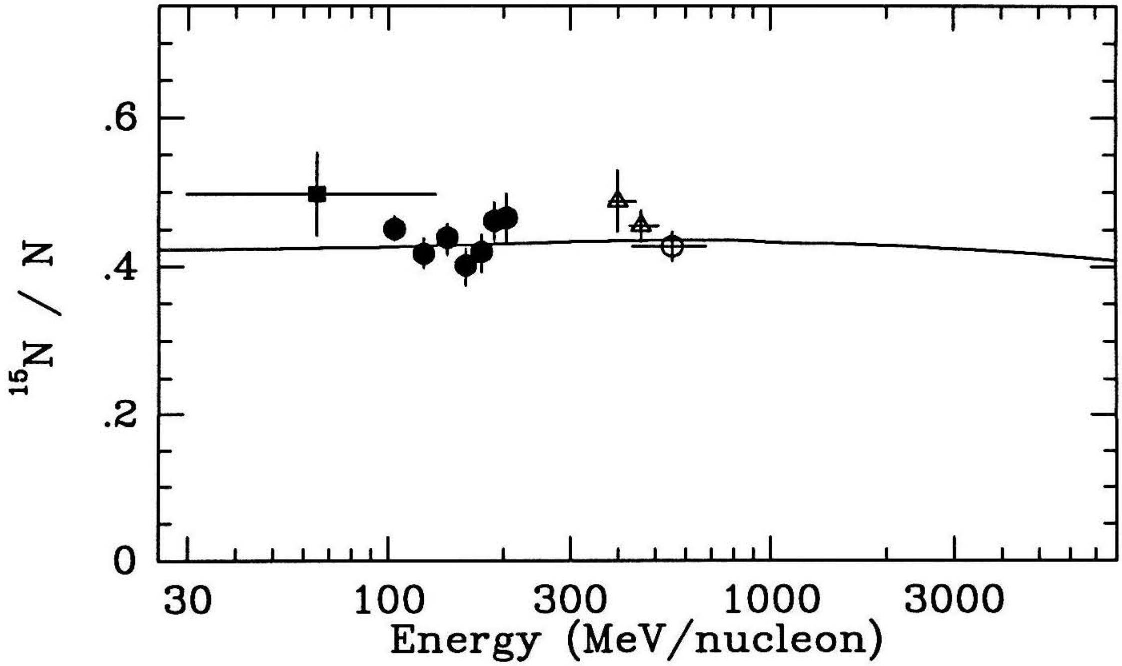

^{15}N / N
0
.2
.4
.6
30
100
300
1000
3000
Energy (MeV/nucleon)

Figure 6.2(b)

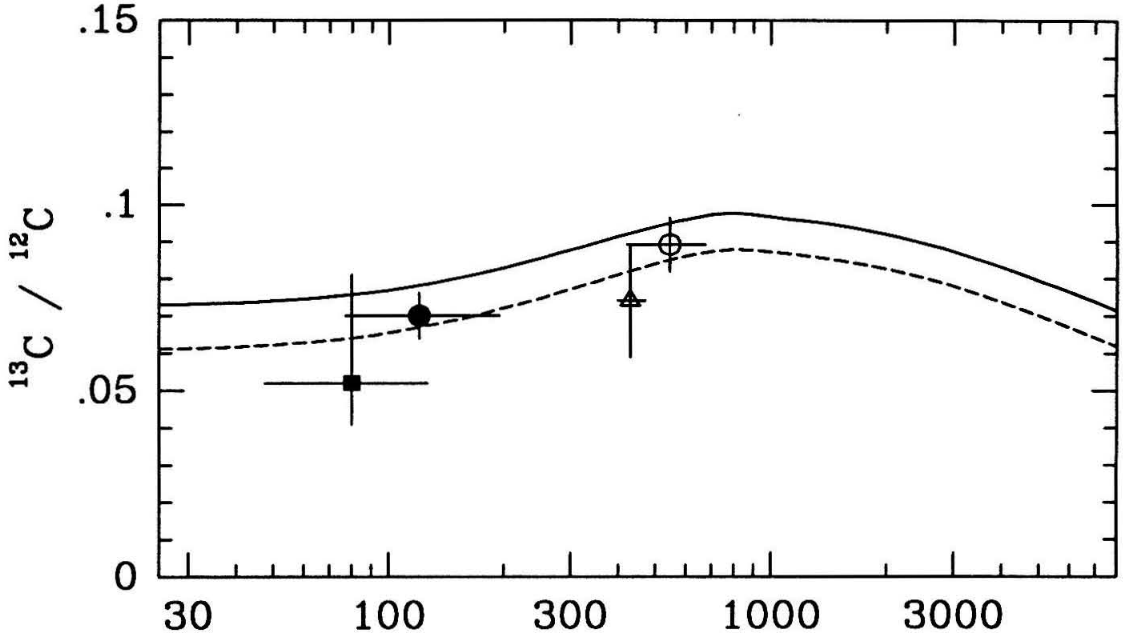

Figure 6.2(c)

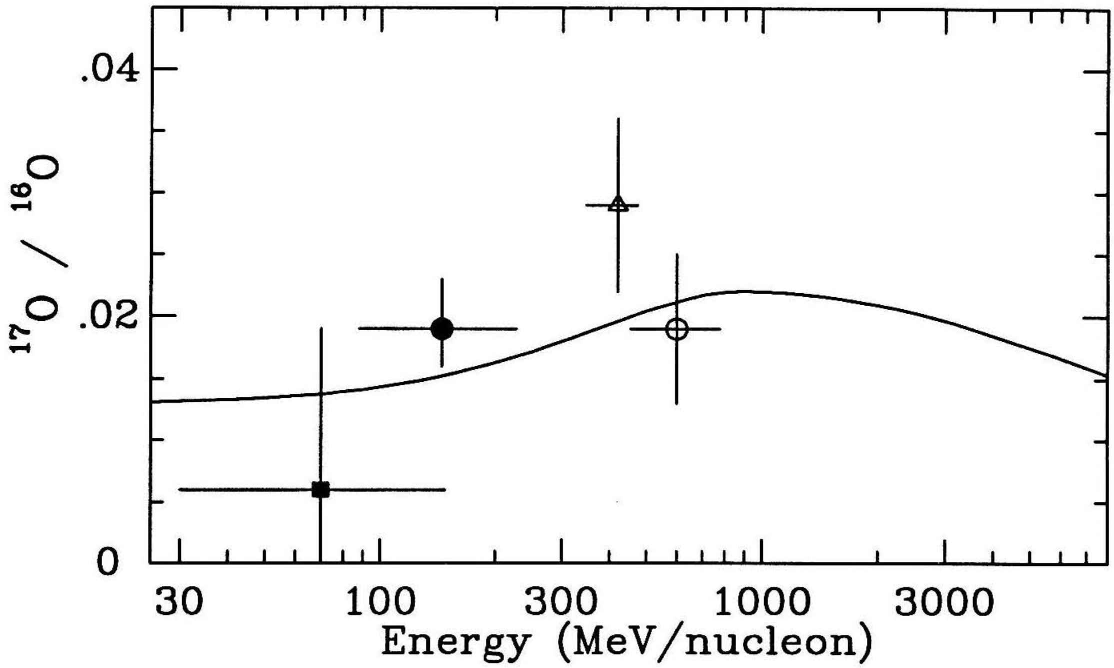
.04
.02
0
^{17}O / ^{16}O
30
100
300
1000
3000
Energy (MeV/nucleon)

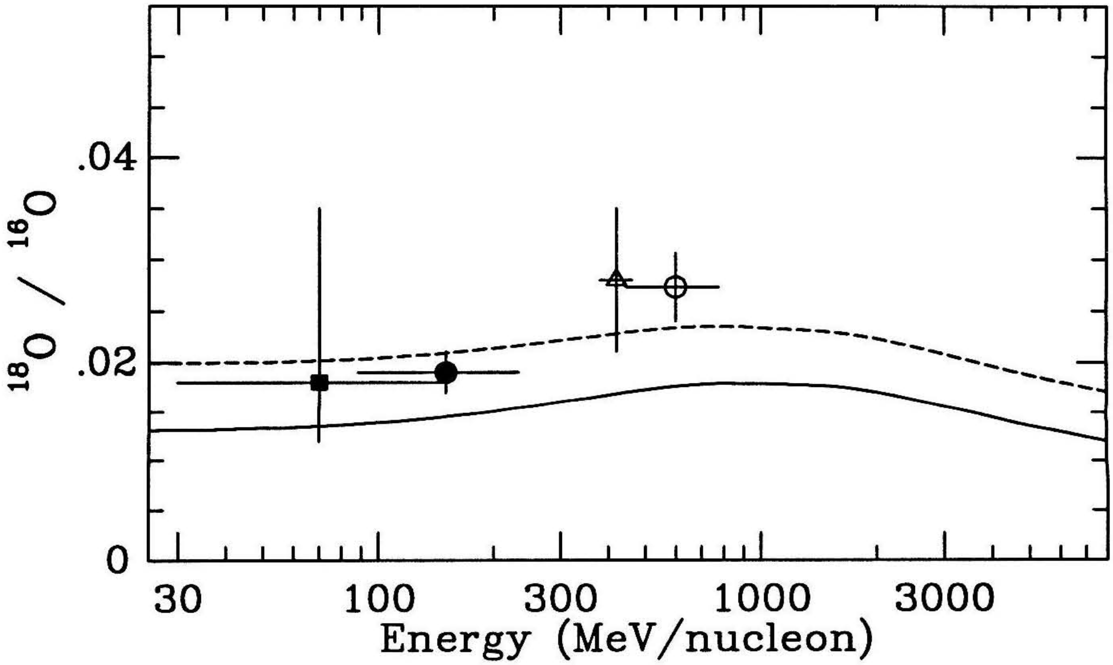
.04
.02
0
^{18}O / ^{16}O
30
100
300
1000
3000
Energy (MeV/nucleon)

Figure 6.3

A summary of the measured isotopic abundance ratios in the cosmic rays, normalized to solar system ratios. The solid circles are the weighted average results reported in this thesis. The solid squares are from the review by Mewaldt (1989). The open circles are abundances which have been more recently revised by Webber et al. (1990) using new fragmentation cross sections, and the open squares are an average of the silicon measurements by Wiedenbeck and Greiner (1981b) and Hesse et al. (1991) interpreted using our propagation model. Also shown are the values predicted by the Wolf-Rayet model calculation of Prantzos et al. (1986) and the supermetallicity model (Woosley and Weaver, 1981).

Figure 6.3

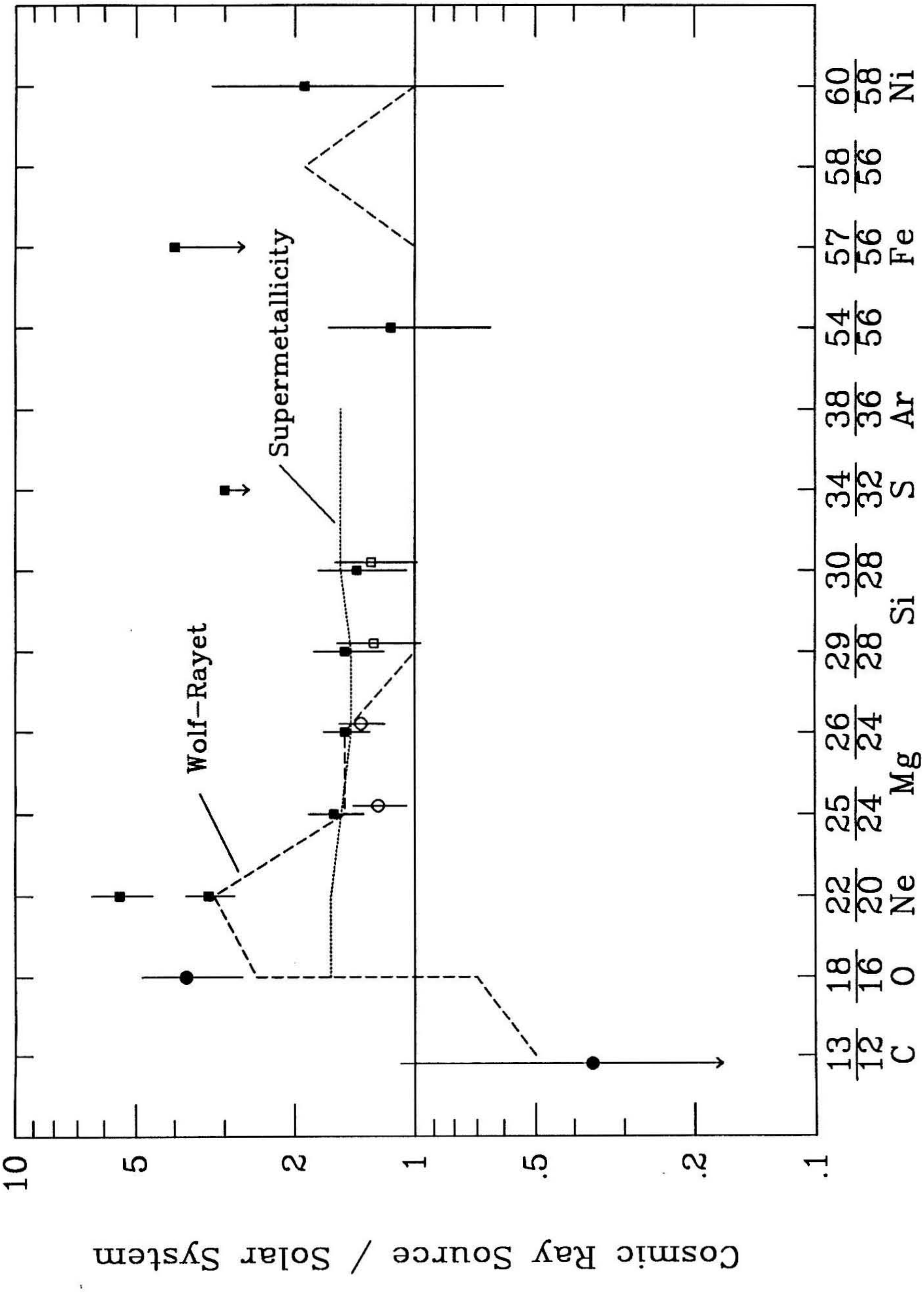
Cosmic Ray Source / Solar System
10
5
2
1
.5
.2
.1
13/12 C
18/16 O
22/20 Ne
25/24
26/24 Mg
29/28
30/28 Si
34/32 S
38/36 Ar
54/56
57/56 Fe
58/56
60/58 Ni
Wolf—Rayet
Supermetallicity

measurements. Also shown are predictions of the Wolf-Rayet model and the supermetallicity model of cosmic ray origin, which are discussed below.

6.2.1. Chemical Evolution of the ISM

As noted above, models of the chemical evolution of our galaxy predict that the elemental and isotopic abundances in the ISM have changed since the formation of the solar system $4.5\text{x}10^9$ years ago. Cosmic rays, which are believed to have been accelerated within the last 10-15 million years (Wiedenbeck and Greiner 1980; Garcia-Munoz et al. 1977; Simpson and Garcia-Munoz 1987 and references therein), serve as one test of galactic evolution models, if cosmic rays represent a sample of ISM material. Several models predict an increase in the $^{13}C/^{12}C$ ratio with galactic age (Tosi 1982; Greggio and Tosi 1986; Tosi 1988; Audouze 1985; Gusten and Mezger 1982). Models constructed by Audouze (1985) and Gusten and Ungerechts (1985) also predict an increase with time in the $^{14}N/^{15}N$ ratio in agreement with radio measurements of the $^{14}N/^{15}N$ ratio in interstellar molecular clouds.

Radio, optical, and ultraviolet (UV) observations of emission and absorption lines from interstellar molecular clouds have been used to study the abundances of carbon, nitrogen, and oxygen isotopes in the interstellar medium (ISM). A brief summary of these measurements is given below. In the cosmic ray literature, isotopic ratios are commonly presented as a fraction of the total elemental abundance (e.g., $^{14}N/N$) or with the less abundant isotope in the numerator (e.g., $^{13}C/^{12}C$), the astronomy community commonly presents measurements in terms of the ratio of the more abundant isotope to the less abundant (e.g. $^{12}C/^{13}C$). In the following discussion of astronomical results, we will follow the convention used in the astronomical literature.

A number of groups have made optical measurements of the carbon isotope ratio, several of which are for the molecular cloud in the direction of ζ Ophiuchus. The results span the range of $^{12}C/^{13}C = \sim 40\text{-}80$, and the actual ISM value remains a matter of contention, although it does seem to be larger than the solar system value of $^{12}C/^{13}C = 89$.

Hawkins and Jura (1987) calculated a weighted average of the results of measurements of $^{12}CH^+/^{13}CH^+$ toward five stars in order to estimate the $^{12}C/^{13}C$ ratio for the "local" interstellar medium. They find a mean $^{12}C/^{13}C$ ratio of 43 ± 4 ($^{13}C/^{12}C = 0.023 \pm .003$) in agreement with their earlier reported measurement of 43 ± 6 (Hawkins et al. 1985) toward ζ Oph. However, Crane, Hegyi, and Lambert (1991) note that Vanden Bout and Snell (1980) reported a value of $^{12}C/^{13}C$ of 77 (+17; -12), and Stahl et al. (1989) found a value of 77 ± 3 in measurements of CH^+ toward ζ Oph. Crane, Hegyi, and Lambert determined the $^{12}CH^+/^{13}CH^+$ abundance ratio to be 67.6 ± 4, and conclude that the Hawkins and Jura value may be anomalous since it is significantly lower than the three other independent measurements by different groups. After additional observations, Stahl and Wilson (1991) indicate a "most likely" ratio toward ζ Oph of 70.

From radio observation of carbon monoxide toward ζ Oph Langer, Glassgold, and Wilson (1987) found the $^{12}C/^{13}C$ ratio to be 80(+70; -10), and Langer and Penzias (1990) found evidence for a systematic gradient in the Galactic $^{12}C/^{13}C$ ratio from analyzing a series of millimeter-wave observations of nine interstellar molecular clouds. By observing the doubly rare isotope of carbon monoxide, $^{13}C^{18}O$, and the rare species $^{12}C^{18}O$, they find a gradient across the Galaxy for which the $^{12}C/^{13}C$ ratio changes from about 30 at a radius of 5 kpc to about 70 at 12 kpc. They find a Galactic center value of 24, and an average value of 57 near the solar radius, which lies between the values determined from CH^+ absorption measurements. Also, Wannier, Penzias, and Jenkins (1982) have measured ultraviolet absorption lines of ^{12}CO and ^{13}CO toward ζ Oph and find an isotope ratio of 55 ± 11. In addition to these interstellar measurements, the $^{12}C/^{13}C$ abundance ratio for Comet Halley was measured (Wyckoff et al. 1989) to be 65 ± 9. Thus both Comet Halley and the interstellar medium appear to have an enhanced level of ^{13}C relative to the solar system $^{13}C/^{12}C$ value.

Models of galactic elemental evolution (see §5.7.1) predict that the $^{13}C/^{12}C$ ratio should increase with time because ^{13}C is a product of secondary nuclear processing; so, finding a higher ^{13}C abundance near the more evolved central regions of the Galaxy is consistent with the models. The $^{12}C/^{13}C$ ratio in the local ISM at the present stage of evolution is predicted to lie within the range of 40 to 75 (Tosi 1982; Gusten and Mezger 1982; Audouze 1985) as compared to 89 for solar system material which condensed ~4.5 billion years ago.

The isotopic abundance of interstellar oxygen has been studied at radio wavelengths by Penzias (1981) who found a uniformity in the $^{18}O/^{17}O$ ratios measured in molecular clouds ranging from the Galactic center out to a maximum distance of 12 kpc. The results of these measurements and of carbon, nitrogen, and oxygen isotope measurements of molecular envelopes around red giant stars are reviewed by Wannier (1985), and additional measurements are given by Wannier and Sahai (1987), and Wannier et al. (1991). For the red giant observations, the $^{17}O/^{18}O$ values varied considerably but were in all cases higher than in the solar system or the ISM. The $^{12}C/^{13}C$ ratio also ranged from 6 to 53, always showing a ^{13}C enhancement relative to the solar system value.

A summary of isotope ratios at various astrophysical locations has been adapted from Wannier et al. (1991) and is given in Table 6.3. Wannier suggests that the solar system is representative of the interstellar abundances of about five billion years ago while the galactic disk values represent current interstellar abundances. The molecular clouds in the galactic center represent more evolved material as evidenced by the galactic center's higher metallicity and older stellar population. He suggests that red giants may represent a source of highly processed material which is currently enriching the ISM. If cosmic rays represent a recent sample of ISM material, then they should also have abundances which are more evolved than solar system material.

As evidence of this progressive evolution, note that both the $^{13}C/^{12}C$ and $^{17}O/^{16}O$ ratios increase from solar system to the galactic disk to the red giant values, both of which are expected to increase with exposure to CNO processing. From recent observations of nitrogen isotopes in molecular envelopes surrounding red giant stars, Wannier et al. (1991) find that the $^{14}N/^{15}N$ ratio also shows a systematic increase as is predicted for material with increased nuclear processing. The uniformity of the $^{18}O/^{17}O$ values measured in 14 molecular clouds, including two near the galactic center region, is puzzling as ^{18}O is thought to be produced primarily in supernovae while ^{17}O is produced by red giants and novae. The galactic evolution of ^{18}O is not well understood, but some evolution models (Audouze, 1985) predict that the $^{18}O/^{16}O$ ratio should decrease with time.

Table 6.3 Compilation of CNO Isotopic Abundance Ratios
(Normalized to Solar System Values)

	Solar System Value				
Location	$^{17}O/^{18}O$ = 1/5.5	$^{13}C/^{12}C$ = 1/89	$^{17}O/^{16}O$ =1/2630	$^{18}O/^{16}O$ =1/490	$^{14}N/^{15}N$ =273/1
Solar System	1.0	1.0	1.0	1.0	1.0
ISM(radio)	1.48 ±.05	1.4 ±0.3	1.1 ±0.3	1.0 ±0.2	1.1 ±0.15
ISM(optical)		1.1 - 2.0			
CRS (ave)	<6.0	0.4 ±0.9	6.8 ±7.5	3.7 ±1.2	>0.6
Galactic Center	1.59 ±.10	3.2 ±0.8	2.9 ±1.2	2.0 ±0.8	2.5 ±0.6
Red Giants	9(2.2-16)	6(1-16)	6(2.4-16)	0.9 ±0.3	(>1 to >15)

Due to the large uncertainties in the cosmic ray source abundances, few definite conclusions can be drawn. The abundance of ^{15}N may be depleted at the cosmic ray source, in agreement with evolved source material, but a precise value of $^{14}N/^{15}N$ at the cosmic ray source is difficult to determine due to the large secondary contribution to cosmic ray nitrogen. Similarly, there is no convincing evidence of an excess of ^{17}O in cosmic rays although an excess of ~20 is allowed by the data (Table 6.2). Present measurements of cosmic ray $^{13}C/^{12}C$ suggest that the cosmic rays may be depleted in ^{13}C relative to the ISM instead of being enhanced as galactic evolution models would predict, but the large uncertainties in both the CRS and ISM values do not rule out consistency between the values. As noted before, improvements in cross section measurements and new cosmic ray and ISM abundance measurements should continue to improve the accuracy of these comparisons.

6.2.2. Wolf-Rayet Stars

The Wolf-Rayet model for cosmic ray origin (e.g., Casse and Paul 1982) proposes that a fraction of cosmic rays come from material expelled by Wolf-Rayet (WR) stars. Wolf-Rayet stars' intense stellar winds, with velocities of several thousand km/sec, make WR stars an attractive source of cosmic ray material. The winds drive WR stars' mass loss rates of ~ 5×10^{-5} solar masses per year and the stellar wind termination shock surrounding these stars would be expected to accelerate the ejected material to modest energies, where it may be further accelerated by shock waves from supernovae. Wolf-Rayet stars eject mass into the ISM at a total rate comparable to the mass input from all OB stars, but this rate is still a factor of 4 smaller than that from late-type stars and planetary nebula (Abbot and Conti 1987). The high mass loss also has the effect of ejecting the outer layers of the stars so that core burning products are exposed at the stellar surfaces. Wolf-Rayet stars are divided into subtypes based on spectral determinations of their elemental surface compositions. WN stars display spectral emission lines of helium and nitrogen. WC spectra contain the lines of carbon, oxygen, and helium ions, and the less numerous WO stars have strong O VI lines.

The evolution and nucleosythesis of Wolf-Rayet stars has been modeled in order to understand the stars' evolution, the nuclear abundances in the interiors and at the surfaces of the stars, and to predict the composition of the stars' ejecta (Prantzos et al. 1986; Prantzos et al. 1987; Maeder 1990; Maeder and Meynet 1987). In the models of Prantzos et al., the Wolf-Rayet star evolves from a massive O type progenitor which enters the WN phase after the onset of core He burning. As illustrated in Figure 6.4, the stellar surface of the WN star is enhanced in nitrogen which has been produced during the preceding CNO cycle hydrogen burning. When mass loss strips away this nitrogen rich envelope exposing the products of helium burning, the surface becomes enriched in carbon and oxygen and enters the

WC phase. Near the end of core He burning, the oxygen abundance at the surface may surpass the carbon abundance and send the star into the WO phase of evolution. About 80% of the $\sim 5 \times 10^5$ yr lifetime of a Wolf-Rayet star is spent in the WC phase.

Most of the star's initial carbon, nitrogen, and oxygen is burned into ^{14}N when the CNO cycle hydrogen burning nears completion. At the onset of core He burning, the ^{14}N is changed into ^{18}O by the reaction $^{14}\mathrm{N}(\alpha,\gamma)\,^{18}\mathrm{F}(e^+\nu)\,^{18}\mathrm{O}$, and for a short period of time ^{18}O becomes the second most abundant species in the core. The ^{18}O is destroyed mainly through $^{18}\mathrm{O}(\alpha,\gamma)^{22}\mathrm{Ne}$ and also through $^{18}\mathrm{O}(\alpha,n)^{21}\mathrm{Ne}$. Also, the much smaller abundances of ^{13}C and ^{17}O are destroyed at the beginning of He burning by (α,n) reactions. Throughout most of the He burning stage, the major nuclides present are ^{4}He, ^{12}C produced by the 3–α reaction, ^{16}O produced from $^{12}\mathrm{C}(\alpha,\gamma)^{16}\mathrm{O}$, and ^{22}Ne. During helium burning, the abundances of ^{25}Mg and ^{26}Mg also become significant by steadily increasing through $^{22}\mathrm{Ne}(\alpha,n)\,^{25}\mathrm{Mg}$ and $^{22}\mathrm{Ne}(\alpha,\gamma)\,^{26}\mathrm{Mg}$.

After a ^{22}Ne excess was observed in cosmic ray nuclei, Casse and Paul (1982) proposed that a fraction of the cosmic rays originate from material expelled by Wolf-Rayet stars. They predicted that diluting the WR material by a factor of 60 would fit a factor of three excess of ^{22}Ne in cosmic rays (relative to solar system $^{22}\mathrm{Ne}/^{20}\mathrm{Ne}$). Their calculations also predicted an enhancement in ^{12}C by a factor of ~ 2, an enhancement in ^{18}O by a factor of ~ 2.5, and an $\sim 30\%$ enhancement in ^{14}N. This dilution factor of 60 is averaged over all cosmic ray species including hydrogen and helium and may be somewhat misleading in terms of the relative WR contribution to heavier nuclei such as C, O, and ^{22}Ne, which are greatly enhanced in WR stars. Using this dilution factor, over 20% of CNO nuclei in cosmic rays would come from Wolf-Rayet sources.

In view of the similarity in the elemental composition of the cosmic ray source and solar energetic particles, Meyer (1985a) suggested that the "normal" material in which the Wolf-Rayet ejecta is diluted are cosmic rays extracted from the coronae of ordinary F to M type stars. This explains in a natural way the similarity of cosmic

Figure 6.4

Evolution of the abundances, expressed in mass fraction, at the surface of a star which has a "zero age" main sequence mass of 60 solar masses (from Prantzos, Doom, Arnould, and de Loore, 1986). The evolution of species with mass number A<20 and A>20 are shown in separate diagrams for clarity. The stellar phases are indicated at the top of the diagrams. Note that a change in the time scale occurs near the onset of He burning.

Figure 6.4

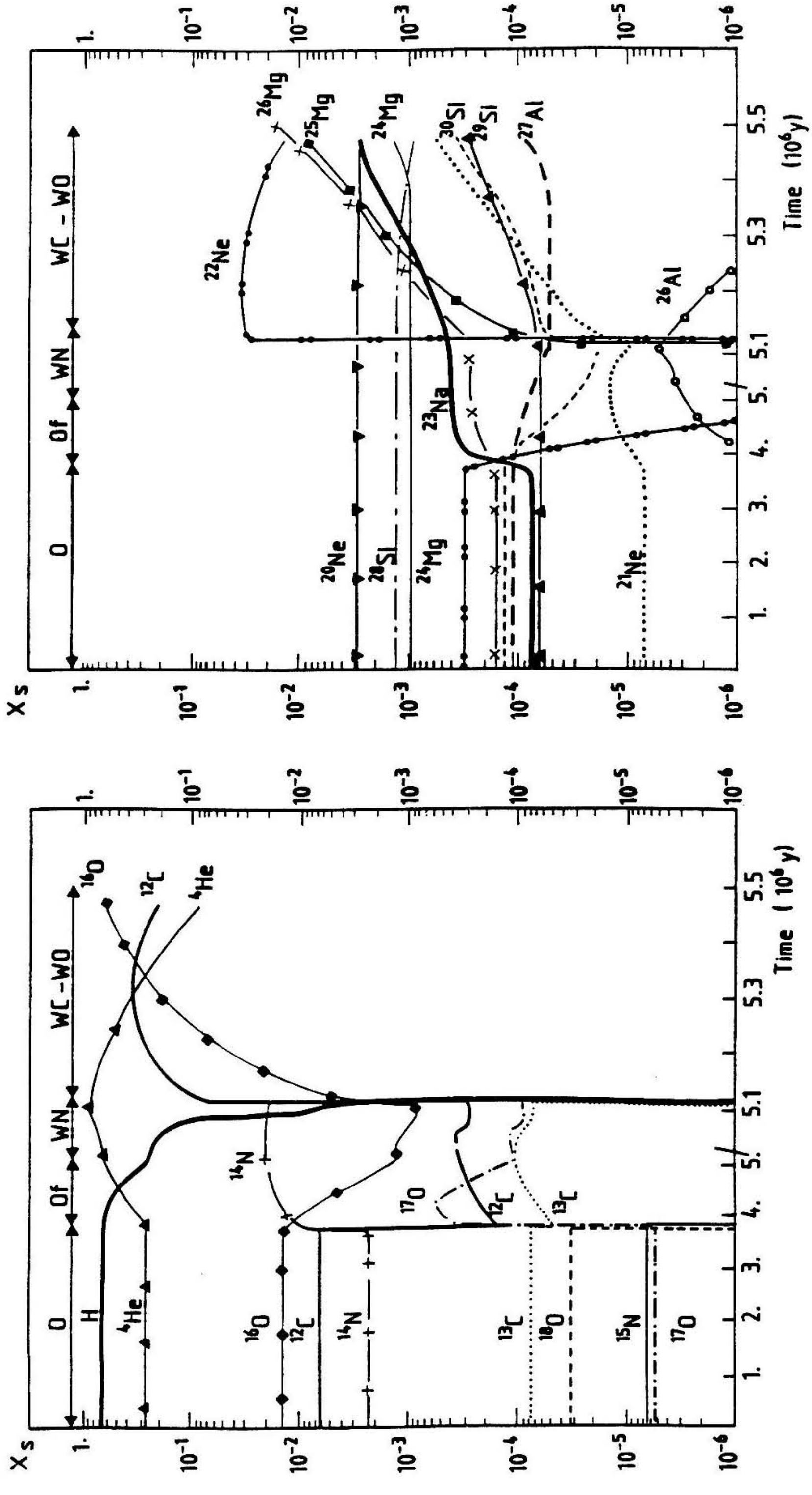
Xs
1.
10^-1
10^-2
10^-3
10^-4
10^-5
10^-6
Time (10^6 y)
1.
2.
3.
4.
5.
5.1
5.3
5.5
O
Of
WN
WC - WO
H
4He
16O
12C
14N
13C
18O
15N
17O
22Ne
26Mg
25Mg
24Mg
30Si
29Si
27Al
26Al
23Na
20Ne
28Si
21Ne

ray and solar energetic particle abundances, since the same processes are assumed to operate in the solar corona and in the coronae of F to M stars.

Meyer (1985a) notes that the comparable ^{22}Ne and ^{12}C excesses predicted by models of Wolf-Rayet evolution are highly model independent, but that the amount of ^{18}O and ^{16}O ejected are model dependent upon assumed stellar masses and the total mass loss during the WO phase, respectively. Simulations of WR star evolution by Prantzos et al. (1986, 1987) do indicate a large ^{18}O excess in these stars during the first few thousand years of core helium burning, but the lifetime of this excess may be too short for the stars to expel an amount of ^{18}O sufficient to cause an enhancement in the cosmic rays. Prantzos et al. (1986) show that the amount of ^{18}O expelled is quite sensitive to the assumed stellar mass, and make no prediction for cosmic ray ^{18}O.

Noting recent observations which found that a number of Wolf-Rayet stars show both WN and WC spectral signatures, N. Langer (1991) estimates that ~6% of the average lifetime of a Wolf-Rayet star may be spent in the WN/WC state where the surface composition appears to be a mixture of H and He-burning products. Langer has developed a stellar model in which a slow, semiconvective mixing process between the He-burning core and an overlying mantle layer consisting of the ashes of complete hydrogen burning (~99% He, ~1% ^{14}N) creates a transition layer with an intermediate composition. The semiconvective transition layer controls the rate of mixing between the convective core and the convective overlying mantle. This model results in a WN/WC phase with surface abundance enhancements of ^{14}N, ^{12}C, ^{22}Ne, and ^{18}O lasting for $\sim 3\ 10^4$ yr.

While Wolf-Rayet models also predict that cosmic ray ^{25}Mg/^{24}Mg and ^{26}Mg/^{24}Mg ratios will be a factor of 1.5 greater solar system values, Meyer (1985b, 1987) pointed out that because fractionation based on atomic first ionization potential (FIP) affects ordinary cosmic ray material, this main component in which the WR material is being diluted has a Mg (a "low-FIP" element) abundance which is ~6 times higher than "high-FIP" Ne, C, and O. So, unless the WR material is also fractionated, the predicted enhancements in ^{25}Mg and ^{26}Mg will be small. Since it is not obvious why Wolf-Rayet ejecta would suffer FIP fractionation similar to that of material from ordinary F to M stars, Prantzos, Arnould, and Arcoragi (1987) have calculated the abundances which result from mixing a FIP fractionated main component and an unfractionated WR component. Their results are summarized in Table 6.4. They argue that the lack of knowledge about cosmic ray acceleration sites and mechanisms does not allow any firm conclusions to be drawn regarding the relative fractionation of the normal and WR components. They suggest that the WR component could be accelerated in a medium far from the WR star, where FIP selection effects similar to those fractionating the main component could exist, resulting in no relative fractionation between the two components.

In summary, current models of Wolf-Rayet stars normalized to account for the ^{22}Ne excess in cosmic rays also predict a ^{12}C excess consistent with the observed carbon overabundance and with the possible underabundance in ^{13}C relative to the solar system ^{13}C/^{12}C ratio. The Wolf-Rayet model of Prantzos et al. also predict an overabundance of oxygen, but the oxygen excess is not sufficient to explain the N/O ratio in cosmic rays when combined with the dilution factor of 1/60 which seems to fit the ^{22}Ne/^{20}Ne, ^{13}C/^{12}C, and C/O observations. The WR model also appears to fit the small overabundance observed in the neutron-rich isotopes of Mg. The possible factor of $\sim$1.5 excess of ^{29}Si and ^{30}Si reported by Wiedenbeck and Greiner (1981b) is reduced when interpreted using the new cross section measurements of Webber et al. (1990a-d)(see also Webber, Soutoul, Ferrando, and Gupta 1990). Using our propagation model to interpret the Si observations of Wiedenbeck and Greiner (1981b) and Hesse et al. (1991) leads to an excess in silicon's neutron-rich isotopes by a factor of approximately 1.3 ± 0.3, consistent with the WR model prediction of no excess for these isotopes. While there is much less certainty in the WR prediction of an ^{18}O excess, current models may still allow for this possibility.

Table 6.4 WR Model CRS Excesses

(relative to solar system values)

	FIP fractionation	
Normal component	yes	yes
WR component	yes	no
Species		
C	2.0	2.0
O	1.4	1.4
^{21}Ne	1.5	1.5
^{22}Ne	3.2	3.2
Na	1.4	1.1
^{25}Mg	1.5	1.1
^{26}Mg	1.5	1.1
^{29}Si	1.0	1.0
^{30}Si	1.1	1.0
^{58}Fe	1.9	1.2

6.2.3. Supermetallicity Model

A possible explanation for the ^{22}Ne enhancement in cosmic rays proposed by Woosley and Weaver (1981) is that the stars responsible for cosmic-ray production are typically super-metal-rich by a factor of 2-3 over the solar metallicity value. The production of neutron-rich nuclei in massive stars is proportional to their initial metallicity, the fraction of elements with charge greater than helium. As noted above, hydrogen burning via the complete CNO cycle burns all initial CNO nuclei into ^{14}N which is subsequently transformed into ^{22}Ne at the onset of He burning. The ^{22}Ne excess produces excesses in other neutron-rich isotopes via the reaction

^{22}Ne(α,n)^{25}Mg, a source of neutrons which can be captured by other species. The "supermetallicity" model predicts that, if cosmic rays originate in regions of the galaxy that are metal-rich compared to the solar system, they would have roughly equal enhancements in the neutron rich nuclei ^{18}O, ^{22}Ne, ^{25}Mg, ^{26}Mg, ^{29}Si, ^{30}Si , ^{34}S, and ^{38}Ar. If normalized to fit the observed cosmic ray Mg isotope abundances, the model falls short of explaining the full magnitude of the observed excess of ^{22}Ne, and predicts only a weak excess of ^{18}O. If normalized to fit ^{22}Ne and ^{18}O, it would predict larger enhancements for the neutron rich Mg and Si isotopes than observed (Mewaldt 1989). In the future, accurate measurements of the Si isotopes in CRS material should allow a key comparison to be made with the predictions of this model.

6.2.4. The Anomalous Solar System

Olive and Schramm (1982) suggest that cosmic rays may be representative of the ISM composition, and that solar system abundances may not be representative of the galaxy as a whole. They argue that if the solar system was formed as part of an OB association, its formation could have followed the explosion of at least one supernova within the association, which would have modified the composition of the proto-solar material mainly by the addition of α-particle nuclei such as ^{12}C, ^{16}O, and ^{20}Ne. Normalizing to this "anomalous" solar system composition, the model predicts that both the ISM and cosmic rays will show apparent enhancements in the ^{22}Ne/^{20}Ne and the ^{17}O/^{16}O ratios by a factor of $\sim$2, and in the ^{13}C/^{12}C ratio by a factor of $\sim$1.1 to $\sim$4.5 . The model also predicts that the ISM and cosmic rays will have larger C/O and ^{18}O/^{16}O ratios than solar system material since cosmic rays are assumed by this model to be representative of the ISM. The model is qualitatively in agreement with the observed cosmic ray enhancements in ^{22}Ne, ^{18}O, and C/O, and although cosmic rays may not have a ^{13}C/^{12}C ratio larger than the solar system, there are indications that the ISM does (§6.1). It is not yet clear whether cosmic rays and the ISM have the same composition, but anomalous cosmic rays, which may be representative of the local ISM, clearly have less ^{22}Ne than galactic cosmic rays (Mewaldt, Spalding, and Stone 1984; Cummings, Stone, and Webber 1991).

6.3. Conclusions

We have reported a $^{13}C/^{12}C$ abundance ratio of 0.089±.008 and an $^{18}O/^{16}O$ ratio of 0.027±.003 in the energy intervals ~430-670 MeV/nucleon for carbon and ~450-780 MeV/nucleon for oxygen at the top of the atmosphere, higher energies than previous direct mass measurements. We have also reported boron and nitrogen isotopic ratios of $^{10}B/B$ = 0.285±.016 and $^{15}N/N$ = 0.541±.025, consistent with earlier observations. Using a propagation model which includes recently improved fragmentation cross sections, we find that the abundances measured near Earth correspond to abundances at the cosmic ray source of $^{13}C/^{12}C$ = 0.005±.010 and $^{18}O/^{16}O$ = 0.0115±.0036. The ratios of the nitrogen isotopes to oxygen at the CRS are $^{14}N/O$ = 0.042±0.014 and $^{15}N/O \leq 0.040$, favoring no ^{15}N at the source. The carbon isotope ratio is consistent with the solar system value of $^{13}C/^{12}C$ = 0.011, but the oxygen measurement indicates a significant enhancement of ^{18}O in the cosmic rays compared to the solar system ratio of $^{18}O/^{16}O$ = 0.0020.

Combining our oxygen data with the previous high resolution measurements of Wiedenbeck and Greiner (1981a), Mewaldt et al. (1981) and Webber et al. (1985), we find $^{18}O/^{16}O$ = 0.0075±.0021 at the cosmic ray source. Indicating that $^{18}O/^{16}O$ in cosmic ray material is enhanced by a factor of 3.75 ±1.2.

There are a number of measured differences between the composition of cosmic rays and solar system material. Cosmic rays have C/O ~2 times the solar system ratio and N/O of ~1/3rd the solar system value. The helium burning products ^{18}O, ^{22}Ne, ^{25}Mg, and ^{26}Mg are also overabundant in cosmic ray material. These observed differences have been compared to the predictions of cosmic ray source models. The supermetallicity model in which cosmic rays originate from metal-rich regions of the Galaxy predicts roughly equal enhancements for ^{18}O, ^{22}Ne, ^{25}Mg, ^{26}Mg, ^{29}Si, ^{30}Si, and other neutron-rich nuclei. When normalized to fit the ^{22}Ne and ^{18}O excesses in cosmic rays, it predicts enhancements for the neutron rich Mg and Si isotopes that are larger than those observed. The Wolf-Rayet model in which a fraction of the cosmic rays originate from material expelled by Wolf-Rayet stars, predicts enhancements in ^{12}C, ^{16}O, ^{22}Ne, ^{25}Mg, and ^{26}Mg. The model, again normalized to fit the ^{22}Ne excess in cosmic rays, appears to fit the cosmic ray Mg and Si observations and predicts that the CRS ratio for ^{13}C/^{12}C should be lower than in the solar system. Whether the model can explain the N/O and ^{18}O/^{16}O ratios in cosmic rays is still in question. The "anomalous" solar system model predicts that both the ISM and cosmic rays will show enhancements in C/O, ^{22}Ne, ^{17}O, ^{18}O, and ^{13}C, qualitatively consistent with the observations except that we find no evidence for a ^{13}C excess in the cosmic rays. Also, there is some evidence that cosmic rays may not be representative of ISM material. In conclusion, the Wolf-Rayet model appears to come the closest to predicting the observed isotopic ratios, but none of the presently available models quantitatively account for all of the observed differences between cosmic rays and solar system material.

References

Abbott, D. C., and P. S. Conti, *Annual Reviews in Astronomy and Astrophysics*, **25**, 113 (1987)

Abramowitz, M. and I. A. Stegun, *Handbook of Mathematical Functions* (National Bureau of Standards: Washington, D.C., 1964)

Ahlen, S. P., *Reviews of Modern Physics*, **52**, 121 (1980)

Ahlen, S. P., B. G. Cartwright, and G. Tarlé, *Nuclear Instruments and Methods*, **136**, 235 (1976)

Ahlen, S. P., and M. H. Salamon, *Physical Review A*, **19**, 1084 (1979)

Anders, E. and N. Grevesse, *Geochimica et Cosmochimica Acta*, **53**, 197 (1989)

Audouze, J., in *Proceedings of the ESO Workshop on Production and Distribution of C, N, O Elements*. ed. I. J. Danziger, F. Matteucci, and K. Kjar, p.373 (European Southern Observatory, 1985)

Bevington, P. R., *Data Reduction and Error Analysis for the Physical Sciences*, (McGraw-Hill, 1969)

Binns, W. R., T. L. Garrard, P. S. Gibner, M. H. Israel, M. P. Kertzman, J. Klarmann, B. J. Newport, E. C. Stone, and C. J. Waddington, *Astrophysical Journal*, **346**, 997 (1989a)

Binns, W. R., T. L. Garrard, M. H. Israel, J. Klarmann, E. C. Stone, and C. J. Waddington, in *AIP Conference Proceedings 183, Cosmic Abundances of Matter*, ed. C. J. Waddington (New York: AIP, 1989b)

Blandford, R., and D. Eichler, *Physics Reports*, **154**, 1 (1987)

Breneman, H. H., and E. C. Stone, *Astrophysical Journal (Letters)*, **299**, L57 (1985)

Brynak, B., N.-Y. Herrstrom, N. Lund, B. Peters, I. L. Rasmussen, M. Rotenberg, N. J. Westergaard, P. Ferrando, P. Goret, L. Koch-Miramond, and A. Soutoul, *Proceedings of the 18th International Cosmic Ray Conference (Bangalore)*, **9**, 135 (1983)

Cameron, A. G. W., in *Essays in Astrophysics*, ed. C. A. Barnes, D. O. Clayton, and D. N. Schramm, p.23 (Cambridge: Cambridge University Press, 1982)

Cassé, M., and P. Goret, *Astrophysical Journal*, **221**, 703 (1978)

Cassé, M., and J. A. Paul, *Astrophysical Journal*, **258**, 860 (1982)

Christian, E. R., J. E. Grove, R. A. Mewaldt, S. M. Schindler, T. Zukowski, J. C. Kish, and W. R. Webber, *Proceedings of the 20th International Cosmic Ray Conference (Moscow)*, **2**, 382 (1987)

Crane, P., D. J. Hegyi, and D. L. Lambert, *Astrophysical Journal*, **378**, 181 (1991)

Cummings, A. C., and E. C. Stone, *Proceedings of the 20th International Cosmic Ray Conference (Moscow)*, **3**, 413 (1987)

Cummings, A. C., E. C. Stone, and W. R. Webber, *Proc. 22nd International Cosmic Ray Conf. (Dublin)*, in press (1991)

Dwyer, R., and P. Meyer, *Astrophysical Journal*, **322**, 981 (1987)

Engelmann, J. J., P. Ferrando, A. Soutoul, P. Goret, E. Juliusson, L. Koch-Miramond, N. Lund, P. Masse, B. Peters, N. Petrou, and I. L. Rasmussen , *Astronomy and Astrophysics*, **233**, 96 (1990)

Ferrando, P., J. J. Engelmann, P. Goret, L. Koch-Miramond, N. Petrou, A. Soutoul, N. Y. Herrstrom, B. Brynak, N. Lund, B. Peters, I. L. Rasmussen, M. Rotenberg, and N. J. Westergaard, *Astronomy and Astrophysics*, **193**, 69 (1988)

Ferrando, P., N. Lal, F. B. McDonald, and W. R. Webber, *Astronomy and Astrophysics*, **247**, 163 (1991)

Fisk, L. A., *Journal of Geophysical Research*, **76**, 221 (1971)

Fowler, P. H., R. N. F. Walker, M. R. W. Masheder, R. T. Moses, A. Worley, and A. M. Gay, *Astrophysical Journal*, **314**, 739 (1987)

Garcia-Munoz, M., G. M. Mason, and J. A. Simpson, *Astrophysical Journal*, **217**, 859 (1977)

Garcia-Munoz, M., and J. A. Simpson, *Proceedings of the 16th International Cosmic Ray Conference (Kyoto)*, **1**, 270 (1979)

Garcia-Munoz, M., J. A. Simpson, T. G. Guzik, J. P. Wefel, and S. H. Margolis, *Astrophysical Journal Supplement*, **64**, 269 (1987)

Gleeson, L. J., and W. I. Axford, *Astrophysical Journal*, **154**, 1011 (1968)

Goret, P., J. J. Engelmann, P. Ferrando, L. Koch-Miramond, N. Petrou, A. Soutoul, B. Brynak, N.-Y. Herrstrom, N. Lund, B. Peters, I. L. Rasmussen, M. Rotenberg, and N. J. Westergaard, *Proceedings of the 18th International Cosmic Ray Conference (Bangalore)*, **9**, 139 (1983)

Greggio, L., and M. Tosi, *Astronomy and Astrophysics (Letters)*, **156**, L1 (1986)

Grove, J. E., Ph.D. Thesis, California Institute of Technology (1989)

Grove, J. E., and R. A. Mewaldt, *Nuclear Instruments and Methods in Physics Research*, in press

Gupta, M, and W. R. Webber, *Astrophysical Journal*, **340**, 1124 (1989)

Gusten, R., and P. G. Mezger, *Vistas in Astronomy*, **26**, 159 (1982)

Gusten, R., and H. Ungerechts, *Astronomy and Astrophysics*, **145**, 241 (1985)

Guzik, T. G., *Astrophysical Journal*, **244**, 695 (1981)

Hawkins, I., and M. Jura, *Astrophysical Journal*, **317**, 926 (1987)

Hawkins, I., M. Jura, and D. M. Meyer, *Astrophysical Journal (Letters)*, **294**, L131 (1985)

Hawley, S. A., *Astrophysical Journal*, **224**, 417 (1978)

Hesse, A., B. S. Acharya, U. Heinbach, W. Heinrich, M. Henkel, C. Koch, B. Luzzietti, C. Pfeiffer, M. Simon, J. A. Esposito, V. K. Balasubramanyan, L. M. Barbier, E. R. Christian, J. F. Ormes, and R. E. Streitmatter, *Proceedings of the 22nd International Cosmic Ray Conf. (Dublin)*, in press (1991)

Jelley, J. V., *Cerenkov Radiation and its Applications* (Pergamon: New York, 1958)

Kox, S., A. Gamp, C. Perrin, J. Arvieux, R. Bertholet, J.F. Bruandet, M. Buenerd, R. Cherkaoui, A.J. Cole, Y. El-Masri, N. Longequeue, J. Menet, F. Merchez, and J.B. Viano, *Physical Review C*, **35**, 1678 (1987)

Krombel, K. E., and M. E. Wiedenbeck, *Astrophysical Journal*, **328**, 940 (1988)

Langer, N., *Astronomy and Astrophysics*, **248**, 531 (1991)

Langer, W. D., A. E. Glassgold, and R. W. Wilson, *Astrophysical Journal*, **322**, 450 (1987)

Langer, W. D., and A. A. Penzias, *Astrophysical Journal*, **357**, 477 (1990)

Lau, K. H., Ph.D. Thesis, California Institute of Technology (1985)

Lezniak, J. A., *Nuclear Instruments and Methods*, **136**, 299 (1976)

Lund, N., in *Cosmic Radiation in Contemporary Astrophysics*, ed. M. M. Shapiro, p.1 (Reidel: Dordrecht, Holland 1986)

Lukasiak, A, Ferrando, P., McDonald, F. B. and Webber, W. R. 1991, *Proceedings of the 22nd International Cosmic Ray Conf. (Dublin)*, in press (1991)

Maeder, A., *Astronomy and Astrophysics Supplement*, **84**, 139 (1990)

Maeder, A., and G. Meynet, *Astronomy and Astrophysics*, **182**, 243 (1987)

Mewaldt, R. A., *Reviews of Geophysics and Space Physics*, **21**, 295 (1983)

Mewaldt, R. A., in *AIP Conference Proceedings 183, Cosmic Abundances of Matter*, ed. C. J. Waddington (New York: AIP, 1989)

Mewaldt, R. A., J. D. Spalding, and E. C. Stone, *Astrophysical Journal*, **283**, 450 (1984)

Mewaldt, R. A., J. D. Spalding, E. C. Stone, and R. E. Vogt, *Astrophysical Journal (Letters)*, **251**, L27 (1981)

Meyer, J.-P., *Astrophysical Journal Supplement*, **57**, 173 (1985a)

Meyer, J.-P., *Proceedings of the 19th International Cosmic Ray Conf.(La Jolla)*, **9**, 141 (1985b)

Meyer, J.-P., in *Origin and Distribution of the Elements*, ed. G. J. Mathews (World Scientific: Singapore, 1987)

Millikan, R. A., and G. H. Cameron, *Physical Review*, **28**, 851 (1926)

Newport, B. J., Ph.D. Thesis, California Institute of Technology (1986)

Olive, K. A, and D. N. Schramm, *Astrophysical Journal*, **257**, 276 (1982)

Ormes, J. F., and R. J. Protheroe, *Astrophysical Journal*, **272**, 756 (1983)

Peimbert, M., and S. Torres-Peimbert, *Monthly Notices of the Royal Astronomical Society*, **179**, 217 (1977)

Penzias, A. A., *Astrophysical Journal*, **249**, 518 (1981)

Prantzos, N., M. Arnould, and J.-P. Arcoragi, *Astrophysical Journal*, **315**, 209 (1987)

Prantzos, N., C. Doom, M. Arnould, and C. de Loore, *Astrophysical Journal*, **304**, 695 (1986) 695

Preszler, A. M., J. C. Kish, J. A. Lezniak, G. Simpson, and W. R. Webber, *Proceedings of the 14th International Cosmic Ray Conference (Munich)*, **12**, 4096 (1975)

Rosa, M. R., and J. S. Mathis, in *Proceedings of the ESO Workshop on Production and Distribution of C, N, O Elements*. ed. I. J. Danziger, F. Matteucci, and K. Kjar, p.207 (European Southern Observatory, 1985)

Rossi, B., *High Energy Particles* (Prentice-Hall: New York, 1952)

Salamon, M. H., *Lawrence Berkeley Laboratory Publication No. 10446* (1980)

Salamon, M. H., and S. P. Ahlen, *Physical Review B*, **B24**, 5026 (1981)

Silberberg, R., M. M. Shapiro, and C. H. Tsao, *Proceedings of the 14th International Cosmic Ray Conference (Munich)*, **2**, 451 (1975)

Silberberg, R., and C. H. Tsao, *Astrophysical Journal (Letters)*, **352**, L49 (1990)

Simpson, J. A., *Annual Reviews of Nuclear and Particle Science*, **33**, 323 (1983)

Simpson, J. A., and M. Garcia-Munoz, *Space Science Reviews*, **46**, 205 (1988)

Soutoul, A., J. J. Engelmann, P. Goret, J. Jorrand, L. Koch-Miramond, P. Masse, N. Petrou, N. Herrstrom, and N. Lund, *Proceedings of the 18th International Cosmic Ray Conference (Bangalore)*, **9**, 143 (1983)

Spalding, J., Ph.D. Thesis, California Institute of Technology (1983)

Stahl, O., and T. L. Wilson, preprint (1991)

Stahl, O., T. L. Wilson, C. Henkel, and I. Appenzeller, *Astronomy and Astrophysics*, **221**, 321 (1989)

Swordy, S. P., D. Muller, P. Meyer, J. L'Heureux, and J. M. Grunsfeld, *Astrophysical Journal*, **349**, 625 (1990)

Tarlé, G., S. P. Ahlen, and B. G. Cartwright, *Astrophysical Journal*, **230**, 607 (1979)

Tosi, M., *Astrophysical Journal*, **254**, 699 (1982)

Tosi, M., *Astronomy and Astrophysics*, **197**, 33 (1988)

Tsao, C. H., and R. Silberberg, *Proceedings of the 16th International Cosmic Ray Conference (Kyoto)*, **2**, 202 (1979)

van Sciver, W. J., and L. Bogart, *Bulletin of the American Physical Society*, **2**, 142 (1957)

Vanden Bout, P. A., and R. L. Snell, *Astrophysical Journal*, **236**, 460 (1980); erratum, *Astrophysical Journal*, **246**, 1045 (1981)

Wannier, P. G., in *Proceedings of the ESO Workshop on Production and Distribution of C, N, O Elements*. ed. I. J. Danziger, F. Matteucci, and K. Kjar, p.233 (European Southern Observatory, 1985)

Wannier, P. G., B-G Andersson, H. Olofsson, N. Ukita, and K. Young, *Astrophysical Journal*, **380**, 593 (1991)

Wannier, P. G., A. A. Penzias, and E. B. Jenkins, *Astrophysical Journal*, **254**, 100 (1982)

Wannier, P. G., and R. Sahai, *Astrophysical Journal*, **319**, 367 (1987)

Webber, W. R., *Astrophysical Journal*, **252**, 386 (1982)

Webber, W. R., *Proceedings of the 18th International Cosmic Ray Conference (Bangalore)*, **9**, 151 (1983)

Webber, W. R., private communication. (1990)

Webber, W. R., and J. C. Kish, *Proceedings of the 16th International Cosmic Ray Conference (Kyoto)*, **1**, 389 (1979)

Webber, W. R., J. C. Kish, and D. A. Schrier, *Proceedings of the 19th International Cosmic Ray Conf.(La Jolla)*, **2**, 88 (1985)

Webber, W. R., J. C. Kish, and D. A. Schrier, *Physical Review C*, **41**, 520 (1990a)

Webber, W. R., J. C. Kish, and D. A. Schrier, *Physical Review C*, **41**, 533 (1990b)

Webber, W. R., J. C. Kish, and D. A. Schrier, *Physical Review C*, **41**, 547 (1990c)

Webber, W. R., J. C. Kish, and D. A. Schrier, *Physical Review C*, **41**, 566 (1990d)

Webber, W. R., J. A. Lezniak, and J. C. Kish, *Nuclear Instruments and Methods*, **111**, 301 (1973)

Webber, W. R., and A. Soutoul, *Astronomy and Astrophysics*,. **215**, 128 (1989)

Webber, W. R., A. Soutoul, P. Ferrando, and M. Gupta, *Astrophysical Journal*, **348**, 611 (1990)

Wiedenbeck, M. E., and D. E. Greiner, *Astrophysical Journal (Letters)*, **239**, L139 (1980)

Wiedenbeck, M. E., and D. E. Greiner, *Physical Review (Letters)*, **46**, 682 (1981a)

Wiedenbeck, M. E., and D. E. Greiner, *Astrophysical Journal (Letters)*, **247**, L119 (1981b)

Wiedenbeck, M. E, D. E. Greiner, F. S. Bieser, H. J. Crawford, H. H. Heckman, and P. J. Lindstrom, *Proceedings of the 16th International Cosmic Ray Conference (Kyoto)*, **1**, 412 (1979)

Woosley, S. E., and T. A. Weaver, *Astrophysical Journal*, **243**, 651 (1981)

Wyckoff, S., E. Lindhold, P. A. Wehinger, B. A. Peterson, J.-M. Zucconi, and M. C. Festou, *Astrophysical Journal*, **339**, 488 (1989)

Yamashita, M., *Radiation Detectors and Their Uses*, ed. M. Miyajima and S. Sasaki (1988)

York, D. G., *Astrophysical Journal*, **264**, 172 (1983)